CONVECTION ANALYSIS IN CLOSED CAVITY VIA FEM APPROACH

STUDENT NAME: SYED SAQIB SHAH

ENROLLMENT NO: 01-283181-003

SUPERVISOR: DR. RIZWAN UL HAQ

A thesis submitted in fulfilment of the requirements for the award of degree of DOCTOR OF PHILOSOPHY (Mathematics)

Department of Computer Science

BAHRIA UNIVERSITY ISLAMABAD

May 25, 2023

Approval of Examination

Scholar Name: SYED SAQIB SHAH

Registration Number: 56462

Enrollment: 01-283181-003

Program of Study: Ph.D MATHEMATICS

Thesis Title: Convection analysis in closed cavity via FEM approach.

It is to certify that the above scholar's thesis has been completed to my satisfaction and, to my belief, its standard is appropriate for submission for examination. I have also conducted plagiarism test of this thesis using HEC prescribed software and found similarity index 12%. That is within the permissible limit set by the HEC for the Ph.D degree thesis. I have also found the thesis in a format recognized by the BU for the Ph.D thesis.

Principal Supervisor Name: DR. Rizwan Ul Haq

Principal Supervisor Signature:

Date:

Author's Declaration

I, SYED SAQIB SHAH hereby state that my Ph.D thesis titled is my own work and has not been submitted previously by me for taking any degree from Bahria University or anywhere else in the country/world. At any time if my statement is found to be incorrect even after my graduation, the university has the right to withdraw/cancel my Ph.D degree.

Name of Scholar: Syed Saqib Shah

Date:

Plagiarism Undertaking

I, solemnly declare that research work presented in the thesis titled **"Convection analysis in closed cavity via FEM approach"** is solely my research work with no significant contribution from any other person. Small contribution/help wherever taken has been duly acknowledged and that complete thesis has been written by me. I understand the zero tolerance policy of the HEC and Bahria University towards plagiarism. Therefore I as an Author of the above titled thesis declare that no portion of my thesis has been plagiarized and any material used as reference is properly referred or cited.

I undertake that if I am found guilty of any formal plagiarism in the above titled thesis even after award of Ph.D degree, the university reserves the right to withdraw/revoke my Ph.D degree and that HEC and the University has the right to publish my name on the HEC/University website on which names of scholars are placed who submitted plagiarized thesis.

Name of Scholar: Syed Saqib Shah

Date:

Dedication

Dedicated to

My worthy parents and respected teachers

whose prays and support have always been a source of inspiration

and encouragement for me.

Acknowledgements

I am thankful to Almighty **ALLAH** Who has enabled me to learn and to achieve milestones towards my destination and His beloved Prophet Hazrat **Muhammad** (ﷺ). Who is forever a constant source of guidance, a source of knowledge and blessing for entire creation. His teachings show us a way to live with dignity, stand with honor and learn to be humble.

My acknowledgment is to my kind, diligent and highly zealous supervisor, Dr. Rizwan Ul Haq, who supported me with his cherished opinions and inspirational discussions. His valuable expertise, comments, suggestions and instructions are most welcome that greatly improved the clarity of this document. I am placing my earnest thanks to Dr. Rizwan Ul Haq. I am so grateful to work under the supervision of such a great person. My gratitude is to my honorable professors who took me to the apex of my academia with their guidance. In particular, Prof. Dr. Muhammad Ramzan and Dr. Jafar Hasnain who have always been supportive in all of my course work and kept encouraging me throughout the session in Bahria University, Islamabad Campus. They are the true teachers who have made Mathematics Department of BUIC, a real place of learning. My intense recognition is to my mother,father, brothers, sisters and Uncle (for every thing) who are always real pillars for my encouragement and showered their everlasting love, care and support throughout my life. Humble prayers, continuing support and encouragement of my family are as always highly appreciated. As usual, so many friends and my class-mates have helped me throughout my Ph.D that I cannot list them all. In particular, Ali Raza and Umar Ali Shah were specially remained enormously helpful throughout the period of my Ph.D studies.

Consequently, My all plea is to **Allah**, the Almighty, the beneficent whose blessings are always showered upon me via strengthening my wisdom and bestowed me with the knowledge of what he wants.

Abstract

Thermal management in closed cavity is one of the most important analysis in recent decade. Such type of heat analysis in the presence of molecular movement is convection. The simulation of Heat and mass transfer through various type of convection in complex geometries is studied in this dissertation. The analysis of FEM on heat transportation in a two dimensional closed cavity is much challenging and depending upon the complex nature of the problem. However, to ensure the efficient and accurate analysis, the following considerations of significant criteria may be taken as; Mesh density, Element type, Boundary Conditions, Material Properties of structure, the solution and its method and the criteria to check its convergence. Aim of this work is to develop various geometries (square, trapezoidal, circular, curved and corrugated) for engineering and industries as cooling equipment, thermal energy storage, thermal solar equipments etc. through fins, obstacles and lid walls. Mathematical non-linear Partial Differential Equations (PDEs) and boundary conditions are developed. For such physical two dimensional problems, steady-state equations of continuity, momentum, energy and concentration are developed, which are non-dimensionalized by using suitable dimensionless variables. For solution of strong non-linear PDEs in dimensionless form in this thesis, computational method as Finite Element Method (FEM) is adopted. For numerical approach, Glarekin residual approach of FEM is applied in which first domain is discretized into sub-domain in the form of quadrilateral and triangular form etc. Each sub-domain formulation occurs with combination of nodes, which form elements. Acquired elements are solved in the form of simultaneous algebraic equations for unknown interior nodes, these elements of sub-domain develop stiffness matrix for numerical simulation. Union of elements form domain of the cavity or enclosure. Simulation of structure for natural, forced and mixed convection are taken in this thesis. Impact of various rising parameters on streamlines, isotherms, iso-concentration, velocity, tempera-

ture, local and average Nusselt number are presented in the form of graphs. The emphasis on heat transfer in cavity due to forced, natural and mixed convection are obtained. Numerical and graphical interpretation of problems are discussed in comparison with experimental and numerical results. Mesh analysis and grid independence test for various cavity are analysed for average Nusselt number. Number of nodes or response of meshes on rate of heat transfer are calculated. Validation of the current work with literature in limited cases are explored. In case of square cavity, size of heated fin increases the heat transfer inside cavity. Convection process shows significant transfer rate of heat at mean position with increase in nanoparticles in enclosure. Heat driven through lid walls in case of forced convection in porous corrugated duct in the presence of heat generation. Partially lid driven of top lid walls move inside direction generate more heat in enclosure. In concentration of nanofluids, Lewis number and buoyancy increase mass transfer and Re increases heat transfer inside enclosure. Forced convection in circular duct through triangular fins is significantly affected with Re, Da and ϕ. Reynolds number increases heat in cavity while porosity and nanoparticle decrease heat in cavity with increasing the parameter. $Q > 0$ plays a vital role for heat generation inside cavity in all problems.

TABLE OF CONTENTS

LIST OF TABLES

LIST OF FIGURES

LIST OF SYMBOLS

Br	Buoyancy ratio
B_o	Strength of magnetic field
c^*	Species concentration
C	Dimensionless species concentration
D	Mass diffusivity
Gr	Grashof number
Re	Reynold number
Le	Lewis number
Ri	Richardson number
Pr	Prandtl number
Sh	Sherwood number
Ra	Rayleigh number
Da	Darcy number
K	Mass transfer coefficient
Q	Heat generation/absorption parameter
Ha	Hartmann number
T_h^*	Steady temperature
c_h^*	Steady concentration

LIST OF SYMBOLS

g	Gravitational acceleration
k	Thermal conductivity
L	Enclosure length
M	Dimensionless mass function
n	Unit normal vector
Nu	Nusselt number
Sh	Sherwood number
R	Gas constant
$\mathbf{b}$	body force
e	Element of the domain
V_h	Dimensional space
h_i	Element size
S	Shape function
m	Shape of nanoparticle
r	radius of circular obstacle
A_1	tensor
k	nodal element
p^*	pressure

LIST OF SYMBOLS

P	Dimensionless pressure
(u^*, v^*)	Velocity components
(U, V)	Dimensionless velocity components
(x^*, y^*)	Coordinates in dimensional form
(X, Y)	Dimensionless coordinates

Greek symbols

α^*	Thermal diffusivity
β_{c^*}	Coefficient of solutal expansion
β_{T^*}	Coefficient of thermal expansion
Υ	Cauchy stress tensor
γ	Penalty parameter
Φ	Angle of Magnetic field acting
ω	Test function
Γ^e	Outward normal
θ	Dimensionless temperature
μ	Dynamic viscosity
ν	Kinematic viscosity
α^*	Thermal conductivity ratio

LIST OF SYMBOLS

r_l	radius of spherical shape of nanoparticle
σ	electric conductivity
ρ	density (kg/m^3)
ξ	x-coordinate of element
η	y-coordinate of element
ϕ_i	irreversibility distribution ratios
Ψ	dimensionless stream function
$\mathbf{\Omega}$	Computational domain
Ω	Sub-domain

Subscripts

0	reference state
avg	average or mean
f	Base fluid
nf	Nanofluid
p	Nanoparticle

CHAPTER 1

INTRODUCTION AND HISTORICAL BACKGROUND

1.1 Background

The development and transfer of heat in enclosures have attained more attention in recent research. Differential equations that appear in physics and engineering can be solved numerically using the finite element method (FEM). From its initial introduction in the 1940s, it has developed into a popular tool for the design and analysis of complicated structures. Finding a precise and effective method of discretizing the domain is one of the key issues of FEM. This entails deciding on the right element size and form as well the quantity of elements required to reach the desired level of accuracy. It is frequently necessary to strike a balance between computational cost and accuracy since the kind and size of the elements can have a considerable impact on the solution's accuracy and efficiency. Convection transfer in enclosures (free, forced, and mixed) has received the most emphasis on different geometries whereas heat transfer by conduction and radiation has got very little consideration. The literature section discusses the various kind of geometries that are present for the heat transfer rate analysis. Different numerical methods are applied to deal the above analysis. Finite element method is one of the most appropriate numerical procedure in an engineering and industrial sectors for thermal heat generation through particle movement in the prescribed cavity.

Numerous industries including mechanical, civil, aeronautical, and electrical engineering, use the Finite Element Method (FEM) for cavity design. Some of the FEM cavity modelling projects are; Fluid flow assessment, Thermal analysis, Analysis of structural behaviour of cavities, Electronic equipment and Analysis of the behaviour.

FEM is also used in blood flow modelling to help researchers and medical professionals better understand the intricate flow patterns and fluid-structure interactions that take place within the cardiovascular system. Numerous notable FEM applications in blood flow modelling entail; Hemodynamics, Medical device design, Blood clot formation and Fluid-structure interaction.

1.2 Research gap

1.2.1 Theoretical gap

After reviewing a variety of literature, the gap was looked at, and convection in an irregular closed enclosure has identified as follows:

- Haq *et al.* [1] executed a thermal experiment in a closed triangle-shaped cavity whereas by utilizing the mathematical equations of [1], a square cavity is developed and the equation is applied to evaluate the thermal experience via natural convection in the enclosure with horizontal and vertical fins which can be seen in chapter 4.

- Chapter 5 has been designed by adding porosity and heat generation/absorption terms to the curved closed cavity which is partially heated.

- For Forced convection, Bakar *et al.* [2] has studied the steady flow in a square lid-driven cavity which is then extended to the curved corrugated cavity in a porous medium filled with CuO in Chapter 6.

- In chapter 6's context, chapter 7 is designed for a double-sided lid driven in a corrugated duct flow containing nanoparticles.

- Extension of Ababaei *et al.* [3] research to mixed convection in a lid driven trapezoidal cavity with a split lid and an elliptic-shaped obstacle is addressed in Chapter 8.

- Chapter 9 of the thesis examines an extension of Bakar *et al.* [4] work on forced convection for thermal drift over partially heated triangular fins in a circular porous duct.

1.2.2 Contextual analysis

In contemporary convection context, the following shows, how the relevance of convection in 2-D steady state models is strengthened:

- Haq *et al.* [1] suggested triangular cavity inscribed cylindrical obstacle while for increasing heat transfer various size of heated fins in a square cavity has been dealt for its vital role.

- Heat generation coefficient has a strong inclination to create streamlines and isotherms in curved partially heated porous cavity.

- Until to current study, modelling of the interacting phenomena that enhance the development of efficiency of heat transfer. The study is focused on either the thermal "flow" or process models of structure processes that may produce much more thermal "mechanical" performance. Flow can be accelerated by the lid wall if the flow is mechanically slower. An irregular corrugated porous cavity with heat generation coefficient is established through the vertical lid wall in chapter 6's analysis of heat transfer.

- With the motive from chapter 6 carried over to chapter 7, a corrugated

domain was established to double the lid-driven cavity and double the transfer rate via lid walls.

- With the help of partially split lid walls, heat can be produced to any direction inside/outside the cavity and trapezoidal cavity model is examined in chapter 8 for the said purposes.

- One of the engineering tools used for maintaining heat in a cavity is the circular duct. Such a maintenance assessment with partially heated triangular fins is addressed in chapter 9.

1.3 Problem statement

We desire to look into the following problem statements with the execution of a systematic review of literature.

- An investigation of the water-based SWCNTs' natural convection heat transfer through parallel horizontal and vertical fins is carried out inside a square cavity. Chapter 4 contains a comprehensive graphical and theoretical result.

- Chapter 5 is expanded for combined heat generation and natural convection for copper oxide – water nanofluid in enclosed curved partially heated porous cavity with the enthusiasm of natural convection in square cavity discussed chapter 4.

- In the presence of heat generation and absorption, a numerical simulation of lid-driven flow in a curved corrugated porous cavity filled with CuO-water is examined. Forced convection in a corrugated cavity is the emphasis of Chapter 6.

- The curved duct is examined as a double lid driven in Chapter 7, which is a continuation of Chapter 6. The impact of various shape of nanoparticles have been assessed in this chapter.

- In chapter 8, a split lid driven trapezoidal cavity with an elliptic-shaped obstacle for mixed convection has been addressed.

- In chapter 9, special attention is given to thermal drift and forced convection on water-based single wall carbon nanotubes (SWCNTs) in a porous circular duct. Equilateral triangular fins that are moving inside a circular cavity that has triangular fins on both the vertical and horizontal axes. To calculate the thermal drift, internal heat generation and absorption are taken.

1.4 Research questions

The following questions for each chapter in thesis have been arisen:

- What is the impact of heat transfer due to the horizontal and vertical fins in a square cavity?

- How does the partially heated curve transfer heat in the porous curved cavity via natural convection?

- How is heat generated in a porous corrugated cavity on the lid walls through forced convection?

- What are the impacts of heat generation/absorption on a double-sided lid driven in porous corrugated duct?

- What are the effects of various directional partially split lid walls with the elliptical obstacle in a trapezoidal cavity?

- What are the impacts of heat generation in a circular duct with the partially heated triangular fins in the presence of an inclined MHD?

1.5 Research objectives

The main objective of this research is to construct and demonstrate the accuracy of a numerical method for the assessment of heat transfer in numerous cavities via convection. The focus of work is the finite element approaches to the solution of fundamental equations of motion and energy, and an experimental analysis is also undertaken to validate the analysis. This work is an extension of ongoing research aimed at improving our understanding of the physics underlying factors and creating models for engineers and commercial enterprises without the need for prototype development. To reduce necessity physical prototypes during the design phase, FEM can be modified to satisfy specific accuracy requirements. Multiple prototypical iterations are typically expensive and time-consuming to be produced. The developer can model several ideas and materials using software in a matter of hours rather than spending weeks on actual prototyping.

1.6 Research limitations

For heat transfer in cavity through convection, it has limitation of method itself and the method on cavity. Mesh distribution is taken essentially as the stability of FEM depends on the quality of mesh. The most important aspect of the widely used finite element method is the consideration of shape functions that are linear or quadratic. In Cartesian coordinates, two-dimensional steady laminar flow research is being conducted. Limitations on cavities are assumed to be closed and have been taken for the designs of squares, curves, corrugations, trapezoidal, and circular enclosures.

1.7 Significance of research

The creation of model reduction techniques satisfies the industry's urgent need for engineering problem simulations that happen quickly and almost

in real time. Numerous types of heat and energy transfer models are being developed. For engineering use, FEM has the capacity to produce approximative structural geometry. The purpose of this research is to create various cavities for the exchange of mass and heat. While physically simulating a various structural deformity can be unfeasible, a computer implementing FEM can resolve the issue accurately.

1.8 Thesis organization

Main aim to develop the thesis is to construct mathematical models based upon various engineering structures associated with different kind of fluids. These models consists of non-linear partial differential equations with boundary conditions. These equations are based upon law of conservation of mass, momentum, energy and concentration. These models consist of various parameters and the nanofluid's relationship that determine the fluid pattern (streamline), heat transfer in the different portion of cavity (isotherms), velocity profiles along all the directions and rate of heat at the interface where fluid and solid interact (Nusselt number). To determine these results, finite element method (FEM) is adopted with Glariken approach. The detail description of this method is discussed at the end of chapter 3. The breakup of the entire thesis is divided into the Ten chapters. After detailed literature review process, thesis is further divided into the pattern:

Chapter 3 contains literature, basic definitions and physical principles that apply to this endeavour. These laws consist of mass, momentum, energy and concentration equation.

Chapter 4 focuses on Haq *et al.* [1] .'s study article. The constant natural convection flow water based SWCNTs through parallel fins enclosed by square cavity is examined in this chapter. The non-linear coupled PDEs are numerically solved using the Galerkin finite element technique after an appropriate transformation, is performed to convert equations guiding the flow

into non-dimensional form. For different parameters like Pr, Ra, position of heated fin and length of heated fin, numerical results are produced. **This chapter is published in International Communications in Heat and Mass Transfer: Vol 119, pp. 104797, (2020).**

Chapter 5 discussed the natural convection in extended form Haq *et al.* [1] in normal curved shape of deformable cavity with heat generation/absorption and porosity parameter. Effect of rising parameters in case of multiple effecting parameters discussed graphically.

In **chapter 6** numerical simualtions are studied in a porous curved corrugated cavity. Cavity is filled with nanoparticles and heat generation/absorption in uniform form is developed. Cylindrical obstacle inscribed in cavity. Influence of rising parameter and various state of obstacle on streamlines, isotherms, velocity and Nusselt number is discussed. Result validation and mesh analysis againt the Nusselt number described graphically. **This chapter is published in Alexandria Engineering Journal: (2021).**

Chapter 7 contains the extension of partially lid-driven to double lid-driven porous curved corrugated cavity. Governed equations are converted to dimensionless form with suitable transformation, then solved by numerical finite element method. **The contents of this chapter are published in Journal of Molecular Liquids: pp. 118046, (2021).**

Chapter 8 contains mixed convection simulation in a split lid-driven cavity with elliptic shaped obstacle for Boussinesq approximation. Effect of upper wall directional movement on isotherms, streamlines and iso-concentration are reported. **This chapter is published in : International Communications in Heat and Mass Transfer: Vol 126, pp. 105448, (2021).**

In **chapter 9**, the work in circular porous enclousre with partially heated triangular fins. Idea of circular cavity explored for inclined MHD with heat generation/absorption in presence of heated fins in triangluar form. The non-dimensional PDEs are solved through Glarkin approximation of FEM with

bi-quadratic discretization of elements. Effect of various dimensionless parameters on streamlines, isotherms, temperature and local Nusselt number at vertical and horizontal mean position are discussed graphically and theoretically. **This chapter is published in Physica Scripta: Vol 96, pp. 065701, (2021).**

Relation of various type of convection and effect of various parameters in computational analysis of varying shape of complex cavities has been explored in **chapter 10**. Rate of heat transfer in cavity has variated with increase in nanoparticles, size of fins and other parameters. Such effects on heat flow and mass transfer have been discussed in last unit.

CHAPTER 2

LITERATURE REVIEW AND BASIC CONCEPTS

2.1 Brief literature review

In this chapter, basic concept of various cavity models and its application which are applicable in natural science are discussed. Factor affecting the cavity models for ranging heat flow structure and creation of heat has been discussed in detailed in this chapter. Application of different complex structural enclosure by various structures used at the industrial level is discussed. In order to handle the complex structure, a numerical schemes which are used by various researchers is presented in the current chapter.

Heat and mass transfer are prominent transport processes in a variety of contexts, including the natural world, living beings, and the engineering process, etc. This thesis focuses on the most recent advances in applying fundamental heat and mass transport theory as well as novel technologies to a wide range of industrial applications exploiting complex cavity models. This thesis will offer readers with a recent numerical method, Computational Fluid Dynamics (CFD) simulation, and innovative investigations of heat and mass transfer themes related to a variety of engineering disciplines, including flow regime, nanoparticles, surface tension, battery heating systems, and engineering processes such as different solvents and resistance welding. The thesis aims to provide unique insight into heat and mass transfer patterns, as well as to operate as a space for the exchange of novel ideas and in the advancement

of fields. Nanofluids have been the subject of significant research around the world since pioneering researchers discovered the distinct thermal behaviour of suspended nanoparticles in conventional fluids, dubbed nanofluids.

For numerous reasons, the cavity problem is an useful measurement problem. Initially, it is one of the most basic enclosed contact issues that can be practically and theoretically analyzed. Second, there has been some emphasis in the literature that addresses the cavity problem. There exist both theoretical and experimental data for limiting cases to compare the recent development in mathematical models. Third, there are several practical applications that are interrelated to the cavity problem. Due to numerous engineering applications, researchers are interested in studying convection heat transfer and fluid flow in cavities, which have wide range of applications in solar thermal systems, heat exchangers, erecting cooling/heating, room aeration, condensation of electronic equipment, drying devices, thermal energy storage systems, supercapacitors, storage tanks, geothermal system, nuclear and preservative reactors, and food processing, etc. Due to thermal non-equilibrium and pressure variations inside the cavity, convection heat transfer in cavities is defined as the energy and mass interaction between the surrounding (of regular or irregular flow regime) and the working fluid flowing inside the cavity. Depending on the buoyancy and external pressures ratio, this interaction might be natural, mixed, or forced convection. Interest of researchers is developed based upon several barrier arising while constructing the fluids characteristics, deformation process, configuration of model, heat source, its methodology to handle the mathematical model and the validation of entire process with existing literature and experimental approach.

The theory of heat transfer is concerned with the rate of energy exchange and temperature distribution in a thermal system in closed enclosure. It can occur in three modes, which is conduction, convection and radiation. As this experiment involves convective heat transfer, the principle of convection

is presented. Convection is the mode of propagation of energy between a solid surface and the associated liquid that is in motion regardless of a change in temperature. Process of natural convection arises in many phenomena but here, the core determination to discuss this process that is associated with nanofluids application [5–13]. Overall, the results show that as the volume fraction of nanoparticles increases, heat transfer becomes more efficient. Performance of heat transfer due to free convection in various complex cavities employing numerous parameters is discussed [14–22]. The effect of magnetic field on the heat transfer in rectangular cavity is investigated by Rudraiah *et al.* [23]. In another study, Kim and Ha [24] investigated the laminar free convection in annuli having internal fans. They have concluded that if the number of fins increase then the Nusselt number decreases.

The enhancement of heat transfer properties takes place in circular ducts with fins which are commonly used in many engineering and industrial applications. They are; HVAC systems, Electronic cooling, Automotive cooling, Process cooling, and Solar collectors. These applications basically depend on the heat transfer system such as in an automotive cooling the circular ducts with fins used in automobile cooling systems to transport heat from the engine to its surrounding air. The functioning of fins in the system widens its surface area for a better and efficient performance. Venkatadri *et al.* [25] measured the natural convection flow for the transportation of energy in trapezoidal enclosures. They contend that they are able to achieve higher heat transfer rates when enclosure is designed properly. They conclude that the Rayleigh number is enhanced by the rates of the transfer of heat and fluid flow, and that the rate of heat transfer is greater at the top corner of a hot wall than anywhere else, while the local Nusselt number gradually decreases from bottom to top of the wall before suddenly increasing as we get closer to the top corner. In a rectangular cavity, Abir *et al.* [26] investigated the impact of Marangoni convection on the steady natural convection flow and heat transfer in a two-layered fluid

system composed up of air and water. They deduced from the numerical simulations that a greater buoyancy force, or larger Rayleigh numbers, promises improved heat transmission through conduction and convection. Poulikakos and Bejan [27] found the experimental result of attic-shaped space in natural convection heat transfer. Xu *et al.* [28] investigated concentric triangle closure, where horizontal cylinder is placed in triangle. In a partially heated enclosure, adopting nanofluid with different types of nanoparticles are worked by Oztop *et al.* [29]. In another work, Haq *et al.* [1] discussed the simulation of nanofluid in a partially heated triangular cavity by considering the different constrained cylindrical obstacle. Brownian motion and thermophoresis are crucial effects in the concept of nanofluid addressed by Sheikholeslami *et al.* [30]. The temperature of the inner sinusoidal and outer circular walls is kept constant, while the other two walls are thermally insulated. The data show that when the buoyancy ratio rises, the average Nusselt number drops until it hits a considerable value, at which point it begins to rise again. This lowest value occurs with increasing buoyancy ratio numbers as Lewis number grows. Sheikholeslami *et al.* [31] examined natural convection in a circular enclosure with an interior heated sinusoidal cylinder. The results demonstrate that the Rayleigh number, amplitude values, and the number of undulations in the enclosure have a substantial influence on streamlines, isotherms, and the number, size, and development of the molecules inside the enclosure. Heat transfer enhancement with buoyancy driven in inclined triangular enclosure simulated by Billah *et al.* [32]. They declared that Heat distribution increases with increase in quantity of volume fraction of nanoparticles in cavity.

For decades, heat transfer in the cavity with a moving boundary in mixed convection is a fascinating phenomenon that helps the engineers in construction of models. The study of convection in a lid-driven cavity has attracted the perceptible attention of researchers due to numerous applications in the field of industrial microelectronics, nuclear power plant, food processing,

renewable energy system etc. [33–37]. Mixed convection flow in a low heated square driven cavity was numerically examined by Moallemi and Jang [38]. They have proposed the effect of Prandtl number on the flow and heat transfer mechanism. Additionally they have discussed the buoyancy effects are more prevailing for higher values of Prandtl number in a square lid driven enclosure. Chamkha *et al.* [39] worked on the unsteady, mixed convection flow and heat transfer due to the heat generation/absorption fluid in a vertical lid driven cavity at uniform magnetic field. They summarized that the average Nusselt number decreases with an increase in internal heat generation coefficient but increases for the opposing flow. Sivakumar *et al.* [40] analysed numerically the heat transfer and fluid flow of mixed convection in lid-driven cavities where the left vertical wall is partially heated. The variation of length and position of heated part of vertical wall is investigated and explores the transfer of heat and fluid flow in a cavity. On 3-dimensional structures, the numerical study was performed by Ouertatani *et al.* [41]. In a crown wavy enclosure free convection simulated by Dogonchi *et al.* [42]. Porous medium has significant impact on rate of heat transfer.

In the process of force convection, external source is applied to yield the fluid motion such as pump, tool used for suction, fan, etc., which is one of effective way of heat transfer. Such process is frequently utilized in maximum temperature of the systems like surface benchmarking to improve heat transfer, cooling channel, automatic control cooling, automobile industry cooling etc. Selimefendigil and Oztop [43] explore the magnetohydrodynamics forced convection of CNT-water nanofluid in a layered a U-form vented cavity with a porous section under the influence of wall corrugation. They conclusion that the bottom wall's triangular corrugation, which can be used as a tool for fluid flow and heat transfer features, was found to be effective. The average heat transfer rate decreases with a higher number of corrugation waves, while it initially increases and then decreases with a higher corrugation height. Shafee

et al. [44] using LBM, it is possible to tackle the problem of hydromagnetic-forced convective nanoliquid flow inside a porous enclosure with a moving top divider. Yields show that the convective role improves with Re's rise, while it diminishes with the rise in Lorentz powers. Ha's turn-around association is thermal inclination. Dariush *et al.* [45] analysed the combined convection laminar heat transfer(HT) in CESC. Volume fraction of nanoparticle increases the HT rate inside the enclosure. Lid velocity has also significant impact on the temperature distribution in cavity. Influence of fin length on heat transfer in sinosedial cavity is studied by Fayz-Al-Asad *et al.* [46]. They depicted that increase the length of vertical heated fin has greater impact on isotherms profile and flow building inside cavity.

Utilising FEM, it is possible to determine the temperature distribution inside the cavity by solving the heat transfer equations, which explain the movement of heat. Analysis of structural behaviour of cavities, such as those in underground tunnels, dams, and structures, is possible using FEM. Using FEM, it is possible to determine how much stress and strain is present inside the cavity, which can aid in the structure's design and efficiency. Electronic equipment, such as microwave ovens, and other cavities can be studied using FEM to deal the behaviour of electromagnetic fields. To determine how the electric and magnetic fields are distributed inside the cavity, the Maxwell's equations describe how electromagnetic fields behave these equations can be solved using FEM. Zhang *et al.* [47] discussed free convection HT in L-shaped enclosure. They elaborated the effect of heat source and magnetic field (MF) in cavity. For the weak MF more heat transfer rate when radiation mechanism neglected. Zheng *et al.* [48] studied the NC in square cavity in the presence of two tubes (cold, hot). They summarized that more HT when cold tube posted above the heated tube. Majdi *et al.* [49] performed simulation in triangular lid cavity in the presence of circular body inside enclosure. They conclude that with rise of Ri, Nu_{avg} decreases and Nu_{avg} increases with increase in

concentration of CuO. Hamid *et al.* [50] developed simulation on trapezoidal partially heated cavity containing casson fluid. They summarized that increase in heated length more heat generated in cavity. Khan *et al.* [51] conducted experiment for HNF in a split lid driven cavity with inscription of Y- shaped obstacle. For inner direction of lid movement case local Nusselt number increases and Ri has opposite impact on Nu_{avg}. In a porous 3-D cubic enclosure forced convection HT through LMB simulated by Sajjadi *et al.* [52]. They depict that convective HT in enclosure reduces with increase in MHD parameter. In a lid driven cavity, study of micro-polar flow developed by Ali *et al.* [53]. They found that strong inertial $Re = 10$, streamlines and isotherms are symmetrically developed and high thermal conductivity received. Gangawane *et al.* [54] performed simulation of mixed convection through heated triangular block in domain. They conclude that the size of the block significantly affected the fluid flow and HT. Selimefendigil and Oztop [55] performed simulation on partially heated triangular enclosure having partially flexible wall taken. Re and Ri decrease and local Nusselt number and Nu_{avg} increased. Muthtamilselvan *et al.* [56] worked on lid wall cavity. They performed heat generation in cavity through uniform bottom wall which is heated. They concluded that nanofluid has significant influence flow and Nusselt number. They depicted that Ri is dominant when forced convection was considered.

In many situations, conventional cooling techniques involving the transfer of both free and forced convection heat are not satisfactory. Enclosure preceding corrugated geometry is another specific type of attractive geometry and apposite, and finds usefulness in solar corrugated accumulator design and roof top design of houses. Porous substrates with high thermal conductivity are used in many applications such as industrial cooling equipment, heat interfaces or exchange, and solar collectors to improve forced-convection heat transfer. In view of the above work, [57–59] investigated the convection in porous medium and examined the heat transfer using a thermal non-equilibrium model. They

analysed the effects of viscous and thermal dissipation porosity and inertial coefficient. Izadi *et al.* [60] analysed the forced convection in annulus. That annulus filled with Al_2O_3 nanofluid concertation. In this case, they reported that friction coefficient is highly dependent on the nanofluid concentration. Many scholars utilise a number of approaches to deal with heat transfer or heat and mass transfer in porous media [61–71], as well as related fields, among which the finite element method has been a popular option among many researchers. The finite element approach has been effectively used to a variety of phenomena involving porous media and various effects [62–71].

Magnetohydrodynamics is the study of how a moving highly conductive fluid reacts with an electromagnetic field (MHD). Lorentz force occurs when a magnetic field exists. The buoyant force causes natural convection fluid flow. Lorentz force and buoyancy force interact with one an other when a magnetic field is applied to a fluid, influencing flow fields and heat distribution. Due to the reduced velocities, the magnetic field suppresses convection. To estimate MHD natural convection in cavities, several numerical studies have been carried out. Free convection in a square cavity was examined by Mahmoudi *et al.* [72]. They drew the conclusion that magnetic field direction modulates flow and temperature fields. Miroshnichenko *et al.* [73] demonstrate the magnetic influence on free convective flow in a trapezoidal cavity at varied inclinations. It has been observed that an increase in the Hartmann number diminishes thermal resistance, but an increase in the nanoparticles volume fraction improves heat transfer. Sheremet *et al.* [74] interrogate the magnetohydrodynamics impulsive convection flow in a wavy inclined cage holding nanofluid. The impact of these factors on fluid flow and heat transfer inside the hollow have received the most attention. In the form of streamlines, isotherms, and average Nusselt numbers, numerical data have been offered. Parvin and Akhter [75] demonstrate that magnetic fields impact natural convection in a prismatic cavity. The Hartmann number modulates heat exchange

in cavity with buoyancy significance. Sahi *et al.* [76] investigate free convective flow in a T-shaped confinement. The results emphasised the enclosure's performance condition and disclosed that the Rayleigh number, as well as the strength and direction of the magnetic field, had an impact on the heat and fluid flows. Increasing the Hartmann number deadens fluid flow, reduces convection currents, reduces the average Nusselt number at the cold surface, and has the effect of delaying the transition to convection and extends the conduction region. The free convective flow of MHD fluid in a corrugated enclosure was studied by Haq *et al.* [77]. For complicated shapes, various numerical and theoretical work has been done to assess the effects of magnetic field on mixed convection heat movement in the wall driven enclosure. Chamkha *et al.* [78] numerically analyzed the study of the influence of a heat sink and a source of heat, as well as their lengths and orientations, on MHD mixed convection flow and heat transfer in a porous enclosure filled with a Cu-water nanofluid in the presence of partial slip effect. Both of the lid-driven vertical walls are thermally segregated and move in their own axis at uniform and equal velocities, with partial slip imposed at both ends. Along all the cavity, it is discovered that adding nanoparticles diminishes rate of heat transfer inside the porous cavity. The results concerning the impacts of the magnetic field reveal that when the Hartmann number increases, the average Nusselt number decreases significantly. Saha *et al.* [79] explored numerically mixed convection flow in the presence of a magnetic field in a lid-driven square cavity with internal heat generation/absorption with uniform heat at bottom wall. Variations in the Richardson number, Hartmann number, and the heat generation/absorption parameter for heat transfer rate (Nuesselt number) were thoroughly investigated. As the intensity of the applied magnetic field was raised, the average Nusselt number decreased. Furthermore, heat creation is expected to lower the average Nusselt number, whilst heat absorption is expected to raise it.

We made an assumption that the flow inside a cavity is two-dimensional

steady laminar flows while executing our computations. The majority of computational experiments on driven cavity flow likewise demonstrate this to be the case. Use fine grid meshes in cavity designs for flow stability. The overall findings, which are based on the engineering and industrial aspects covered in this thesis, can be used as an evidence for decision by industries to choose the suitable design for better heat transfer. The analysis and discussions also provide a framework for future study and investigation to gain insight on the application of CFD simulations for model improvement through various types of convection.

2.2 Basic definitions

2.2.1 Fluid

Solids, liquids, and gases are the three states of matter, with liquid and gas being both fluids. A fluid is a substance (gas or liquid) that keeps changing form under the influence of external forces, or any material that flows continuously. Because a fluid cannot resist deformation pressure, it moves or flows under the influence of the force, changing its shape constantly as long as the force is applied. As seen, fluid flow is a regular phenomenon in our daily situations. According to earlier centuries, the four basic elements are earth, air, fire, and water, with air, fire, and water being fluids among these three. Fluids are classified into two categories: ideal and viscous fluids. The most effective internal force in ideal or inviscid fluids is pressure, which operates in such a way that the fluid flows from high stress to low stress. The viscosity of Newtonian fluids is independent of shear rate, which means that the viscosity remains constant at any temperature and pressure. Furthermore, these are the fluids that follow Newton's viscosity law, which stipulates that the shear stress is proportional to the shear rate.

2.2.2 Heat transfer phenomenon

Many natural, industrial, and biological systems rely on heat transfer mechanisms to function. The shift of energy in response to temperature variations is known as heat transfer. Heat transportation occurs in three ways: conduction, convection, and radiation. The temperature differential inside a medium causes conductive heat transfer in solids by causing molecular energetic mobility. The exchange of thermal energy between two or more bodies using electromagnetic waves is referred to as radiative heat transfer. Surprisingly, no medium is required. The transmission of energy through liquids, gases, and fluids in general moving near the surface is known as convective heat transfer. Convection heat exchange may be further split into three types: forced convection, natural convection, and mixed convection. The fluid flow in a forced convection process is aided by external sources like as fans, suction devices, and pumps. When a fluid is heated, only natural buoyancy forces are responsible for fluid motion, a process known as natural or free convection. Density differences in various parts of the fluid create natural convection flow. This density shift, along with gravity's effect, creates a buoyancy force, which causes the heavier fluid to sink and the lighter fluid to rise. The density variation in natural convection flows might be caused by temperature variations or changes in chemical species concentrations. Air flows around our rooms and other technical applications are examples of frequent buoyant fluxes. When these two heat transmission mechanisms (forced and natural convection) occur together, the condition is known as mixed convection. Heat transfer is a very significant phenomena in which fluid plays a vital part in speeding up the process. Another major source for increasing the heat transfer rate is the inclusion of solid nanoparticles in the base fluid.

2.3 Nanofluids

Modifying the flow shape, changing the boundary conditions, or increasing the thermal conductivity of the base fluid can all help to enhance the convective heat transfer process. Maxwell [80] discovered in 1881 that by mixing micro-sized particles in the base fluid, the heat transfer rate may be increased. After Maxwell, it was discovered that, while adding micro-sized material particles to the base fluid increased the rate of heat transfer, the issues of clogging, rapid sedimentation, erosion, and high pressure drop caused by these particles kept the technology from being used in practical applications for a long time. Masuda *et al.* [81] initially demonstrated that combining nanoparticles to the base fluid boosts its thermal conductivity. Choi [82] invented the term nanofluid in 1995 while working at Argonne National Laboratory in U.S.A. A nanofluid is a suspension of solid nanoparticles (with diameters ranging from 1-100 nm) in a familiar liquid such as water, oil, or ethylene glycol. Nanofluids accelerated heat transfer phenomena, making them useful in a variety of heat transfer applications such as fuel cell technology, microelectronics, hybrid turbines, and pharmaceutical applications. In comparison to the pure fluid, nanofluids have a higher convective heat transfer efficiency and thermal conductivity. Nanofluid can be created using various nanoparticle and base fluid combinations. The thermophysical features of nanoparticles influence the heat transfer rate of nanofluid. Viscosity, density, specific heat, thermal diffusivity, and thermal conductivity are some of the physical properties of nanoparticles. These parameters' numerical values change when the nanoparticle ingredient and the base fluid change. For the material properties of nanofluids, scientists and researchers utilize well-known inferential relations.

2.3.1 Thermophysical properties of nanofluid

Thermophysical characteristics of nanofluid have a significant impact on the flow issues under consideration. Several scientists have developed various sorts of models for describing the thermophysical characteristics of nanofluids. Thermal conductivity, electrical conductivity, density, viscosity, and specific heat are estimated using formulae that are used as an empirical relationship between the base fluid and nanoparticles.

Table 2.1: Thermophysical properties of Water and various Nanoparticles

Physical properties	Base fluid (water)	SWCNT	Cu	CuO	Al_2O_3
$C_p(J/kgK)$	4179	425	383.1	535.6	765
$\rho(kg/m^3)$	997.1	2600	8954	6500	3970
$k(W/mK)$	0.613	6600	386	20	40
$\beta \times 10^(-5)(1/K)$	21	0.33	1.67	1.8	0.85
$\sigma(S/m)$	0.05	1×10^5	5.96×10^7	-	3.7×10^7

2.3.2 Density

The density of nanofluid may be determined analytically using the physical concept of the mixing law. This rule may be used to calculate the weight and volume of coagulation and the density of nanofluid. Knowing the densities of both components and nanofluid density may be used to calculate the particle volume fraction. Recognizing the densities of both components and nanofluid density generally used to estimate the particle of volume fraction (ϕ)

as [83–85]

$$\rho_{nf} = (1-\phi)\rho_f + \phi\rho_p. \tag{2.1}$$

2.3.3 Specific Heat

Specific heat capacity is defined as the amount of heat required to increase the temperature of one kilogramme of a material by one Kelvin. In convective heat transfer nanofluid flows, specific heat is expressed as and is based on basic mixing theory.

$$(\rho c_p)_{nf} = (1-\phi)(\rho c_p)_f + \phi(\rho c_p)_p. \tag{2.2}$$

2.3.4 Thermal conductivity

In the prior literature, there are several theoretical models that can predict the effective thermal conductivity augmentation of CNT suspensions. Fourier's law of heat conduction is used in all of these models. Maxwell [80] demonstrated in 1873 that adding solid particles to a liquid increases its thermal conductivity and presented a mature relationship between the thermal conductivity of nanoparticles and the base fluid, expressed as

$$\frac{k_{nf}}{k_f} = \frac{(k_p + 2k_f) - 2\phi(k_f - k_p)}{(k_f + 2k_f) + \phi(k_f - k_p)}. \tag{2.3}$$

In (1904) Maxwell [86] specified an explicit association between the effective thermal conductivity in term of the thermal conductivity ratio $\alpha^* = \frac{k_{CNT}}{k_f}$, and the volume fraction:

$$\frac{k_{nf}}{k_f} = 1 + \frac{3(\alpha^* - 1)\phi}{(\alpha^* + 2) + (\alpha^* - 1)\phi}. \tag{2.4}$$

Hamilton and Crosser [87] in (1962) established a theoretical model that takes into consideration the particle shape feature.

$$\frac{k_{nf}}{k_f} = \frac{\alpha^* + (n-1) - (n-1)(1-\alpha^*)\phi}{\alpha^* + (n-1) + (1-\alpha^*)\phi}. \tag{2.5}$$

where n represents the shape of nanoparticles. The earlier models, according to Xue (2005), are only applicable for spherical or rotatory elliptical particles with a modest axial ratio. Furthermore, these models ignore the influence of the CNTs' spatial distribution on thermal conductivity. Xue [88] developed a theoretical framework based on Maxwell theory that takes account rotational elliptical nanotubes with a large axial ratio and compensate for the effects of spatial distribution on CNTs.

$$\frac{k_{nf}}{k_f} = \frac{1-\phi+2\phi\frac{k_{CNT}}{k_{CNT}-k_f}ln\frac{k_{CNT}+k_f}{2k_f}}{1-\phi+2\phi\frac{k_f}{k_{CNT}-k_f}ln\frac{k_{CNT}+k_f}{2k_f}}. \tag{2.6}$$

2.3.5 Effective electrical conductivity

With increasing particle concentration and temperature, the electrical conductivity of nanofluid improves. When the concentration of nanoparticles is fixed, electrical conductivity is shown to be greater for smaller particles in nanofluid. Maxwell [83–85] stated the effective electric conductivity of nanofluid as

$$\frac{\sigma_{nf}}{\sigma_f} = 1 + \frac{3\left(\frac{\sigma_p}{\sigma_f}-1\right)\phi}{\left(\frac{\sigma_p}{\sigma_f}+2\right)+\phi\left(\frac{\sigma_p}{\sigma_f}-1\right)}. \tag{2.7}$$

2.3.6 Thermal diffusivity

It is the rate at which heat is carried out from a thermal body. It is the ratio of thermal conductivity to volumetric heat capacity in mathematics. In convective heat exchangers, the thermal diffusivity of nanofluid is expressed as

$$\alpha_{nf} = \frac{k_{nf}}{(\rho c_p)_{nf}}. \tag{2.8}$$

2.3.7 Viscosity

Engineers and scientists use a variety of methods to calculate the effective dynamic viscosity of a nanofluid as a function of solid volume percentage.

As a function of low volume fraction, Einstein [89–91] calculated the effective viscosity of a suspension of spherical solid particles (less than two percent). Brinkman [92] later proposed a new relationship by altering Einstein's equation of viscosity correlation for particle volume fractions smaller than four percent. The basic mixing theory [83–85] may be used to calculate the nanofluid's viscosity, which is given as

$$\mu_{nf} = \frac{\mu_f}{(1-\phi)^{2.5}}. \tag{2.9}$$

2.4 Dimensionless numbers in heat and mass transfer

The transfer co-efficient is usually stated in terms of Nusselt number in the study of heat and mass transfer because it is helpful to display the transport co-efficient as well as other critical characteristics in terms of experiencing positive dimensionless groups in many circumstances. In dimensionless groupings, other important variables and properties that influence the heat and mass transfer coefficient are also listed.

2.4.1 Prandtl Number

The Prandtl number (Pr) is named after Ludwig Prandtl, a German mathematician who played a pivotal role in viscous flow studies in the early twentieth century. Pr denotes the ratio of momentum diffusion coefficient to heat diffusion coefficient.

$$Pr = \frac{\nu}{\alpha} = \frac{\mu/\rho}{k/(\rho c_p))} = \frac{\mu c_p}{k}, \tag{2.10}$$

where, μ is the dynamic viscosity,

c_p is the specific heat

and k is the thermal conductivity.

Prandtl number is a non-dimensional number.

2.4.2 Grashof Number

The ratio between the buoyancy force to viscous force is called Grashof number, which is a dimensionless number and is used in flow analysis in natural convection. Mathematically,

$$Gr = \frac{g\beta(T_h^* - T_c^*)L^3}{\nu}, \tag{2.11}$$

where, g is the gravitational acceleration, β is the coefficient of thermal expansion, $(T_h^* - T_c^*)$ difference of heated and cold wall temperature. In free convection, it is the most important parameter that governs the flow design.

2.4.3 Reynolds Number

It is the ratio between the inertial and viscous force and is denoted by Re. Mathematically,

$$Re = \frac{V_o L}{\nu}. \tag{2.12}$$

Reynolds number is dimensionless and its varies for different flow like the flow is laminar for $Re < 2000$, it is unstable for $2000 < Re < 4000$ and the flow is turbulent for $Re > 4000$, accordingly.

2.4.4 Nusselt Number

Nusselt number is a dimensionless number that describes the relationship between convection and conduction heat transport over a boundary. Heat transfer by convection is $h\nabla T^*$, while heat transfer by conduction is $\frac{k\nabla T^*}{L}$. As a consequence, Nusselt number is rendered as

$$Nu = \frac{h\nabla T^*}{k\nabla T^*/L} = \frac{hL}{k}. \tag{2.13}$$

The larger the Nusselt number, the more heat is transferred by convection, whereas $Nu = 1$ means heat is transferred by conduction. The average Nusselt number is obtained by integrating the local Nusselt number along the heated

surface (Ω) and is defined as:

$$Nu_{avg} = \frac{1}{\Omega}\int_{\Omega} Nu_{x^*} d\Omega. \tag{2.14}$$

2.4.5 Rayleigh Number

It is the dimensionless number affiliated with the buoyancy driven flow called as free or natural convection. It can also be defined as, "The product of the Grashof number and the Prandtl number". Mathematically,

$$Ra = Gr.Pr = \frac{g\beta(T_h^* - T_c^*)L^3}{\alpha\nu}. \tag{2.15}$$

2.4.6 Richardson Number

Richardson number is a dimensionless number that describes the relative intensity of buoyancy and compressive stresses. It's also easy to express it in terms of the Grashof and Reynolds numbers.

$$Ri = \frac{Gr}{Re^2}. \tag{2.16}$$

For $Ri < 0.1$, natural convection is almost negligible and for $Ri > 10$, natural convection dominates. Whereas, significant effect of natural and forced convection dominate for Richardson number between 0.1 to 10. However, forced convection is large as compared to natural convection.

2.4.7 Darcy Number

It is the dimensionless number and is defined as "The ratio between the permeability of the medium to its cross-section area". Mathematically,

$$Da = \frac{k}{L^2}, \tag{2.17}$$

where k is the permeability of the medium and L is the characteristic length.

2.4.8 Hartmann number

Hartmann number is a dimensionless number that explains the correlation between electromagnetic and viscous forces. It can be written as

$$Ha = B_o L \sqrt{\frac{\sigma}{\mu}}, \tag{2.18}$$

where B_o denotes the strength of the magnetic field, μ the dynamic viscosity, and σ the electrical conductivity of the fluid. It determines the effect of magnetic fields on electrically conducting fluid mobility.

2.4.9 Sherwood number

The dimensionless number is defined as "The ratio of the convective and diffusive mass tansfer". Mathematically,

$$Sh = \frac{KL}{D}, \tag{2.19}$$

where, K is the mass transfer coefficient and D is the mass diffusivity. Since the Nusselt number is used as heat transfer, so the Sherwood number is used as mass transfer.

2.5 Mathematical form of basic law

The essential governing equations for nanofluid flow, especially the laws of mass, momentum, and energy conservation, are the same as for pure fluid flow. Taking nanofluids into consideration, however, modifies these aspects to some extend. Using the Buongiorno model and the Tiwari and Das model, two well-known nanofluid models were used. As a result, there must be a modification in the controlling constitution.

2.5.1 Equation of continuity

The continuity equation, which is written in vector notation as follows, is a well-known principle of mass conservation for fluid flow.

$$\frac{1}{\rho_f}\frac{\partial \rho_f}{\partial t} + \nabla \cdot \boldsymbol{V^*} = 0. \tag{2.20}$$

The above equation is appropriate for pure fluid and Buongiorno formulations, however ρ_f has been substituted by ρ_{nf} for Tiwari and Das configurations. Because the density of an incompressible fluid is constant, the equation of continuity (2.21) reduces to

$$\nabla \cdot \boldsymbol{V^*} = 0. \tag{2.21}$$

2.5.2 Law of Conservation of Momentum

When a fluid particle is at rest, in a steady state, or in constant motion, it obeys Newton's second law of motion. The sum of all external forces acting on an item equals the temporal rate of change of its linear momentum, according to this rule. This law is written as in vector notation for steady state problem as;

$$\rho(\mathbf{V}^* \cdot \nabla)\mathbf{V}^* = div\Upsilon + \rho\mathbf{b}, \tag{2.22}$$

whenever it concerns towards the Navier-Stokes equation,

$$\Upsilon = -p^* I + +\mu A_1^*, \tag{2.23}$$

where A_1^* is the tensor and Rivlin-Erickson constructed it for the first instance.

$$A_1^* = grad\ \boldsymbol{V^*} + grad\ \boldsymbol{V^{*t}}. \tag{2.24}$$

The material time derivative or total derivative is denoted by $\frac{d}{dt}$, $\boldsymbol{V^*}$ is the velocity field, ρ density, Υ Cauchy stress tensor, $\mathbf{b}$ is the body forces, and p^* is the pressure and μ dynamic viscosity in the preceding equations.

In matrix form, the stress tensor is displayed as

$$\Upsilon = \begin{pmatrix} \sigma^*_{x^*x^*} & \Upsilon_{x^*y^*} & \Upsilon_{x^*z^*} \\ \Upsilon_{y^*x^*} & \sigma^*_{y^*y^*} & \Upsilon_{y^*z^*} \\ \Upsilon_{z^*x^*} & \Upsilon_{z^*y^*} & \sigma^*_{z^*z^*} \end{pmatrix}. \tag{2.25}$$

The normal stresses are $\sigma^*_{x^*x^*}$, $\sigma^*_{y^*y^*}$ and $\sigma^*_{z^*z^*}$ be although the shear stresses are otherwise. For two-dimensional, we have $\boldsymbol{V^*} = [u^*(x^*, y^*, 0), v^*(x^*, y^*, 0), 0]$ and thus

$$grad \;\; \boldsymbol{V^*} = \begin{pmatrix} \frac{\partial u^*}{\partial x^*} & \frac{\partial u^*}{\partial y^*} & 0 \\ \frac{\partial v^*}{\partial x^*} & \frac{\partial v^*}{\partial y^*} & 0 \\ 0 & 0 & 0 \end{pmatrix}. \tag{2.26}$$

For steady momentum equation will take form along x^*-component

$$*\frac{\partial u^*}{\partial x^*} + v^*\frac{\partial u^*}{\partial y^*} = -\frac{1}{\rho}\frac{\partial p^*}{\partial x^*} + \nu\left(\frac{\partial^2 u^*}{\partial {x^*}^2} + \frac{\partial^2 u^*}{\partial {y^*}^2}\right), \tag{2.27}$$

Similarly, again with y^*-component, we repeat the method as follows:

$$u^*\frac{\partial v^*}{\partial x^*} + v^*\frac{\partial v^*}{\partial y^*} = -\frac{1}{\rho}\frac{\partial p^*}{\partial x^*} + \nu\left(\frac{\partial^2 v^*}{\partial {x^*}^2} + \frac{\partial^2 v^*}{\partial {y^*}^2}\right). \tag{2.28}$$

2.5.3 Energy Equation

The first law of thermodynamics, when applied to the flowing fluid constituent, is a statement of this premise. The steady, incompressible and two dimensional flow of energy equation is;

$$(\rho c_p)\left[(\boldsymbol{V^*}.\nabla)\, T^*\right] = -div\,\overrightarrow{q}, \tag{2.29}$$

where,

$$\overrightarrow{q} = -k\nabla T^* = -k\left(\frac{\partial T^*}{\partial x^*} + \frac{\partial T^*}{\partial y^*}\right), \tag{2.30}$$

$$(\rho c_p)\left[u^*\frac{\partial T^*}{\partial x^*} + v^*\frac{\partial T^*}{\partial y^*}\right] = -div\left[-k\left(\frac{\partial T^*}{\partial x^*} + \frac{\partial T^*}{\partial y^*}\right)\right], \tag{2.31}$$

$$(\rho c_p)\left[u^*\frac{\partial T^*}{\partial x^*} + v^*\frac{\partial T^*}{\partial y^*}\right] = k\left(\frac{\partial^2 T^*}{\partial {x^*}^2} + \frac{\partial^2 T^*}{\partial {y^*}^2}\right). \tag{2.32}$$

CHAPTER 3

RESEARCH METHODOLOGY

3.1 Research epistemology

Utilizing FEM computation, the interim concept of parametrization framework is built and refined in engineering heat exchange systems with epistemic uncertainty, confronted with constrained experimental measurements, and the results are compared for validation. Iteration or mesh efficiency approach is suggested as a predicted computational response interval in order to increase computational efficiency.

3.2 Research approach

Convection heat transfer assessment using many irregular cavities is developed. Various restrictions are made to the cavity's walls. Heat produced inside the cavity by simulation through fin or lid walls. On a staggered grid system, the governing mathematical equations have been discretized using the finite element method. Simulations are performed for a range of rising values of parameters in the cavity problem.

3.3 Research strategy

The literature contains a number of geometric models for the convectional exchange of heat. This thesis uses the finite element approach for cavity

models. Heat transfer is studied for geometries like square, curved, corrugated, trapezoidal, and circular. Prior to creating meshes, discretize the domain into subdomains. Elements develop out of nodes, and each element is described by an algebraic equation. System of equations is simulated for unknown function through simulation. Mesh is modified until solution converges.

3.4 Solution methodology

3.4.1 Finite Element Method

Clough was the first to develop the finite element method, which is now regarded as a strong computer-oriented methodology. It is a method for estimating the response to physics and engineering concerns. The finite element technique splits a considerable variation into smaller, finite elements. The primary idea behind FEM is to convert the governing equations into a weak or variational form that is more suitable. The governing equations are multiplied by certain appropriate functions termed weight functions or test functions in a weak formulation, and then integrated over the entire domain. The weighted residual technique of the Glarekin approach was used to formulate the subdomain. FEM is used to model the behaviour of fluids, such as air, water, and oil, inside cavities. To determine the pressure, velocity, and other characteristics of the fluid inside the cavity, the Navier-Stokes equations, which describe the motion of fluids can be solved using FEM.

Galerkin weighted residual method process

The Galerkin weighted residual technique is the most prevalent approach for computing the global stiffness matrix among the finite element methods. The following steps are followed to resolve the problems using the finite element method.

- Multiply both sides of the problem is actually conservation equations by

the test function $w(x) \in W$, which is fading away on the domain's edges, where W is a test field.

- Perform segment integration such that some derivative from the trial function is conveyed to the test function.

- In the perimeter integrals, impose intrinsic boundary conditions, and in the testing and trial spaces, impose necessary boundary conditions. This is referred to as a weak formulation or variational formulation.

- Create a mesh or a triangulation, whoever is most appropriate. Construct non-overlapping items out of the full domain. Mesh is a set of points in one dimension, $x_0^* = 0,\ x_1^*,\ x_2^*, ...,\ x_N^* = 1$; where x_i^* is a node and $e_i = [x_i^*, x_{i+1}^*]$, is an element such that $e_i \cap e_j = \Phi$ for $i \neq j$. Let $h_i = x_i^* - x_{i-1}^*$ for $i = 0,\ 1,\ 2,\ 3,\ ..., N$. h_i is the mesh size.

- Use the bounded dimensions spaces V_h and W_h to approximate the infinite dimensional trial and testing spaces V and W, respectively.

$$V_h^*(\text{finite dimensional space}) \subset V^*(\text{the solution space}). \tag{3.1}$$

Following example to demonstrate the Galerkin weighted residual procedure.

Example:

Using Galerkin weight residual method to solve the possion equation

$$-\nabla(a\nabla u^*) = f, \tag{3.2}$$

where the unknown functions are $a(x^*, y^*),\ f(x^*, y^*)$ and $u^*(x^*, y^*)$. In the xy-plane equation becomes

$$-\frac{\partial}{\partial x^*}\left(a\frac{\partial u^*}{\partial x^*}\right) - \frac{\partial}{\partial y^*}\left(a\frac{\partial u^*}{\partial y^*}\right) = f, \tag{3.3}$$

weight residual integral statement of this DE is

$$\int_\Omega \left[-aw\frac{\partial^2 u^*}{\partial x^{*2}} - aw\frac{\partial u^{*2}}{\partial y^{*2}} - fw\right] d\Omega = 0. \tag{3.4}$$

Second order derivative of u^* can be reduced to First order using the following general equations

$$\int_\Omega w\frac{\partial F}{\partial x^*} = -\int_\Gamma F\frac{\partial w}{\partial x^*}d\Omega + \oint_\Gamma wFn_{x^*}d\Gamma, \tag{3.5}$$

$$\int_\Omega w\frac{\partial F}{\partial y^*} = -\int_\Gamma F\frac{\partial w}{\partial y^*}d\Omega + \oint_\Gamma wFn_{y^*}d\Gamma. \tag{3.6}$$

Eq. (3.4) takes form after applying the above general equations

$$\int_\Omega \left[-w\frac{\partial}{\partial x^*}\left(a\frac{\partial u^*}{\partial x^*}\right) - w\frac{\partial}{\partial y^*}\left(a\frac{\partial u^*}{\partial y^*}\right) - wf\right]d\Omega = 0. \tag{3.7}$$

$$\begin{aligned} -\int_\Omega a\frac{\partial u^*}{\partial x^*}\frac{\partial w}{\partial x^*}d\Omega + \oint_\Gamma aw\frac{\partial u^*}{\partial x^*}n_{x^*}d\Gamma \\ -\int_\Omega a\frac{\partial u^*}{\partial y^*}\frac{\partial w}{\partial y^*}d\Omega + \oint_\Gamma aw\frac{\partial u^*}{\partial y^*}n_{y^*}d\Gamma = 0. \end{aligned} \tag{3.8}$$

Elemental weak form is:

$$\begin{aligned} -\int_{\Omega^e} a\left(\frac{\partial u^*}{\partial x^*}\frac{\partial w}{\partial x^*} + \frac{\partial u^*}{\partial y^*}\frac{\partial w}{\partial y^*}\right)d\Omega = \int_{\Omega^e} wfd\Omega \\ + \oint_{\Omega^e} w\left(a\frac{\partial u^*}{\partial x^*}n_{x^*} + a\frac{\partial u^*}{\partial y^*}n_{y^*}\right)d\Gamma. \end{aligned} \tag{3.9}$$

Where n_{x^*} and n_{y^*} are the Cartesian components of the unit outward normal of Γ^e. Approximate solution over an element is

$$u^{*^e} = \sum_{j=1}^{NEN} u^*_{j^e}S_{j^e}(x^*, y^*). \tag{3.10}$$

To get the i-th equation of element e. Substituting approximate u^{*^e} into the elemental weak form and selected $w = S^e_i$.

$$\begin{aligned} \int_{\Omega^e} a\left[\frac{\partial}{\partial x^*}\left(\sum_{j=1}^{NEN} u_j^{*^e}S_j^e\frac{\partial S_i^e}{\partial x^*}\right) + \frac{\partial}{\partial y^*}\left(\sum_{j=1}^{NEN} u_j^{*^e}S_j^e\frac{\partial S_i^e}{\partial y^*}\right)\right]d\Omega \\ = \int_{\Omega^e} S_i^e f d\Omega + \oint_\Gamma^e S_i^e q_n d\Gamma, \end{aligned} \tag{3.11}$$

$$\sum_{j=1}^{NEN}\left[\int_{\Omega^e}\left(a\frac{\partial S_j^e}{\partial x^*}\frac{\partial S_i^e}{\partial x^*} + \frac{\partial S_j^e}{\partial y^*}\frac{\partial S_i^e}{\partial y^*}\right)d\Omega\right]u_j^{*^e} = \int_{\Omega^e} S_i^e f d\Omega + \oint_{\Gamma^e} S_i^e q_n d\Gamma. \tag{3.12}$$

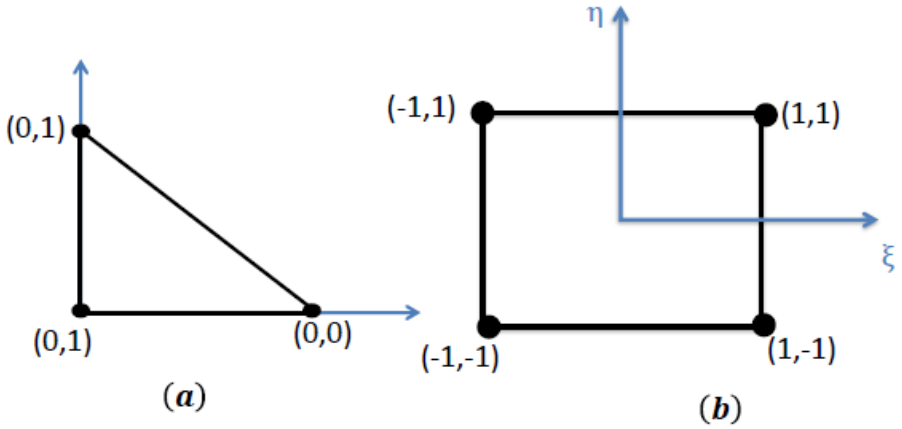

Figure 3.1: 2-D Quadrilateral and Triangular master element for shape functions

NEN × NEN elemental system is

$$[K^e]u^{*^e} = F^e + Q^e,$$

$$K^e_{ij} = \int_{\Omega^e} \left(a \frac{\partial S^e_j}{\partial x^*} \frac{\partial S^e_i}{\partial x^*} + \frac{\partial S^e_j}{\partial y^*} \frac{\partial S^e_i}{\partial y^*} \right) d\Omega,$$

$$F^e_i = \int_{\Omega^e} S^e_i f d\Omega,$$

$$Q^e_i = \oint_{\Gamma^e} S^e_i q_n d\Gamma.$$

To calculate the above integrals, we will introduce master elements in the triangular and quadrilateral form. The master element coordinates used for shape function. 2-D Jacobian transformation for that elements. To regain integral GQ used in the form of partition. Master element is in the form of square in the case of quadrilateral of size 2×2. The order of numbering of nodes are taken in CCW order, it start from corner $(-1, -1)$.

Shape function for two dimensional Quadrilateral master element:

The general form of two-dimensional for Four nodal element:

$$S = \mathbf{A} + \mathbf{B}\xi^* + \mathbf{C}\eta^* + \ \mathbf{D}\xi^*\eta^*. \tag{3.13}$$

Unknown **A**, **B**, **C** and **D** obtained using the property Kronecker Delta, which satisfy the shape function. The shape function equation in that case:

$$\begin{aligned} S_1 &= \frac{1}{4}\left(1-\xi^*\right)\left(1-\eta^*\right), \\ S_2 &= \frac{1}{4}\left(1+\xi^*\right)\left(1-\eta^*\right), \\ S_3 &= \frac{1}{4}\left(1+\xi^*\right)\left(1+\eta^*\right), \\ S_4 &= \frac{1}{4}\left(1-\xi^*\right)\left(1+\eta^*\right). \end{aligned} \tag{3.14}$$

Shape function for two dimensional Triangular master element:

The general form of two-dimensional for three nodal element:

$$S = A + B\xi^* + C\eta^*. \tag{3.15}$$

Unknown A, B and C obtained using the property Kronecker Delta, which satisfy the shape function. The shape function equation in that case:

$$\begin{aligned} S_1 &= 1 - \xi^* - \eta^*, \\ S_2 &= \xi^*, \\ S_3 &= \eta^*. \end{aligned} \tag{3.16}$$

In K_{ij}^e the derivative of S w.r.t x^* and y^* appear. But that coordinate are in the form of ξ^*, η^*. For 1-D relation:

$$x^* = \frac{h^e}{2}\xi^* + \frac{x_1^{*^e} + x_2^{*^e}}{2}. \tag{3.17}$$

This relation expressed as:

$$x^* = \sum_{j=1}^{NEN} x_j^{*^e} S_j. \tag{3.18}$$

Similarly, for y^*-axis,

$$y^* = \sum_{j=1}^{NEN} y_j^{*^e} S_j. \tag{3.19}$$

These are used for both quadrilateral and triangular element and that will be the corner point of the element.

Te transformation from one to other coordinate will be in the form of

$$\begin{aligned} \frac{\partial S}{\partial \xi^*} &= \frac{\partial S}{\partial x^*}\frac{\partial x^*}{\partial \xi^*} + \frac{\partial S}{\partial y^*}\frac{\partial y^*}{\partial \xi^*} \\ \frac{\partial S}{\partial \eta^*} &= \frac{\partial S}{\partial x^*}\frac{\partial x^*}{\partial \eta^*} + \frac{\partial S}{\partial y^*}\frac{\partial y^*}{\partial \eta^*}. \end{aligned} \tag{3.20}$$

Nodes and Elements:

The enclosing domain is discretized into tiny sections in FEA. These are called finite elements. All of the unique points (called Nodes) on their circumference are linked by these elements. Shape functions are a series of equations that form this "connection." Nodes and elements in FEM are employed in cavity models to discretize the cavity region into smaller, simpler elements in order to solve for the distribution of the electric field and other physical parameters inside the cavity. In the FEM cavity model, the elements represent the small, simplified sections of the cavity region that connect the nodes, while the nodes indicate the places at which the cavity region is divided. By meshing the cavity region with the help of an appropriate meshing technique, which creates the nodes and elements, the cavity model is normally built. Once the FEM cavity model has been established, it can be used to solve the distribution of electromagnetic fields inside the cavity, which is essential for identifying how the cavity operates. To accomplish this, an ensemble of partial differential equations that explain how the electric field behaves inside each component of the cavity are solved. The resulting solution offers a thorough representation of the electric field distribution inside the cavity, which can be used to enhance the cavity's performance and design. In the end, the use of nodes and elements in FEM cavity models enables precise and effec-

tive study of the electric field distribution within the cavity, which is essential for the design and operation of several devices, including particle accelerators, microwave cavities, and laser resonators.

Numerical Algorithm:

The partial differential equations in the cavity problems are numerically solved by FEM and simulated by open source freefem++ software, the programming of the software is based upon the C++ language.

1. ***Set***

→ The initial form for the shape of domain (Ω) has a triangular mesh Λ.

Solve ∇ u = f on Ω and u = g on Γ.

mesh Th = domain(m,m); // *unite square*

→ Choose a starting value for the augments coefficient $l_0, b_0 > 0$.

2. ***Principle loop for n = 0,...***

func f=1; func g=0;

Vh u,v;

(I) On the mesh Λ of Ω, determine the solution (u^m, v^m) to the Navier-Stokes equation. Stokes problem A(u,v,solver) =

double integral(Th)(dx(u) ∗ dx(v)+dy(u) ∗ dy(v))

+ intalledges(Th) (// loop on all edge of all triangle)

- *double integral*(Th)(f ∗ v)

- *integral*(Th)(g ∗ dn(v) ∗ g ∗ v) ;

(II) Establish the partial derivatives system on Ω^m solution (V^m, q^m).

(III) Determine the shape gradient (ϕ^m) of $\Omega^m \rightarrow (\Omega, l_0, b_0)$.

int n = Vh.ndof, n1 = n+1; func f=1+x-y;

Grad(u) [dx(u),dy(u)] //

varf va(uh,vh) = *double integral*(Th)(Grad(uh) ∗ Grad(vh)) ;

varf vL(uh,vh) = *double integral*(Th)(f ∗ vh) ;

varf vb(uh,vh)= *double integral*(Th)(1. ∗ vh);

```
matrix A=va(Vh,Vh);
real[int] b=vL(0,Vh), B = vb(0,Vh);
real[int] bb(n1),x(n1),b1(1),l(1); b1=0;
matrix AA = [ [ A , B ] , [ B', 0 ] ] ; bb = [ b, b1];
set(AA,solver);          // set the type of linear solver.
x = AA^-1 * bb; [uh [ ],l] = x;       // solve the linear system
plot(uh,wait=1);                      // set the value
```

(IV) If the ultimate mesh is inappropriate, revert to step 1 and modify the mesh quantity.

3.5 Mesh independency analysis

In a computational finite element approach, the accuracy of the result is checked in the form of convergence of the solution and mesh number independence. Mesh convergence specifies how many elements are necessary in a framework to ensure that increasing the mesh size has no effect on the analysis. With decreasing number of nodes, the response of the system (stress, deformity) will converge to a consistent solution. Further mesh improvement after convergence has no influence on the outcomes. The model and its output is now independent of the mesh. The FEA model has convergent to a solution, according to a mesh convergence analysis. It also justifies mesh independence, indicating that further improvement is useless. In cavity models, which involve the simulation of heat transfer within an enclosed space, the accuracy of the simulation depends on how well the flow and temperature fields are resolved within the cavity. This, in turn, depends on the quality of the mesh used in the simulation as shown in Fig. 3.2. A coarse mesh can lead to inaccurate results, while a fine mesh can lead to excessively long simulation time and can increases computational costs.

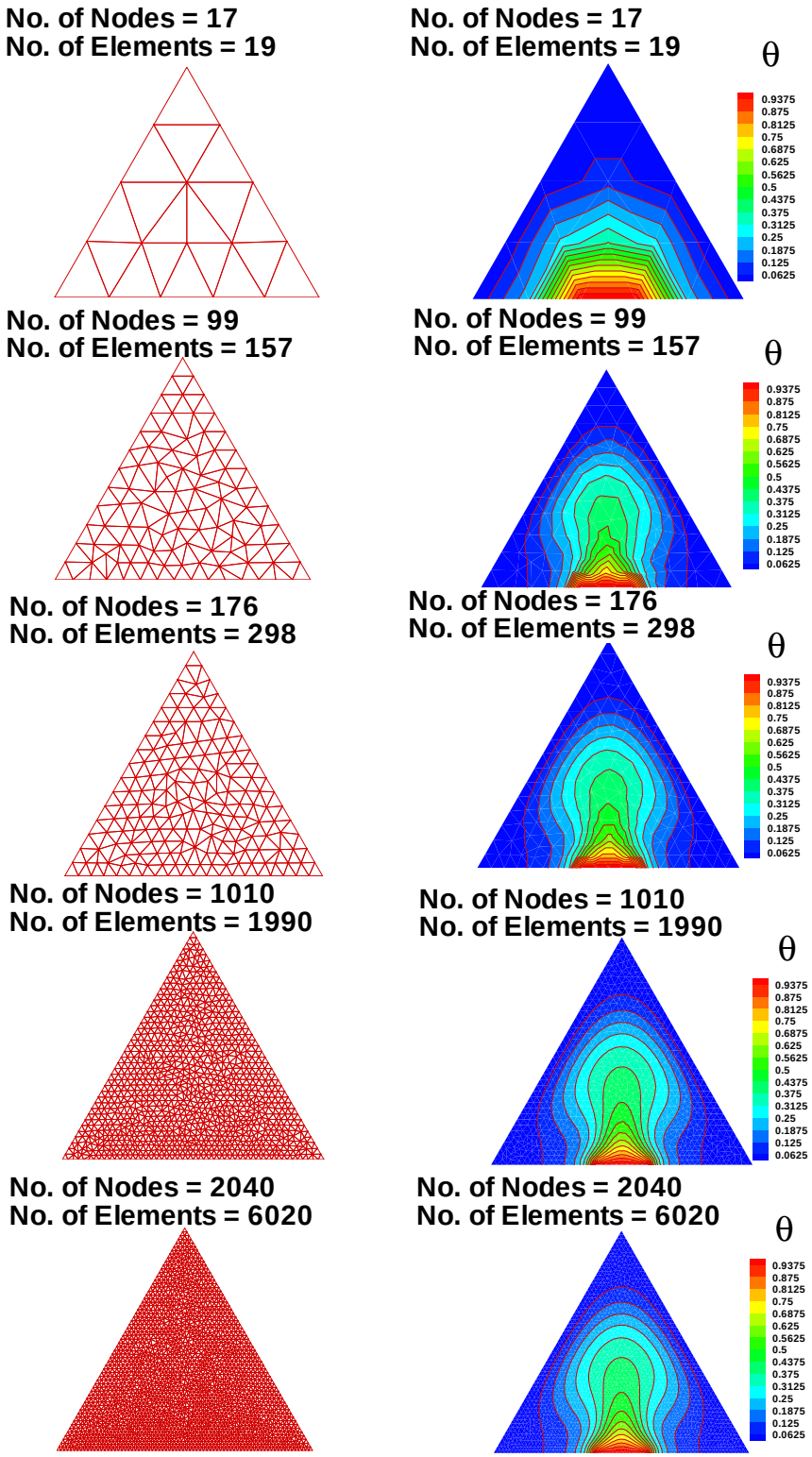

Figure 3.2: Response of isotherm profile against of different number of nodes and elements

CHAPTER 4

HEAT TRANSFER ANALYSIS OF WATER BASED SWCNTS THROUGH PARALLEL FINS ENCLOSED BY SQUARE CAVITY

4.1 Introduction

To enhance heat transfer inside a square cavity, heated and cold fins are frequently utilised in engineering applications. Electronic cooling uses heated and cooled fins physically applied in a square cavity. Analysis of natural convection due to various positions of bottom heated fin is performed in a square cavity that is filled by water-based Single Wall Carbon Nanotubes (SWCNTs) via finite element method (FEM). Three vertical parallel fins and one top horizontal fin is placed inside the cavity. The upper surface of the cavity is adiabatic, however the rest of three parts of the square cavity are cold. Convection is driven through lower horizontal fin and vertically central fin. For convection, horizontal and middle vertical fins are heated with uniform temperature T_h^* and remaining vertical parallel fins are fixed as cold (T_c^*). Mathematical structure is constructed in the form of system of nonlinear partial differential equations (PDEs) with constraint at the surface expressions of nanofluid relations are incorporated into the mathematical model. Effective thermal conductivity model of nanofluid is depending upon the radius of nanoparticle and fluid molecules at nanoscale. Dimensionless form of PDEs

are tackled through Galerkin technique-based finite element method. Results are obtained for temperature profile and stream function that includes emerging parameters such as: Rayleigh number (Ra), nanoparticle volume fraction (ϕ), position of heated horizontal fin, variation in length for bottom heated fin H_{T^*}, Hartmann number (Ha) and effect of middle vertical fin (adiabatic, cold, hot). The analysis describes the significant effect of heat transfer which is obtained in the presence of nanoparticles and heated length of bottom fin. Heat transfer rate increases by enlarging the heated length of the lower horizontal fin, and decreases by improving the value of Ra and solid volume fraction of nanoparticles.

Table 4.1: A table demonstrating the contrasts between the approaches being offered

Authors	Enclosure	Nanofluids	Fins	MHD	Method
Garoosi *et al.* [5]	Square	CuO	No	No	FEM
Jou *et al.* [8]	Rectangular	Cu	No	No	FDM
Sheremet *et al.* [10]	Trapezoidal	Concentration	No	No	FDM
Khanafer *et al.* [16]	Square	No	Yes	Yes	ADI
Haq *et al.* [1]	Triangular	SWCNTs	No	Yes	FEM
Present	Square	SWCNTs	Yes	Yes	FEM

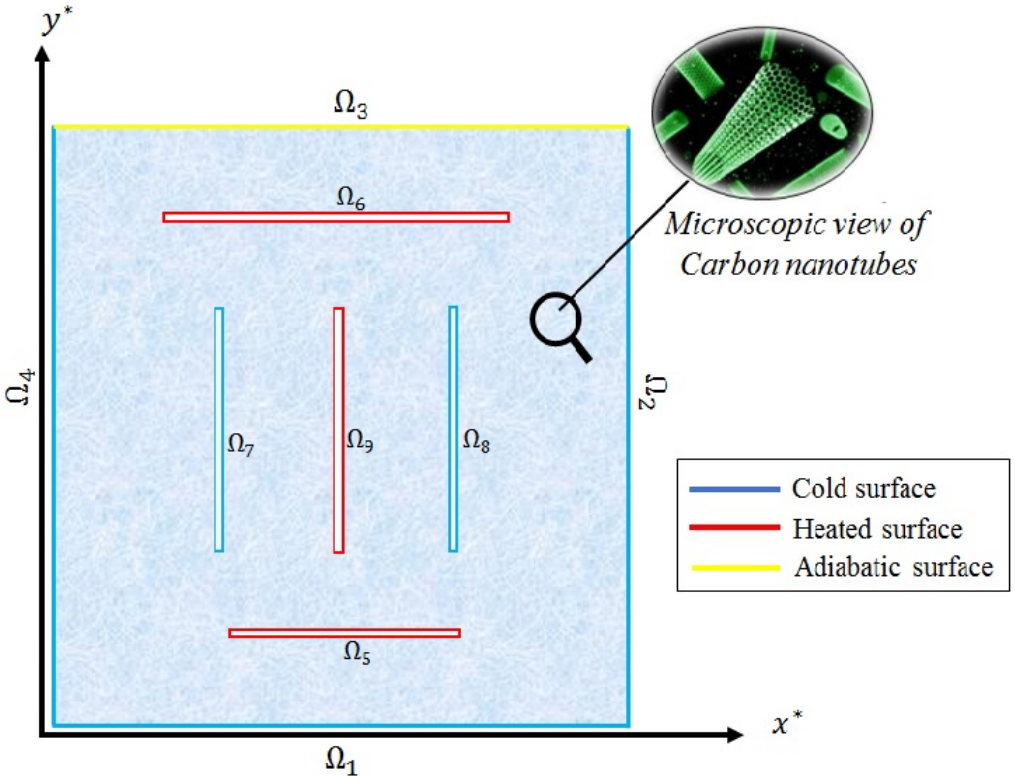

Figure 4.1: Physical domain of the mathematical model

4.2 Problem Formulation

In this section, necessary assumptions have been introduced, in order to construct the mathematical model. For this we have considered the two dimensional flow enclosed in a square cavity that contains horizontal and vertical parallel fins which are heated from different side. Cavity is filled with water based single wall carbon nanotubes (SWCNTs). Various constraints have been adjusted at fins to handle the heat transfer performance within the closed cavity. The constraint at outer square walls are defined in such a way that, top wall is consider to be adiabatic $\frac{\partial T^*}{\partial y^*} = 0$ and rest of wall are consider to be cold $T^* = T_c^*$. Different cases have been implemented at central vertical fin by considering three modes (heated,cold and adiabatic). Fig. 5.1 describes the description of entire structure of the model.

4.2.1 Mathematical Model

Based upon the constraints defined in the problem description, mathematical model is constructed that is emerged with nanofluid expressions in the form of conservation law of mass, momentum and energy:

$$\nabla \cdot \mathbf{V}^* = 0, \tag{4.1}$$

$$\mathbf{V}^* \cdot \nabla u^* = -\frac{1}{\rho_{nf}} \frac{\partial p^*}{\partial x^*} + \frac{\mu_{nf}}{\rho_{nf}} \nabla^2 u^*, \tag{4.2}$$

$$\mathbf{V}^* \cdot \nabla v^* = -\frac{1}{\rho_{nf}} \frac{\partial p^*}{\partial y^*} + \frac{\mu_{nf}}{\rho_{nf}} \nabla^2 v^* - \frac{\sigma}{\rho_{nf}} B_o^2 v^* + \frac{g(\rho\beta)_{nf}}{\rho_{nf}} (T^* - T_c^*), \tag{4.3}$$

$$\mathbf{V}^* \cdot \nabla T^* = \frac{k_{nf}}{(\rho C_p)_{nf}} \nabla^2 T^*. \tag{4.4}$$

In the above equation $\mathbf{V}^* = (u^*, v^*, 0)$ and $\nabla = \left(\frac{\partial}{\partial x^*}, \frac{\partial}{\partial y^*}, 0\right)$ represents the velocity field and nabla operator for two dimensional fluid flow. The expression of nanofluid with physical quantities are density ρ_{nf}, dynamic viscosity μ_{nf}, specific heat capacity $(C_p)_{nf}$ and thermal expansion coefficient of nanofluid β_{nf}, developed by Tiwari and Das [93].

$$\begin{aligned} \mu_{nf} &= \mu_f (1-\phi)^{-2.5}, \\ (\rho\beta)_{nf} &= (1-\phi)(\rho\beta)_f + \phi(\rho\beta)_p, \\ (\rho C_p)_{nf} &= (1-\phi)(\rho C_p)_f + \phi(\rho C_p)_p. \end{aligned} \tag{4.5}$$

Thermal conductivity model [94] is

$$\frac{k_{nf}}{k_f} = 1 + \frac{k_{CNT}\phi r_l}{3k_l(1-\phi)r_{CNT}}. \tag{4.6}$$

The numerical of all expression based upon base fluid and CNT are defined in Table. 4.3.

4.2.2 Boundary conditions:

At outer square wall

:

$$\begin{aligned}
u^*(x^*,y^*)=v^*(x^*,y^*)=0 \ \text{ and } \ T^*(x^*,y^*)=T_c^* \ \text{ at } \ \Omega_1\cup\Omega_2\cup\Omega_4,\\
u^*(x^*,y^*)=v^*(x^*,y^*)=\frac{\partial T^*}{\partial y^*}=0 \ \text{ at } \ \Omega_3,\\
\Omega_1=\{x^*,y^*\in\mathcal{R}\ /0\le x^*<L \ \ \wedge \ \ y^*=0\},\\
\Omega_2=\{x^*,y^*\in\mathcal{R}\ /x^*=L \ \ \wedge \ \ 0\le y^*<L\},\\
\Omega_3=\{x^*,y^*\in\mathcal{R}\ /0\le x^*<L \ \ \wedge \ \ y^*=L\},\\
\Omega_4=\{x^*,y^*\in\mathcal{R}\ /x^*=0 \ \ \wedge \ \ 0\le y^*<L\}.
\end{aligned} \tag{4.7}$$

Inner horizontal and vertical fins:

$$\begin{aligned}
u^*(x^*,y^*)=v^*(x^*,y^*)=0 \ \text{ and } \ T^*(x^*,y^*)=T_h^* \ \text{ at } \ \Omega_5,\\
u^*(x^*,y^*)=v^*(x^*,y^*)=0 \ \text{ and } \ T^*(x^*,y^*)=T_c^* \ \text{ at } \ \Omega_6,\\
u^*(x^*,y^*)=v^*(x^*,y^*)=0 \ \text{ and } \ T^*(x^*,y^*)=T_h^* \ \text{ at } \ \Omega_7,\\
u^*(x^*,y^*)=v^*(x^*,y^*)=0 \ \text{ and } \ T^*(x^*,y^*)=T_c^* \ \text{ at } \ \Omega_8,\\
u^*(x^*,y^*)=v^*(x^*,y^*)=0 \ \text{ and } \ T^*(x^*,y^*)=T_h^* \ \text{ at } \ \Omega_9,\\
\Omega_5=\{x^*,y^*\in\mathcal{R}/aL\le x^*<bL \ \ \wedge \ \ y^*=a_1L\ ,\ b_1L\},\\
\Omega_6=\{(x^*,y^*\in\mathcal{R}/cL\le y^*<dL \ \wedge \ \ x^*=c_1L\ ,\ d_1L\},\\
\Omega_7=\{x^*,y^*\in\mathcal{R}/eL\le x^*<fL \ \ \wedge \ \ y^*=e_1L\ ,\ f_1L\},\\
\Omega_8=\{x^*,y^*\in\mathcal{R}/gL\le y^*<hL \ \wedge \ \ x^*=g_1L\ ,\ h_1L\},\\
\Omega_9=\{x^*,y^*\in\mathcal{R}/iL\le y^*<jL \ \ \wedge \ \ x^*=i_1L\ ,\ j_1L\}.
\end{aligned} \tag{4.8}$$

To non-dimensionalize form of the variables are:

$$\begin{aligned}
X=\frac{x^*}{L},\ \ Y=\frac{y^*}{L},\ \ U=\frac{u^*L}{\alpha_f},\ \ V=\frac{v^*L}{\alpha_f},\ \ \theta=\frac{T^*-T_c^*}{T_h^*-T_c^*},\\
P=\frac{p^*L^2}{\rho_f\alpha_f^2},\ \ \nu_f=\frac{\mu_f}{\rho_f},\ \ Ra=\frac{g\beta_f(T_h^*-T_c^*)L^3}{\nu_f\alpha_f},\\
Ha=B_oL\sqrt{\frac{\sigma}{\rho_f\nu_f}},\ \ Pr=\frac{\nu_f}{\alpha_f},\ \ \alpha_{nf}=\frac{k_{nf}}{(\rho C)_{nf}}.
\end{aligned} \tag{4.9}$$

Where L, ν_f, Ra and Pr show the characteristic length, kinematic viscosity, Rayleigh number, and Prandtl number, respectively. Using the above non-dimensional, equation in Eqs. (4.1)–(4.4), we get

$$\frac{\partial U}{\partial X}+\frac{\partial V}{\partial Y}=0, \tag{4.10}$$

$$U\frac{\partial U}{\partial X}+V\frac{\partial U}{\partial Y}=-\frac{\rho_f}{\rho_{nf}}\frac{\partial P}{\partial Y}+Pr\frac{\nu_{nf}}{\nu_f}\left(\frac{\partial^2 V}{\partial X^2}+\frac{\partial^2 V}{\partial Y^2}\right), \tag{4.11}$$

$$\begin{aligned} U\frac{\partial V}{\partial X}+V\frac{\partial V}{\partial Y}=&-\frac{\rho_f}{\rho_{nf}}\frac{\partial P}{\partial Y}+Pr\frac{\nu_{nf}}{\nu_f}\left(\frac{\partial^2 V}{\partial X^2}+\frac{\partial^2 V}{\partial Y^2}\right) \\ &-Ha^2PrV+\frac{(1-\phi)\rho_f\beta_f+\phi\rho_p\beta_p}{\rho_f\beta_f}RaPr\theta, \end{aligned} \tag{4.12}$$

$$U\frac{\partial \theta}{\partial X}+V\frac{\partial \theta}{\partial Y}=\frac{\alpha_{nf}}{\alpha_f}\left(\frac{\partial^2 \theta}{\partial X^2}+\frac{\partial^2 \theta}{\partial Y^2}\right). \tag{4.13}$$

4.2.3 Dimensionless boundary conditions:

At outer square wall

:

$$\begin{aligned} U(X,Y)=V(X,Y)=0 \ \text{ and } \ \theta(X,Y)=0 \ \text{ at } \ \Omega_1\cup\Omega_2\cup\Omega_4,\\ U(X,Y)=V(X,Y)=\frac{\partial\theta}{\partial Y}=0 \ \text{ at } \ \Omega_3,\\ \Omega_1=\{X,Y\in\mathcal{R}/0\le X<1 \ \wedge \ Y=0\},\\ \Omega_2=\{X,Y\in\mathcal{R}/X=1 \ \wedge \ 0\le Y<1\},\\ \Omega_3=\{X,Y\in\mathcal{R}/0\le X<1 \ \wedge \ Y=1\},\\ \Omega_4=\{X,Y\in\mathcal{R}/X=0 \ \wedge \ 0\le Y<1\}. \end{aligned} \tag{4.14}$$

At inner horizontal and vertical fins in dimensionless form:

$$\begin{aligned} U(X,Y)=V(X,Y)=0 \text{ and } \ \theta(X,Y)=1 \ \text{ at } \ \Omega_5,\\ U(X,Y)=V(X,Y)=0 \text{ and } \ \theta(X,Y)=0 \ \text{ at } \ \Omega_6,\\ U(x,Y)=V(X,Y)=0 \text{ and } \ \theta(X,Y)=1 \ \text{ at } \ \Omega_7,\\ U(X,Y)=V(X,Y)=0 \text{ and } \ \theta(X,Y)=0 \ \text{ at } \ \Omega_8,\\ U(X,Y)=V(X,Y)=0 \text{ and } \ \theta(X,Y)=1 \ \text{ at } \ \Omega_9. \end{aligned} \tag{4.15}$$

$$
\begin{aligned}
\Omega_5 &= \{X, Y \in \mathcal{R}/a \leq X < b \quad \wedge \quad Y = a_1 \quad \wedge \quad b_1\}, \\
\Omega_6 &= \{X, Y \in \mathcal{R}/c \leq Y < d \quad \wedge \quad X = c_1 \quad \wedge \quad d_1\}, \\
\Omega_7 &= \{X, Y \in \mathcal{R}/e \leq X < f \quad \wedge \quad Y = e_1 \quad \wedge \quad f_1\}, \\
\Omega_8 &= \{X, Y \in \mathcal{R}/g \leq Y < h \quad \wedge \quad X = g_1 \quad \wedge \quad h_1\}, \\
\Omega_9 &= \{X, Y \in \mathcal{R}/i \leq Y < j \quad \wedge \quad X = i_1 \quad \wedge \quad j_1\}.
\end{aligned} \tag{4.16}
$$

All the above mentioned lengths for both horizontal and vertical cases vary, that depends upon the coordinates $a, b, c, d, e, f, g, h, i, j, a_1, b_1, c_1, d_1, e_1, f_1, g_1, h_1, i_1, j_1$. In the ordered pair form, these lengths can be described as: (a, b), (c, d) and (a_1, b_1), (c_1, d_1) be the coordinate of length and width of horizontal fins, respectively. Similarly, the coordinate of vertical fins along horizontal varies are (e, f), (i, j), (g, h) and (e_1, f_1), (i_1, j_1), (g_1, h_1), respectively. To perform the simulation the middle fin is considered to be heated.

Table 4.2: Position of fins according to coordinate system

$a = 0.3$	$b = 0.7$	$a_1 = 0.19$	$b_1 = 1$
$c = 0.3$	$d = 0.7$	$c_1 = 0.80$	$d_1 = 0.81$
$e = 0.3$	$f = 0.7$	$e_1 = 0.29$	$f_1 = 0.30$
$g = 0.3$	$h = 0.7$	$g_1 = 0.70$	$h_1 = 0.71$
$i = 0.3$	$j = 0.7$	$i_1 = 0.80$	$j_1 = 0.81$

4.3 Numerical Procedure

Using the Galerkin weighted residual method to solve the equation (4.11)-(4.13) subject to boundary conditions (4.14)-(4.16). To eliminate pres-

Table 4.3: Thermophysical properties of Water and Nanofluid

Physical properties	Base fluid (water)	SWCNT
C_p(J/kgK)	4179	425
ρ(kg/m^3)	997.1	2600
K(W/mK)	0.613	6600
β (1/K)	21×10^5	0.33×10^5
r (nm)	0.1	10

sure terms using continuity equation, for that applying Penalty method. Using the incompressible condition, the Penalty parameter γ is developed as follows:

$$P = -\gamma \left(\frac{\partial U}{\partial X} + \frac{\partial V}{\partial Y} \right). \tag{4.17}$$

Using (4.17) in Eqs. (4.11)-(4.13), we get

$$U\frac{\partial U}{\partial X} + V\frac{\partial V}{\partial Y} = \gamma \frac{\rho_f}{\rho_{nf}} \frac{\partial}{\partial X} \left(\frac{\partial U}{\partial Y} + \frac{\partial V}{\partial Y} \right) + Pr \frac{\nu_{nf}}{\nu_f} \left(\frac{\partial^2 U}{\partial X^2} + \frac{\partial^2 U}{\partial Y^2} \right), \tag{4.18}$$

$$\begin{aligned} U\frac{\partial V}{\partial X} + V\frac{\partial V}{\partial Y} = \gamma \frac{\rho_f}{\rho_{nf}} \frac{\partial}{\partial Y} \left(\frac{\partial U}{\partial X} + \frac{\partial V}{\partial Y} \right) + Pr \frac{\nu_{nf}}{\nu_f} \left(\frac{\partial^2 U}{\partial X^2} + \frac{\partial^2 U}{\partial Y^2} \right) \\ -Ha^2 PrV + \frac{(1-\phi)\rho_f \beta_f + \phi \rho_p \beta_p}{\rho_f \beta_f} RaPr\theta. \end{aligned} \tag{4.19}$$

Using bi-quadratic basis functions to approximate the unknown velocity and temperature functions. $S_{k=i}$ be the 4-nodal square elements such as

$$U = \sum_{k=1}^{4} U_k \phi_k^*(X,Y), \quad V = \sum_{k=1}^{4} V_k \phi_k^*(X,Y), \quad \theta = \sum_{n=1}^{4} T_k \phi_k^*(X,Y). \tag{4.20}$$

Nonlinear residual equations obtained by using the Glarekin weighted residual technique used inside the domain of Ω.

$$\begin{aligned} R_j^1 = &\sum_{k=1}^{N} U_k \int_\Omega \left[\left(\sum_{k=1}^{N} U_k \phi_k^* \right) \frac{\partial \phi_k^*}{\partial X} + \left(\sum_{k=1}^{N} V_k \phi_k^* \right) \frac{\partial \phi_k^*}{\partial Y} \right] \phi_j^* dX dY \\ &+ \gamma \frac{\rho_f}{\rho_{nf}} \left[\sum_{k=1}^{N} U_k \int_\Omega \frac{\partial \phi_j^*}{\partial X} \frac{\partial \phi_k^*}{\partial X} dX dY + \sum_{k=1}^{N} V_k \int_\Omega \frac{\partial \phi_j^*}{\partial X} \frac{\partial \phi_k^*}{\partial Y} dX dY \right] \\ &+ Pr \frac{\nu_{nf}}{\nu_f} \sum_{k=1}^{N} U_k \int_\Omega \left[\frac{\partial \phi_j^*}{\partial X} \frac{\partial \phi_k^*}{\partial X} + \frac{\partial \phi_j^*}{\partial Y} \frac{\partial \phi_k^*}{\partial Y} \right] dX dY, \end{aligned} \tag{4.21}$$

$$\begin{aligned} R_j^2 = &\sum_{k=1}^{N} V_k \int_\Omega \left[\left(\sum_{k=1}^{N} U_k \phi_k^* \right) \frac{\partial \phi_k^*}{\partial X} + \left(\sum_{k=1}^{N} V_k \phi_k^* \right) \frac{\partial \phi_k^*}{\partial Y} \right] \phi_j^* dX dY \\ &+ \gamma \frac{\rho_f}{\rho_{nf}} \left[\sum_{k=1}^{N} U_k \int_\Omega \frac{\partial \phi_j^*}{\partial Y} \frac{\partial \phi_k^*}{\partial X} dX dY + \sum_{k=1}^{N} V_k \int_\Omega \frac{\partial \phi_j^*}{\partial Y} \frac{\partial \phi_k^*}{\partial Y} dX dY \right] \\ &+ Pr \frac{\nu_{nf}}{\nu_f} \sum_{k=1}^{N} U_k \int_\Omega \left[\frac{\partial \phi_j^*}{\partial X} \frac{\partial \phi_k^*}{\partial X} + \frac{\partial \phi_j^*}{\partial Y} \frac{\partial \phi_k^*}{\partial Y} \right] dX dY \\ &- Ha^2 Pr \int_\Omega \left[\sum_{k=1}^{N} U_k \phi_k^* \right] \phi_j^* dX dY \\ &+ \frac{(1-\phi)\rho_f \beta_f + \phi \rho_p \beta_p}{\rho_f \beta_f} RaPr \int_\Omega \left[\sum_{k=1}^{N} T_k \phi_k^* \right] \phi_j dX dY, \end{aligned} \tag{4.22}$$

$$\begin{aligned} R_j^3 = &\sum_{k=1}^{N} T_k \int_\Omega \left[\left(\sum_{k=1}^{N} U_k \phi_k^* \right) \frac{\partial \phi_k^*}{\partial X} + \left(\sum_{k=1}^{N} V_k \phi_k^* \right) \frac{\partial \phi_k^*}{\partial Y} \right] \phi_j^* dX dY \\ &+ \frac{\alpha_{nf}}{\alpha_f} \left(\sum_{k=1}^{N} T_k \int_\Omega \left[\frac{\partial \phi_j^*}{\partial X} \frac{\partial \phi_k^*}{\partial X} + \frac{\partial \phi_j^*}{\partial Y} \frac{\partial \phi_k^*}{\partial Y} \right] dX dY \right) \phi_j^* dX dY. \end{aligned} \tag{4.23}$$

To approximate the solution using the Newton-Raphson technique iteratively. Using the relation of velocity in the form of stream functions for fluid motion is as follow:

$$U = \frac{\partial \psi}{\partial Y}, \quad V = -\frac{\partial \psi}{\partial X}. \tag{4.24}$$

4.3.1 Comparison of results and Grid Independency

In this section a comparsion is presented with the existing literature published by Khanfer *et al.* [7]. Numerical result of average Nusselt number

of present work compared with [7] as shown in Table. 4.4. Consider different number of nodes along the X-axis and Y-axis of cavity. We can observe that increase the grid size the maximum and minimum value of stream functions are repeating as shown in Table. 4.5. This shows that results are repeated and no longer affected on the higher number of grids and hence this procedure is known as grid independency. Fig. 4.2 represents the comparison of current work with the experimental result developed by Parocini and Covaro [95] which are based upon isotherms plots. Fig. 4.3 is mesh generation at different positions of the square cavity.

Table 4.4: Comparison between present results and other works for the average Nusslet number: (Nu_{avg})

Ra	Present work	Khanfer *et al.* [7]	%Error
10^3	1.05012	1.118	6
10^4	1.926	2.245	16
10^5	4.06148	4.522	11
10^6	8.05925	8.826	9

4.4 Results and Discussion

In this section the numerical result has been analysed to determine the natural convection of nanofluid. The simulation is performed in square cavity filled with carbon nanoparticles and obstacles are adjusted in the form of thin fins. The magnetic filed has been carried out through these fins. This

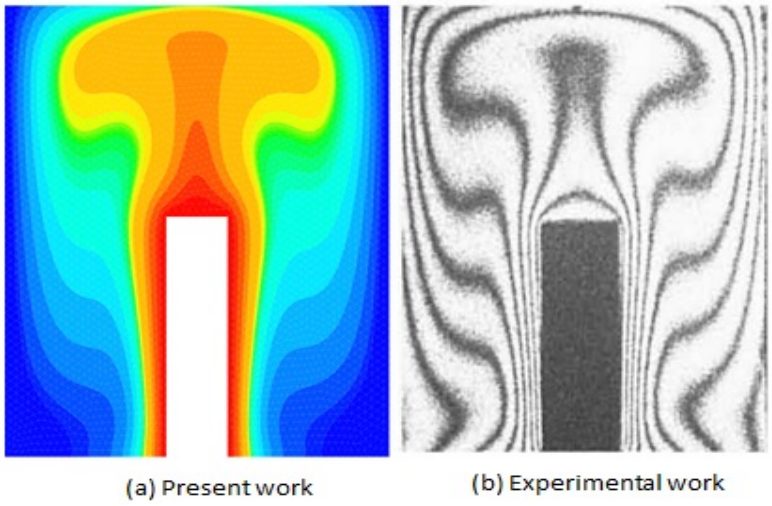

Figure 4.2: Isotherm comparison between the experimental present work and numerical study of Parocini and Covaro [95], , $Pr = 6.2$, $Ra = 1.24 \times 10^5$, $H_L = 0.25$

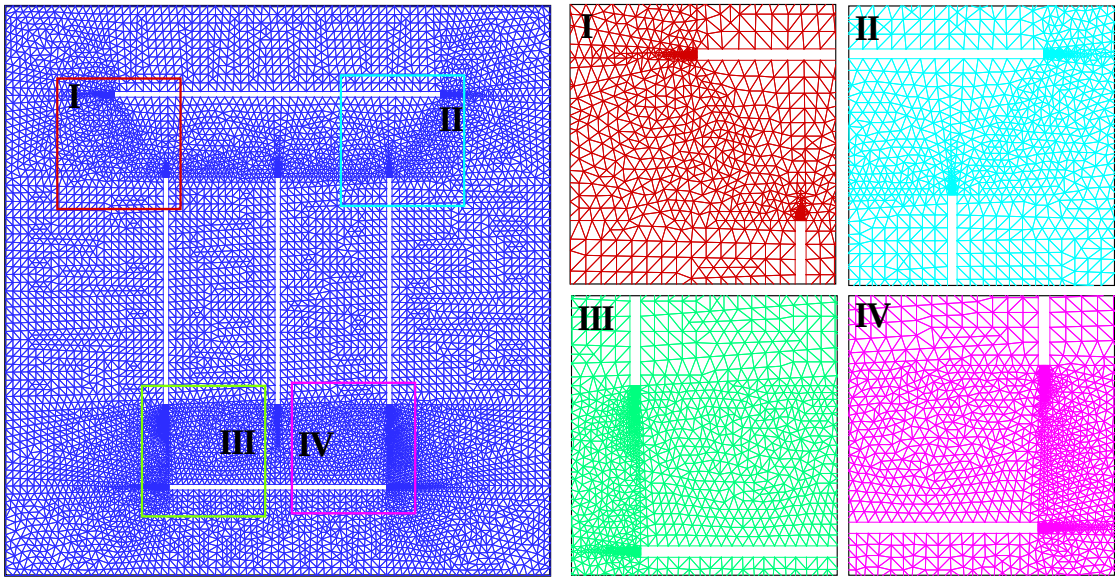

Figure 4.3: Mesh generation at different vertices of cavity

Table 4.5: Comparison of the ψ for different grid resolution by removing the inner fins from the square cavity at $Pr = 6.2$, $Ra = 10^6$, $\phi = 0.1$, $Ha = 0$.

No of Grid	ψ_{min}	ψ_{max}
20×20	-156.021	155.871
30×30	-157.409	157.514
40×40	-155.872	156.458
50×50	-157.038	156.394
55×55	-156.57	156.703

computational result acquired by using Finite element method. Here, the simulation inside the square cavity along with the various constraints at middle fins (cold, adiabatic, hot) and other physical parameters: Rayleigh number ($10^5, 10^6$ and 10^7), Hartmann number ($0 \leq Ha \leq 10$), length variation in heated lower fin, at different positions of lower heated fin and nanoparticle volume fraction ($\phi = 0.0, 0.1$ and 0.2). For such simulation Prandtl number is considered to be 6.2. The valuable results are obtained through simulation and effects of heat transfer rate, velocity and temperature distribution are plotted for emerging parameters.

Effects of various condition on vertical middle fin:

Engineer uses for heated and cooled fins range from electronic cooling to industrial drying and refrigeration. They are an important tool in the design and optimization of thermal processes since their application can considerably increase a system's performance and efficiency. In refrigeration systems, cold

fins are frequently utilised. The fins in a refrigeration system are used to transfer heat from the air around it to a refrigerant. The system's heat is subsequently removed by the refrigerant, which cools the air inside the square cavity. The effect of middle vertical fin (cold, adiabatic, hot) on the streamline and isotherm are expressed in Fig. 4.4(a-f) for the value of fixed parameter $Pr = 6.2, Ha = 0, Ra = 10^6, \phi = 0.1$. In such cases, the cold middle vertical fin creates strong streamline around the lower heated fin. This streamline is stronger than heated and adiabatic middle vertical fin. Fig. 4.4(a and c) demonstrate that around the vertical fins, the streamline shows the strong concentration of molecules around the vertical sides of fin. However, these effects vanish when cold case is considered. In Fig. 4.4(c), the concentration of molecules are much stronger along a vertical side fins. It seems that the streamlines are in excess case of hot vertical fin than cold in cavity. Fig. 4.4(d)-(f) be the isotherms result for different cases of middle fin. Fig. 4.4(e) describes that heat cannot pass through vertical fins to upward, it is restricted around the lower horizontal fin, due to the cold vertical fin. But Fig. 4.4(f) reveals that the heat flows upward inside the entire cavity. Buoyancy forces play their role to transfer the heat in the upward direction.

The heat transfer rate, velocity and temperature distribution for different vertical middle fin (cold, adiabatic, hot) is described in Fig. 4.5(a-e). The heat transfer rate at the lower face of bottom fin is higher for heated vertical fin than the cold and adiabatic fin. Fig. 4.5(c) shows that at the end point of the lower face of bottom fin is the highest rate, as well as the upper face of bottom fin is maximum for heated vertical fin. But in case of adiabatic fin normal heat rate flows for both faces of fin. In Fig. 4.5(d) one can depict the effects on temperature due to various middle fins. In the first half, between left vertical fin, temperature increases due to the heated middle fin and also satisfies its boundary condition. But in case of cold fin, temperature suddenly decreases and it tends to come at zero. At the middle of vertical fins, it again

rises up due to the bottom hot fin and it attains maximum heat. In heated fin, the case along the mean path increases and satisfies the boundary condition towards the end point. At the boundary or away from the middle fin, there is consistent temperature in all cases. The effect of cold, adiabatic and hot fins in horizontal and vertical velocity in Fig. 4.5(a)-(b) is demonstrated. In all three cases, the effect on horizontal velocity are different. In case of hot, middle fin velocity attains maximum and minimum molecular motion in mean path near the walls of square cavity. On the other hand, at the middle, the motion of molecule is less in case of hot fin than that of adiabatic case.

Effects of length in various heated fin:

The streamline and isotherms behaviour in a square cavity is described in Fig. 4.6(a-f). Heat transfer is dominant and intensed with respect to increase in length of heated portion. From Fig. 4.6(a-c), which depicts that length of heated portion may reduce the flow rate of streamlines. However, on the other hand isotherms behaviour is significantly enhanced due to enlargement of heated bottom length. It can be further observed that, due to small heated length, isotherms just pass through vertically parallel fins. However, when we increase the length of heated bottom portion then isotherms are expanded outside of the vertically parallel fins. Fig. 4.7(a) and (b) describes the variation of velocities (U and V) along the X and Y-directions, respectively. One can observe the variation of velocity for three different heated portion lengths are ($H_T = 0.2, 0.4$ and 0.8). Symmetric but inverse behaviour of velocity U is observed and higher velocity distribution is attained with respect to extended length of heated fin. In Fig. 4.7(b), velocity is quite dominant near to the lower heated fin but low behaviour of velocity moves away from heated portion due to high fluid's molecular motion. Nusselt number at upper and lower face of heated portion has been plotted in Fig. 4.6(c-d). In both upper and lower faces of the heated portion, heat transfer behaviour at the surface of fin is increasing with respect to the increase in heated length. Temperature

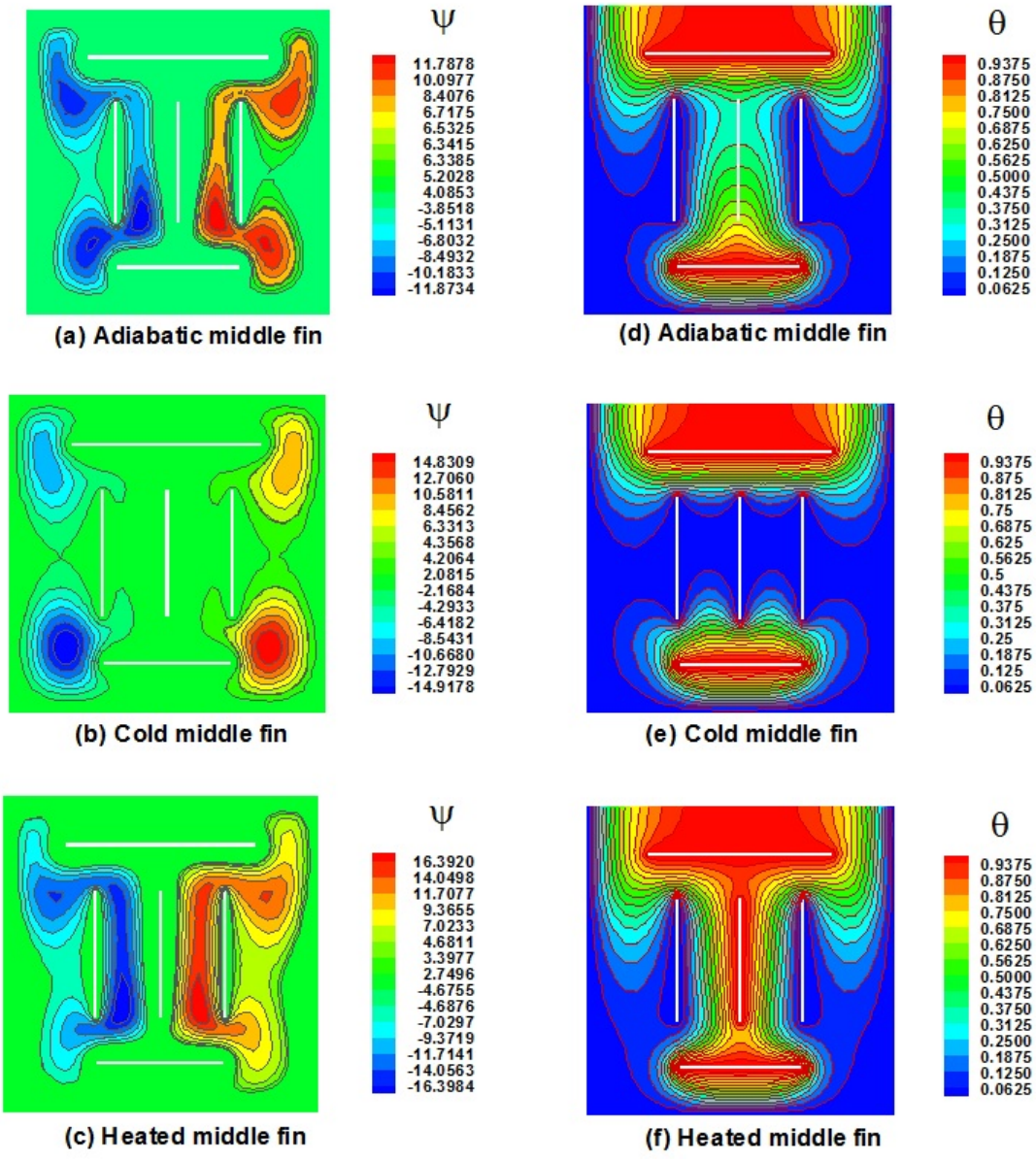

Figure 4.4: Effects on streamline and isotherms due to variation of middle fin

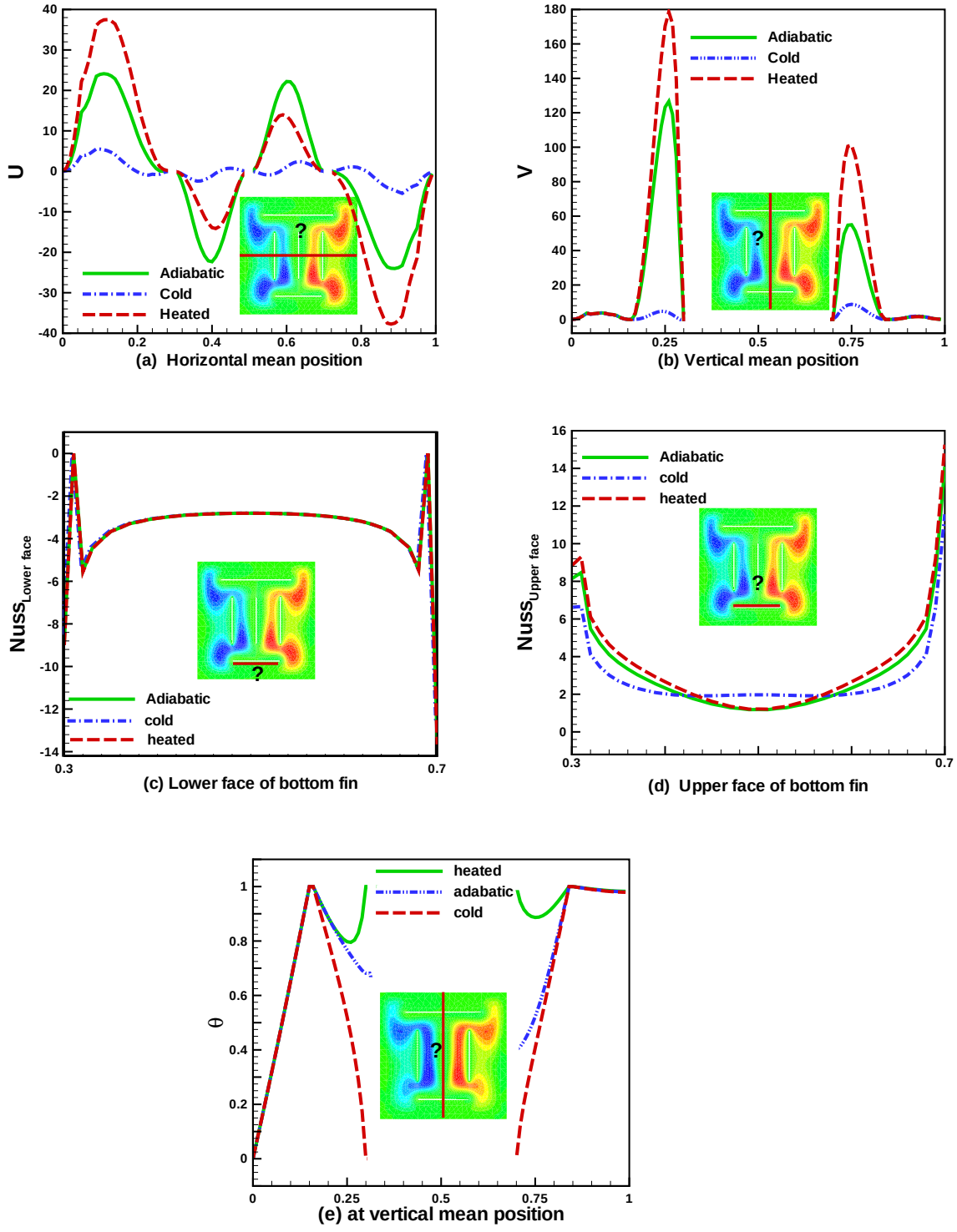

Figure 4.5: Effects of variation in middle fin on the velocity, temperature distribution and Nusselt number

profiles along vertically mean position is plotted in Fig. 4.7(e). Since outer cavity is adjusted for cold walls, therefore temperature profile starts from zero and attains the maximum heat which is being adjusted for heated fin.

Table 4.6: Influence of heat transfer rate in cavity due to increasing heated fin's length from 0.2 to 0.8

Length of heated fin	Nu_{avg}	% Increased
0.2	2.16	-
0.4	2.39	10
0.8	2.51	16

Effects of position of lower fin on the cavity:

Fig. 4.8(a-f), demonstrates the position of heated bottom length and one can observe that both isotherms and streamlines behave with respect to the position of heated length at different positions (right, left, mean), the position of fin. In Fig. 4.8(a) the heated fin is on the left position, then the maximum flow of streamline passes through right vertical fin. But in Fig. 4.8(c) when the position of heated fin at the right position the streamline is enhanced through left vertical fin. Streamline is symmetric in cavity when the heated fin is at the mean position as shown in Fig. 4.8(c). Fig. 4.8(d-f) illustrates the effects on isotherms due to the position of that heated fin. Heat transfer through the heated lower fin, that is why flow of heat depends on the position of fin, when fin is placed at left position, flow of heat is maximum near the heated fin similarly when fin is placed it right position, isotherm generates through the right. In Fig. 4.8(e) isotherm is equally distributed throughout in cavity.

Fig. 4.9(a-e) shows the effect of position of heated fin on velocity,

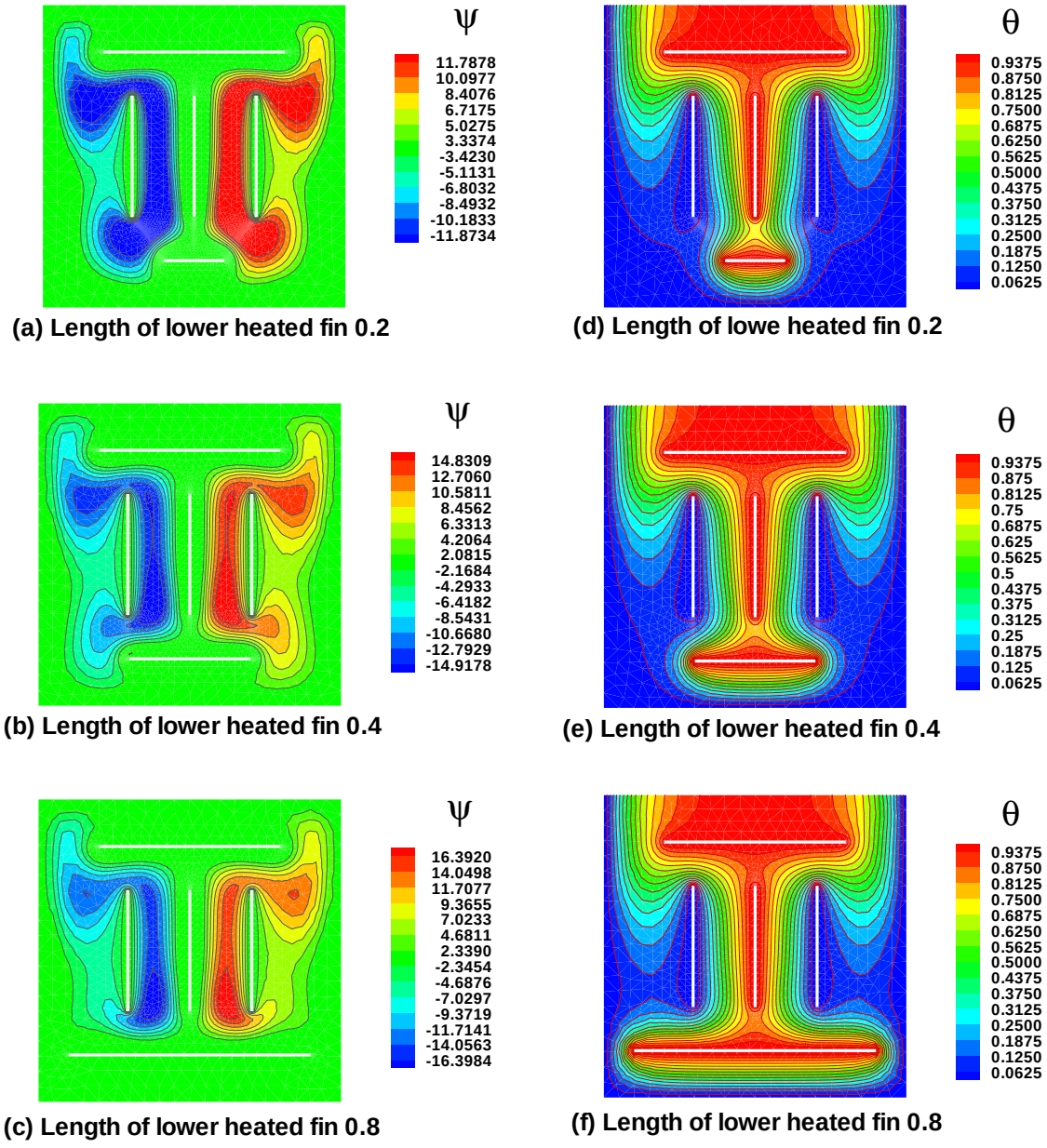

(a) Length of lower heated fin 0.2

(d) Length of lowe heated fin 0.2

(b) Length of lower heated fin 0.4

(e) Length of lower heated fin 0.4

(c) Length of lower heated fin 0.8

(f) Length of lower heated fin 0.8

Figure 4.6: Effects on streamline and isotherms due to variation in length of middle fin

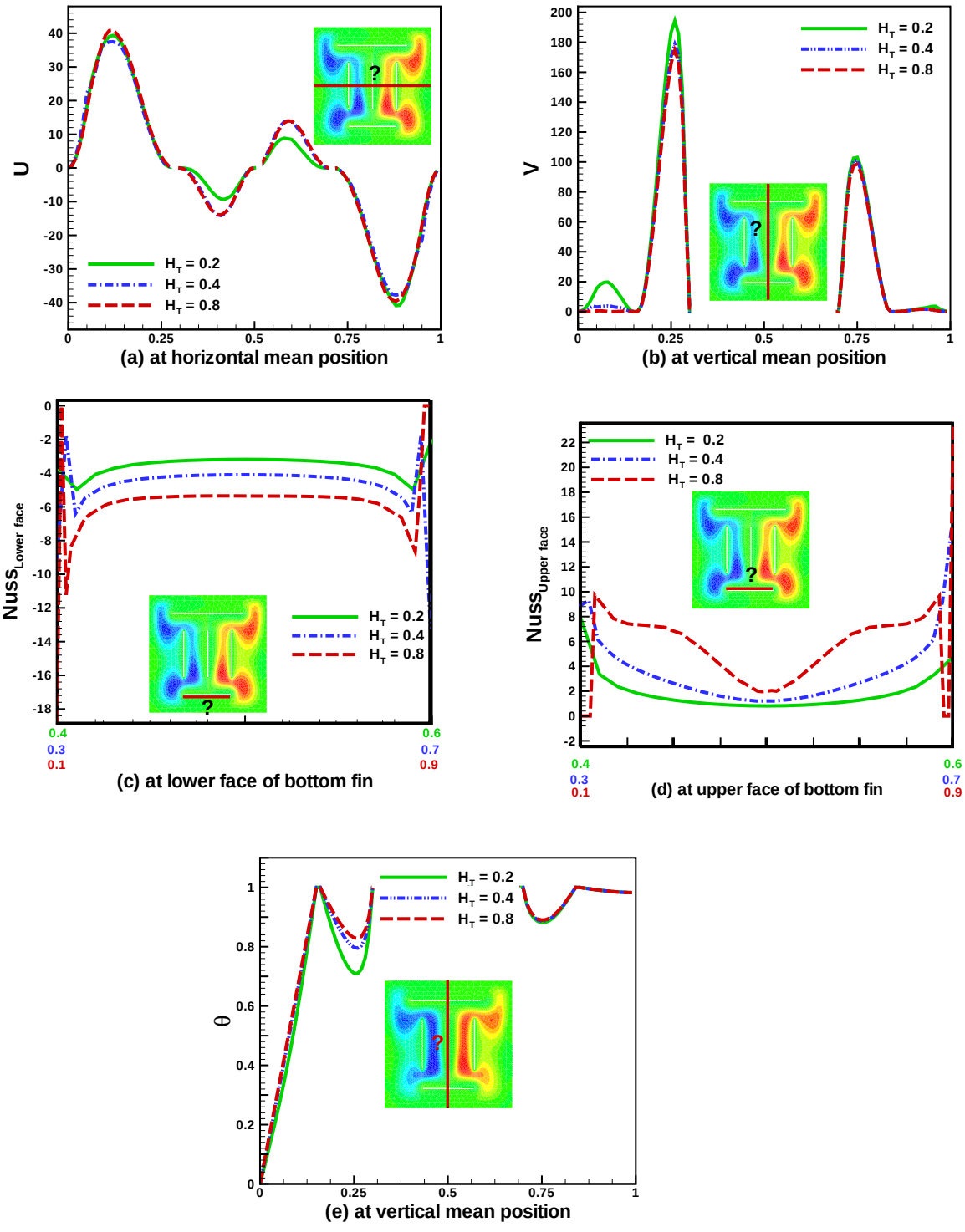

Figure 4.7: Effects of length variation in lower fin on the velocity, temperature distribution and Nusselt number

temperature and Nusselt number. Fig. 4.9(a) clearly describes that horizontal velocity increases on the right position when heated fin is in the left position. When heated fin is placed on the right position, velocity increases on the left side. Vertical velocity in Fig. 4.9(b) signifies maximum on the left side when fin is placed on left side but when it is placed on right side velocity is uniform. On Nusselt number, the effect of heated fin position is shown in Fig. 4.9(c and d). The lower face of heated fin could not have significant effect because of the position of heated fin on Nusselt number. Similarly, in the upper face of heated fin, when the fin is moved towards left to right as shown in Fig. 4.9(d). Fig. 4.9(e) depicts that the temperature is distributed equally when fin is moved towards its mean position and when placed on the right side, temperature move towards the right side.

Table 4.7: Effect of heated fin placement inside the square cavity

Position	Nu_{avg}	% Error
Mean position	3.33	-
left position	3.47	4.2
Right position	3.49	4.80

Effects of Rayleigh number:

The effects of Rayleigh ($10^5 \leq Ra \leq 10^7$) on isotherm and streamlines in Fig. 4.10(a-f), which shows that streamlines are stronger with enhancement of Rayleigh number. Fig. 4.10(a-c) describes that the streamlines are strong near the lower heated fin when Rayleigh number is increased. The streamline is closer to the heated fin when in Fig. 4.10(c) as compare to the Fig. 4.10(a and b). In case of isotherm, temperature is distributed when Ra increases. In Fig.

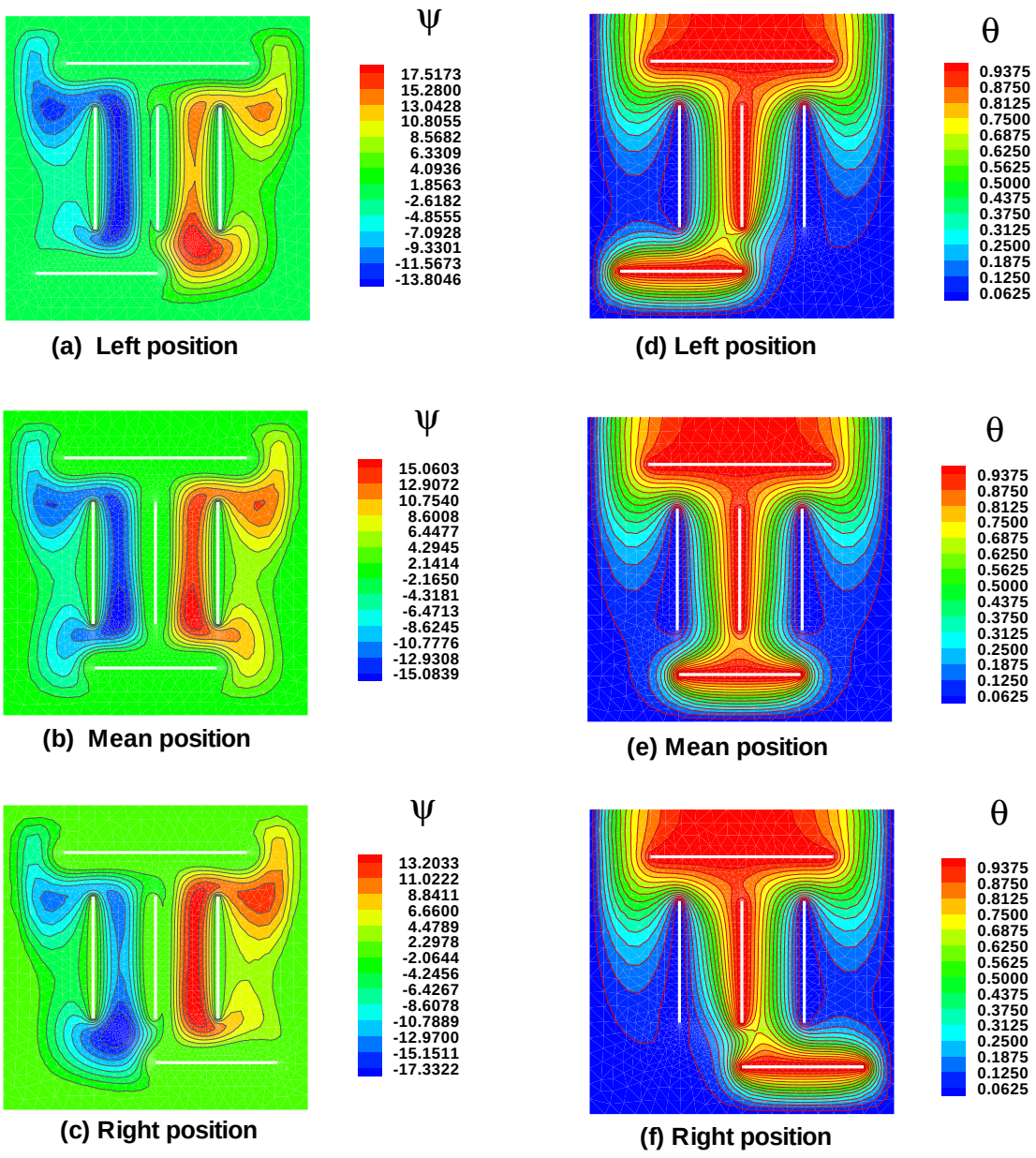

Figure 4.8: Effects on streamlines and isotherm due to position variation of lower fin

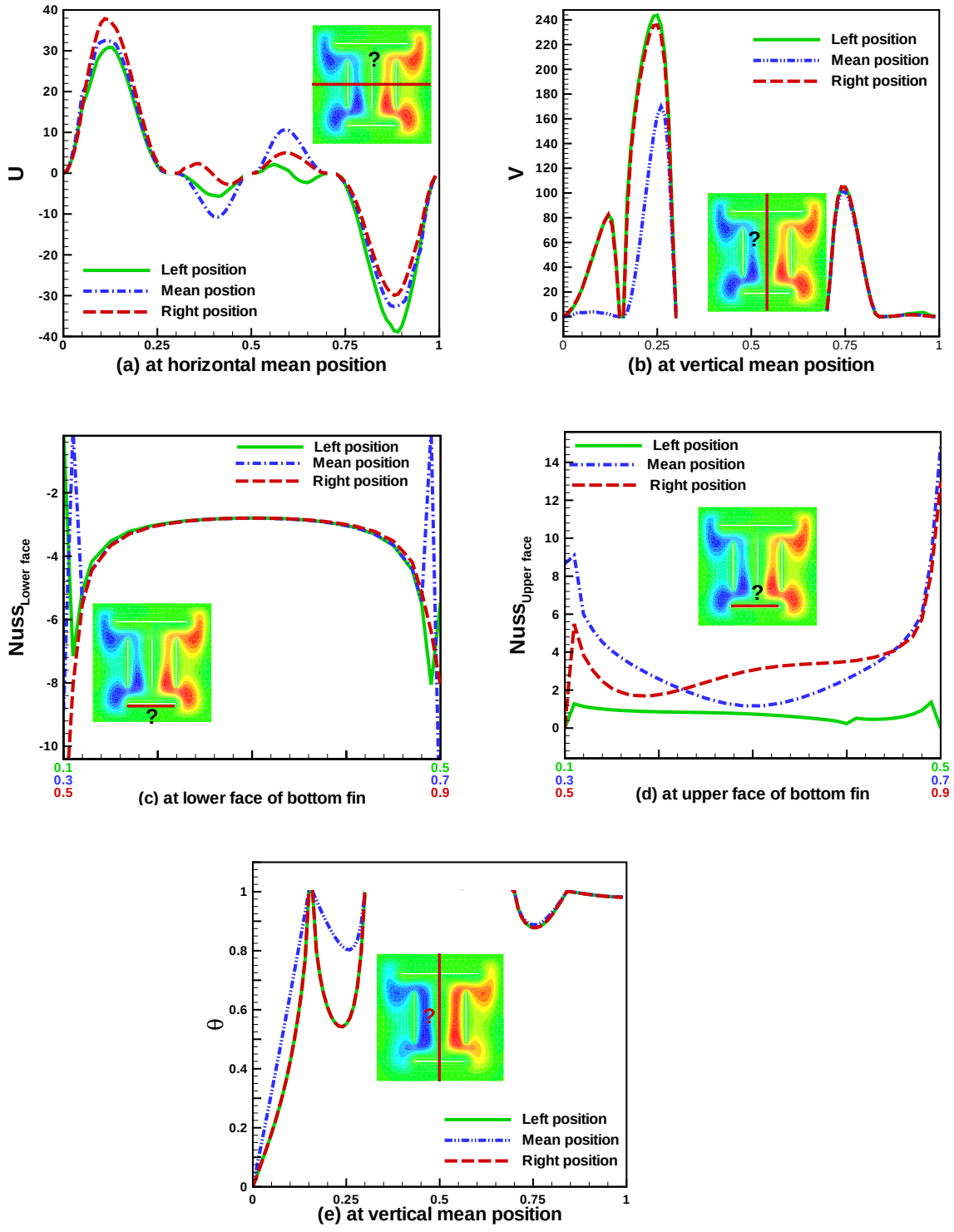

Figure 4.9: Effects of length variation in lower fin on the velocity, temperature distribution and Nusselt number

4.10(d-f), when Ra is increased, more heat is transmitted in cavity. Fig. 4.10(f) is noticeable in which whole cavity is filled with heat. In the case of increasing Ra more intensive free convection on free flow of isotherm is observed. Fig. 4.11(a-e) shows the effect of Rayleigh number on the heat transfer rate at bottom and upper face of lower heated fin, temperature and horizontal and vertical velocity distribution. Velocity attains its maximum position at the end point of vertical fins. Heat transfer enhances as Ra increases. In Fig. 4.11(b) vertical velocity against heated lower fin are increased in cavity when Rayleigh number is increased in the left and right region of vertical fins. It also acquires that velocity is zero towards its end point of solid fins. Flow rate to mean position of bottom face, lower heated fin decreases when Ra is increased. The heat transfer due to the lower face of lower heated fin can clearly be seen in Fig. 4.11(c) which illustrates that the transfer of heat decreases when Rayleigh number increases. Fig. 4.11(d) depicts the heat transfer rate due to the upper face of heated fin. Rayleigh number enhances the heat flow in cavity. Temperature distribution in that case is quite interesting when the Rayleigh number increases. Temperature arises through lower heated fin which moves upward in this case when Ra increases, temperature in cavity also increases.

Effects of volume fraction of nanoparticles:

The effects of nanoparticles on isotherm are expressed in Fig. 4.12(a-c). In first figure, it indicates that streamline is stronger near the heated fin but gradually weakens with increasing nanoparticles ($0 \leq \phi \leq 0.2$). The transfer of heat increases when quantity of ϕ increases. Fig. 4.12(f) illustrates that the temperature increases due to the nanoparticles. Fig. 4.13(a-e) elaborates the effects of nanoparticles on velocity (horizontal and vertical) and heat transfer. Heat transfer rate increases when nanoparticle increases. The transfer of heat increases near the heated fin and maximum heat is transferred at the end point. Fig. 4.13(a) demonstrates that at the end point, Ω_5 there is maximum heat transfer rate. However, that is the transfer of heat on lower face of fin. Fig.

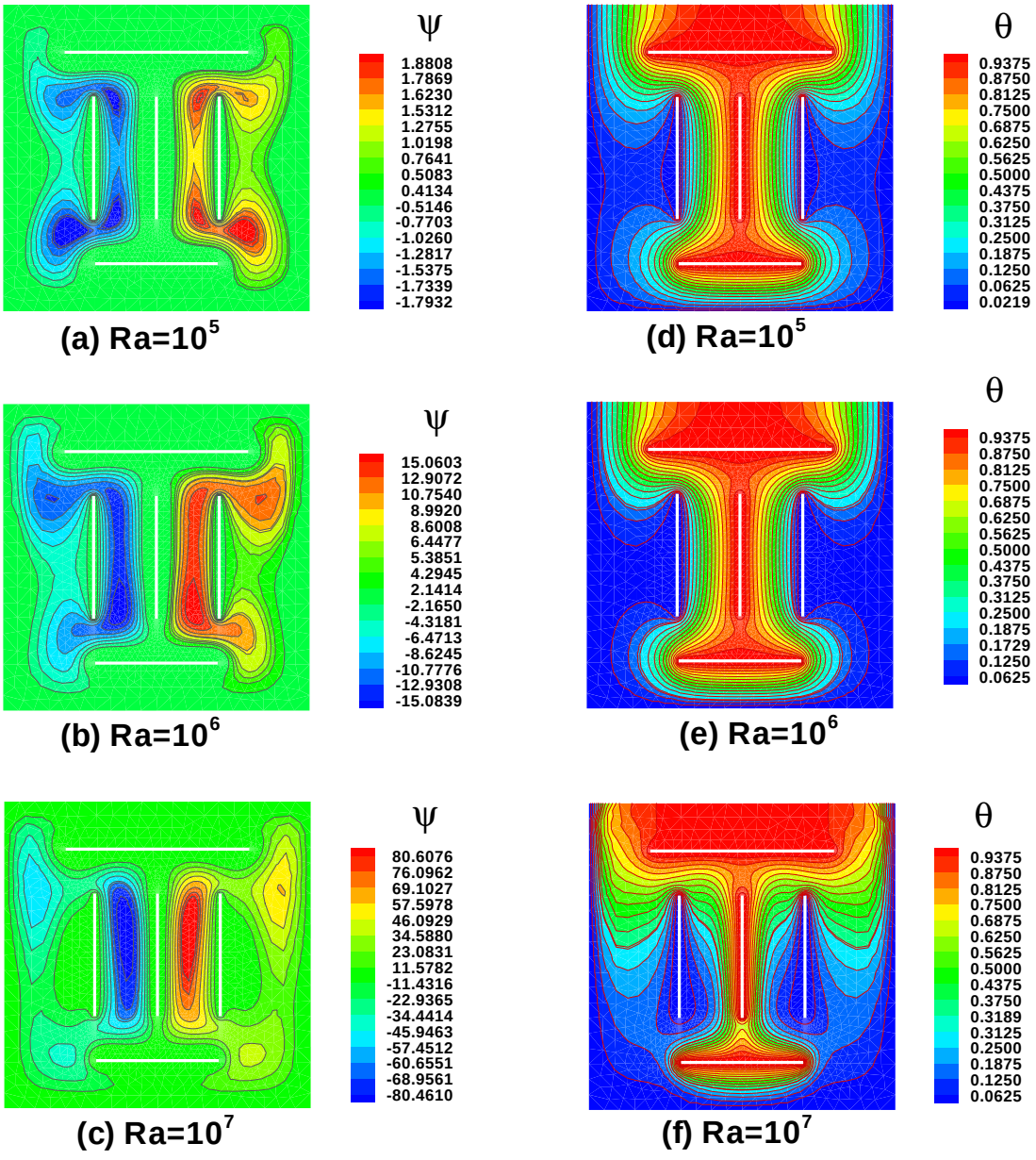

Figure 4.10: Effects on streamline and isotherms due to variation in Ra

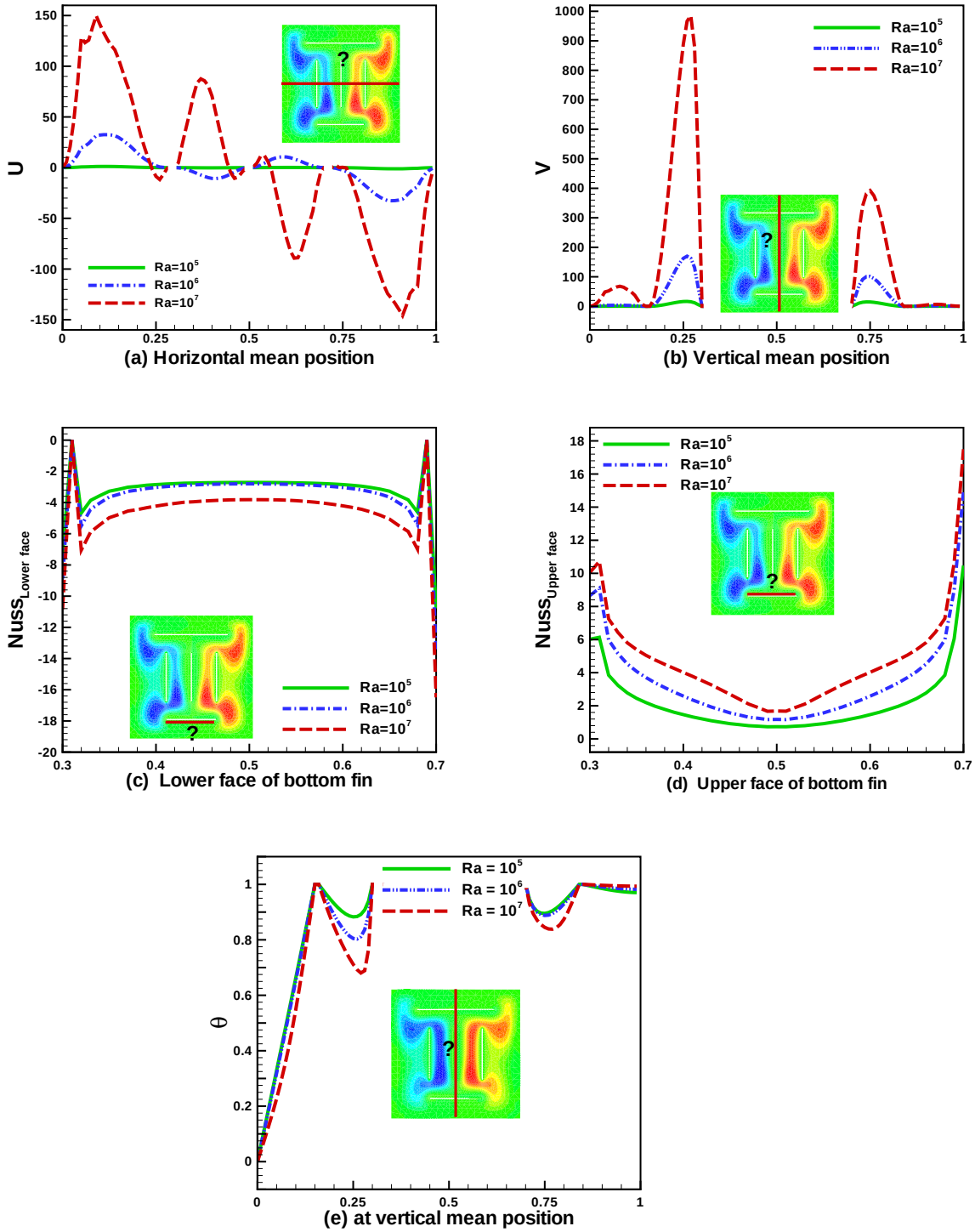

Figure 4.11: Effects of *Ra* on the velocity, temperature distribution and Nusselt number

4.13(d) represents the upper face, heat transfer rate decreases with increasing nanoparticles. It attains maximum position at the end point of heated length which also satisfies the boundary condition. Moreover, horizontal velocity on the left side of heated fin, nanoparticle increases and it has inverse on the right side of fin. Vertical velocity decreases when the nanoparticle increases on both side of heated fin in cavity.

Effects of Hartmann number:

Fig. 4.14(a-f) depicts the effects of Hartmann number ($0 \leq Ha \leq 10$) on the isotherms and streamline. The effects of magnetic field in the presence of nanoparticle do not affect significantly. Isotherms profile depict that in all the cases simulation is quite similar. Fig. 4.15(a-e) also describes that there is no significant effect on heat flow due to the variation of Hartmann number.

4.5 Conclusion

Natural convection with heat generation inside of square cavity having horizontal and vertical thin fins is analyzed in the presence of carbon nanoparticle. The governed partial differential equations are solved by finite element method. The simulation is performed for different state of fins that have various effects (cold, adiabatic, hot) while the position of lower horizontal heated fin is (left, right, mean position), length of heated lower fin is ($T_h = 0.4$), Rayleigh number ($10^5 \leq Ra \leq 10^7$), nanoparticle ($0.0 \leq \phi \leq 0.2$) and magnetic strength (Hartmann number) ($0 \leq Ha \leq 10$) on the velocity, temperature and Nusslet number. After the simulation the following results are concluded:

- For hot, middle vertical thin fin has significant effect on the flow behaviour based upon streamline between vertical fins. Due to the natural convection, more heat transfer is obtained in case of hot middle thin fin.

- Variation of lower heated length has major effects in the heat transfer in

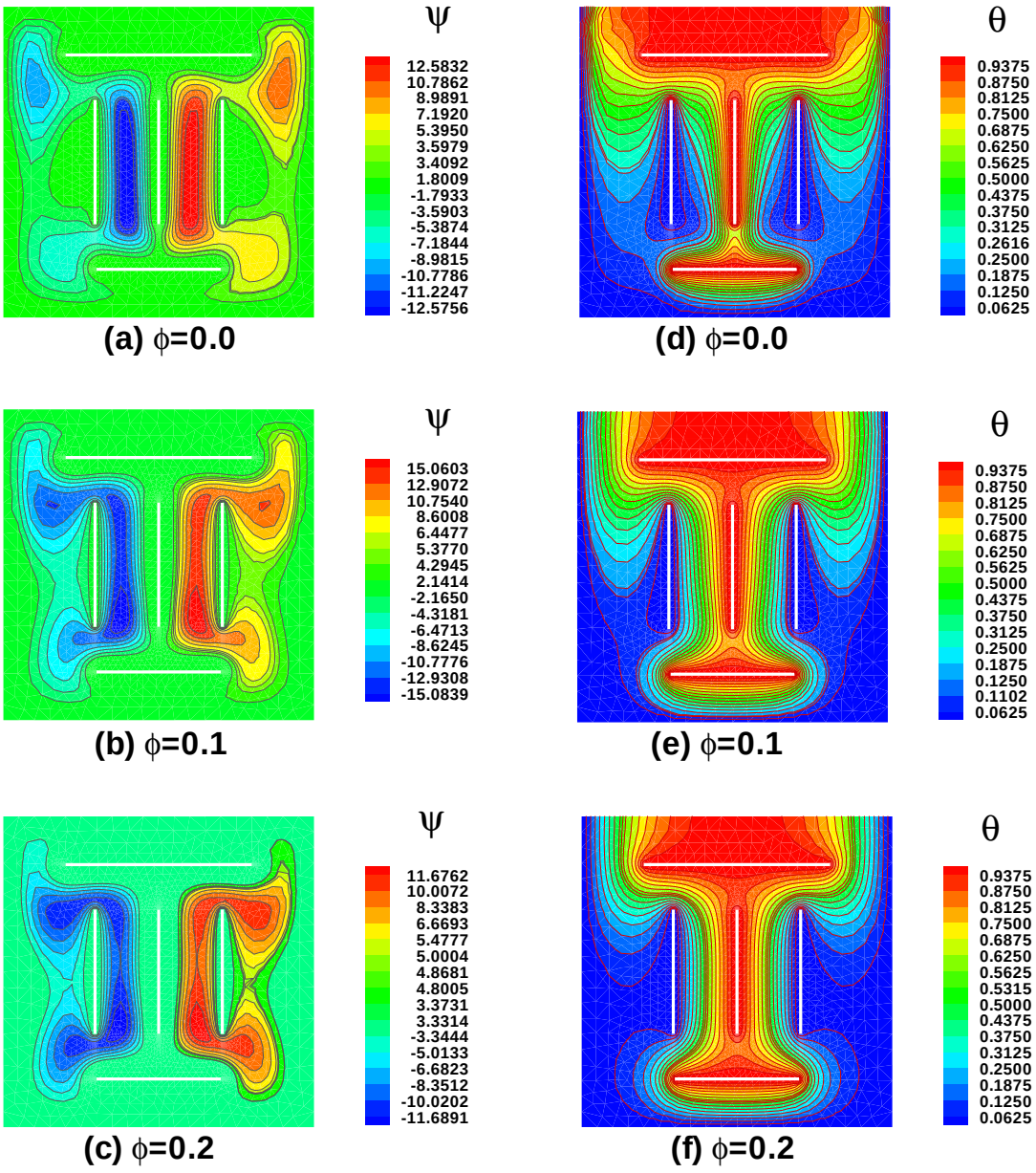

Figure 4.12: Effects on streamline and isotherms due to variation of nanoparticle volume fraction

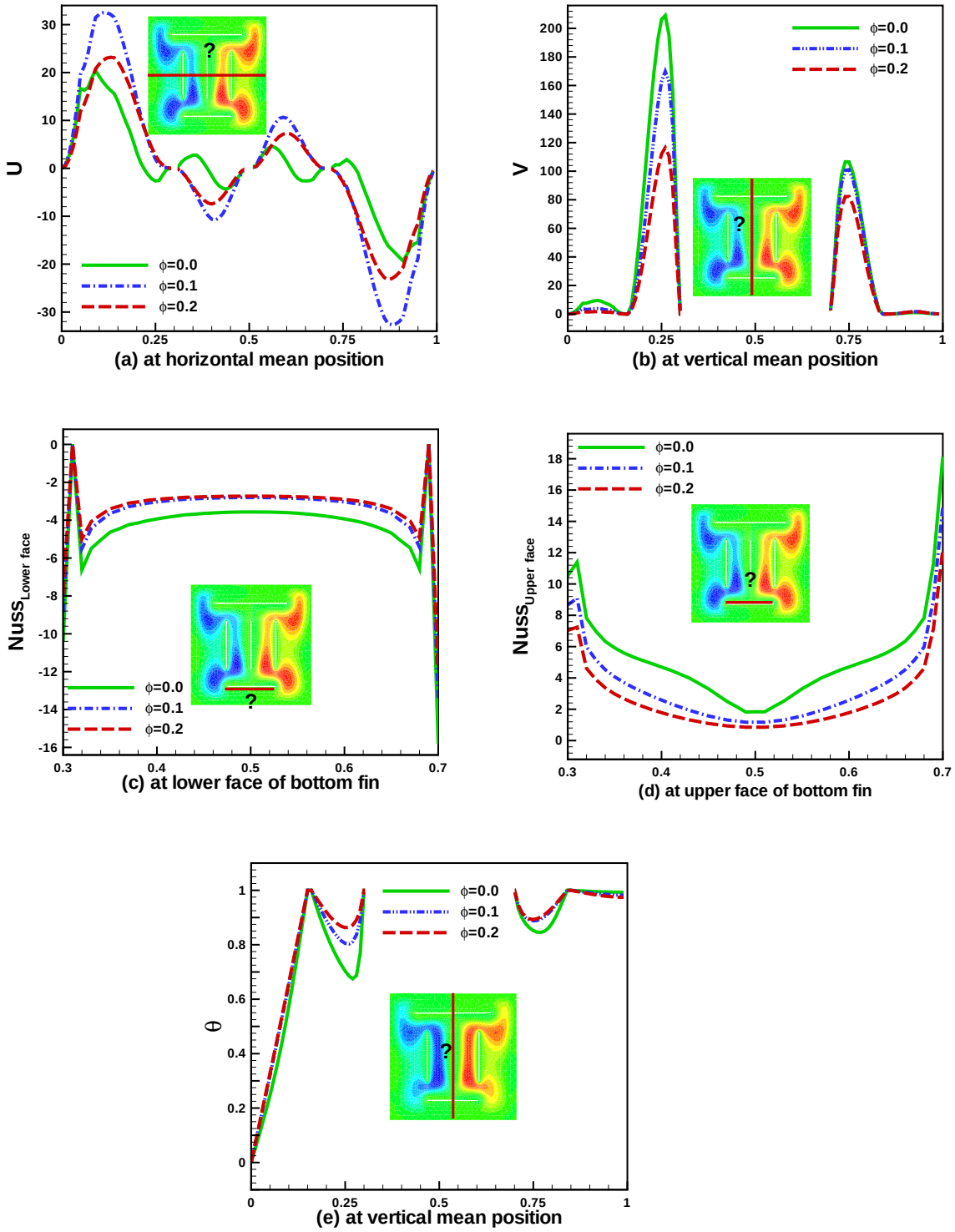

Figure 4.13: Effects of nanoparticles on the velocity, temperature distribution and Nusselt number

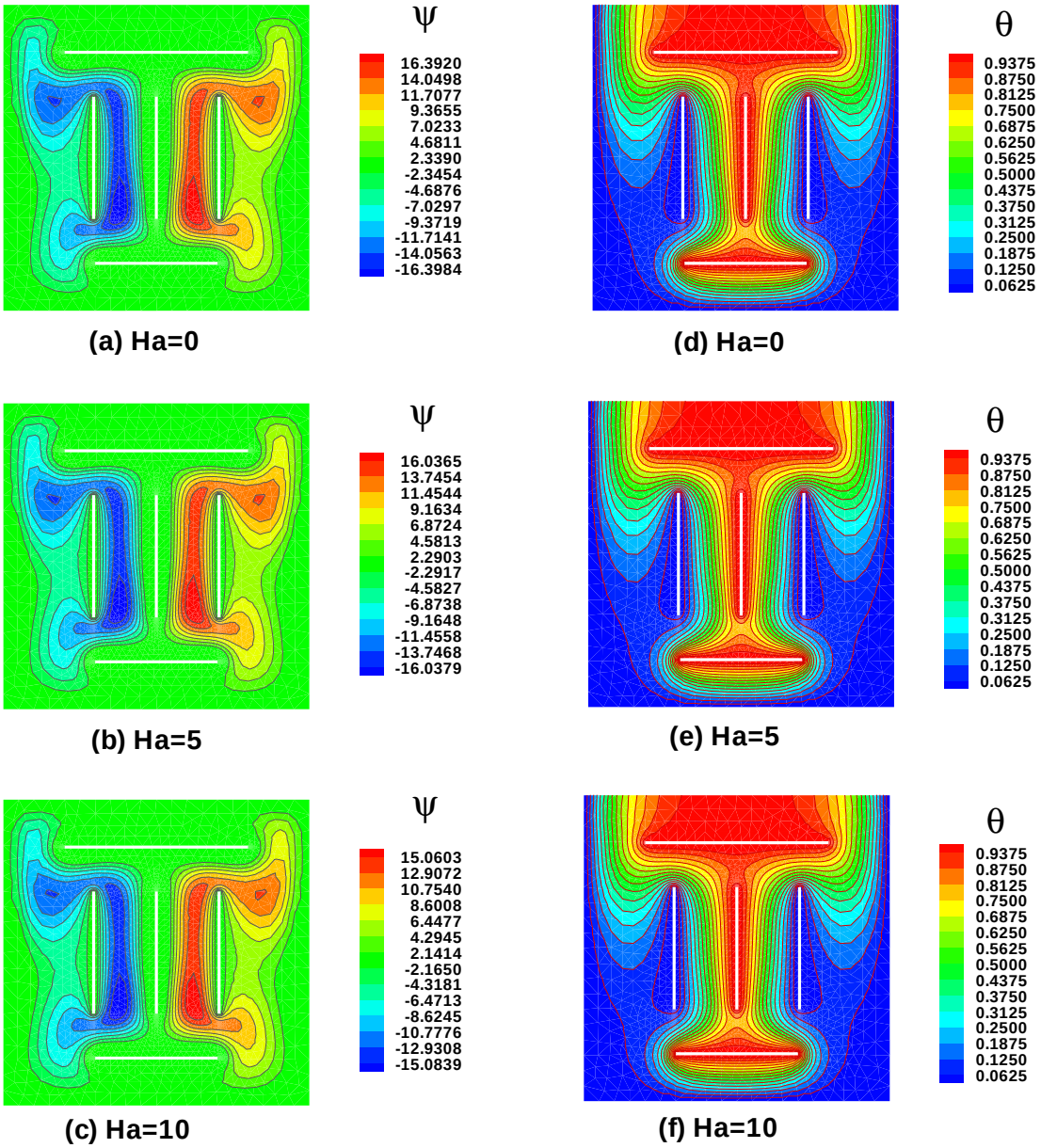

Figure 4.14: Effects on streamline and isotherms due to variation of Ha

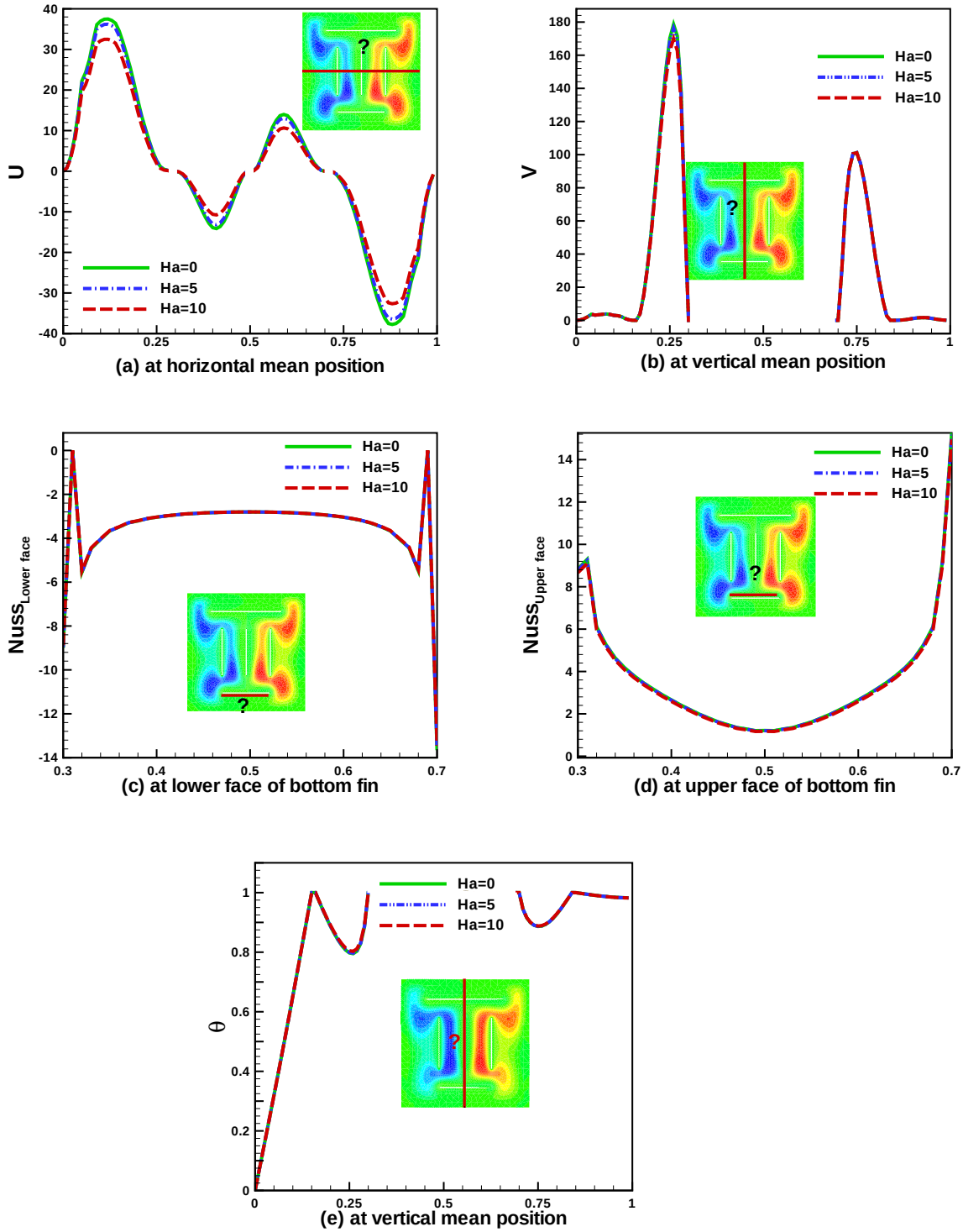

Figure 4.15: Effects of magnetic field on the velocity, temperature distribution and Nusselt number

the cavity for heat generation. For maximum length, transfer of heat is spread in the entire cavity.

- In case of various positions of heated fin, the maximum heat is obtained at the mean position. Nusslet number is variant with the variation of length of thin fin.

- Temperature and Nusslet number increase with the increasing value of Rayleigh number. Isotherm increases and is symmetric with an increase in Re.

- Nusselt number deceases with increase in solid volume fraction of nanoparticles. For smaller value of ϕ isotherm lines are maximum.

- Hartmann number does not have significant effect on the temperature and velocity.

CHAPTER 5

COMBINED HEAT GENERATION AND NATURAL CONVECTION PROCESS FOR COPPER OXIDE-WATER NANOFLUID IN AN ENCLOSED CURVED PARTIALLY HEATED POROUS DOMAIN

5.1 Introduction

In a symmetrical normal shape enclosure, natural convection and fluid flow process has been presented for CuO-water nanofluid that has been assessed numerically by FEM. At the middle of the bottom wall, symmetric heated wall is considered to determine the thermal investigation. Vertical and horizontal walls are considered as cold and central part of symmetric curve is adiabatic. The governed equations are converted into dimensionless PDEs and then solved through FEM with Glariken weighted residual approach. The effect of various parameters such as Rayleigh number (Ra), nanoparticles (ϕ), Darcy number (Da), heat generation and absorption parameter (Q), size of heated wall and shape of nanoparticles are examined. Results are shown in the form of isotherms, streamline, velocity, temperature and average Nusselt number. With higher Rayleigh number, the average Nusselt number increases, the inclusion of porosity while it significantly decreases with the higher value of Q. Vertical velocity at the middle increases with the increase in nanoparticles whereas temperature decreases at vertical mean position.

Table 5.1: A table demonstrating the contrasts between the approaches being offered

Authors	Enclosure	Porosity	Heat generation	Method
Chamkha *et al.* [17]	Triangular	Yes	Yes	FDM
Sheikholeslami *et al.* [31]	Circular	No	No	FEM
Badruddin *et al.* [67]	Square	Yes	No	FEM
Khanafer *et al.* [16]	Square	Yes	Yes	ADI
Parvin *et al.* [75]	Prism	No	No	FEM
Present	Curved	Yes	Yes	FEM

5.2 Problem Formulation

Numerical simulation of natural convection in porous symmetric curve cavity is examined in this chapter. Physical model is being shown in Fig. 5.1(a) with boundary assumptions. Lower heated symmetric curve is considered for convection with heat generation/absorption coefficient. Various size of heated symmetric curve is being examined for convection. Fig. 5.1(b) represents the numerous mesh generation at the various position in cavity model.

5.2.1 Mathematical Model

In two-dimensional Cartesian coordinates, the conservation laws of mass, momentum and energy written in dimensional form as follows:

$$\nabla \cdot \mathbf{V}^* = 0, \tag{5.1}$$

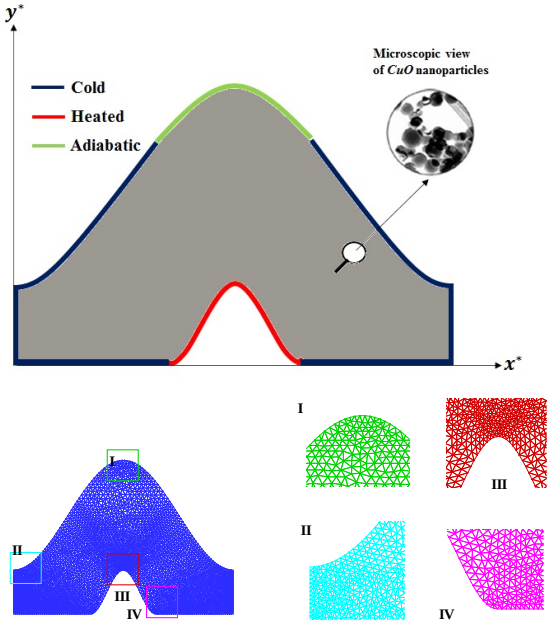

Figure 5.1: Symmetric curve enclosure (a) physical domain (b) Mesh distribution its different position

$$\mathbf{V}^* \cdot \nabla u^* = -\frac{1}{\rho_{nf}} \frac{\partial p^*}{\partial x^*} + \nu_{nf} \nabla^2 u^* - \frac{\nu_{nf}}{k} u^*, \tag{5.2}$$

$$\mathbf{V}^* \cdot \nabla v^* = -\frac{1}{\rho_{nf}} \frac{\partial p^*}{\partial y^*} + \nu_{nf} \nabla^2 v^* - \frac{\nu_{nf}}{k} v^* + \frac{(\rho\beta)_{nf}}{\rho_{nf}} g(T^* - T_c^*), \tag{5.3}$$

$$\mathbf{V}^* \cdot \nabla T^* = \alpha_{nf} \nabla^2 T^* + \frac{Q_0}{(\rho C_p)_{nf}} (T^* - T_c^*). \tag{5.4}$$

To examine the heat transfer in symmetric enclosure, introduce the following dimensionless variables on the Eqs.(5.1)-(5.4);

$$\begin{gathered}(X, Y) = \left(\frac{x^*}{L}, \frac{y^*}{L}\right), \ (U, V) = \left(\frac{u^* L}{\alpha_f}, \frac{v^* L}{\alpha_f}\right), \ T^* = T_c^* + (T_h^* - T_c^*)\,\theta, \\ P = \frac{p^* L^2}{\rho_f \alpha_f^2}, \ Ra = \frac{g\beta_f (T_h^* - T_c^*) L^3}{\nu_f \alpha_f}, \ Pr = \frac{\nu_f}{\alpha_f}, \ Q = \frac{Q_0 L^2}{(\rho C_p)_f \alpha_f}.\end{gathered} \tag{5.5}$$

In non-dimensional form Eqs.(5.1)-(5.4) will take the form as:

$$\frac{\partial V}{\partial Y} + \frac{\partial U}{\partial X} = 0, \tag{5.6}$$

$$V \frac{\partial U}{\partial Y} + U \frac{\partial U}{\partial X} = -\left(\frac{\rho_f}{\rho_{nf}}\right) \frac{\partial P}{\partial X} + Pr \left(\frac{\nu_{nf}}{\nu_f}\right) \left(\frac{\partial^2 U}{\partial Y^2} + \frac{\partial^2 U}{\partial X^2} - \frac{U}{Da}\right), \tag{5.7}$$

Table 5.2: Values of shape factor for various shape of nanoparticles

Particle shapes	Spherical	Cylinder	Platelets	Brick
n	3	4.8	5.7	3.7

Table 5.3: Thermo-physical properties of Based fluid and Nanoparticles

Physical properties	Base fluid (water)	CuO
C_p(J/kgK)	4179	385
ρ(kg/m^3)	997.1	8,933
K(W/mK)	0.613	401
β (1/K)	2.1×10^{-4}	1.67×10^{-5}

$$V\frac{\partial V}{\partial Y} + U\frac{\partial V}{\partial X} = -\left(\frac{\rho_f}{\rho_{nf}}\right)\frac{\partial P}{\partial Y} + Pr\left(\frac{\nu_{nf}}{\nu_f}\right)\left(\frac{\partial^2 V}{\partial Y^2} + \frac{\partial^2 V}{\partial X^2} - \frac{V}{Da}\right) + RaPr\frac{(1-\phi)\rho_f\beta_f + \phi\rho_p\beta_p}{\rho_f\beta_f}\theta, \tag{5.8}$$

$$V\frac{\partial \theta}{\partial Y} + U\frac{\partial \theta}{\partial X} = \left(\frac{\alpha_{nf}}{\alpha_f}\right)\left(\frac{\partial^2 \theta}{\partial Y^2} + \frac{\partial^2 \theta}{\partial X^2}\right) + Q\frac{(\rho C_p)_f}{(\rho C_p)_{nf}}\theta. \tag{5.9}$$

5.2.2 Dimensionless boundary conditions:

At the bottom solid walls(Ω_1)**:**

$$\Omega_1 = \{(X,Y) \in \mathcal{R}/0 \leq X < 0.35 \text{ and } Y = 0\}, \quad (U,V,) = (0,0),\ \theta = 0, \tag{5.10}$$

At the vertical walls (Ω_2):

$$\begin{aligned} \Omega_2 = \ \{(X,Y) \ \in \ \mathcal{R}/0 \leq Y < 0.35 \text{ and } X = 0\}, \\ (U,V,) = (0,0), \ \theta = 0, \end{aligned} \tag{5.11}$$

At the upper lower symmetric curve (Ω_3):

$$\begin{aligned} \Omega_3 = \ \{(X,Y) \ \in \ \mathcal{R}/0.35 < X \leq 0.65 \text{ and } 0 \leq Y \leq 0.2\}, \\ (U,V) = (0,0), \ \theta = 1, \end{aligned} \tag{5.12}$$

At the upper symmetric curve $(\Omega_4 \ \text{ and } \ \Omega_5)$:

$$\begin{aligned} \Omega_4 = \ \{(X,Y) \ \in \ \mathcal{R}/0.7 < X \leq 1 \text{ and } 0.2 < Y \leq 0.5\} \\ (U,V) = (0,0), \ \theta = 0, \\ \Omega_5 = \ \{(X,Y) \ \in \ \mathcal{R}/0.0 \leq X < 0.3 \text{ and } 0.2 \leq Y < 0.5\} \\ (U,V) = (0,0), \ \theta = 0, \end{aligned} \tag{5.13}$$

At the upper surface of the symmetric curve: (Ω_6):

$$\begin{aligned} \Omega_6 = \ \{(X,Y) \ \in \ \mathcal{R}/0.3 \leq X < 0.7 \text{ and } 0.5 \leq Y \leq 0.7\}, \\ (U,V) = (0,0), \ \frac{\partial \theta}{\partial Y} = 0. \end{aligned} \tag{5.14}$$

The average Nusselt number is well-defined to represent rate of heat transfer on the inner single corrugated heated surface as:

$$Nu_{avg} = -\frac{1}{\pi} \int_{\Omega_3} \sqrt{\left(\frac{\partial \theta}{\partial X}\right)^2 + \left(\frac{\partial \theta}{\partial Y}\right)^2} \, \mathrm{d}s. \tag{5.15}$$

5.3 Numerical Procedure:

To solve the Eqs. (5.6)–(5.9) subject to boundary conditions Eqs. (5.10)–(5.14), the Galerkin weighted residual method is being used as discussed in chapter 3. In this section, we validate with other manuscripts of the computational results for the current work on isotherm profile in limiting condition on walls. Numerical results of our mathematical model are validated with the experimental result of Paroncini [95].

Table 5.4: Comparison of average Nusselt number achieved by the present solution with previous for various Rayleigh numbers when $Pr = 0.7$.

Ra	Present work	Sheikholeslami *et al.* [31]	%Error
10^3	1.17	1.14	2.63
10^4	2.29	2.27	0.88
10^5	4.52	4.51	0.22

5.4 Results and Discussion

In this chapter, numerical simulation of natural convection fluid flow and heat transfer of CuO nanofluid inside the porous symmetric curved cavity is depicted with heat generation/absorption. The simulation is performed for various Rayleigh number ($10^3 \leq Ra \leq 10^{5.5}$), Darcy number ($10^{-5} \leq Da \leq 1$), heat generation/absorption coefficient ($-10^3 \leq Q \leq 7.5 \times 10$), volume fraction of nanoparticles ($0 \leq \phi \leq 0.05$), shape of nanoparticles (spherical, cylindrical and bricks) and the length of heated wall. Effects of various parameters on isotherm and streamlines are examined in this study.

Effects of Rayleigh number:

Fig. 5.2(a-f) show the effects of Ra on isotherms and streamline. For fixed quantity of concentration of nanoparticles, the streamlines create eddies, which are stronger for higher values of Rayleigh number. Due to maximum fluid flow, eddies are stronger with increasing Ra. In isotherm case, for smaller value of Rayleigh number, isotherms are congested near the heated wall, and gradually increases the heat inside the enclosure. Due to buoyancy forces, heat is transferred to adiabatic wall in upward direction. Generation of a symmetry

of isotherms are seen inside the cavity. Fig. 5.3 illustrates the vertical velocity and temperature profile for different Rayleigh numbers. Vertical velocity for smaller value of Ra is almost same and moderately increases with increasing Rayleigh numbers. Maximum velocity is observed for maximum value of Ra. In Fig. 5.3(b), temperature distribution at vertical mean position demonstrates that for higher value of Ra, the temperature increases sufficiently. At mean position temperature gradient decreases and increases at the corner of the porous medium as Rayleigh number increases. The isotherm layer remains at rest at the right corner in all cases of Ra in temperature profile.

Effects of volume fraction of nanoparticles:

Fig. 5.4 represents the effect of volume fraction of nanoparticles in spherical shape. In case of base fluid, smaller eddies are developed near the heated symmetric wall as shown in Fig. 5.4(a). Fig. 5.4(b) depicts that the streamlines increase when 2.5% of nanoparticles are added in base fluid as well as the size of the eddies increases. With the 5% of nanoparticles, the intensity of fluid flow increases intensively. Fig. 5.4(d-f) shows the effects of nanoparticles on isotherms, in case of base fluid ($\phi = 0$) the isotherms are dominant near the heated curve and heated lines decrease gradually with increasing nanoparticles with convection dominated in the enclosure. Temperature near the upper curve decreases with increasing concentration of nanoparticles. Fig. 5.5(a-b) represents the vertical velocity and temperature profile at mean position for various nanoparticles of Copper Oxide - Water CuO in spherical shape. Vertical velocity increases with increasing the quantity of nanofluid, it creates symmetric bolus for various quantity of concentration. At the bottom of the right end of enclosure, velocity gets zero and increases in the middle of cavity due to the maximum heat transfer. Temperature distribution shows that on the left portion of the cavity, it attains maximum temperature and gradually decreases but for the maximum value of nanoparticles, smaller temperature is recorded as compared to the base fluid as shown in Fig. 5.5(b).

Effects of Darcy number:

Fig. 5.6(a-h) illustrate the Darcy effect on the fluid flow and heat transfer for fixed value of Prandtl number. For low Darcy number (Da), the heat transfer increases due to conduction in the enclosure. In this case, larger eddies are formed in the streamlines. For higher values of Da, conduction in cavity reduces and convection phenomena dominate so the smaller eddies continue to be formed for maximum value of $Da = 1$ as shown in Fig. 5.6(d). Isotherm profile indicates that for smaller value of Darcy number, heat is congested near the heated wall and significantly heat transfer is reduced for maximum porosity. It shows that the heat distribution in cavity increases near the upper adiabatic wall. Fig. 5.7(a-b) shows the effects of porous medium on velocity and temperature profile at vertical mean position. Velocity and temperature increases with an increase in Darcy number. Due to high convection, more heat transfer occurs inside the cavity and velocity profile creates bolus whose size increases with the increase porosity. Temperature distribution profile indicates that for low Da, minimum heat is recorded and it increases at the middle with increasing porosity.

Effects of heat generation/absorption coefficient:

Fig. 5.8 illustrates the effect of heat generation/absorption coefficient on isotherm. For ($Q < 0$), heat absorptions and ($Q > 0$) heat generation are shown in the Fig. 5.8(a-h). Temperature distribution lines or heat transfer are restricted near the heated wall and heat transportation increases with decreasing heat generation coefficient. For $Q = 0$, stable symmetric heat transfer is recorded inside the cavity. For $Q > 0$, heat generated in cavity due to convection more heated lines are developed near the adiabatic wall as shown in Fig. 5.8(g). For $Q = 75$ the symmetry of the isotherm is distorted, which gradually changes due to linear flow. Vertical velocity increases in case of heat generation coefficient and decreases for absorption as depicted in Fig. 5.9(a). Temperature profile indicates that more heat is created for higher values of

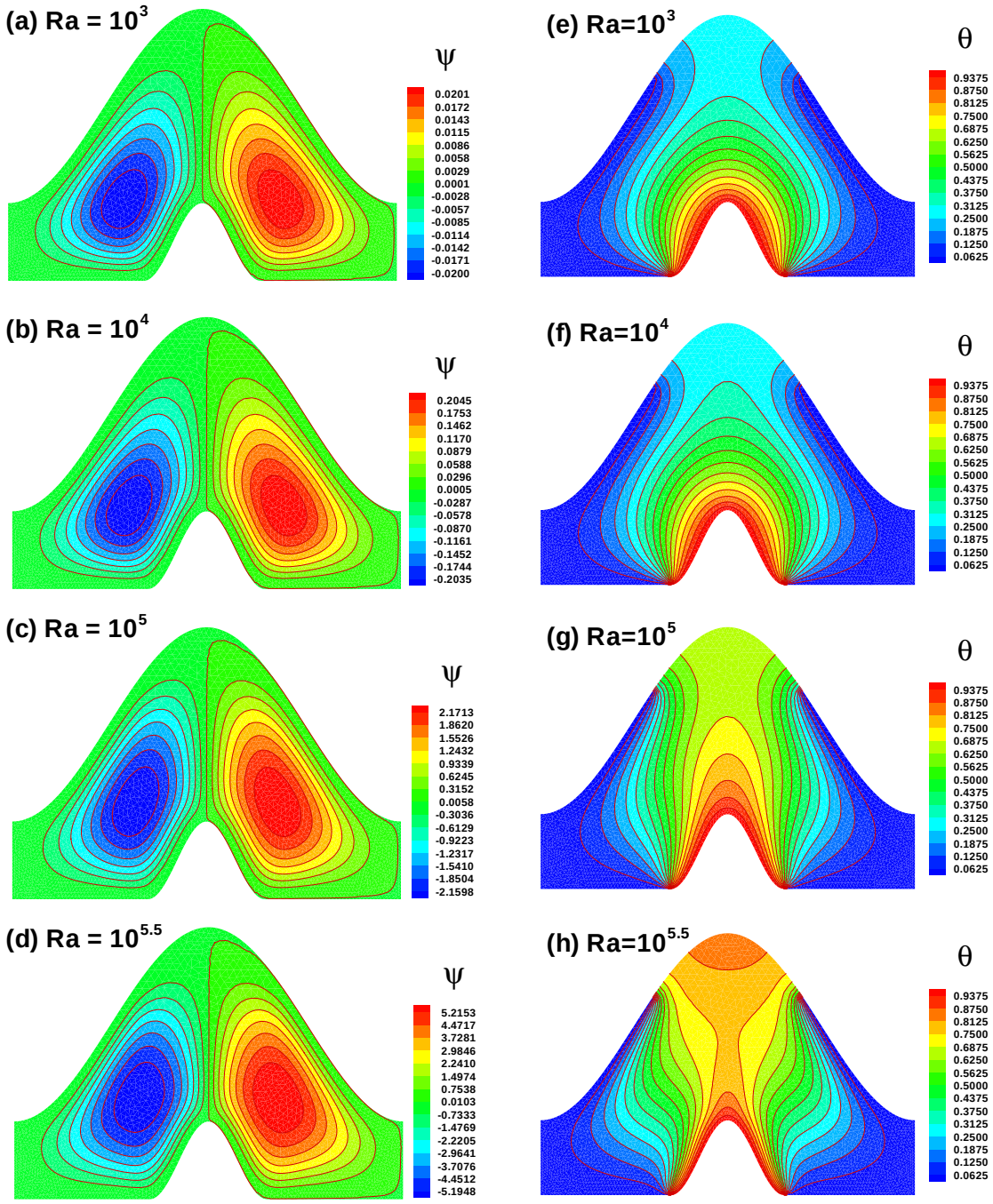

Figure 5.2: Variation of (a)-(d) streamlines and (e)-(h) isotherm with respect to Ra when $Da = 10^{-3}$, $\phi = 0.05$, $Q = 10$, $m = 3$

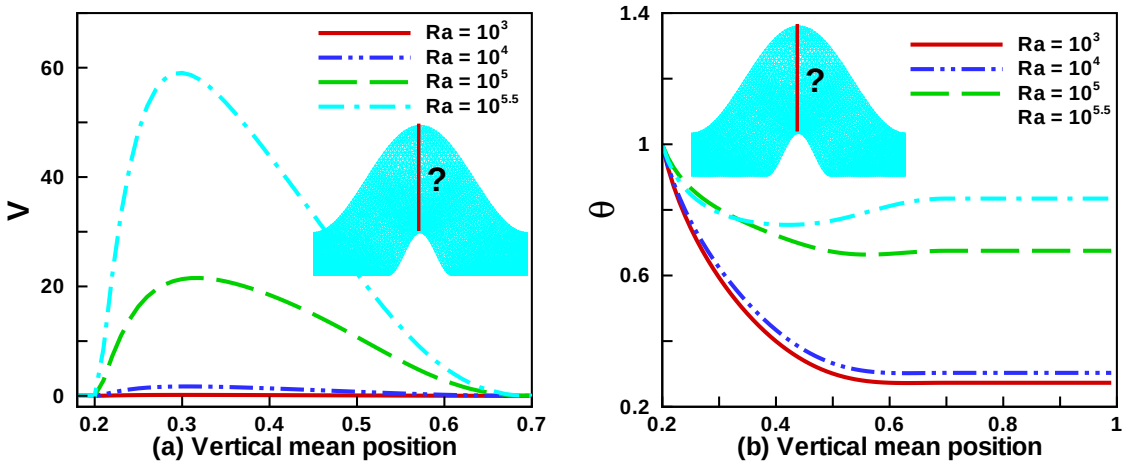

Figure 5.3: Variation of (a) vertical velocity, (b) vertical temperature with respect to Ra

Q. We see that the heat generation has significant effect on the temperature profile.

Effects of various size of heated wall:

Size of heated symmetric wall on isotherm and streamlines are illustrated in Fig. 5.10. Streamlines are symmetric for different size of heated wall but the streamlines increase with the increase in size of heated wall. Elliptic shape of eddies formed in the cavity and the eddies gradually increase the size of eddies with the increase in the shape. Isotherms are recorded minimum for smaller size and more heat flows as the size increases. Isotherms increase near the adiabatic wall with increasing the size of heated wall. Velocity decreases with increasing the size of heated wall as shown in Fig. 5.11(a) at vertical mean position. Temperature profile shows that for larger size of heated wall, more heat flow inside the cavity. At the middle of cavity, temperature profile clearly indicates the significant effects of size.

Effects of various shape of nanoparticles:

Fig. 5.12(a-f) depict the effects of different shape of nanoparticles on fluid flow and heat transfer. Shape of nanoparticle has significant effect

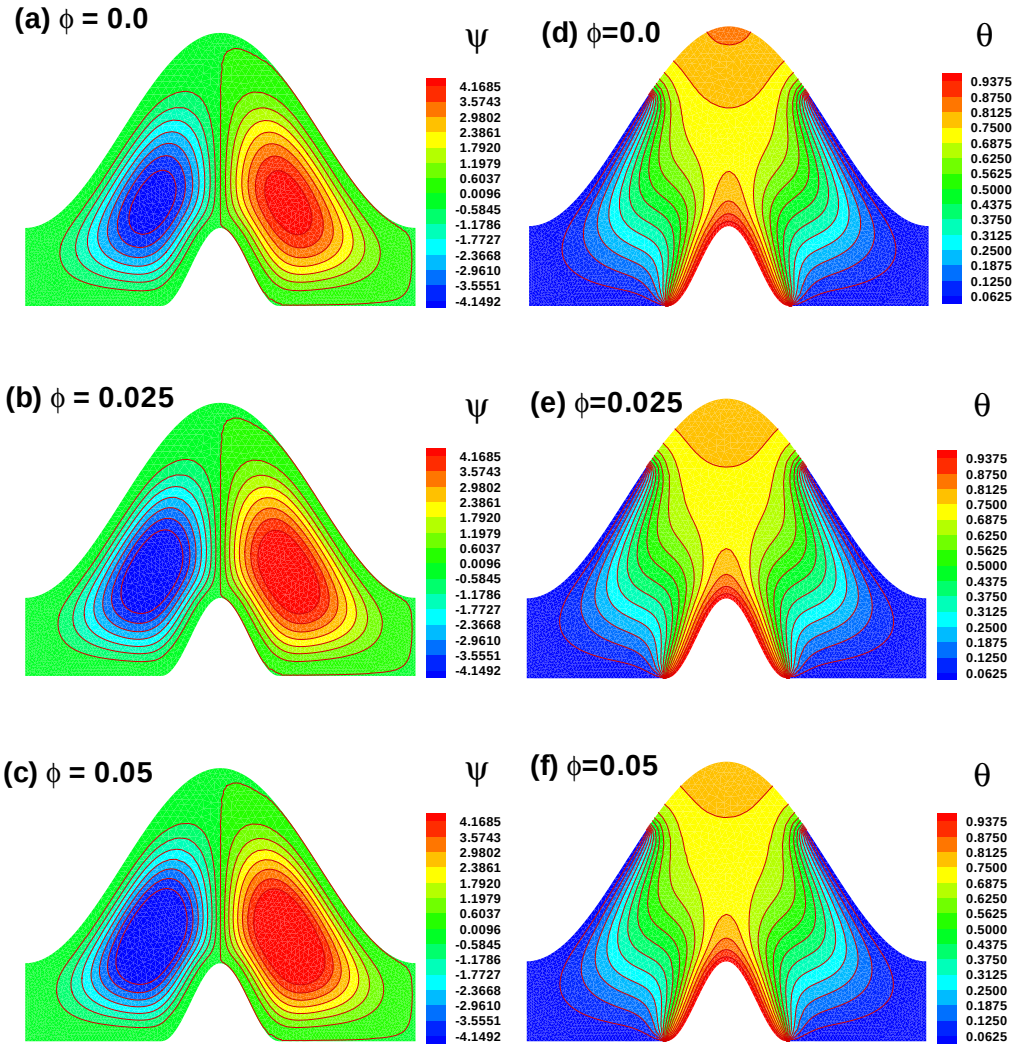

Figure 5.4: Variation of (a)-(c) streamlines and (d)-(f) isotherm with respect to ϕ when $Ra = 10^5$, $Da = 10^{-2}$, $Q = 10$, $m = 3$

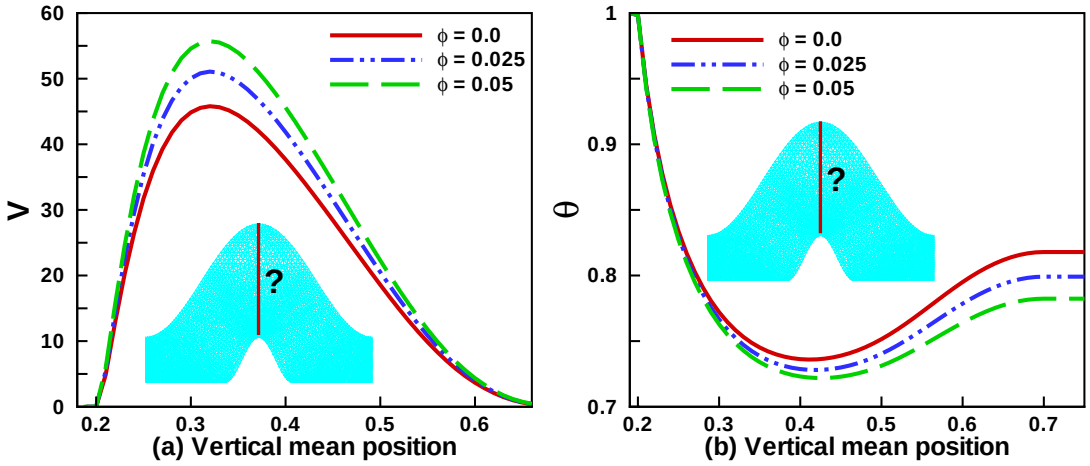

Figure 5.5: Variation of (a) vertical velocity, (b) vertical temperature with respect to ϕ

on the isotherms. Maximum heat is recorded in case of spherical shape near the heated wall. Velocity profile shows that shape of nanoparticle doesn't have significant effect on velocity at vertical mean position as shown in Fig. 5.13(a). Temperature at vertical mean position increases in case of spherical shape of nanoparticles and decreases in platelet's shape.

Fig. 5.14 shows the variation of average Nusselt number with Rayleigh number. Fig. 5.14(a) describes the various heat generation/absorption coefficient effect with variation of Ra. Average Nusselt number increases with increase in Q for its particular case but decreases with comparison of various values of Q. In case of heat absorption, more heat in the fluid flow is recorded than heat generation. For maximum value of Q, there is a minimum heat flow. Fig. 5.14(b) illustrates the effect of porous medium with respect to Ra. A larger average Nusselt number is recorded for larger values due to the active convection of Ra and Da.

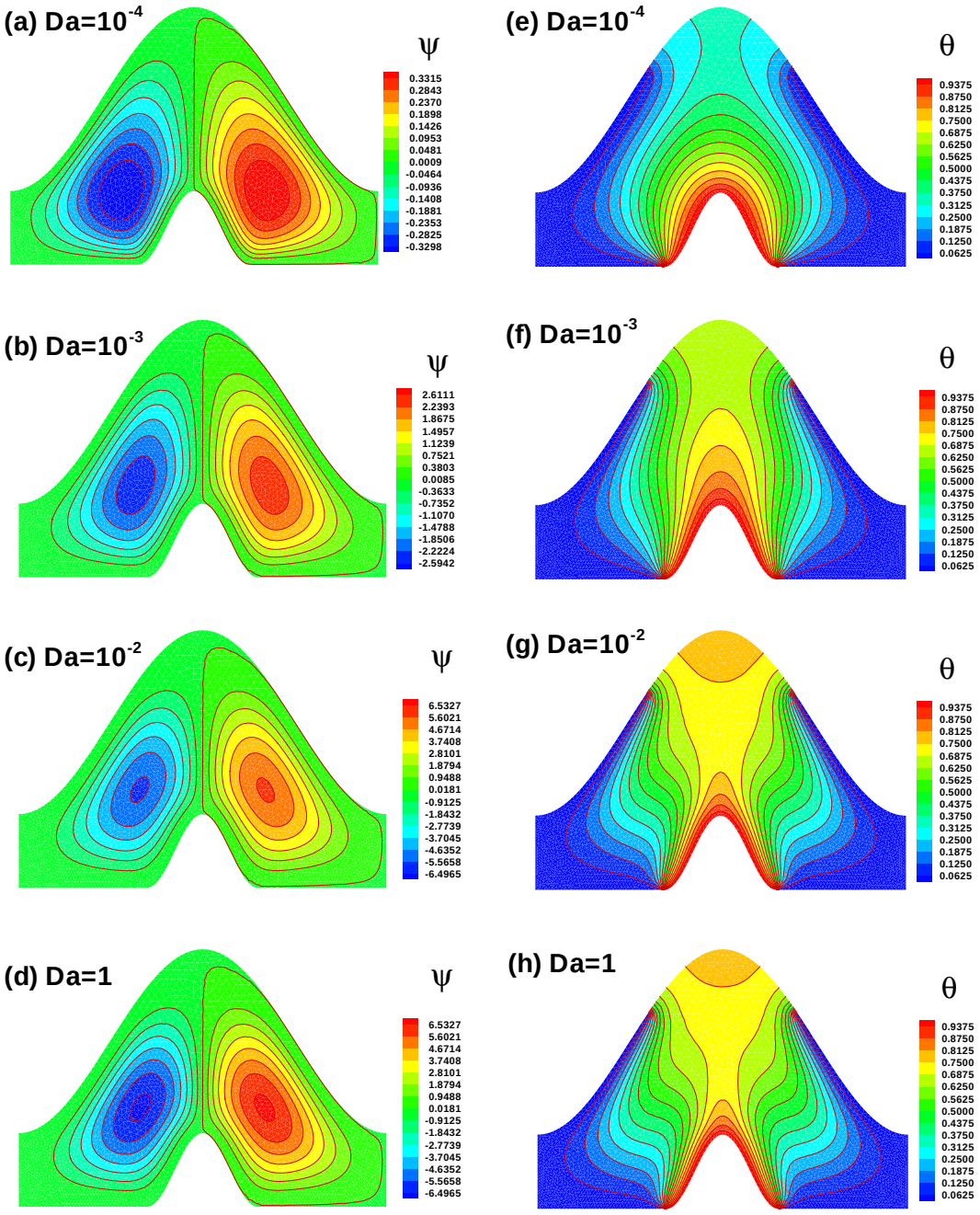

Figure 5.6: Variation of (a)-(d) streamlines and (e)-(h) isotherm with respect to Da when $Ra = 10^5$, $\phi = 0.05$, $Q = 10$, $m = 3$

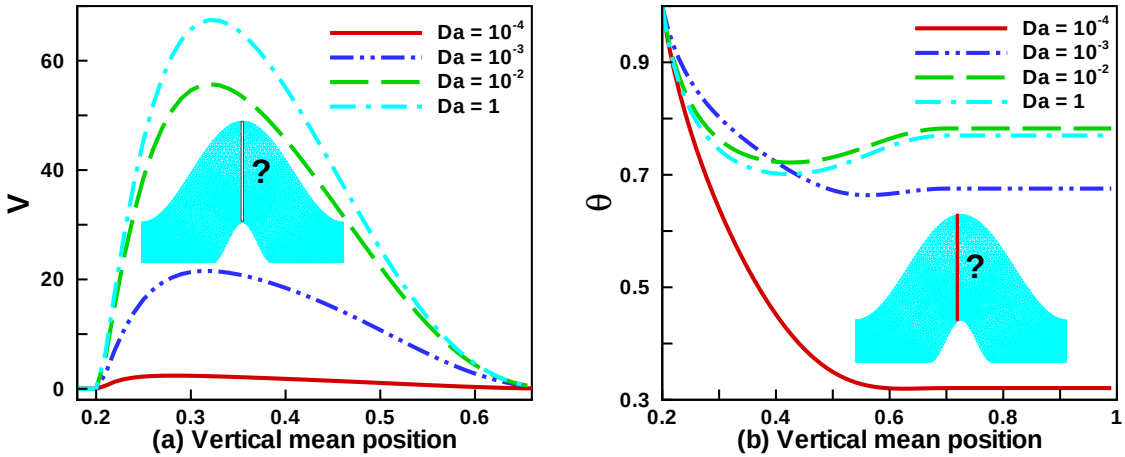

Figure 5.7: Variation of (a) vertical velocity, (b) vertical temperature with respect to Da

5.5 Conclusion

In current work, the effect of CuO water nanofluid on free convection is simulated in a symmetric porous cavity with heat generation/ absorption. At the centre heated symmetric wall is attached to examine the heat flow in cavity. Finite element method is used to solve the problem numerically. The effect of various parameters Rayleigh number ($10^3 \leq Ra \leq 10^{5.5}$), solid volume fractions ($0 \leq \phi \leq 0.05$), Darcy number ($10^{-5} \leq Da \leq 1$), absorption/generation parameter ($-500 \leq Q \leq 75$), shape of nanoparticles (spherical, cylindrical and platelets) and size of heated wall on isotherm, streamline profile, velocity, temperature (at vertical mean position) and average Nusslet number were briefly discussed in this chapter. The study concluded with the following remarks:

- For small value of Rayleigh number heat conduction is dominant. While, as Ra increases, convection increases in cavity.
- Vertical velocity increases with increase in Ra which tends to decrease thermal layer thickness. Temperature increases at the middle with increase in Ra.

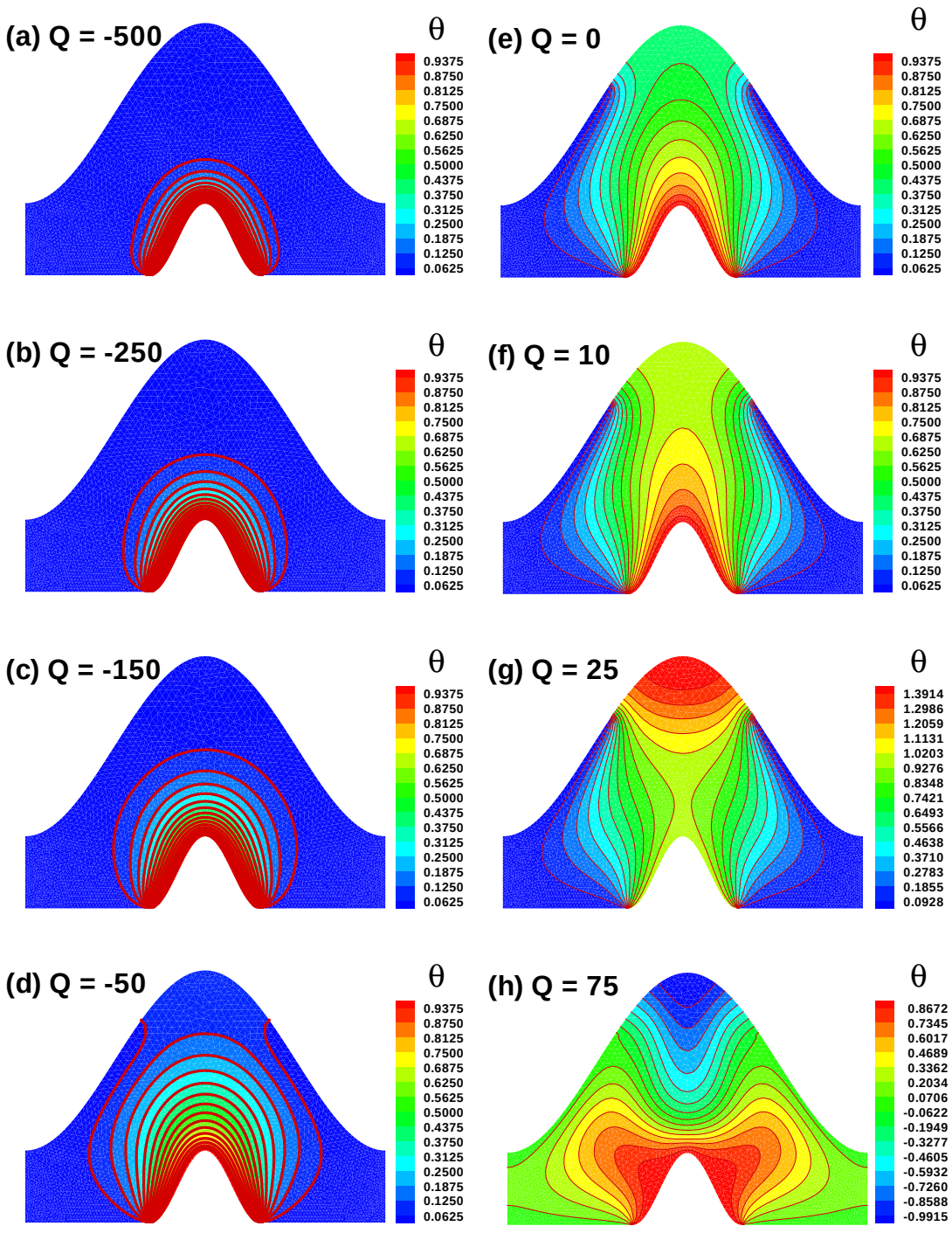

Figure 5.8: Variation of (a)-(h) isotherm with respect to Q when $Ra = 10^5$, $\phi = 0.05$, $Da = 10^{-3}$, $m = 3$

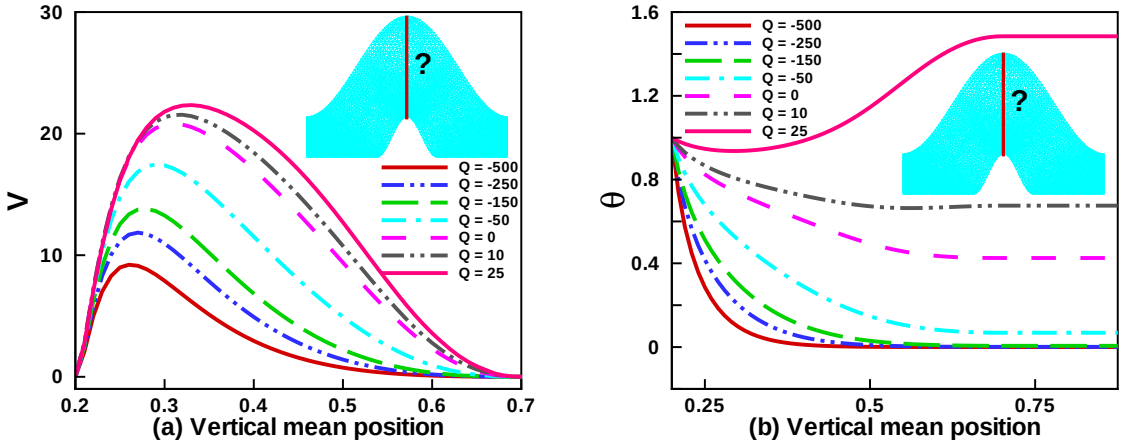

Figure 5.9: Variation of (a) vertical velocity, (b) temperature with respect to Q

- Thermal conductivity increases when spherical shape of nanoparticles are used. For higher value of ϕ, more heat is transferred in cavity.
- Heat flow increases with increasing porosity parameter due to flow of heat. Significant effect of Darcy number on isotherm is recorded.
- More heat is developed near the adiabatic wall for $Q > 0$. Temperature increases and Nusselt number decreases with increasing of heat sink parameter. Due to the heat generation, isotherm lines rapidly increase in cavity.
- Size of heated wall has major effects on isotherm and streamlines formed in elliptic eddies around the heated wall.
- Average Nusselt number decreases when Q increases with increase in Ra. While, average Nusselt number increases with increase in porosity parameter with increase in Rayleigh number.

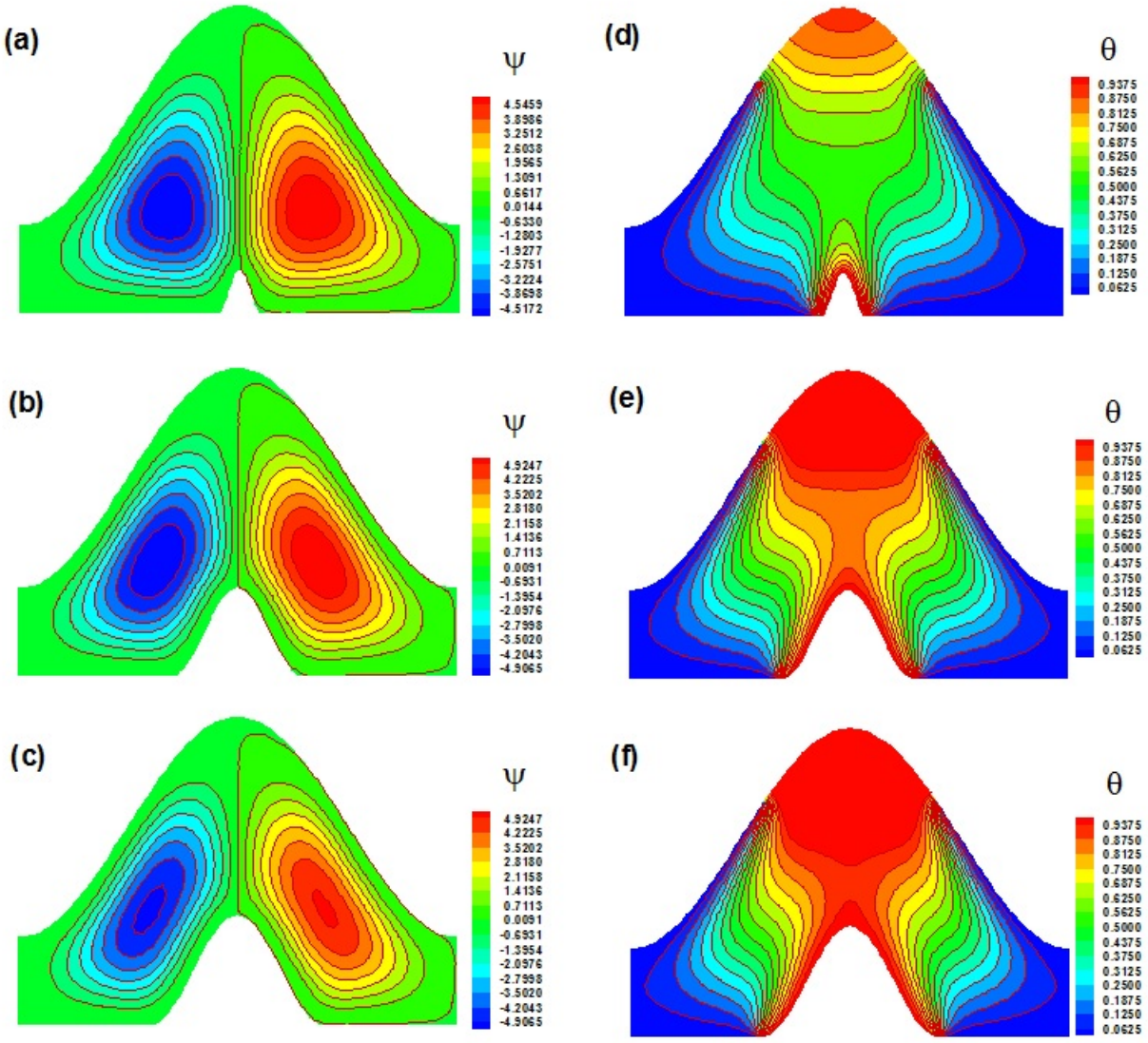

Figure 5.10: Variation of (a)-(c) streamlines and (d)-(f) isotherm with respect to size of heated wall when $Ra = 10^5$, $\phi = 0.05$, $Da = 10^{-2}$, $Q = 25$, $m = 3$

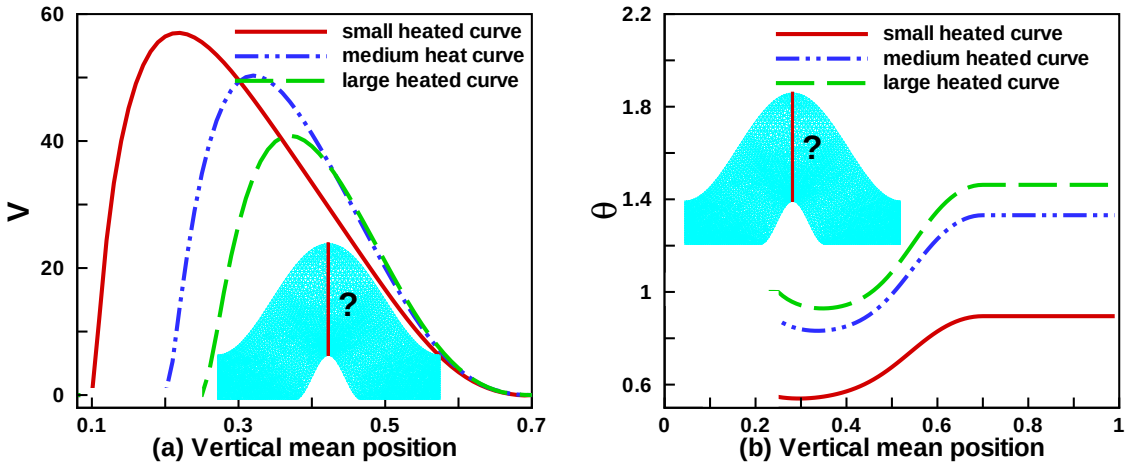

Figure 5.11: Variation of (a) vertical velocity, (b) vertical temperature with respect to sized of heated wall

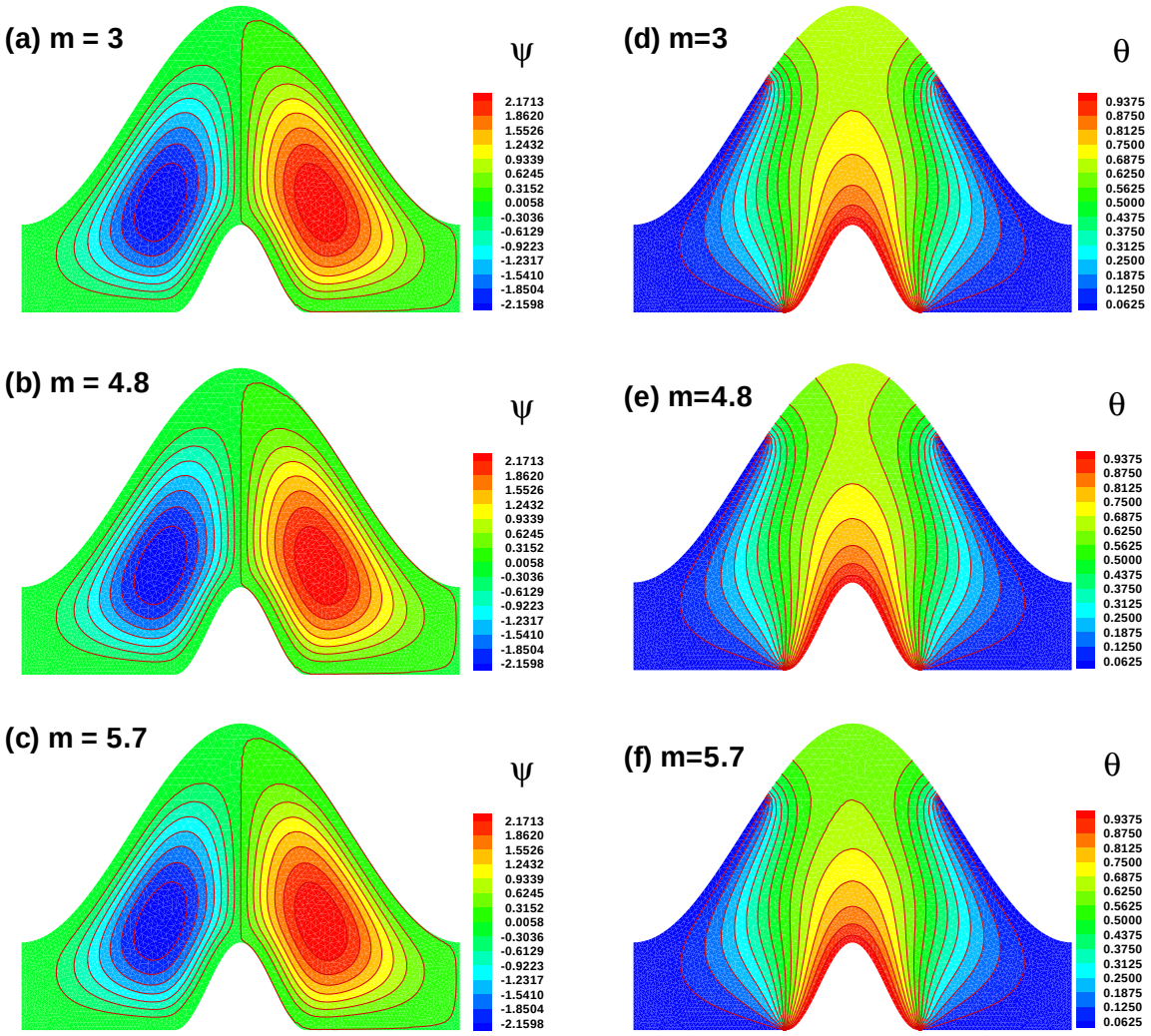

Figure 5.12: Variation of (a)-(c) streamlines and (d)-(f) isotherm with respect to spherical, cylindrical and platelet's shape of nanoparticles when $Ra = 10^5$, $\phi = 0.05$, $Da = 10^{-3}$, $Q = 10$

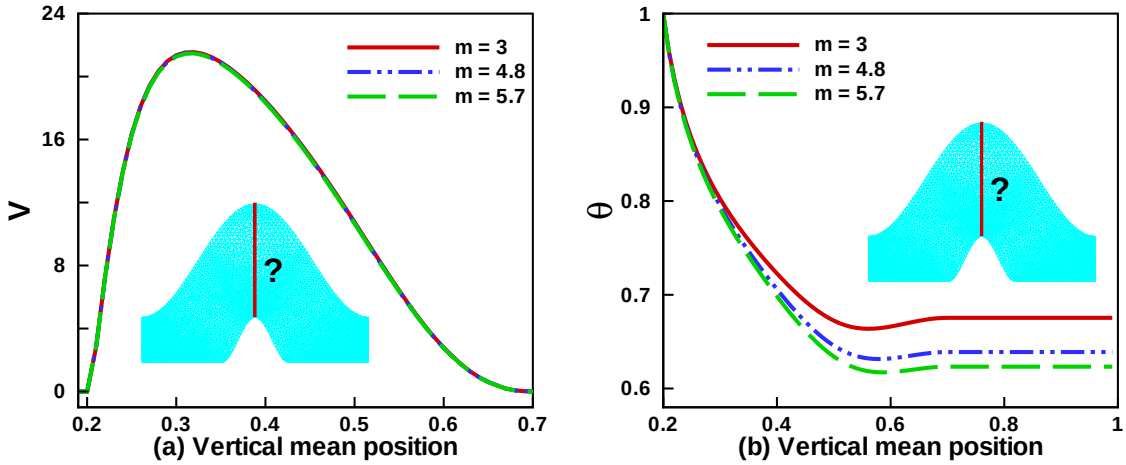

Figure 5.13: Variation of (a) vertical velocity, (b) vertical temperature

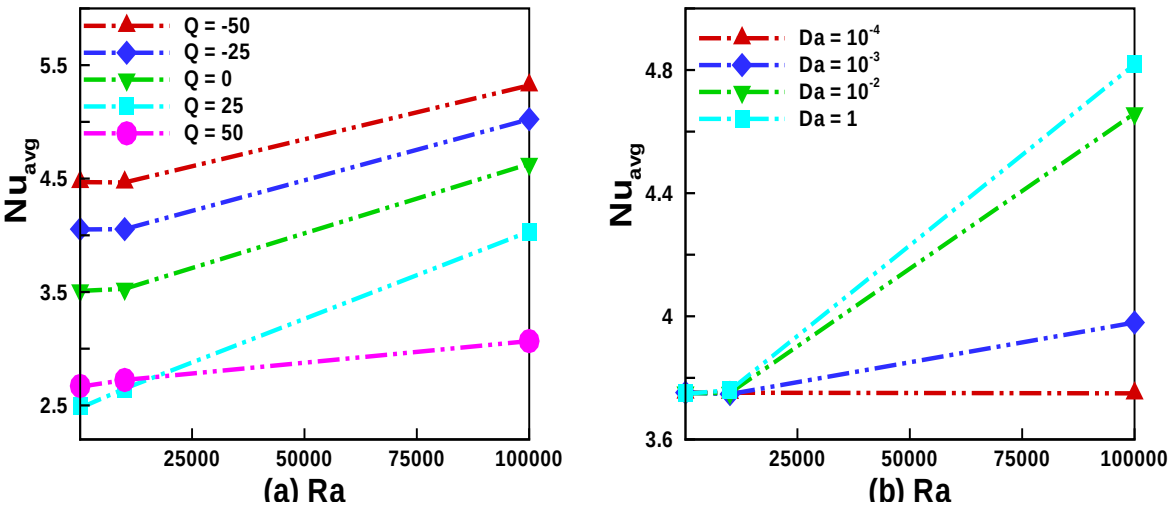

Figure 5.14: Variation of average Nusselt number with respect to the Rayleigh number at the different values of (a) heat generation/absorption coefficient (b) Darcy number

CHAPTER 6

NUMERICAL SIMULATION OF LID DRIVEN FLOW IN A CURVED CORRUGATED CAVITY FILLED WITH COPPER OXIDE-WATER IN THE PRESENCE OF POROUS MEDIUM & HEAT GENERATION/ABSORPTION

6.1 Introduction

In this part of thesis, numerical simulation is performed for mixed convection lid-driven flow of CuO-water nanofluid enclosed in a curved corrugated cavity. Cylindrical obstacle having three different constraints: (adiabatic, cold and heated) at its surface are considered. Internal heat generation/absorption and uniform heat is provided at the vertical wall of the cavity. The bottom wall is insulated, and the curved surfaces are maintained with cold temperature. Mathematical equations are developed from physical problems and solved through Galerkin weighted residual method of FEM formulation. The effects of various Reynolds number (Re), Darcy number (Da), solid volume fraction of nanoparticles (ϕ), heat generation/absorption coefficient (Q) and various cylindrical obstacle on velocity, Nusselt number, molecular movements and the flow structure have been studied. Nusselt number increases for high Darcy number due to the convection in lid cavity. For high Reynolds number generally Nusselt numbers decrease or remain the same at the wall with an increase

in nanoparticles in porous medium. Their significant effects of heat sink coefficient on temperature profile and Nusselt number decrease with increasing Q.

Table 6.1: A table demonstrating the contrasts between the approaches being offered

Authors	Enclosure	Porosity	Heat generation	Obstacle
Hussain *et al.* [20]	Square	No	Yes	No
Alleborn *et al.* [35]	Rectangular	Yes	No	No
Haq *et al.* [77]	Corrugated	Yes	No	No
Sivasankaran *et al.* [96]	Sinusoidal walls	No	No	No
Present	Double Corrugated	Yes	Yes	Yes

6.2 Problem Formulation

Fig. 6.1 illustrates the curved corrugated of two-dimensional porous lid-driven cavity has been examined in this unit. The circular cylindrical obstacle inscribed inside enclosure. The nanofluid is formed of base fluid (water) and copper oxide solid spherical shape of nanoparticles. The fluid is assumed to be laminar and incompressible. The bottom wall is thermally insulated $\left(\frac{\partial T^*}{\partial y^*} = 0\right)$, while the curved surface is sustained with low temperature T_c^* and left vertical wall with high temperature (T_H^*) to induce the buoyancy effect. Left vertical wall moves with uniform velocity. H represents the characteristic length in horizontal and vertical direction in curved corrugated cavity. Various constraints have been adjusted at cylinder (adiabatic, cold and hot) for

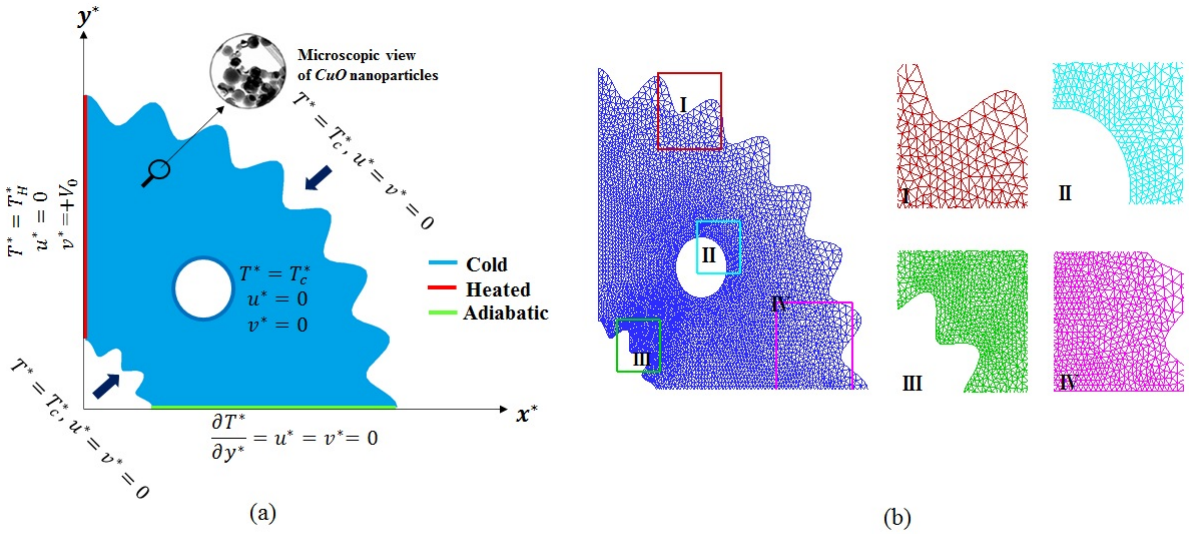

Figure 6.1: Curved Corrugated geometry with its (a) physical domain (b) computational domain with mesh distribution at various positions

observing the heat transfer within the enclosure.

6.2.1 Mathematical Model

The governing equation for incompressible, Newtonian, laminar and steady state (thermal equilibrium) lid driven convection in a curve corrugated enclosure filled with nanofluids in the form of Navier-Stokes formulation (mass, momentum and energy) are written as Eqs.(5.1)-(5.4).

Following dimensionless parameters are introduced;

$$(X,Y)=\left(\frac{x^*}{H},\frac{y^*}{H}\right),\ (U,V)=\left(\frac{u^*}{V_o},\frac{v^*}{V_o}\right),\ T^*=T_c^*+(T_h^*-T_c^*)\,\theta,$$
$$P=\frac{p^*}{\rho_f V_o^2},\ Ri=\frac{Gr}{Re^2},\ Q=\frac{Q_0H^2}{(\rho C_p)_f\alpha_f},\ Pr=\frac{\nu_f}{\alpha_f}, \tag{6.1}$$

into Eqs.(5.1)-(5.4), in dimensionless form equations become

$$\frac{\partial V}{\partial Y}+\frac{\partial U}{\partial X}=0, \tag{6.2}$$

$$V\frac{\partial U}{\partial Y}+U\frac{\partial U}{\partial X}=-\frac{\partial P}{\partial X}+\left(\frac{1}{Re}\right)\left(\frac{\nu_{nf}}{\nu_f}\right)\left(\frac{\partial^2 U}{\partial Y^2}+\frac{\partial^2 U}{\partial X^2}-\frac{U}{Da}\right), \tag{6.3}$$

$$V\frac{\partial V}{\partial Y}+U\frac{\partial V}{\partial X}=-\frac{\partial P}{\partial Y}+\frac{1}{Re}\left(\frac{\nu_{nf}}{\nu_f}\right)\left(\frac{\partial^2 V}{\partial Y^2}+\frac{\partial^2 V}{\partial X^2}-\frac{V}{Da}\right)+Ri\frac{(\rho\beta)_{nf}}{\rho_f\beta_f}\theta, \tag{6.4}$$

$$V\frac{\partial \theta}{\partial Y}+U\frac{\partial \theta}{\partial X}=\left(\frac{\alpha_{nf}}{\alpha_f}\right)\left(\frac{1}{PrRe}\right)\left(\frac{\partial^2 \theta}{\partial Y^2}+\frac{\partial^2 \theta}{\partial X^2}\right)+\left(\frac{Q}{PrRe}\right)\frac{(\rho C_p)_f}{(\rho C_p)_{nf}}\theta. \tag{6.5}$$

6.2.2 Dimensionless boundary conditions:

At the bottom solid wall **(Ω_1):**

$$(U,V)=(0,0),\ \frac{\partial \theta}{\partial Y}=0. \tag{6.6}$$

At the upper curved surface **(Ω_2):**

$$(U,V)=(0,0),\ \theta=0. \tag{6.7}$$

At the left vertical wall **(Ω_3):**

$$(U,V)=(0,1),\ \theta=1. \tag{6.8}$$

At the lower curved surface **(Ω_4):**

$$(U,V)=(0,0),\ \theta=0. \tag{6.9}$$

At the surface of inner circle **(Ω_5):**

$$(U,V)=(0,0),\ \text{and}\ (\theta=0\ \ \text{or}\ \ \theta=1\ \ \text{or}\ \ \frac{\partial \theta}{\partial n_{\Omega_5}}=0). \tag{6.10}$$

The local Nusselt number for the heat transfer rate estimate is calculated as;

$$Nu(Y)=-\frac{k_{nf}}{k_f}\left(\frac{\partial \theta}{\partial X}\right)_{X=0}. \tag{6.11}$$

6.3 Numerical Procedure

The governed dimensionless Eqs. (6.2)-(6.5) along the boundary conditions are solved by Galerkin weighted residual finite element formulation.

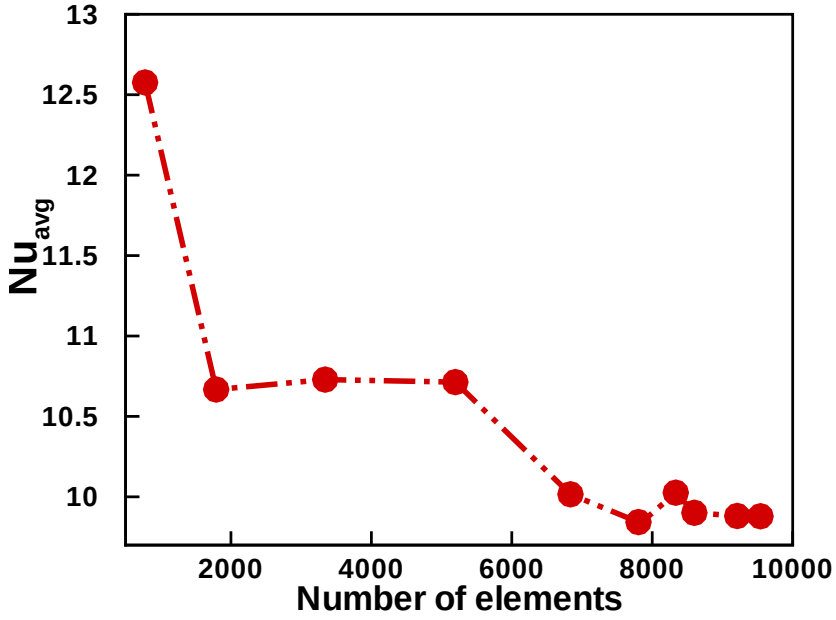

Figure 6.2: Variation of average Nusselt number for various number of elements

6.3.1 Comparison of results and Grid Independency:

The study of various element against the average Nusselt number interpreted in Fig. 6.2. Variation of various number of element in enclosure does not have significant effect on the average Nusselt number. In this section, we validate the computational result of present work with other manuscript. Mixed convection in lid-driven cavity problem is compared to earlier findings by Sivasankaran *et al.* [96] in Fig. 6.3(a), our present thermal contour analysis is depicted in Fig. 6.3(b). Excellent result validation of average Nusselt number against different *Re* to the work of Iwatus *et al.* [33] and Khanafer & Chamkha [34] in limiting case.

Table 6.2: Numerical results comparison of average Nu of present article with Iwatus *et al.* [33] and Khanafer & Chamkha [34] for a vertical gravity at $Ri = 0.01$.

Re	Present work	Iwatus *et al.* [33]	Khanafer & Chamkha [34]	% Error
10^2	2.11	1.94	2.01	8.76
4×10^2	2.84	3.84	3.91	35
10^3	6.27	6.33	6.33	0.95

6.4 Results and Discussion

Improved heat transmission and fluid dynamics are possible with the use of double corrugated enclosures in lid-driven flow. Lid-driven flow describes a fluid's movement within a cavity that is being initiated by a moving lid. In lid-driven flow, the design of heat sinks for electronics cooling is one physical application of double corrugated enclosure. Heat generated by electronic components needs to be dissipated by heat sinks in order to avoid damage and insure optimum efficiency. A more effective heat sink design is made possible by the use of twin corrugated enclosures, which expand the amount of surface area available for heat transfer. A numerical work has been done in this section of thesis to study the flow structure and temperature profile for the various values of Reynolds number ($100 \leq Re \leq 400$), Darcy number ($Da = 10^{-5}$ to 10^{-1}), nanoparticles' volume fraction ($0.0 \leq \phi \leq 0.05$), heat generation/absorption, Richardson number ($0.01 \leq Ri \leq 100$) and different states of circular cylinder (adiabatic, cold and heated) inside the lid-driven cavity. Throughout the numerical computation Prandtl number ($Pr = 6.2$) is

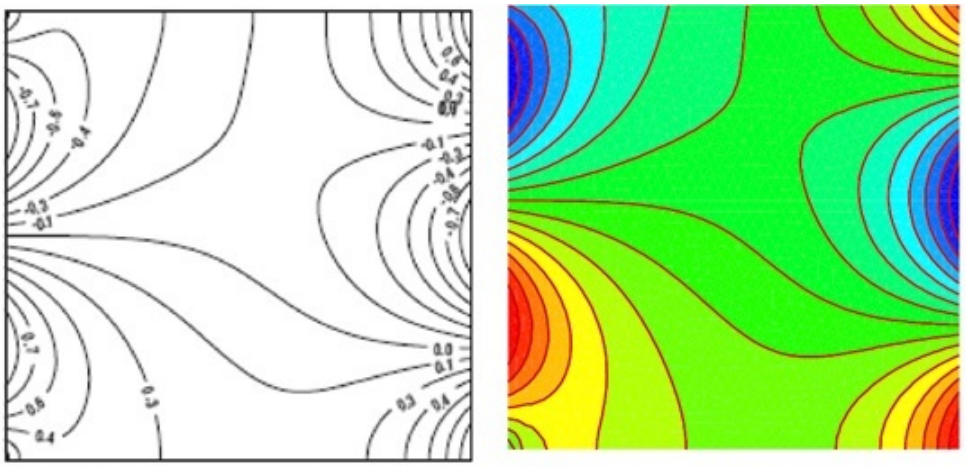

Figure 6.3: Comparison of thermal contour analysis in a square cavity with sinusoidal boundary condition in limiting case: (a) Sivasankaran *et al.* [96] versus (b) Present study

fixed.

Effects of Reynolds number:

Fig. 6.4(a-f) describes the effects of Reynolds number on isotherms and streamline. It indicates that most of the cavity is filled by symmetrical undistorted isotherms, while the isotherms endorse some form of distortion in a small part of the cavity near the top moving lid. For low Reynolds number, the isotherm is distributed on the whole enclosure, and gradually decreases with increasing Re. For maximum Re, the heat effect around the moving heated vertical wall is shown in Fig. 6.4(c). Flow distribution for various number of Re can be seen in Fig. 6.4(d-f). For small Reynolds number, it can be noticed that the circular clockwise rotation of streamlines are developed. Small eddy has generated, and with an increasing values of Re the eddy moves towards the centre. Fig. 6.5(a) represents the effect of horizontal velocity due to the variation of Re. It is clear that the velocity at centre increases with the increase in Reynolds number. For broader aspect, it is obvious that the centre of the vortices layer smaller than near the corner of the cavity. Furthermore, it can

be observed that the layers are established near the boundary along the solid wall as Re increases and heat swings from the solid boundary with a uniform vorticity. Fig. 6.5(b) indicates that velocity near the centre decreases and creates a narrow boundary layer near the walls. Temperature profile at horizontal mean position is shown in Fig. 6.5(c). The average fluid temperature sharply decreases with an increasing Re, due to volume fraction of nanoparticles. Temperature also decreases in the cavity where the forced convection is dominant. Nusselt number against heated vertical wall is illustrated in Fig. 6.5(d).

Effects of nanoparticles:

Fig. 6.6 illustrates the effects of nanoparticle volume fraction on isotherm and streamline. Thermal conductivity and viscosity of fluid enhances when the nanoparticles are mixed with base fluids. Fig. 6.6(a-c) describes the dominant nature of heat transfer of forced convection, which occurs due to the heated mode of vertical lid moving with uniform velocity. Isothermline reveals that the prevailing heat transfer modes are forced convection caused by the movement of vertical velocity. While the free convection is having a limited role in cavity due to the nanoparticles. Fig. 6.6(d-f) represents the streamlines for various values of nanoparticles (ϕ). It can be clearly seen in the graph that at the top of circular cylinder, the eddy is developed due to the interacting of two larger eddy clockwise rotating roles which form a large eddy near the lid wall. With an increase in ϕ, the streamlines are more stronger around the circular surface of the cylindrical obstacle. In Fig. 6.7(a-f), the effects of nanoparticles on the velocity, temperature profile and Nusselt number are illustrated. Horizontal velocity increases with increasing volume fraction of nanoparticles and attains its maximum position at the end points. But vertical velocity decreases with the increase in ϕ. Fig. 6.7(c) represents the temperature distribution against the horizontal mean position. In case of base fluids $\phi = 0$, the cavity temperature remains maximum at the end point but

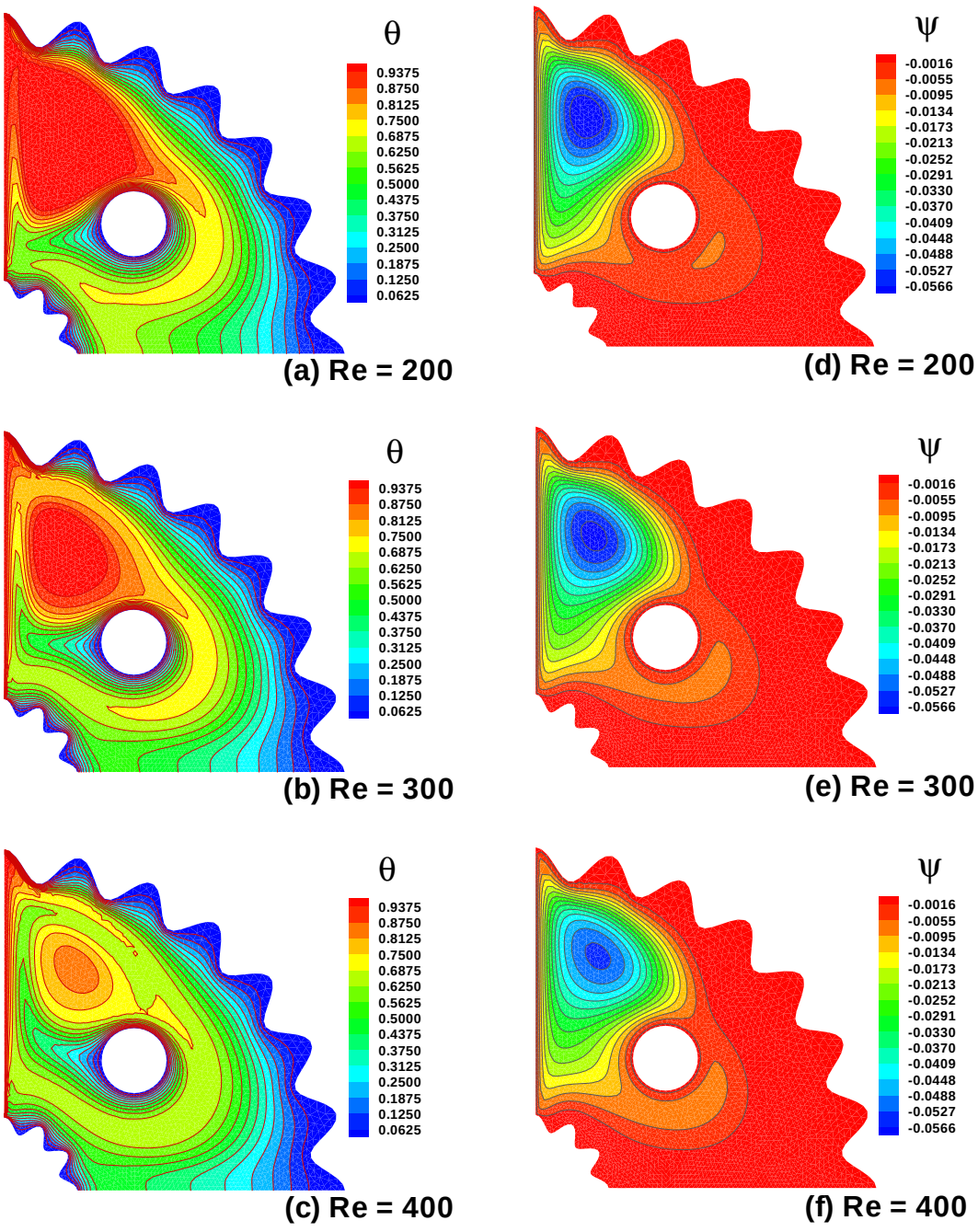

Figure 6.4: Variation of (a)-(c) isotherm and (d)-(f) streamlines with respect to Re when $Ri = 0.01$, $Da = 10$, $\phi = 0.05$, $Q = 50$ for cold cylindrical obstacle

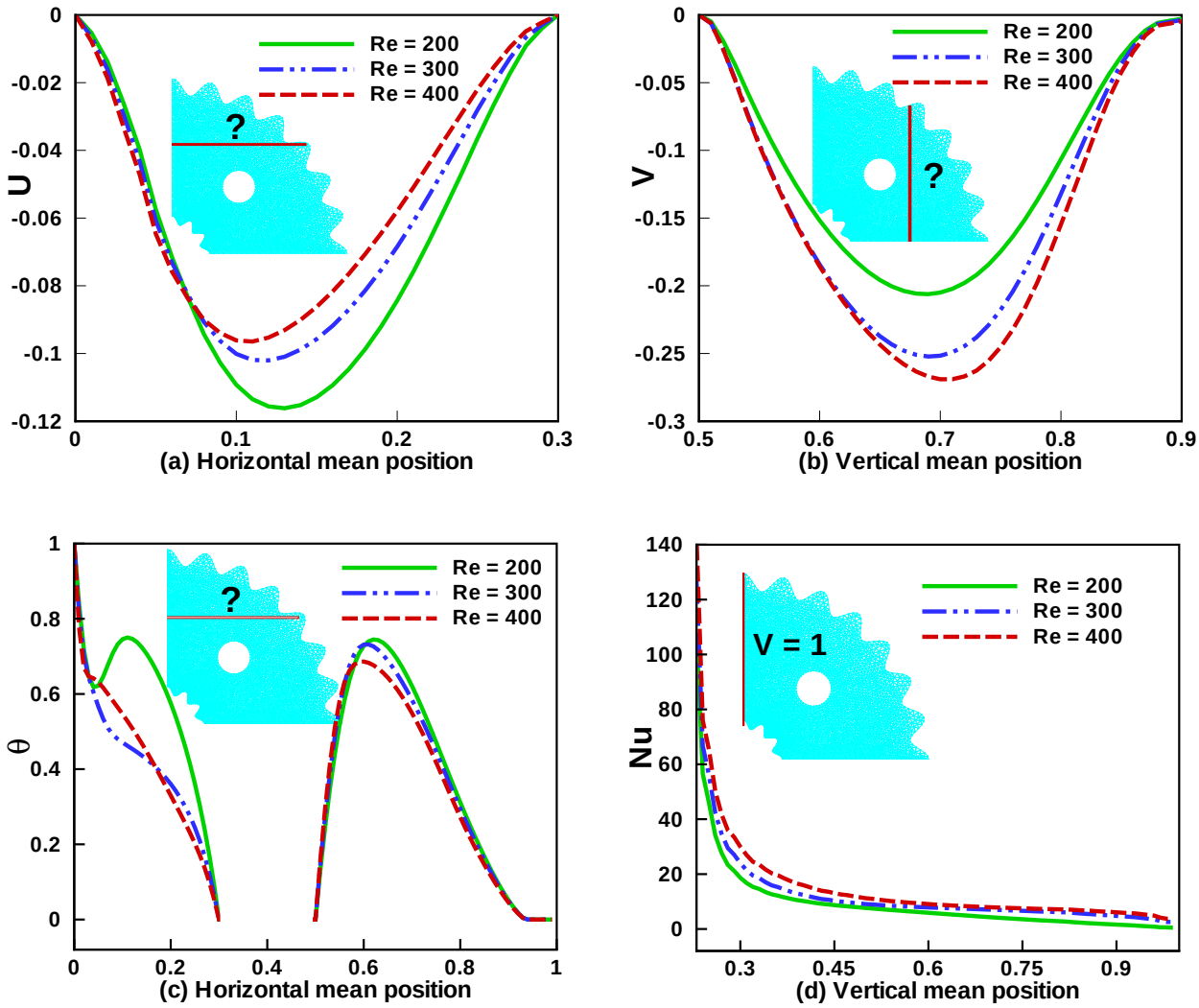

Figure 6.5: Variation of (a) horizontal velocity, (b) vertical velocity, (c) temperature and (d) Nusselt number with respect to *Re* for cold cylindrical obstacle

zero at the centre. While for $\phi = 0.1$ and 0.05 temperature rapidly decreases due to the higher thermal conductivity of nanoparticles and streamlines intensity decreases only significantly, as volume fraction increases, and temperature gradient decreases. With a reduction in temperature gradient and increasing volume fraction, there can be no specific estimation for the overall heat transfer within the cavity. As ϕ increases, nanofluid thermal conductivity also enhances while marginally temperature gradient decreases. In a cavity, as heat transfer rate increases, there will be enhancement in forced convection that can be clearly seen in Fig. 6.7(d) in the form of Nusselt number.

Effects of Richardson number:

Fig. 6.8(a-h) shows the isotherms and streamline of assisting forced flow for different values of Ri at the fixed value of Re. In isotherm, the region affected by the heated vertical lid wall is quite small for small values of Ri and gradually increases with its increasing value. For higher value of Richardson number, the buoyancy effects are much stronger and have more vigorous loops in the enclosure appeared in the figure. The intensity of the circulation in the form of bolus increases with the increase in Ri in the streamline. At $Ri = 0.1$, the forced convection dominates due to the vertical lid driven. However, at this value of Ri, the natural convection has been slightly affected at the corner which can almost be neglected. With the increase in $Ri = 1$, the mixed convection (inertial and buoyancy forces) balanced in the enclosure. At $Ri = 100$, the forced convection decreases and buoyancy effect dominates as seen in Fig. 6.8(d). Fig. 6.9(a-b) shows the variation of velocity against Ri horizontally and vertically. Here, velocity decreases with an increase in the values of Ri for both cases. Forced convection is dominant for the smaller values of Ri and increases with the larger values of Ri which turns to be natural convection as shown in Fig. 6.9(c). Local Nusselt number in the vertical mean position of the lid wall increases for the forced convection and decreases for natural convection.

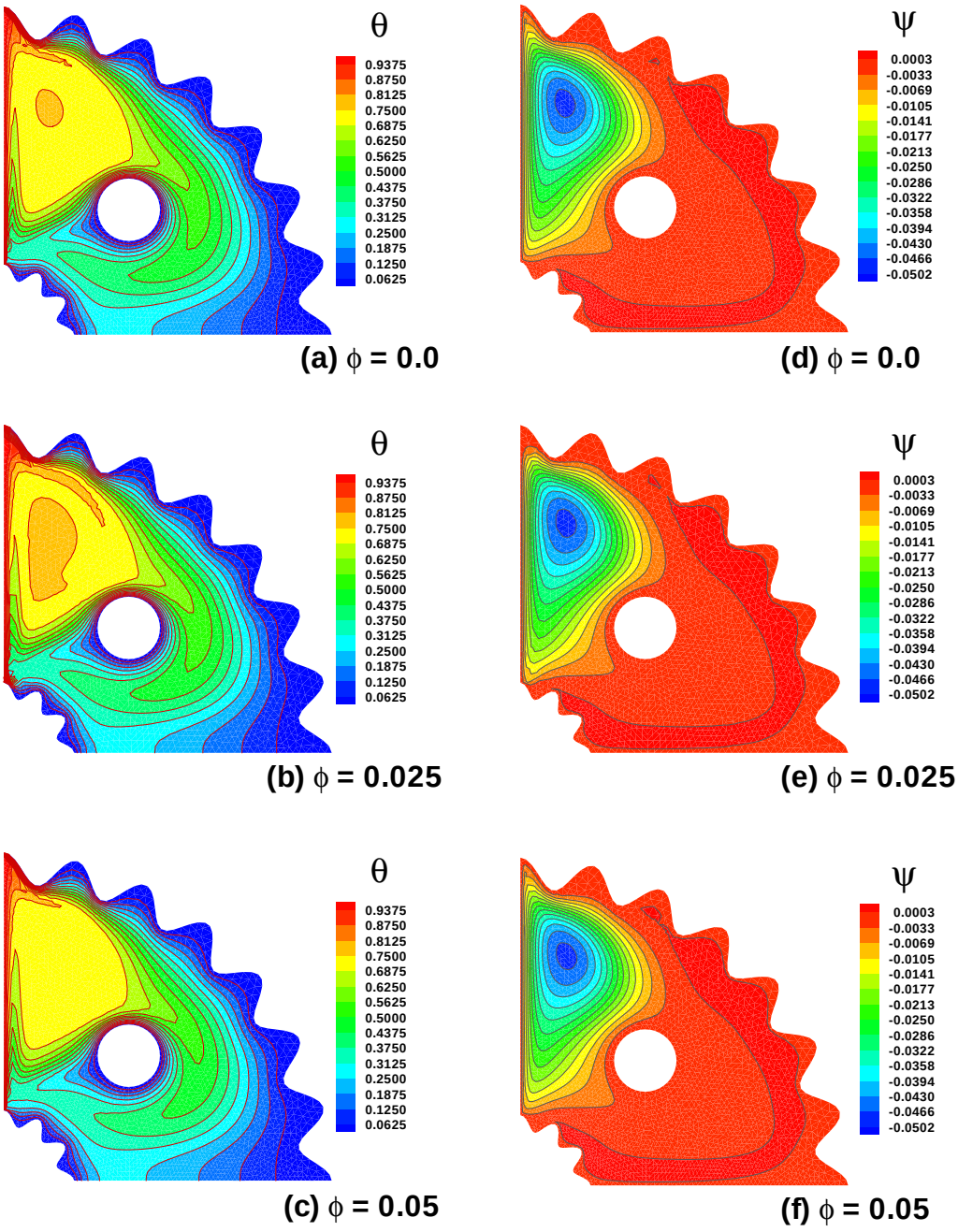

Figure 6.6: Variation of (a)-(c) isotherms and (d)-(f) streamline with respect to ϕ when $Ri = 0.01$, $Da = 0.01$, $Re = 350$, $Q = 10$ for cold cylindrical obstacle

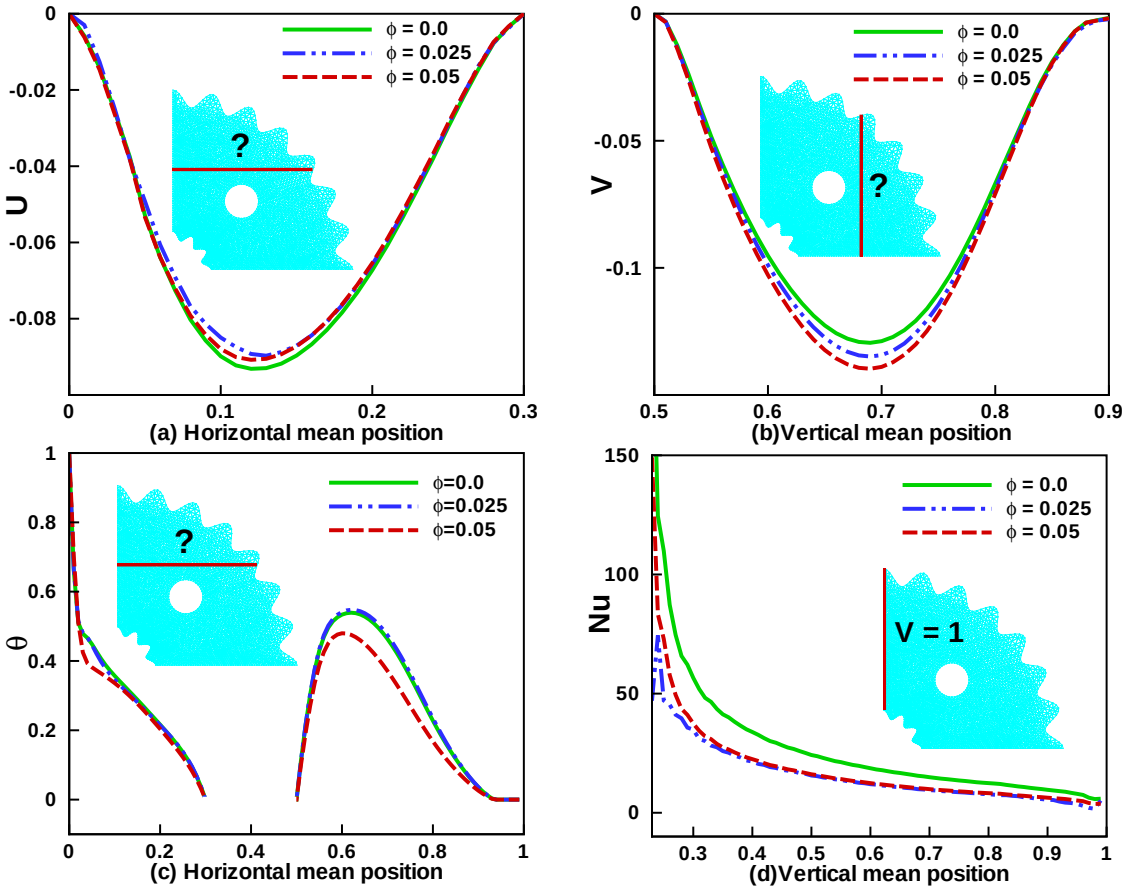

Figure 6.7: Variation of (a) horizontal velocity, (b) vertical velocity, (c) temperature and (d) Nusselt number with respect to ϕ for cold cylindrical obstacle

Effects of porous medium:

Fig. 6.10 illustrates the effects of Darcy number on isotherms and streamlines. The permeability in cavity has significant effects on heat transfer and flow of the molecular movement. For a small number of $Da = 10^{-5}$, heat is located near the lid wall. For $Da = 10^{-3}$, as shown in Fig. 6.10(b), the convection of heat is raised and then heat is moved and is created around the cold circular surface of cylinder. Due to an increasing Da, heat transfer rate is increased. The convection is denominated with the increase in Darcy number. That's why, temperature gradient moves towards the down surface where the conduction is dominant due to the minimal flow activities of the fluid in cavity. Fig. 6.10(d-f) illustrates the result of different Da for maximum value of Reynolds number. For $Da = 10^{-5}$, the flow of lines are restricted near the vertical wall and for the recirculation, small intensity of the flow of fluid is being observed due to the moving lid wall. The streamline for the recirculation flow region is elongated due to the increase in Darcy number. For the Da, the small eddy moves towards downward to the centre point and the lines of stream are symmetric throughout the region. Horizontal and vertical velocity related to various Darcy number is reported in Fig. 6.11. For greater value of Da, both velocities (horizontal and vertical) increase at the centre of the enclosure due to the greater convection for greater value of Da. For energy transportation, the inertial effects are retarded. For higher value of Da, the temperature is slightly titled down to the centre which is shown in Fig. 6.11(c). Temperature in cavity decreases due to the inertial coefficient which decreases with the increase in porosity. Fig. 6.11(d) illustrates the effects of heat transfer. It can be observed in Fig. 6.11(d) that in the middle of cavity, the influence of Da will have a greater impact on Nu due to the convection. The transfer rate of heat is less near the right cold wall but higher near the heated wall for all Da. It can be seen that the porous medium enhances the transformation of energy in enclosure.

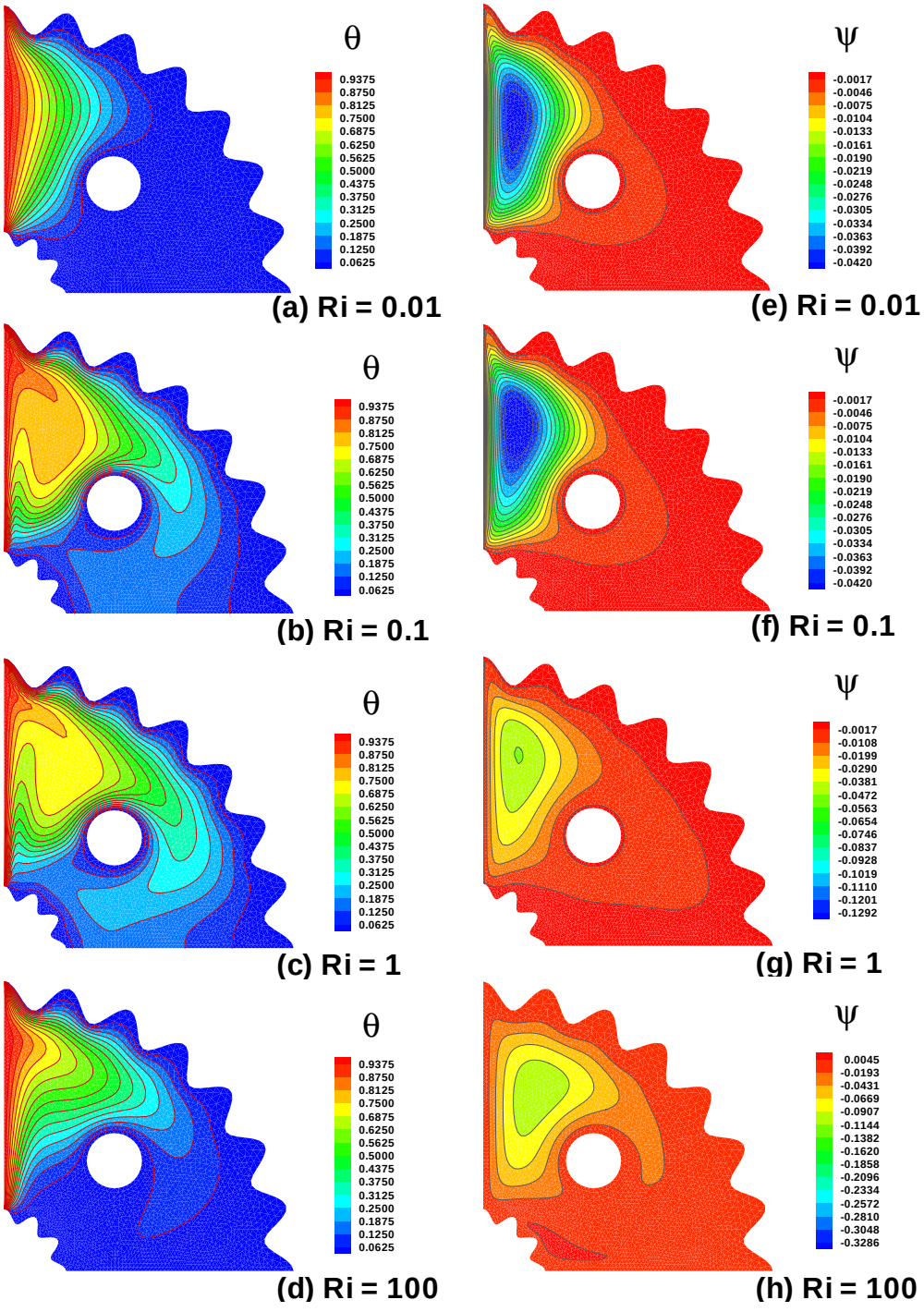

Figure 6.8: Variation of (a)-(d) isotherms and (e)-(h) streamline with respect to Ri when $Re = 100$, $Da = 0.01$, $\phi = 0.05$, $Q = 10$ for cold cylindrical obstacle

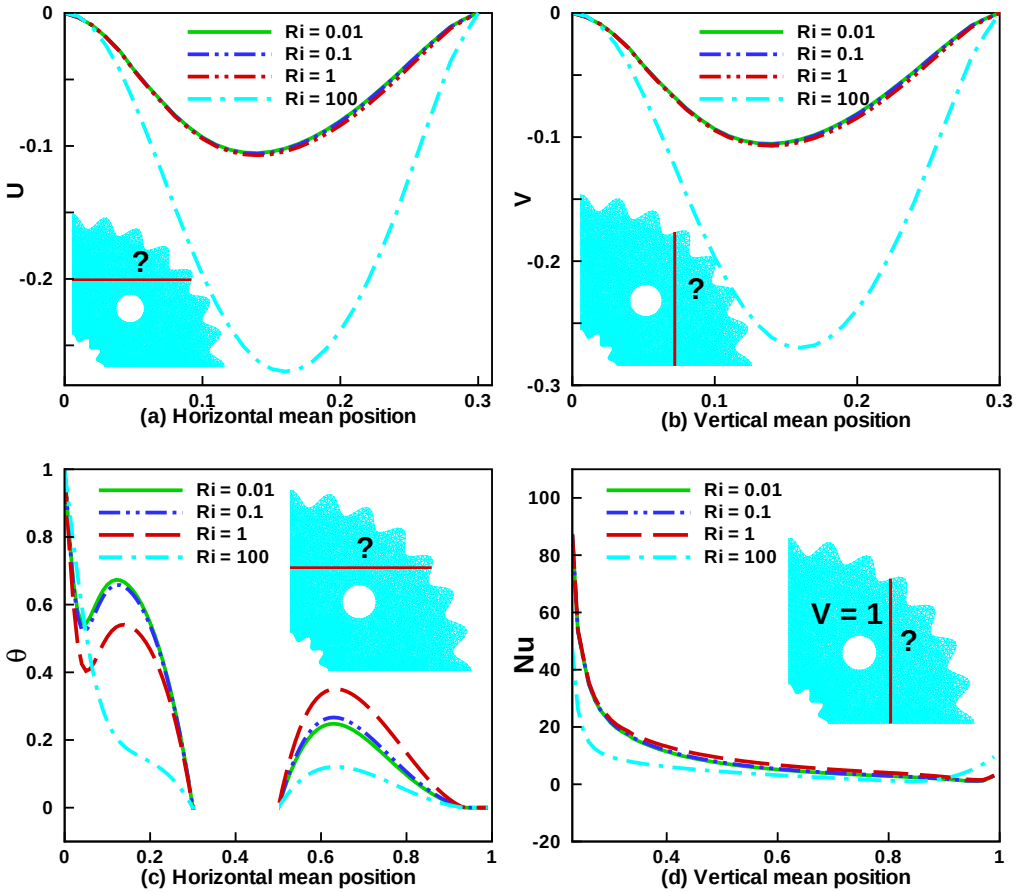

Figure 6.9: Variation of (a) horizontal velocity, (b) vertical velocity, (c) temperature and (d) Nusselt number with respect to Ri for cold cylindrical obstacle

Effects of heat generation/absorption:

Fig. 6.12 shows the effects of heat coefficient parameter Q on the molecular movement and streamline in the curved cavity. It has significant role in energy equation. The variation in isotherms mostly appears due to the dependency on Q as it varies. $Q < 0$ represents the absorption of heat whereas, $Q > 0$ represents the internal heat generation. Near the closer area of the heated wall, the temperature effect becomes less as Q becomes smaller. Furthermore, the heat which is produced in this region increases both the domain temperature as well the temperature gradient near the cold wall. Fig. 6.13(c) illustrates that in case of heat generation ($Q > 0$), the temperature increases in cavity. The internal heating in energy equation represents the temperature rising near the vertical wall specially. Due to the dominant role of heat generation in Nu, it decreases gradually as illustrated in Fig. 6.13(d).

Effects of different of state cylindrical surface:

Isotherms and streamline result due to the various states (adiabatic, cold and heated) of circular cylinder as shown in Fig. 6.14. In cold and adiabatic case, the intensity of heat near the heated wall and circular surface is high and it gradually decreases towards the cold curved wall. Fig. 6.14(d-f) represents the variation of streamline due to the various state of cylinder. In each case, the same eddy is being created near the heated wall which results as the vertical wall moves and the movement of fluid particles in clockwise direction. In adiabatic case, the streamline spreads around the curved surface but in case of hot obstacle, the streamlines are away from the curved surface. The effects on velocities, temperature and Nusselt number are shown in Fig. 6.15. The horizontal velocity is being measured from $(0, 0.3)$ as depicted in Fig. 6.15(a). It seems that the horizontal velocity is same near the heated vertical wall but is away from the wall which decreases in case of cold wall and increases in hot and adiabatic. Due to the hot surface, the velocity attains its maximum point in the middle of cavity. Fig. 6.15(c) represents the tempera-

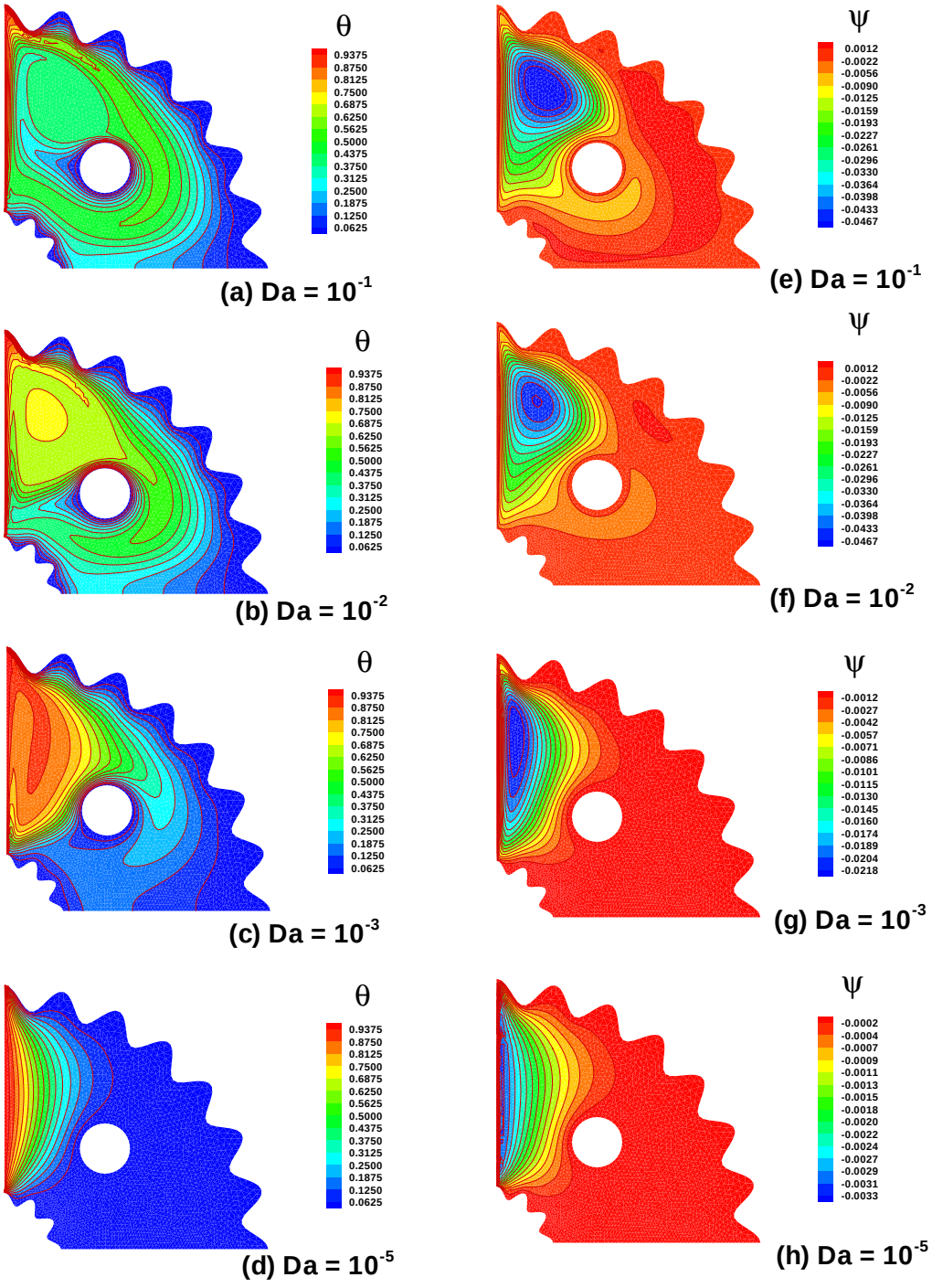

Figure 6.10: Variation of (a)-(d) isotherms and (e)-(h) streamline with respect to Da when $Ri = 0.01$, $\phi = 0.05$, $Re = 450$, $Q = 10$ for cold cylindrical obstacle

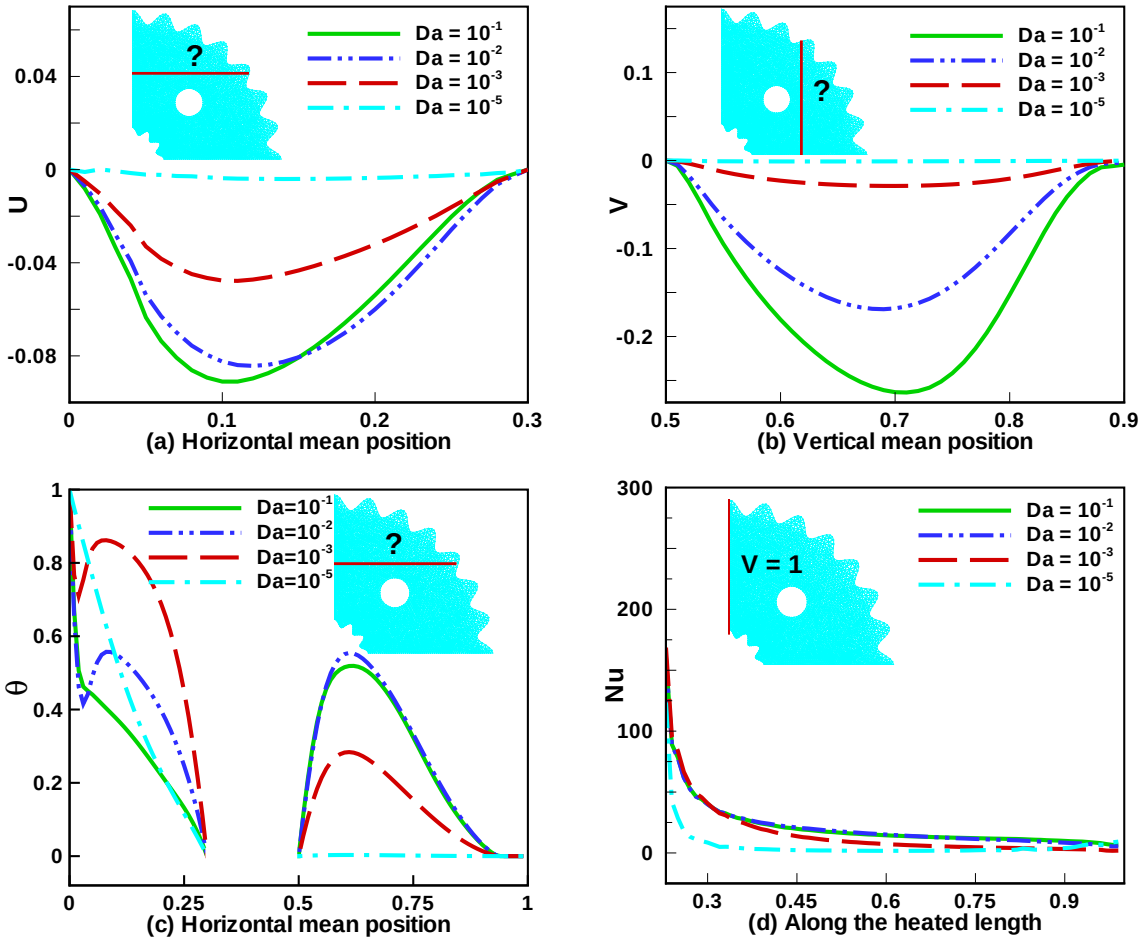

Figure 6.11: Variation of (a) horizontal velocity, (b) vertical velocity, (c) temperature and (d) Nusselt number with respect to *Da* for cold cylindrical obstacle

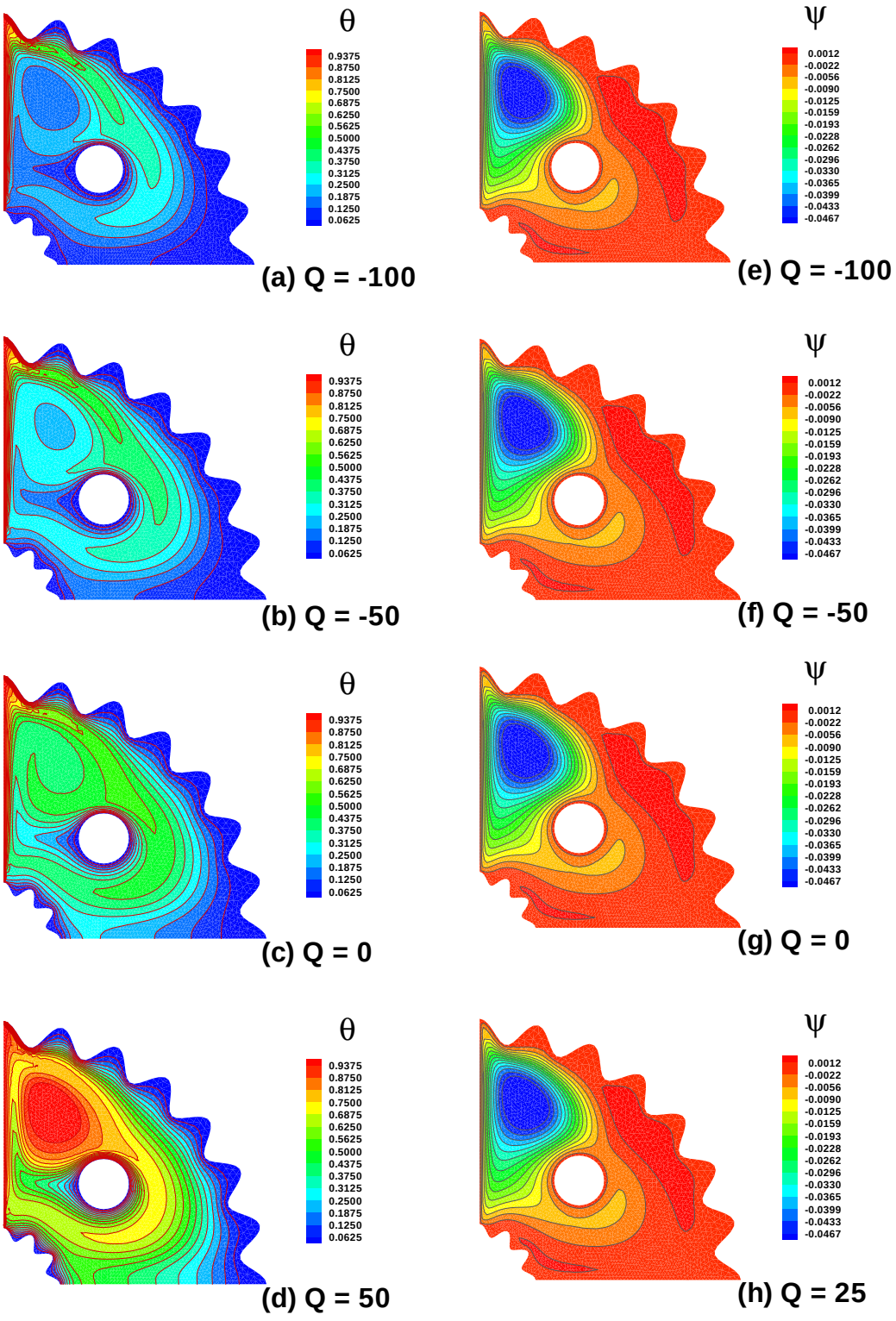

Figure 6.12: Variation of (a)-(d) isotherms and (e)-(h) streamline with respect to Q when $Ri = 0.01$, $\phi = 0.05$, $Re = 350$, $Da = 0.1$ for cold cylindrical obstacle

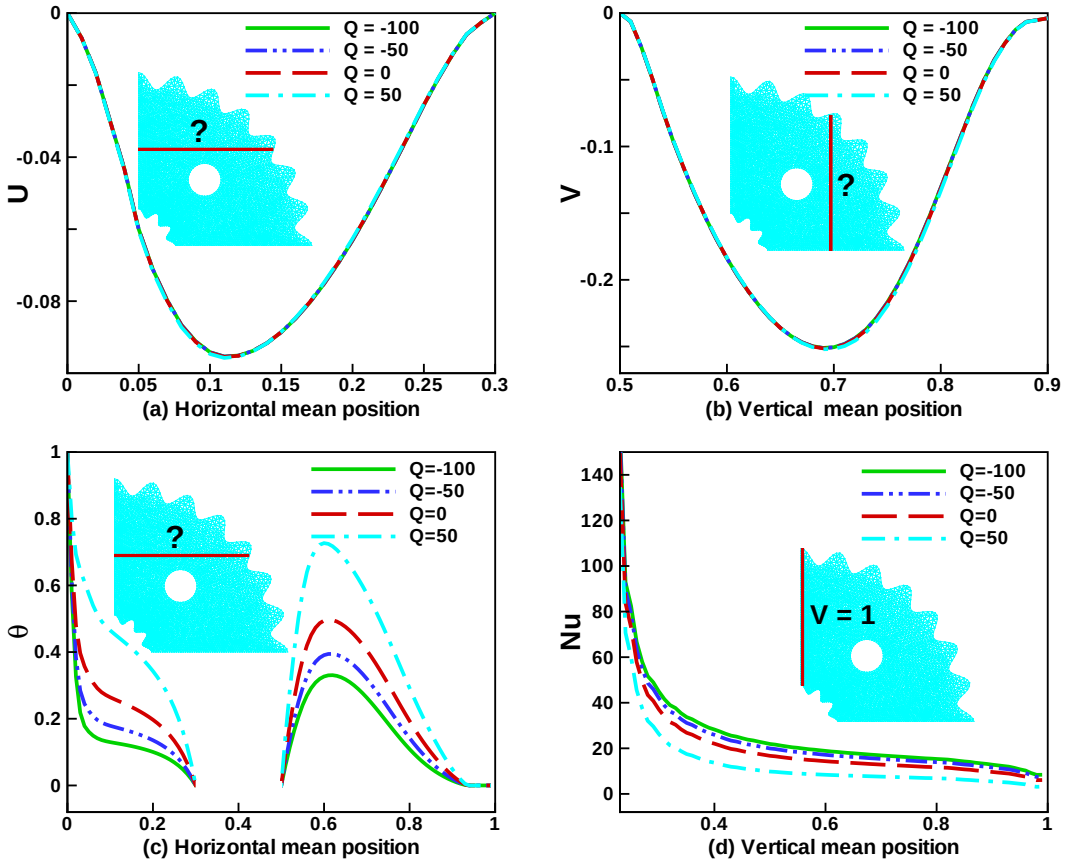

Figure 6.13: Variation of (a) horizontal velocity, (b) vertical velocity, (c) temperature and (d) Nusselt number with respect to Q for cold cylindrical obstacle

ture at horizontal mean position. In case of a cold surface of cylinder, when the temperature from the heated wall moves towards the centre it gradually decreases at zero and for 0.25 it drops to zero. Whereas, in case of the hot cylinder, when the temperature from the cylinder moves towards the cold wall it attains its maximum point at 0.25. Temperature sharply increases in cavity and decreases in case of cold cylinder. Nusselt number decreases in heated curved surface and increases in cold case clearly seen in Fig. 6.15(d).

In Fig. 6.16(a) of an average Nusselt number, increasing the Reynolds number (Re) increases the Richardson number (Ri) due to the vertical heated lid wall. Fig. 6.16(b) depicts the minor increase in the average Nusselt number for smaller values of Darcy number with the increase in Re, whereas the minor increase in Nu_{avg} is observed against the higher values of Da with the same rate of Re. Fig. 6.16(c) shows the effects of heat generation/absorption with respect to fixed Ri and various values of Re. It can be observed that increase in the internal heat absorption increases the convection of heat transfer. Whereas the increase in internal heat generation decreases the average Nusselt number. Fig. 6.16(d) depicts the variation of the average Nusselt number for various values of volume fraction and Reynolds number where it is seen that increasing the volume fraction causes the increase in the heat transfer for different values of Re.

6.5 Conclusion

The effects of Reynolds number ($100 \leq Re \leq 400$), nanoparticles ($0 \leq \phi \leq 0.05$), Darcy number ($10^{-5} \leq Da \leq 0.1$), different state of cylindrical obstacle (adiabatic, cold and heated) and heat generation/absorption parameter ($-100 \leq Q \leq 50$) on isotherms, streamline profile, temperature and Nusslet number were briefly discussed in this section. The study concluded with the following remarks:

- For a high Reynolds number, the forced convection is dominant, so the

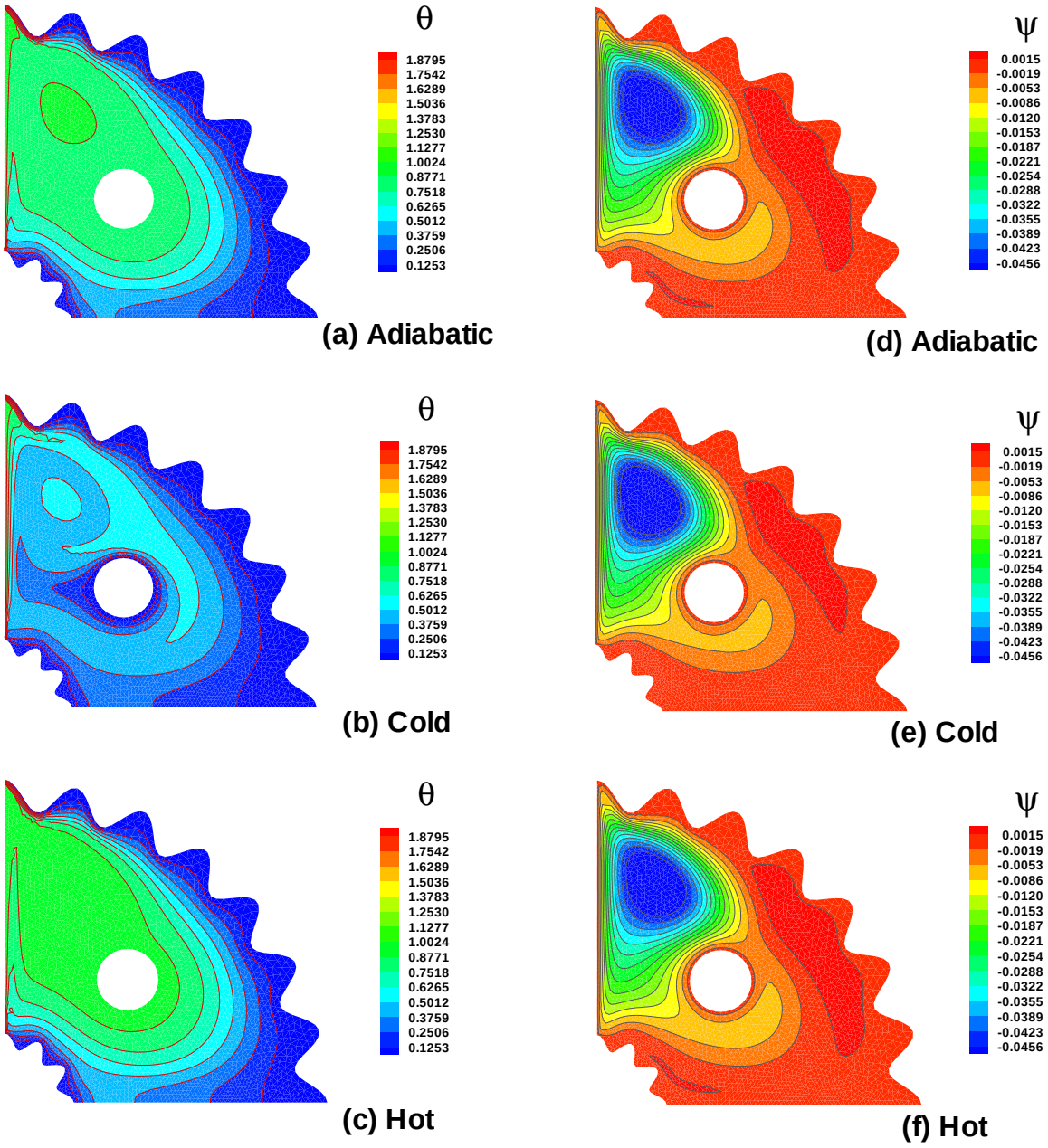

Figure 6.14: Variation of (a)-(c) isotherms and (d)-(f) streamline with respect to adiabatic, cold and hot cylindrical obstacle when $Ri = 0.01$, $\phi = 0.05$, $Re = 350$, $Da = 0.1$ $Q = 10$

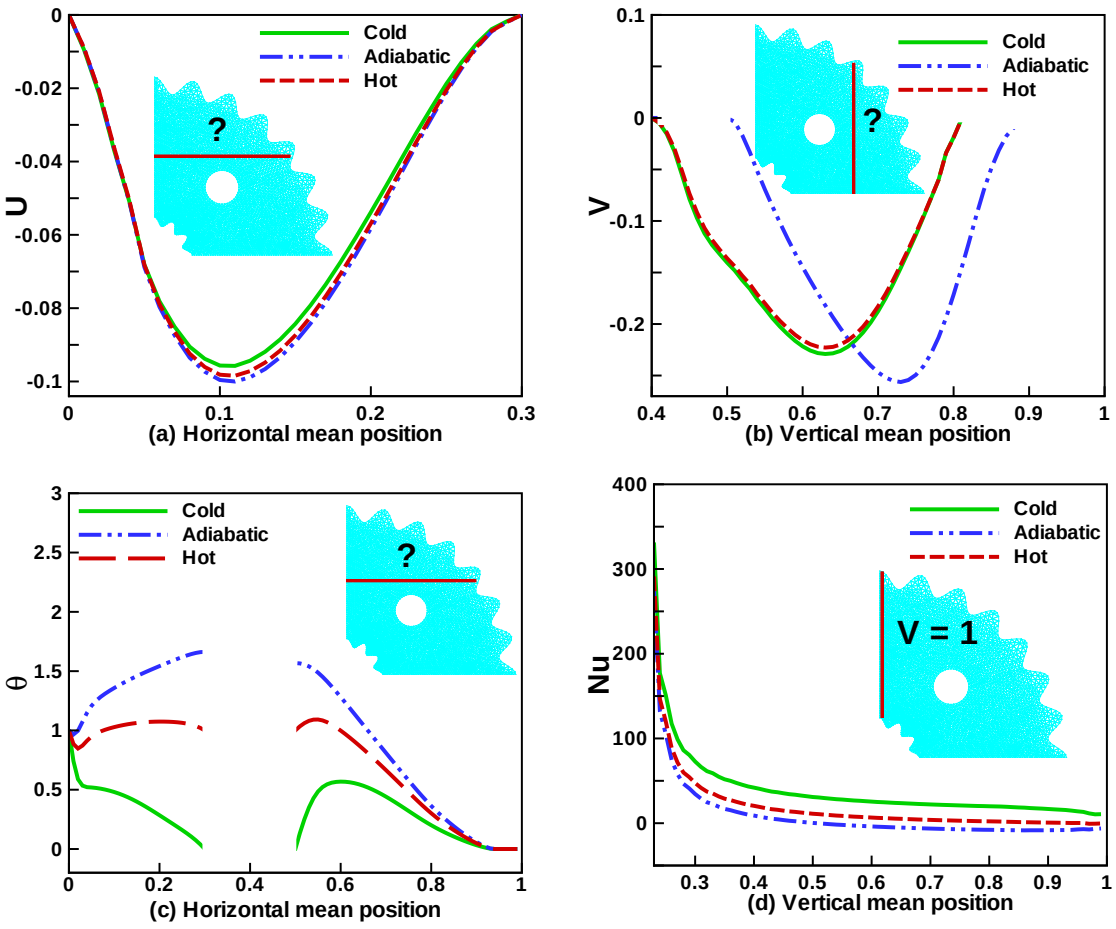

Figure 6.15: Variation of (a) horizontal velocity, (b) vertical velocity, (c) temperature and (d) Nusselt number with respect to cold, adiabatic and hot cylindrical obstacle

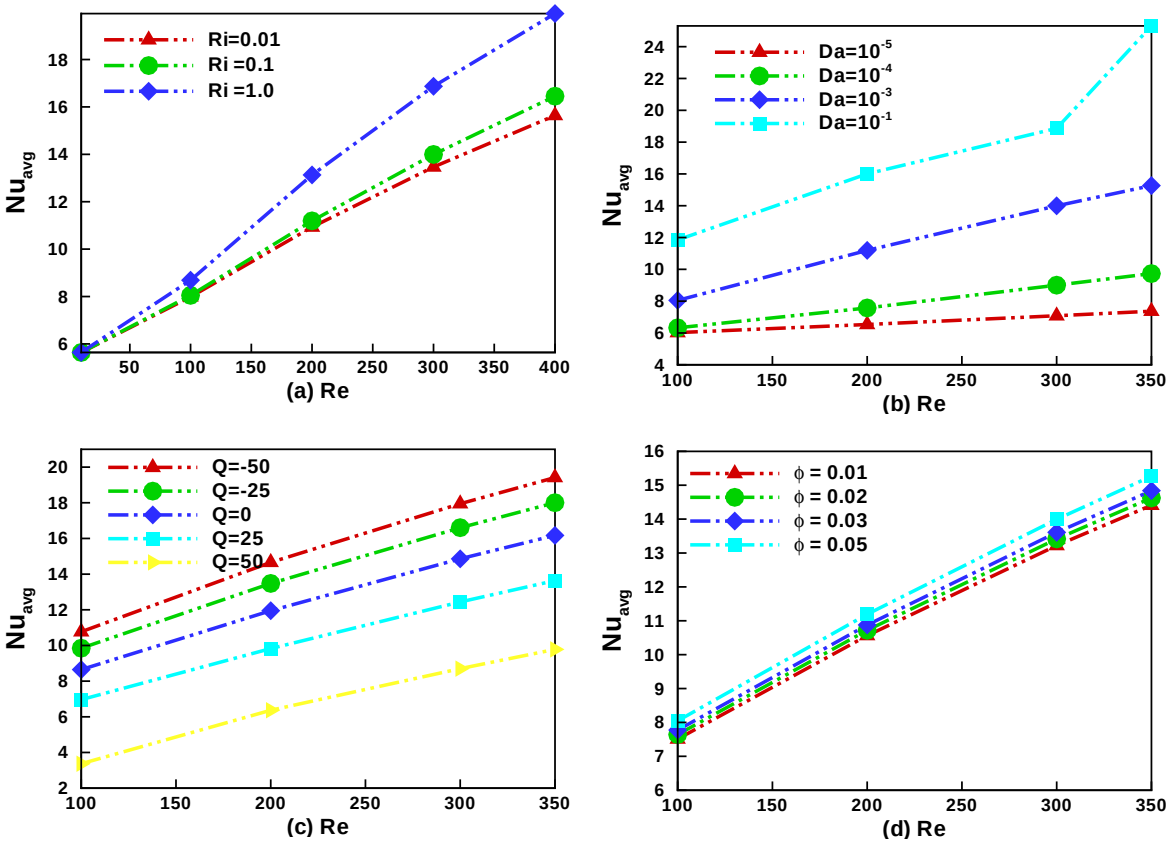

Figure 6.16: Variation of average Nusselt number with respect to the Reynolds number at the different values of (a) Richardson number (b) Darcy number (c) Heat absorption/generation coefficient (d) Volume fraction

heat transfer rate is high. Nusselt number increases with increase in Re.

- With increase in Re, the symmetrical eddy moves towards the centre of cavity.
- Small eddy is created near the wall in streamline due to the clockwise rotation of fluid.
- Nanoparticles enhance the thermal conductivity of the fluid, so greater heat convection in cavity is done when $\phi = 0.05$.
- Temperature distribution decreases near the heated wall with increases in Darcy number. Isotherm lines are gradually limited around the heated vertical wall for high Darcy number.
- Temperature increases in case of heated cylindrical surface and Nusselt number decreases. Heated lines are restricted at end face of heated wall in case of cold obstacle and getting stronger in heated region.
- Maximum heat generation is obtained in the cavity for positive values of Q. Temperature increases and Nusselt number decreases with increasing Q.

CHAPTER 7

THERMAL PERFORMANCE OF WATER DRIVEN FLOW OF NANOPARTICLES' SHAPE DUE TO DOUBLE SIDED FORCED CONVECTION ENCLOSED IN A POROUS CORRUGATED DUCT

7.1 Introduction

In this chapter, a complex nature structure is simulated by introducing the nanofluid that contains various shape of nanoparticles through forced convection and thermal diffusion. Double sided lid-driven in a porous curved cavity is constructed to handle the forced convection phenomena. Additionally, effects of internal heat generation/absorption is also considered. The horizontal and vertical walls are moving with a constant speed U_o and V_o, respectively, which are further divided into two moving lids. The flat and curved walls are kept at constant temperature T_h^* and T_c^*, respectively. The governing equations are discretized and solved through Galerkin residual method by means of finite element method (FEM). The effects of various directional velocities, porous medium (Da), Reynolds number (Re), internal heat generation/absorption coefficient (Q) and solid concentration of nanoparticles (ϕ) are investigated on transfer rate of heat in the form of Nusselt number, isotherms, streamline, temperature and velocity profile. Results reveal that heat is generated in cavity when the direction of velocities of moving wall is in the opposite

inward direction. The heat transfer rate decreases in the case of internal heat generation and increases for nanoparticles.

Table 7.1: A table demonstrating the contrasts between the approaches being offered

Authors	Enclosure	Porosity	Heat generation	Lid driven
Hussain *et al.* [20]	Square	No	Yes	Double
Alleborn *et al.* [35]	Rectangular	Yes	No	Single
Haq *et al.* [77]	Corrugated	Yes	No	No
Sivasankaran *et al.* [96]	Sinusoidal walls	No	No	Single
Present	Corrugated	Yes	Yes	Double Split

7.2 Problem Formulation

Consider the two-dimensional viscous flow enclosed by curved shape that is heated from the bottom and left wall, flow is due to the fully heated walls of lid driven. In order to construct the mathematical model for physical partially corrugated cavity (see Fig. 7.1), with defined various constraints which are mandatory to examine the theoretical investigation.

7.2.1 Mathematical Model

The governing equations of incompressible, Newtonian, laminar and steady state (thermal equilibrium) lid driven convection in a curved corrugated enclosure filled with a nano-fluid in the form of Navier-Stokes formulation

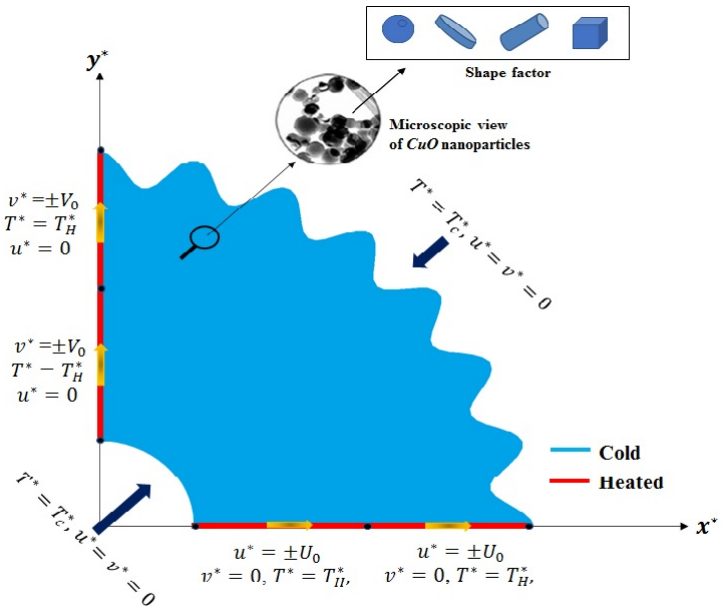

Figure 7.1: Geometry of the lid-driven cavity

(mass, momentum and energy) have already been discussed in Chapter 5. For spherical nanoparticles thermal conductivity (k_{nf}) modelled by [97] is written in Eq. (2.3).

7.2.2 Dimensionless boundary conditions:

At the bottom solid wall **(Ω_1 and Ω_2):**

$$\begin{aligned} (U,V) = (1,0),\ \theta = 0, \text{when} \\ \Omega_1 = \{(X,Y) \in \mathcal{R}^2 / 0.27 \leq X < 0.365 \ \text{ and } \ Y = 0\}, \\ \Omega_2 = \{(X,Y) \in \mathcal{R}^2 / 0.365 \leq X < 1 \ \text{ and } \ Y = 0\}. \end{aligned} \tag{7.1}$$

At the left solid wall **(Ω_3 and Ω_4):**

$$\begin{aligned} (U,V) = (0,1),\ \theta = 1, \text{when} \\ \Omega_3 = \{(X,Y) \in \mathcal{R}^2 / 0.27 < Y \leq 0.365 \ \text{ and } \ X = 0\}, \\ \Omega_4 = \{(X,Y) \in \mathcal{R}^2 / 0.365 < Y \leq 1 \ \text{ and } \ X = 0\}. \end{aligned} \tag{7.2}$$

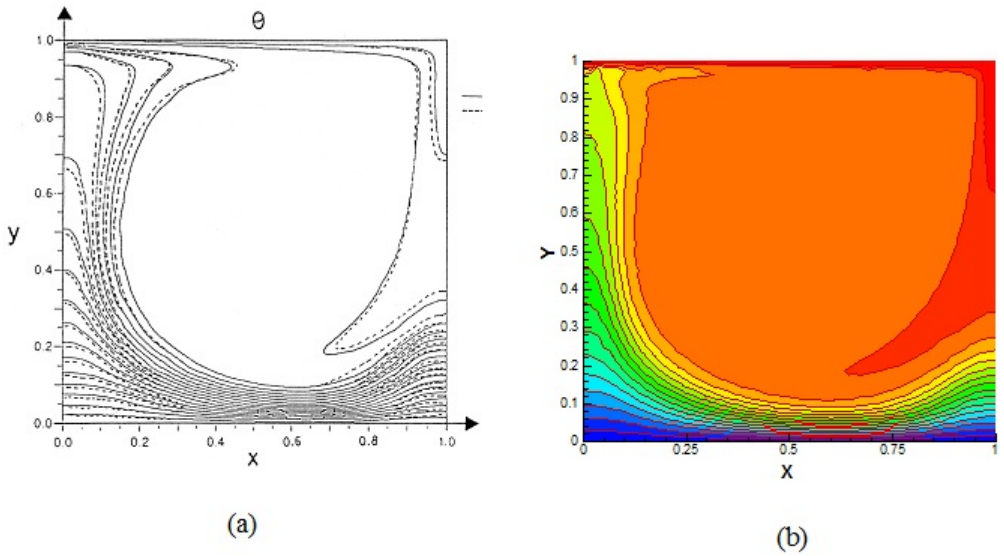

Figure 7.2: Comparison of isotherms in a square cavity: (a) Khanafer and Chamkha [34] (straight line) and Iwatsu *et al.* [33] (dotted line) when $Re = 10^3$ (b) Present work.

***At lower curvy wall*(Ω_5):**

$$(U, V) = (0, 0),\ \theta = 0, \text{when}$$
$$\Omega_5 = \{(X, Y) \in \mathcal{R}^2 / X^2 + Y^2 = r_2^2\}. \tag{7.3}$$

Where center of inner circle is (0,0) and radius is 0.27. The local Nusselt number in dimensionless form at horizontal and vertical lid wall is written in mathematical form as:

$$Nu_{\Omega_1} = Nu_{\Omega_2} = -\frac{k_{nf}}{k_f}\left(\frac{\partial \theta}{\partial Y}\right)_{Y=0}. \tag{7.4}$$

$$Nu_{\Omega_3} = Nu_{\Omega_4} = -\frac{k_{nf}}{k_f}\left(\frac{\partial \theta}{\partial X}\right)_{X=0}. \tag{7.5}$$

7.2.3 Comparison of results and Grid Independency

In this section, we have validated numerical results of present problem with other manuscript. Thermal performance in lid-driven square model can be

compared with earlier work done by Khanafer and Chamkha [34] and Iwatsu *et al.* [33] in Fig.7.2(a), our current thermal work in contour with limiting conditions is depicted in Fig.7.2(b).

7.3 Results and Discussion

In this unit, forced convection of water based nanofluid in a corrugated porous cavity with partially double lid driven wall is investigated using finite element method (FEM). Numerical results are illustrated for various values of Reynolds number (Re = 100 to 400), double lid wall with different uniform velocities, Darcy number (Da = 0.0001 to 10), Heat generation coefficient ($Q = -1000$ to 75) and the solid volume fraction of nanoparticles. In case of spherical shape, maximum values of Nusselt number are recorded. Simulation is performed for different parameters when spherical shape of nanoparticle is used.

Effects of the double moving lid-wall direction:

Case I*: *Horizontal lid moves left to right and vertical lid wall moves bottom to top.

Fig. 7.3(a) represents the streamline due to the moving lid wall with constant temperature. In this case of lid walls, symmetric lines are generated near the lid walls and heat is generated inside the cavity. Fig. 7.3(b) illustrates the streamline profile in this case. Molecular movement of the particles is quite similar around the lid walls. It creates two bigger eddies near the wall.

Case II*: *Lid walls move with opposite inward directional velocities.

Fig. 7.3(c) and (d) illustrate isotherms and streamline profile respectively. The more heat is generated in this case and heat generated inside the enclosure is due to the inside movement of the two-lid moving walls. Heat generation is clearly seen in the middle of the lid walls. Fig. 7.3(d) illustrates the path of the molecular movement inside the enclosure. More eddies are

created due to the opposite direction of lid moving walls and counter clockwise rotation of the molecular movements. This eddy may be the formation of secondary eddies due to the partition of the major eddies.

Case III*: *Lid walls move with opposite outward directional velocities.

From Fig. 7.3(e), it is observed that the isotherm spreads near the wall and a major part of the heat is located near the corrugated wall. The symmetry of the isotherm lines created due to the opposite direction of bottom vertical and left horizontal wall. Fig. 7.3(f) demonstrates streamline in the shape of two larger and two smaller eddies near the wall.

Case IV*: *Horizontal walls move from right to left and vertical walls move from top to bottom.

Fig. 7.3(g) illustrates the effect of inside movement of the lid walls on streamlines. It is observed that the heat distribution near the corrugated wall is maximum than the lid wall and isotherm lines are quite stable away from the lid walls. Through the molecular movement of the particles, two bigger eddies are created which covers the whole cavity in the form of lines.

Fig. 7.4(a)-(e) represents the temperature, velocity profile and Nusselt number for different lid wall constraints. Fig. 7.4(a) illustrates that the maximum heat transfer is noticed because of the right horizontal and top vertical partial wall which moves with the velocity $U_R = V_T = -1$. Inside movement of the walls, more heat is created within cavity. Minimum temperature gradient is recorded in the case of outside movement of all lid walls. Minimum temperature gradient is recorded in case of outside movement of all lid walls. Fig. 7.4(b) and (c) illustrate the Nusselt number horizontal and vertical mean position. Nusselt number decreases in case of outside movement of the lid walls. But attains its maximum flow rate of heat when the velocity of moving wall is $U_L = V_B = -1$. In that case significant Nusselt number increases in the middle of the cavity. Horizontal and vertical velocity profile in this case is

demonstrated in Fig. 7.4(d) and (e). It significantly effects on velocity profile, due to drag forced variation near the moving walls.

Effects of the Reynolds number:

Fig. 7.5(a-h) shows the impact of Reynolds number on streamlines and isotherms for nanofluid particles in a corrugated enclosure. As it can be noticed from isotherm plots that at low Re, the contour is uniformly distributed with the heat on both sides of the lid walls. Isotherm lines create a circular format, and the isotherm lines are stronger as Reynolds number increases. The effects of forced convection in a corrugated enclosure are weaker for decreasing values of Re, the number of heated lines is reduced. However, as the Reynolds number rises, heat in an enclosure steadily rises. For a maximum value of Re, the heat flux rises, making forced convection the dominating mode of transportation of heat in the form of isotherms. This indicates the dominant forced convection of heat in cavity. Due to the lid moving at the middle of the lid walls the heat lines tilt towards the upward direction with the increase in Re. For low Reynolds number, the flow pattern is symmetric and creates eddies around the moving walls. For smaller value of Reynolds number small circular vortex rotation generates near the lid walls. With increase in Re, vortex rotation size increases and remains quite stable for maximum value of parameter. As with increasing of Re, the symmetry of the flow is disturbed as shown in Fig. 7.5(h). Fig. 7.6(a)-(e) present the effects of Re on velocity, temperature and Nusselt number in lid cavity. Fig. 7.6(a) illustrates that the temperature distribution increases inside the cavity with increasing Re. For high Re, greater convection is produced inside the cavity. Heat flow increases due to the molecular movement of the particles. Nusselt number also varies due to the moving lid walls and increasing of Re. In the middle, strong convection is being observed. Horizontal and vertical velocity decreases with the increase in Re in the middle of the cavity. But increases in the end of the cavity due to the moving walls with constant velocities.

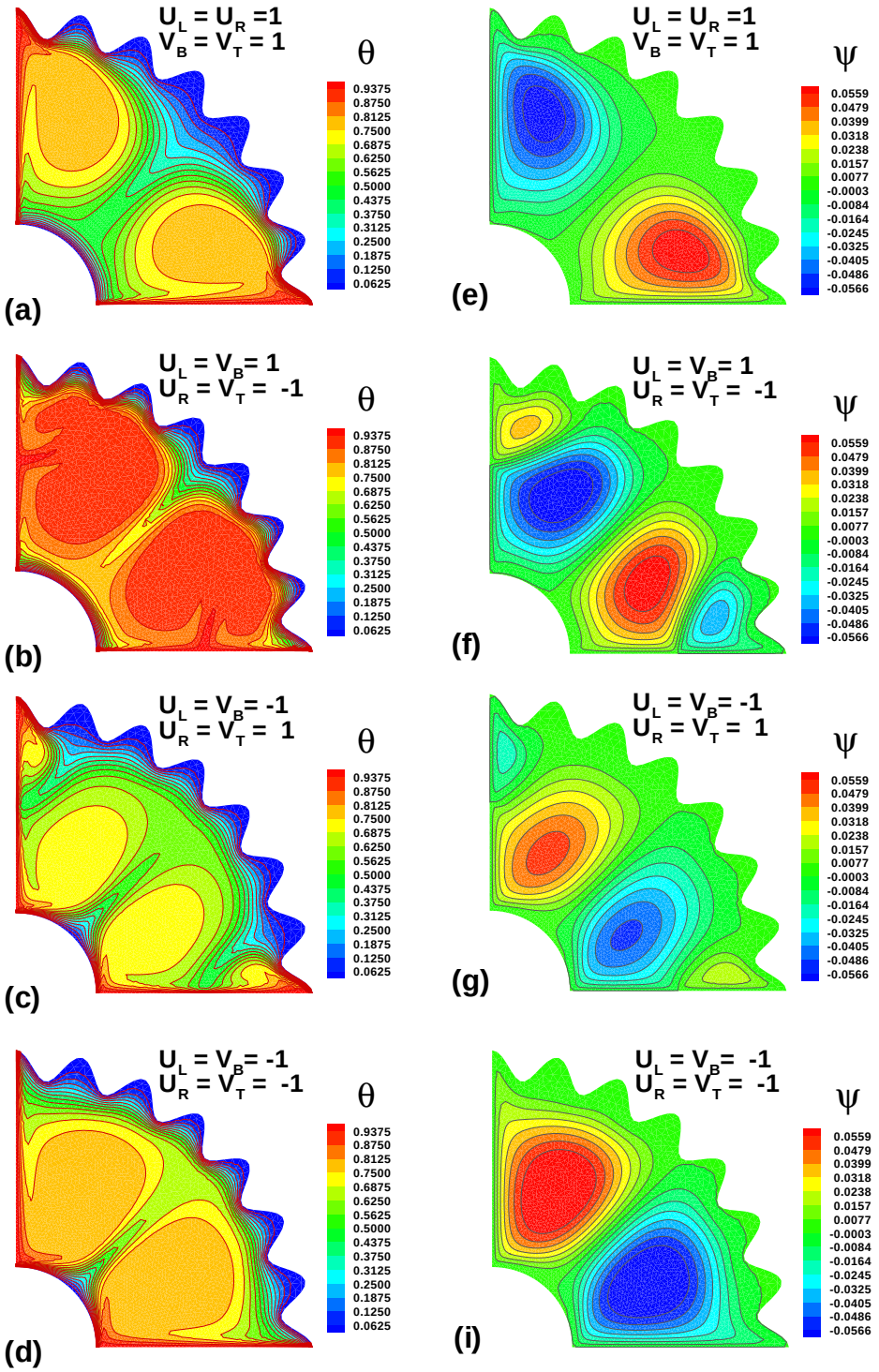

Figure 7.3: Effects of various lid moving walls on the isotherm and streamlines

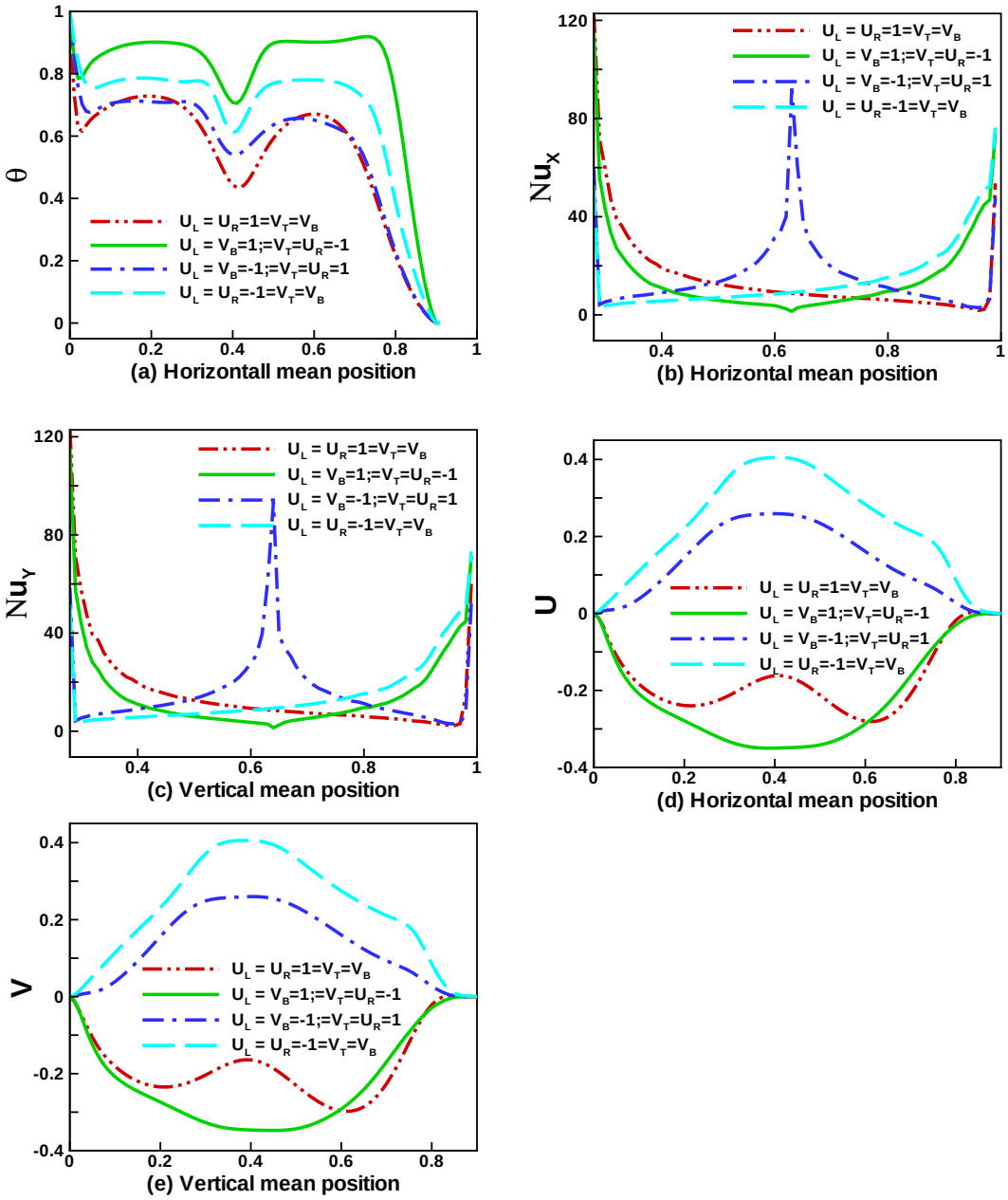

Figure 7.4: Effects of various lid moving walls on the temperature, velocity profile and Nusselt number

Effects of the Porous Medium:

Fig. 7.7(a)-(h) presents the effects of Darcy number on isotherm and streamline profile for maximum value of Reynolds number. The heat transfer rate is maximum at the bottom left corner and lowest at the right corrugated wall. The fluid is revolving anti-clockwise at a high temperature, which is the physical reason for this phenomenon (higher than hot wall temperature). As a result, the hot wall's left bottom corner created a massive temperature, as depicted in figures. It can be observed from the Fig. 7.7(a), when Da is small the convection inside the enclosure is strong and the isotherms are considerably distorted. The flat lines of isotherm in the middle of cavity indicate a small conduction. As Da increases, the forced convection is dominant and circular format of isotherm is created as seen in Fig. 7.7(d). For high number of Da, flat lines are negligible due to the greater convection of lid moving. Fig. 7.7(e)-(h) illustrate the effects on streamline for various Darcy numbers when it moves towards left and bottom lid walls. One can observe that the domain of the cavity is dominated from two re-circular eddies, which are being created from the moving wall with constant velocity. As Da increases from 10^{-5} to 10, the streamline increases and near the lid wall lines are created in thinner form. Convection is expanded across the fluid rather than localized at the boundary as shown in Fig. 7.7(h), for the maximum permeability.

Fig. 7.8(a) shows the effects of Darcy number on temperature profile at horizontal mean position of double lid driven cavity. Because the permeability of the medium increases as the Darcy number rises, the convective mode becomes stronger. As a result, the Darcy number rises, the temperature gradient across the hot wall rises too. For high permeability of the medium more heat is generated near the lid walls. Fig. 7.8(b) and (c) illustrate that the heat transfer increases with increasing of Darcy number. For higher Da, the heat transfer rate is higher in the middle of the cavity and suddenly decreases at 0.9. The external heat increases with increasing or decreasing of internal

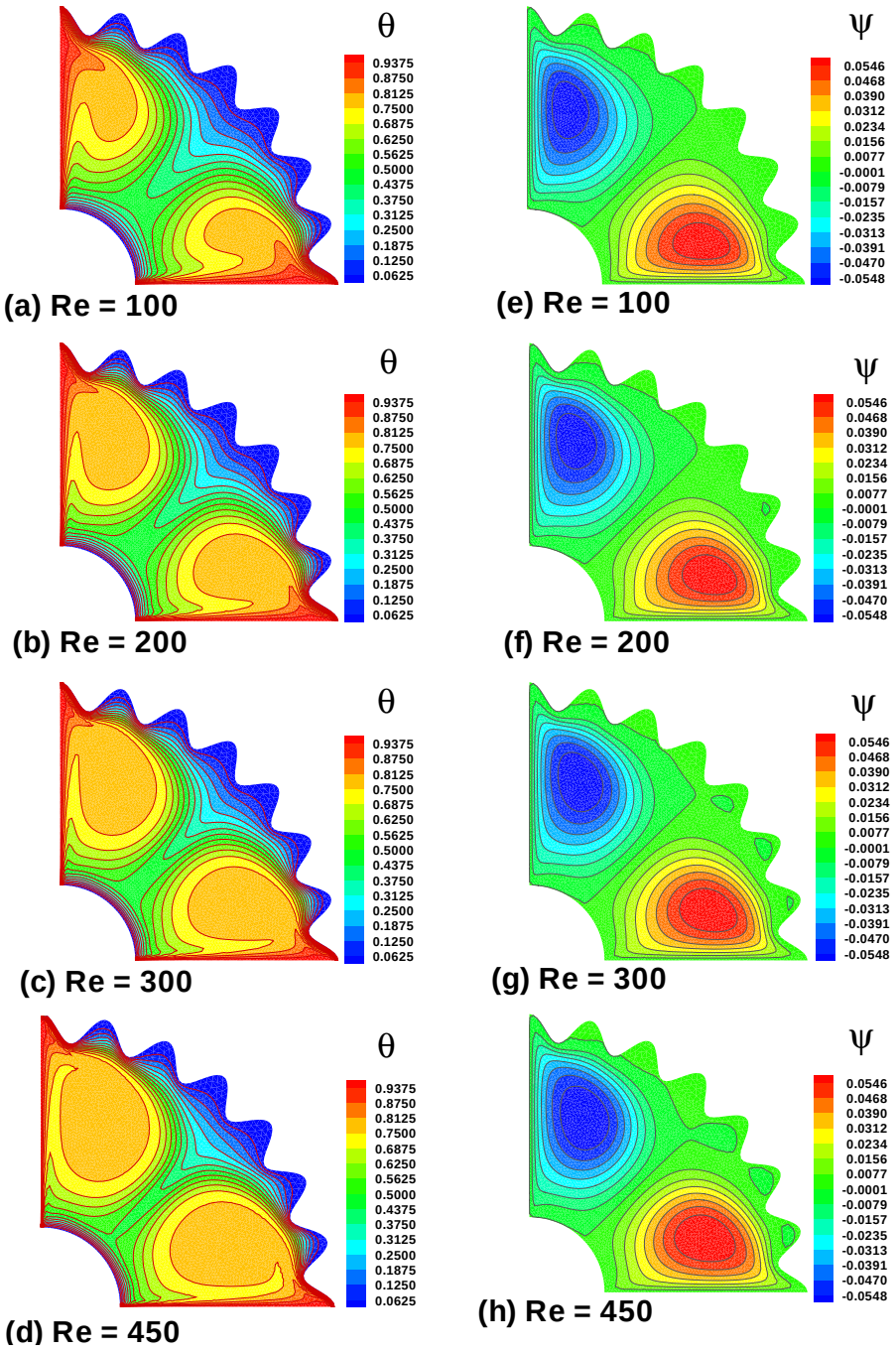

Figure 7.5: Effects of Reynolds number on isotherms (a)-(d) and streamline (e)-(h)

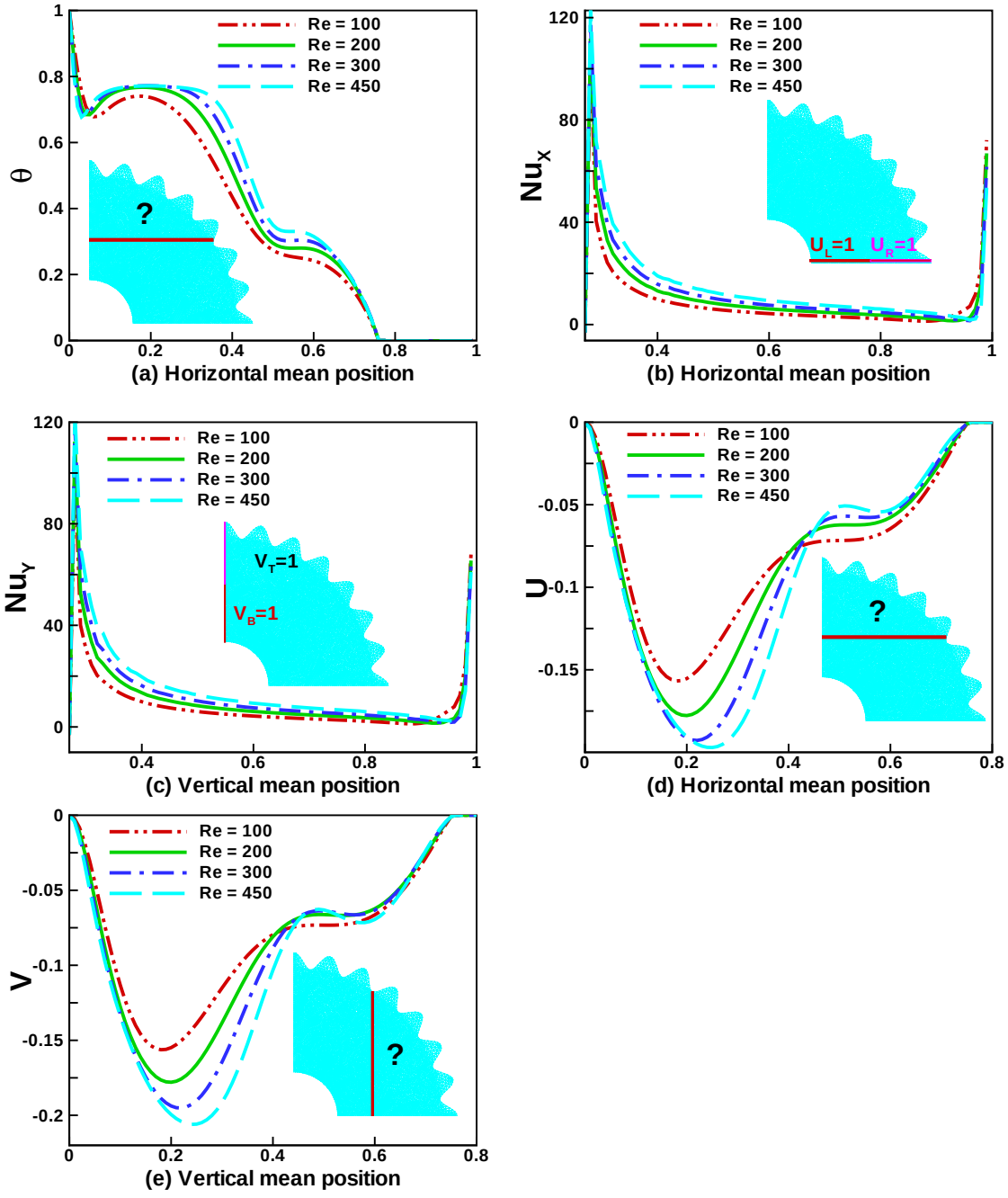

Figure 7.6: Effects of various Reynold's number on the temperature, velocity profiles and Nusselt number

heat. One can see that the localized clusters with consistent Reynolds number of heat concentrated towards the horizontal boundary, and the cooler parts on the curve boundary. Hence, increased Darcy number causes the convection to increase across the medium as permeability is increased. The symmetric behaviour of the bolus can be observed for high number of Da in velocity profile in Fig. 7.8(d) and (e). For smaller Da the horizontal and vertical velocity are same throughout the region.

Effects of heat Generation/Absorption coefficient:

Fig. 7.9(a)-(e) illustrates the absorption coefficient and Fig. 7.9(f)-(i) depicts the internal heat generation coefficient effect on isotherms. The heat transfer is significantly increased in the molecular composition of the fluid with increasing of internal heat inside the cavity. One can see that for $Q = -10^3$ the heat absorption is exceptionally low causing cooler patches within the fluid, however the value of Q increases, it is obvious to observe that the internal heat generation is significantly increased within the domain. As increasing Q we see a gradual convection of heat from the vertical boundary into the clockwise spiral notion towards the center of the cross-section. Similarly, in Fig. 7.9(e)-(f) one can see a more abrupt change in heat flow as the absorption coefficient is increased and heat begins to be generated internally. For maximum value of Q, cavity is filled with heat as shown in Fig. 7.9(i). The heat transfer rate is maximum at the bottom left corner and lowest at the right corrugated wall. The fluid is revolving anti-clockwise at a high temperature, which is the physical reason for this phenomenon (higher than hot wall temperature). As a result, the hot wall's left bottom corner created a massive temperature, as depicted in Figures. Fig. 7.10(a)-(b) shows the effect of Q at temperature and Nusselt number. Temperature gradient inside the cavity increases with the increase in Q. For smaller value of Q internal heat is reduced inside the cavity, which almost approaches to zero due to absorption. Heat transfer rate at horizontal mean position decreases with the increasing Q in Fig. 7.10(b).

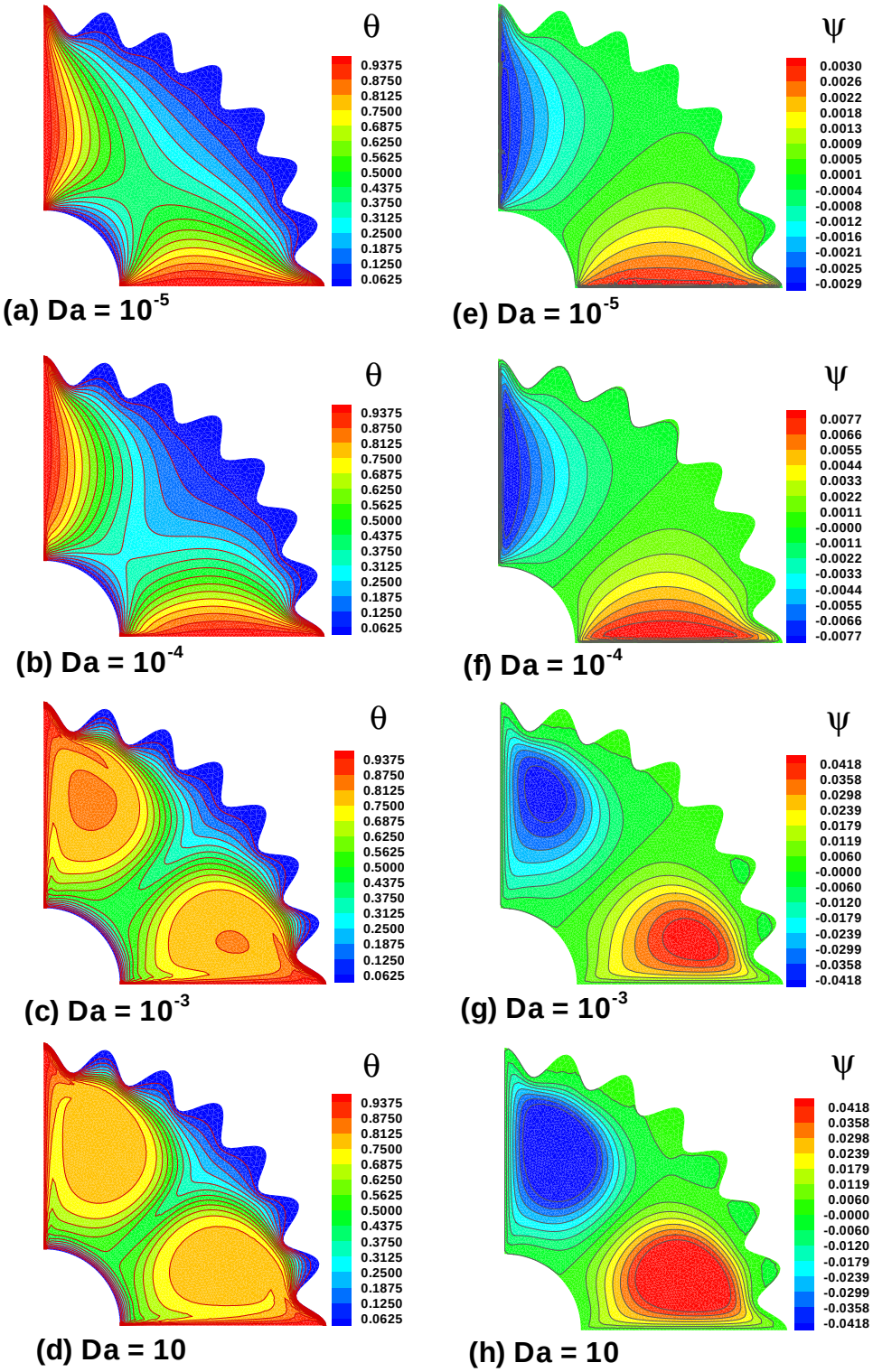

Figure 7.7: Effects of Darcy number on isotherms (a)-(d) and streamline (e)-(h)

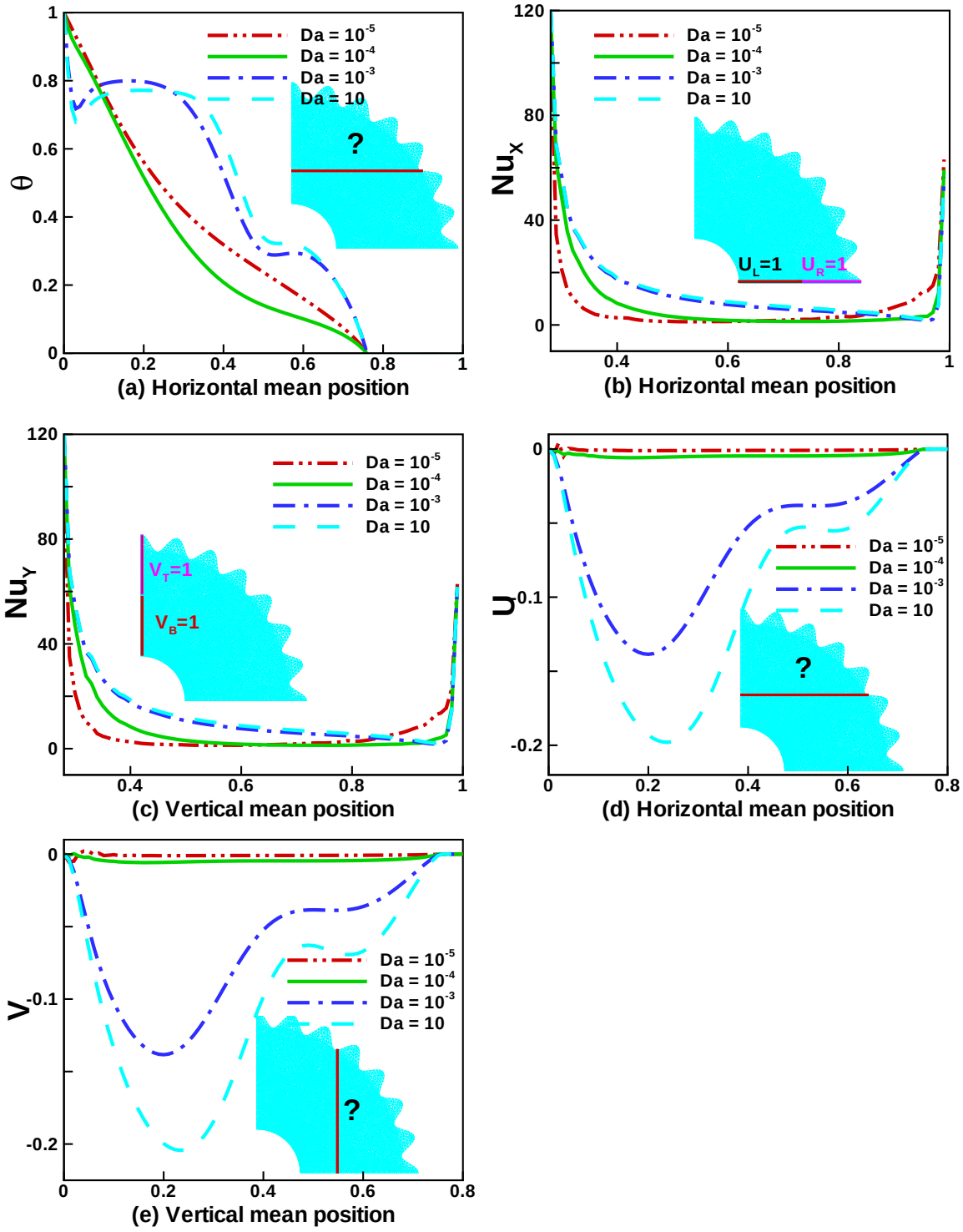

Figure 7.8: Effects of various Darcy number on the temperature, velocity profiles and Nusselt number

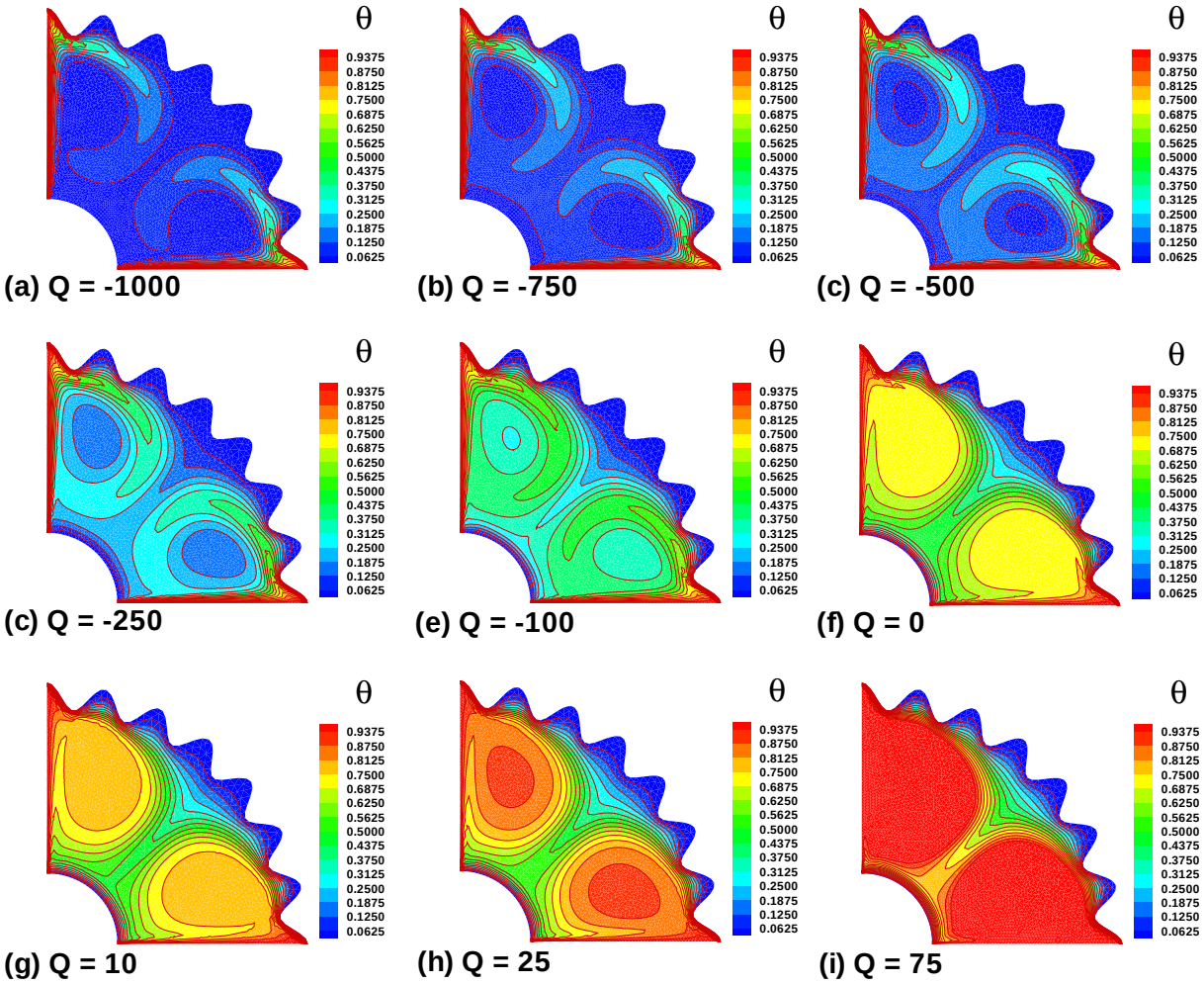

Figure 7.9: Effects of internal heat generation/absorption on isotherms (a)-(i)

Effects of concentration of the nanoparticles:

The effects of concentration of nanoparticles on isotherm and streamlines are shown in Fig. 7.11(a)-(c) and Fig. 7.11(d)-(f), respectively. The heated lines decrease with increasing of nanoparticles and the heat transfer is spirally localized near the lid wall. Hence, heat stemming is increased from the vertical and horizontal lid in Fig. 7.11(a). Where $\phi = 0.0$ although this settles as approach towards Fig. 7.11(c) where $\phi = 0.2$, and hence more cooling effect can be seen. From Fig. 7.11(d) – (f), one can see the streamlines, where the

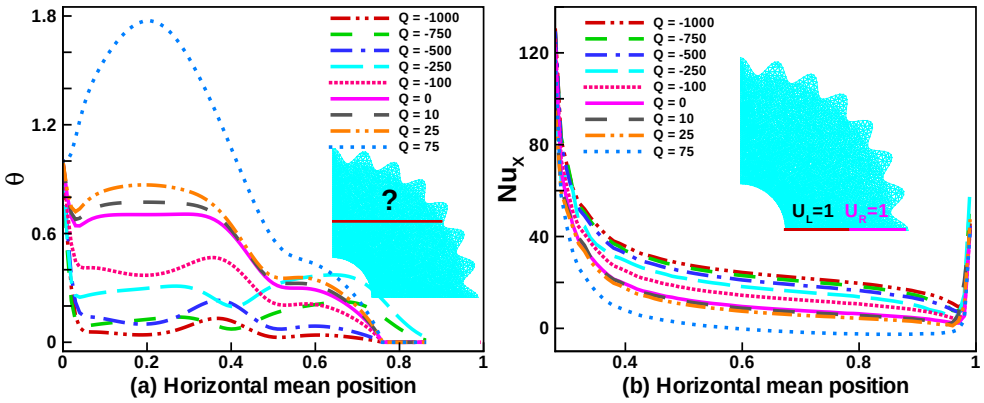

Figure 7.10: Effects of internal heat generation/absorption coefficient temperature profile and Nusselt number

localized hot and cold patches, with the cold regions being vertically dominant, and the greater heat is being more dominant at the horizontal boundary. Fig. 7.12(a)-(f) illustrates the effects of nanoparticles on the Nusselt number, temperature and both horizontal and vertical velocity profiles. For the base fluid, maximum temperature is obtained throughout the cavity. But with the increasing of nanoparticles, temperature gradient gradually decreases. Increasing concentration of solids, increases nanofluid thermal conductivity while marginally decreasing gradient of temperature. Convection in cavity increases so more heat transfer is done in cavity that is clearly seen in Fig. 7.12(b) and (c) in the form of local Nusselt number against the horizontal and vertical moving walls. Both horizontal and vertical velocity decrease at the middle of the cavity with increasing concentration of nanoparticles as shown in Fig. 7.12(d) and (e).

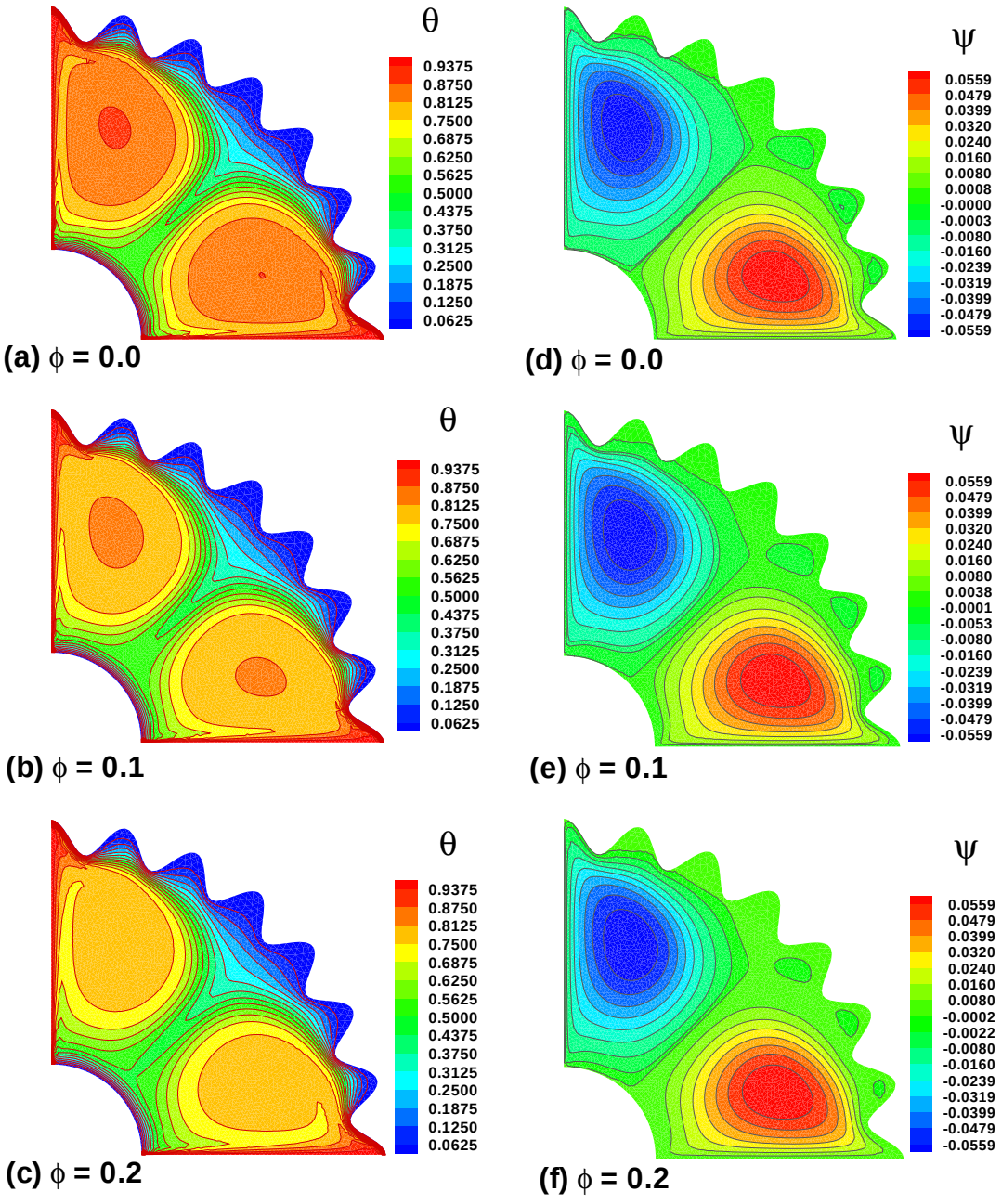

Figure 7.11: Effects of solid volume fraction of nanoparticles on isotherms (a)-(c) and streamline (d)-(f)

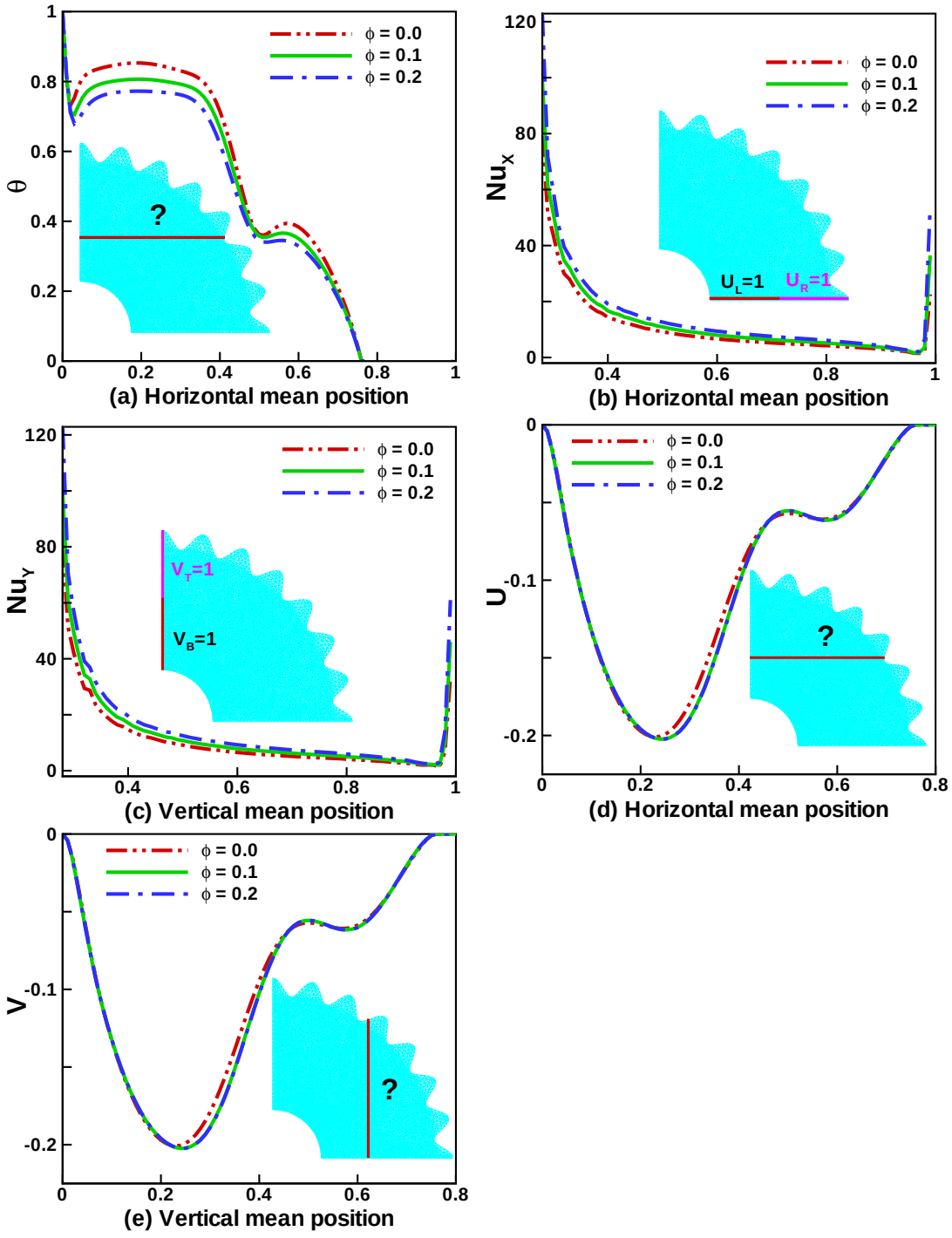

Figure 7.12: Effect of solid volume fraction of nanoparticles on the temperature, velocity profile and Nusselt number

7.4 Conclusion

After carefully examining the present model, we have developed the conclusion that describes the key factor of entire study. As defined in the model that current model is based upon forced convection due to lid driven of left vertical and bottom horizontal walls. We have discussed the different direction of moving lid, then we analyze the model for various value of Reynolds number, Richardson number, heat generation parameter, porous medium and nanoparticle volume fraction. Following are the key findings of present model:

- In isotherms, the opposing directional (inside) movement of the lid walls generate more heat inside the cavity.
- In streamlines, the opposite directions of velocity produce more eddies than the velocity in the same direction.
- The effects of velocities (in opposite outward direction) yields the maximum flow of heat transfer at the mean position from where it acts like a symmetric behaviour in local Nusselt number.
- Increase in Reynolds number has caused an increase in isotherm lines and this effect on streamline causes the eddies movement towards center. Maximum velocity is observed in both ends of the cavity and minimum in the middle with greater Reynolds number.
- An increase in permeability region decreases the heat generation near the lid walls and pushes it away from the lid wall.
- For the minimum value of Q, heat is absorbed in the cavity and restricted to the lid walls whereas there is maximum heat generator in the cavity for greater value of $Q = 75$. Local Nusselt number decreases with an increase in heat absorption coefficient.

CHAPTER 8

MIXED CONVECTION ANALYSIS IN A SPLIT LID-DRIVEN TRAPEZOIDAL CAVITY HAVING ELLIPTIC SHAPED OBSTACLE

8.1 Introduction

Various physical processes, such as fluid mixing, heat transfer, and chemical reactions, can be carried out in a split lid driven trapezoidal cavity. Because it produces vortices and recirculation zones, the trapezoidal cavity's unique shape enhances fluid mixing. Chemical engineers can also employ split lid driven trapezoidal cavity to increase the effectiveness of chemical processes. As a result of improved mass transfer and reactant mixing made possible by the formation of vortices and recirculation zones in the trapezoidal cavity, chemical processes' yield and selectivity can be greatly increased. In this chapter, thermal performance of nanofluid enclosed by a split lid-driven trapezoidal cavity is presented that comprises elliptic shaped obstacle. Bottom wall maintained the constant temperature (cold) and slant walls are considered as insulated (adiabatic). Energy is transferred through top horizontal wall of the cavity and driven from split lid walls which are moving with constant velocities. Finite element method is applied to handle the dimensionless system of partial differential equations for velocity, temperature and concentration. The impact of emerging parameters such as: Richardson number ($10^{-2} \leq Ri \leq 10$), Lewis

number ($0.1 \leq Le \leq 10$), Reynolds number ($300 \leq Re \leq 500$) and buoyancy ratio ($-10 \leq Br \leq 10$) for different directional velocities, temperature and concentration profiles are analysed. To determine the heat transfer rate due to forced convection is manipulated local Nusselt number along the heating surface. Graphical interpretation of these profiles represent that Lewis number has significant impact at isotherms and concentration. For smaller value of buoyancy ratio parameter, maximum heat transfer is obtained inside the direction of lid walls. Lewis number proves the dominant effects at isotherms and concentrations due to high thermal diffusion in the entire domain of the cavity.

Table 8.1: A table demonstrating the contrasts between the approaches being offered

Authors	Enclosure	Obstacle	Method	Lid driven
Hussain *et al.* [20]	Square	No	FEM	Double
Sheikholeslami *et al.* [21]	Curved	No	CVFEM	Single
Alleborn *et al.* [35]	Rectangular	No	FDM	Single
Haq *et al.* [77]	Corrugated	No	FEM	Double
Present	Trapezoidal	Elliptic	FEM	Split

8.2 Problem Formulation

The trapezoidal shape cavity is displayed in Fig. 8.1 with inner elliptic obstacle. It has a length of L and a length of $0.4L$ on its lower wall. The inclined walls of the enclosure are kept insulated. The top wall splits partially

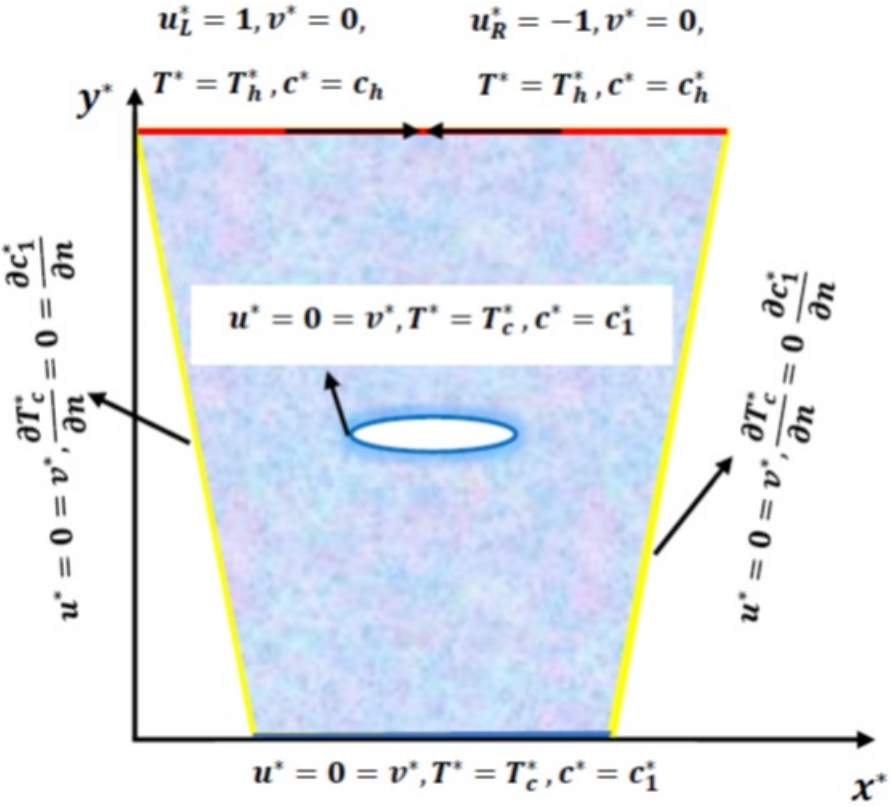

Figure 8.1: Physical domain of partial lid driven trapezoidal cavity

and moves with different velocities from left to right and right to left. The top wall retains the steady temperature T_h^* and concentration c_h^*. The inner elliptical obstacle is considered as cold throughout the numerical investigation. With the exception of the density fluctuations in the buoyancy conditions. If the Boussinesq approximation is used in the following way, all the thermo-physical properties of the fluid are assumed constant.

$$\rho = \rho_o[1 - \beta_{T^*}(T^* - T_c^*) + \beta_{c^*}(c^* - c_1^*)], \tag{8.1}$$

where ρ_o represents the mean density, the mean temperature and concentration of $T_0^* = (T_h^* + T_c^*)/2$ and $c_0^* = (c_h^* + c_1^*)/2$, respectively. β_{T^*} and β_{c^*} be the coefficient of thermal and solutal expansion, respectively.

8.2.1 Mathematical Model

For the steady, laminar, two-dimensional lid-driven heat and mass flow, the established equations of mass, momentum, energy and species concentrations are as follow:

$$\nabla \cdot \mathbf{V}^* = 0, \tag{8.2}$$

$$\mathbf{V}^* \cdot \nabla u^* = -\frac{1}{\rho}\frac{\partial p^*}{\partial x^*} + \nu \nabla^2 u^*, \tag{8.3}$$

$$\mathbf{V}^* \cdot \nabla v^* = -\frac{1}{\rho}\frac{\partial p^*}{\partial y^*} + \nu \nabla^2 v^* + g[\beta_{T^*}(T^* - T_c^*) + \beta_{c^*}(c^* - c_1^*)], \tag{8.4}$$

$$\mathbf{V}^* \cdot \nabla T^* = \alpha \nabla^2 T^*, \tag{8.5}$$

$$\mathbf{V}^* \cdot \nabla c^* = D \nabla^2 c^*. \tag{8.6}$$

In the above equations, $\mathbf{V}^* = (u^*, v^*, 0)$ and $\nabla = \left(\frac{\partial}{\partial x^*}, \frac{\partial}{\partial y^*}\right)$ represent the velocity field and nabla operator for two dimensional fluid flow. ρ and ν are the density and kinematic viscosity of the fluid, respectively. Moreover, T^* the temperature, p^* pressure, c^* the concentration, g the gravitational acceleration, α the thermal diffusivity and D the mass diffusivity are represented in above equations.

By replacing the main parameters with their related dimensionless variables that are specified below, the model Eqs. (8.2)–(8.6) can be modified to their dimensionless forms.

$$(X, Y) = \left(\frac{x^*}{L}, \frac{y^*}{L}\right), \quad (U, V) = \left(\frac{u^*}{u_o}, \frac{v^*}{u_o}\right), T^* = T_c^* + (T_h^* - T_c^*)\,\theta,$$
$$P = \frac{p^*}{\rho u_o^2}, \quad c^* = c_1^* + (c_h^* - c_1^*)\,C, \tag{8.7}$$

$$\frac{\partial U}{\partial X} + \frac{\partial V}{\partial Y} = 0, \tag{8.8}$$

$$V\frac{\partial U}{\partial Y} + U\frac{\partial U}{\partial X} = -\frac{\partial P}{\partial X} + \frac{1}{Re}\left(\frac{\partial^2 U}{\partial Y^2} + \frac{\partial^2 U}{\partial X^2}\right), \tag{8.9}$$

$$V\frac{\partial V}{\partial Y} + U\frac{\partial V}{\partial X} = -\frac{\partial P}{\partial Y} + \frac{1}{Re}\left(\frac{\partial^2 V}{\partial Y^2} + \frac{\partial^2 V}{\partial X^2}\right) + Ri(\theta + BrC), \tag{8.10}$$

$$V\frac{\partial \theta}{\partial Y} + U\frac{\partial \theta}{\partial X} = \left(\frac{1}{RePr}\right)\left(\frac{\partial^2 \theta}{\partial Y^2} + \frac{\partial^2 \theta}{\partial X^2}\right), \tag{8.11}$$

$$V\frac{\partial C}{\partial Y}+U\frac{\partial C}{\partial X}=\left(\frac{1}{RePrLe}\right)\left(\frac{\partial^2 C}{\partial Y^2}+\frac{\partial^2 C}{\partial X^2}\right), \tag{8.12}$$

where the evolving physical parameters are Reynolds number (Re), Richardson number (Ri), Lewis number (Le), Prandtl number (Pr) and the buoyancy ratio (Br) are defined as follows:

$$\begin{aligned} Re=\frac{u_o L}{\nu},\quad Ri=\frac{g\beta_{T^*}(T_h^*-T_c^*)L^3}{\nu^2 Re^2},\\ Le=\frac{\alpha}{D},\ Pr=\frac{\nu}{\alpha},\quad Br=\frac{\beta_{c^*}(c_h^*-c_1)}{\beta_{T^*}(T_h^*-T_c^*)}. \end{aligned} \tag{8.13}$$

The dimensionless boundary conditions to the corresponding Eqs. (8.8)–(8.12) are as follows;

***At bottom wall*(Ω_1):**

$$(U,V)=(0,0),\ \theta=0=C. \tag{8.14}$$

***At inclined wall*(Ω_2 and Ω_5):**

$$(U,V)=(0,0),\ \frac{\partial\theta}{\partial n}=0=\frac{\partial C}{\partial n}. \tag{8.15}$$

***At top left part of wall*(Ω_3):**

$$(U,V)=(-1,0),\ \theta=1=C. \tag{8.16}$$

***At top right part of wall*(Ω_4):**

$$(U,V)=(1,0),\ \theta=1=C. \tag{8.17}$$

***At the surface of inner obstacle*(Ω_6):**

$$(U,V)=(0,0),\ \text{and}\ \theta=0=C. \tag{8.18}$$

The local Nusselt number is determined using the above equations for the heat transfer rate calculation.

$$Nu=-\left(\frac{\partial\theta}{\partial Y}\right)_{Y=0}. \tag{8.19}$$

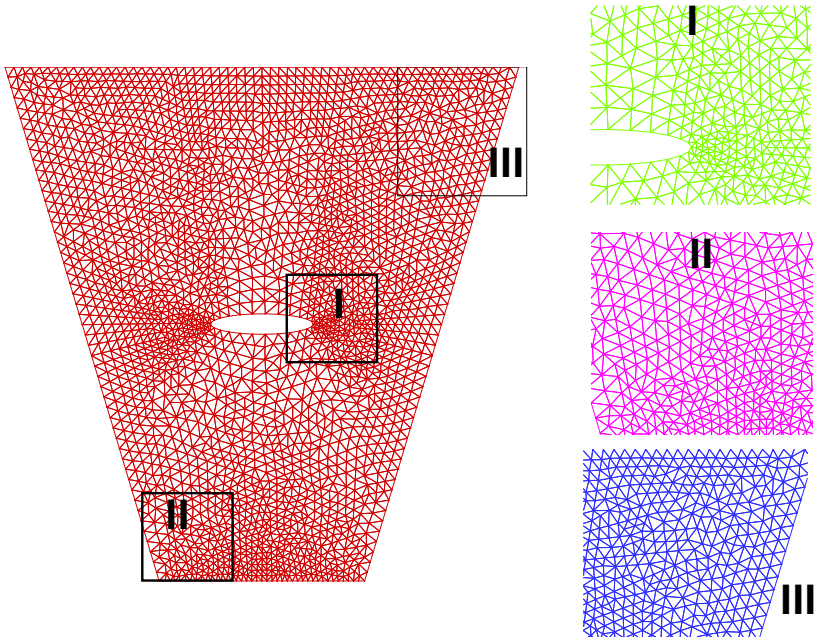

Figure 8.2: Optimizing mesh at various places of the cavity

The following equations are used to measure the average Nusselt and Sherwood numbers along the heat and mass source on the top split wall:

$$Nu_{avg} = \frac{1}{0.5}\int_{\Omega_3}\left(-\frac{\partial\theta}{\partial Y}\right)_{Y=0} dX, \tag{8.20}$$

$$Sh_{avg} = \frac{1}{0.5}\int_{\Omega_3}\left(-\frac{\partial C}{\partial Y}\right)_{Y=0} dX. \tag{8.21}$$

8.3 Numerical Procedure

The governed dimensionless equations along the boundary conditions are solved by Galerkin weighted residual finite element formulation as discussed in chapter 3. We formalize the FEM penalty in order to acquire the numerical solutions of equations.

8.3.1 Mesh Analysis

Mesh analysis at different vertices corners of the enclosure are established in Fig. 8.2. A mesh study of the lid trapezoidal cavity was shown in Fig.

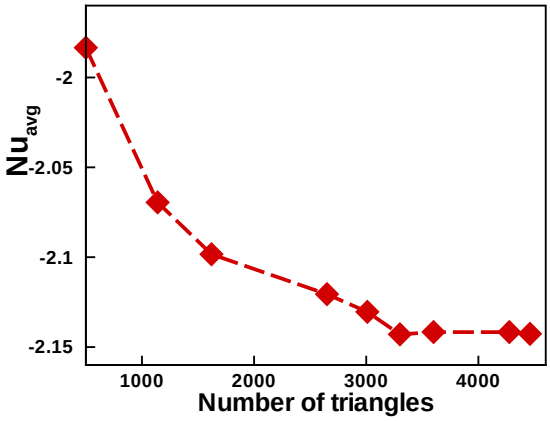

Figure 8.3: Optimizing mesh at various places of the cavity

8.3 against of average Nusselt number. The mesh quantity of convergence was examined against the average Nusselt number. For various numbers of meshes on different walls have been executed, until the repetitive Nusselt number is reached, these are selected as experiment.

8.4 Results and Discussion

The flow structure and temperature profile for the different values of Richardson number ($0.01 \leq Ri \leq 10$), direction of partial lid walls, Reynolds number ($100 \leq Re \leq 500$), Lewis number ($0.1 \leq Le \leq 10$) and buoyancy ratio parameter ($-10 \leq Br \leq 10$) within the partially lid-driven trapezoidal cavity have been analysed numerically in this chapter. In numerical analysis, the Prandtl number ($Pr = 0.71$) and the cold elliptic obstacle are set during the execution.

Effects of Richardson number:

Fig. 8.4(a-f) demonstrate the effects of variation of the Ri on the streamline and isotherms. A small recirculating cell is present in the trapezoidal enclosure for small Richardson number ($Ri = 0.01$) and the heat transfer between the lid walls and elliptic obstacle is medicated by heat conduction and

this is due to the mechanical influence of the forced convection. For small value of Ri, recirculation cells are maximum near the lid wall and gradually recirculation cells move to the lower wall. Fig. 8.4(b) displays temperature field aligned with the opposite configuration. As Ri rise, the isotherms also rises due to the forced convection as the main transport mechanism and some small recirculation non-uniform cells are observed within the cavity. Fig. 8.4(c) illustrates the effect of Ri on concentration field. Concentration ratio decreases with the increase in Richardson number inside of cavity. Heat flow near the lid wall is recorded maximum. Due to forced convection, significance of forced convection mass transfer in cavity is recorded in the form of heat.

Fig. 8.5(a) illustrates that horizontal temperature increases with increase in Ri on the left region of the cavity because the left partial half of the wall moves outside, where the velocity in (0.15–0.4) region increases. Contrary to this, the velocity in the remaining region (0.6–0.85) decreases due to the opposite movement of the left partial half of the wall. Fig. 8.5(b) represents the temperature profile w.r.t. various Ri. For the forced convection, maximum temperature is recorded and it gradually decreases when natural convection is dominated in the cavity. Similar behaviour is depicted in Fig. 8.5(c) for the concentration profile. Fig. 8.5(d) shows that the local Nusselt number increases with the increase in Ri. Since, both the partial lid-wall moves with the opposite velocity to each other, the heat transfer rate increases in partial halves.

Effects of various directional velocities of lid walls:

Fig. 8.6(a-d) depicts the streamlines profile against the different directional velocity of the partial lid-wall. Streamlines increase while the lid-wall moves to the left Fig. 8.6(d) and same behaviour is observed for the lid-wall that moves to the right Fig. 8.6(a). In Fig. 8.6(b), the outward movement of the lid wall reduces the streamlines whereas, in Fig. 8.6(c), we observe a record number of streamlines by the internal movement of the partial lid-wall.

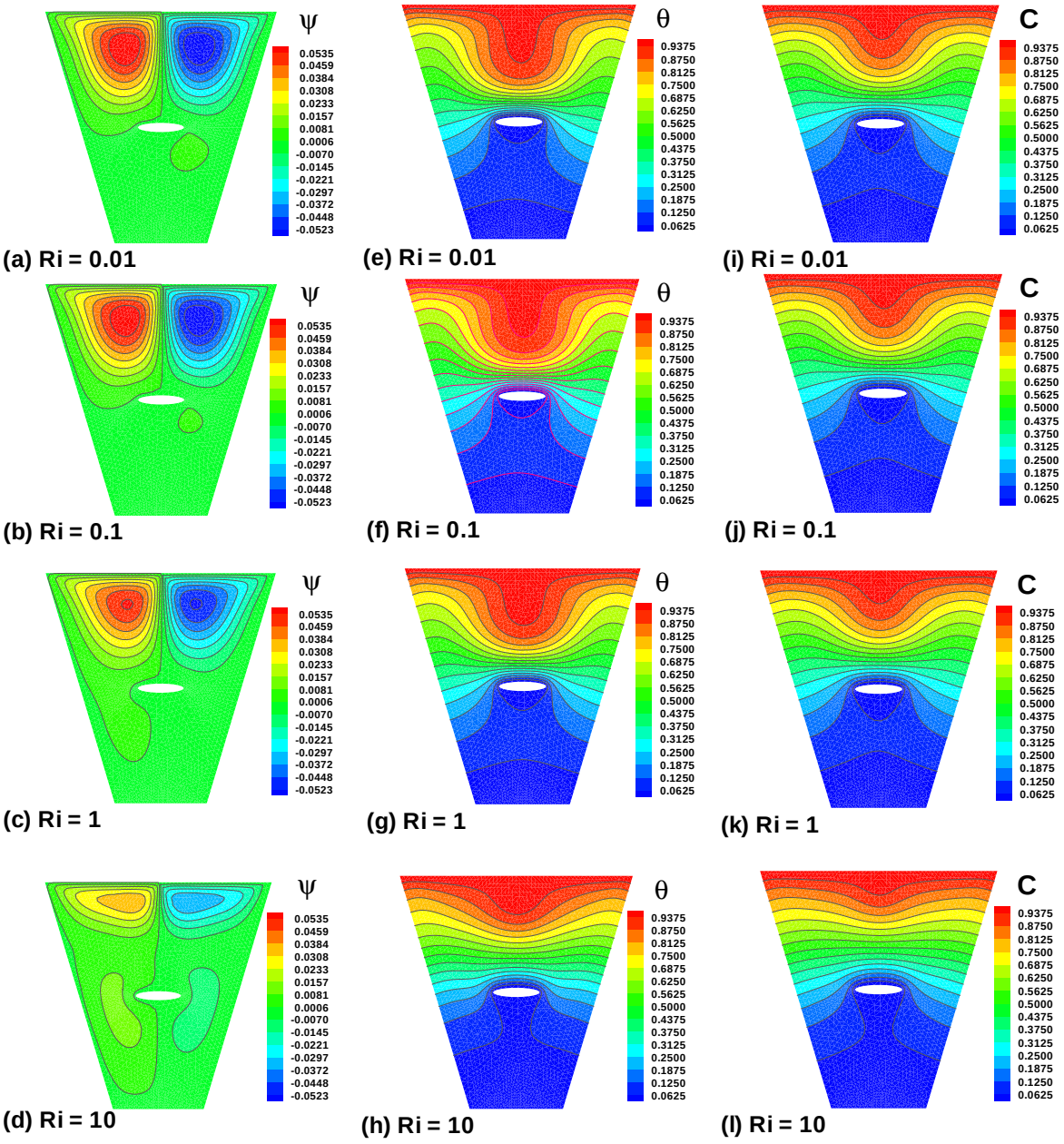

Figure 8.4: Variation of (a-d) streamlines, (e-h) isotherms and (i-l) concentration with respect to Ri when $Re = 10^2$, $Br = 1$, and $Le = 0.5$ for cold elliptic obstacle

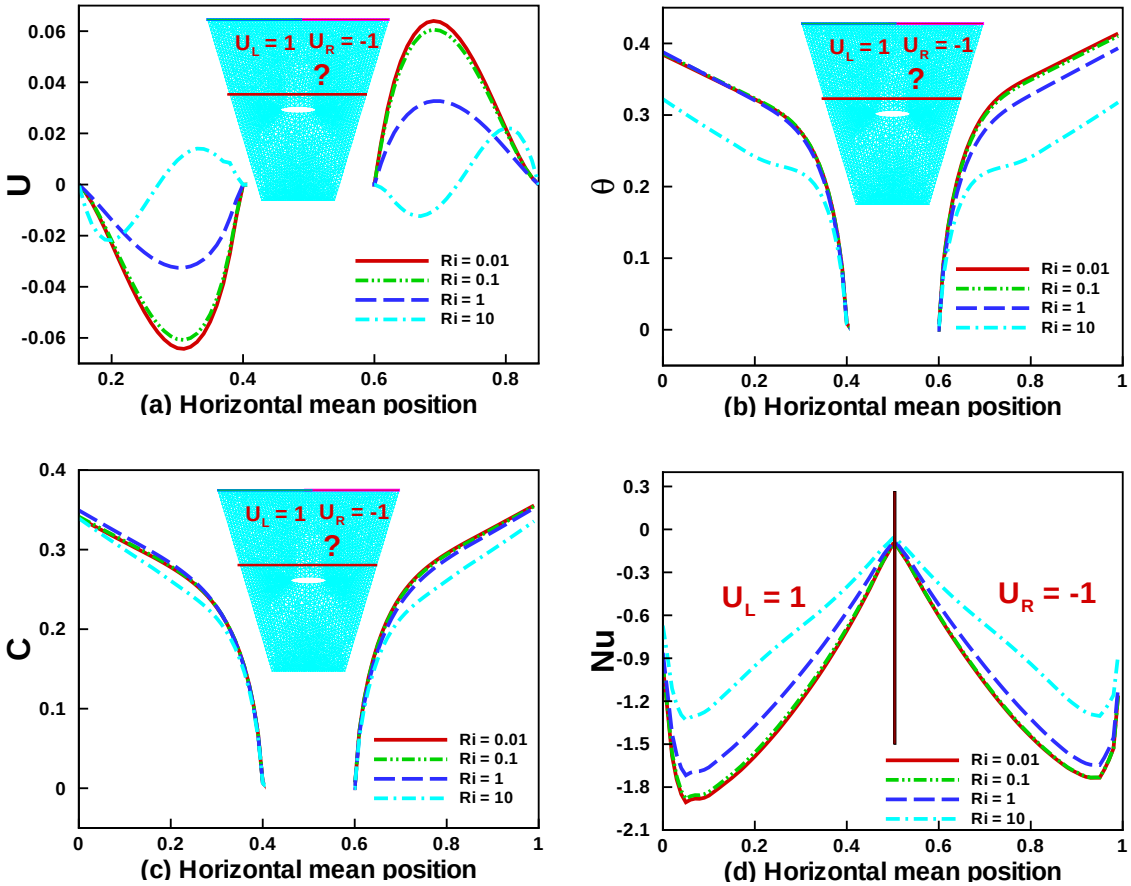

Figure 8.5: Variation of (a) horizontal velocity, (b) temperature, (c) concentration(d) local Nusselt number with respect to *Ri* for cold elliptical obstacle

Fig. 8.6(e-h) and Fig. 8.6(i-l) illustrate the isotherms and iso-concentration profile, respectively. Maximum heat is observed along the same direction of velocity of partial lid wall in Fig. 8.6(e and h). In the opposite direction of the velocity of partial lid-walls, two different nature of heat are seen. When both the partial lid-walls move in opposite direction (outward), maximum heat transfer is developed in the corner lid walls whereas in the opposite (inward) direction of lid-walls, the maximum heat transfer is found in the centre of the lid-walls as shown in Fig. 8.6(f and g). Similar behaviour is observed for the mass transfer profile as depicted in Fig. 8.6(i-l).

Fig. 8.7(a) shows the horizontal velocity against the different directional of the partial lid-walls. The region (0.15–0.3) illustrates the decrease in velocity with the same direction and opposite (inward) direction of lid-walls and it suddenly increases near the cold, elliptic obstacle. However, the region (0.6–0.7) shows that velocity increases with the inward direction of the lid-walls and a sudden decrease in seen near the right adiabatic inclined wall. In Fig. 8.7(b), the region (0–0.4) depicts that the temperature decreases due to the same direction of the movement of lid-walls and increases in the region (0.6–1.0). Symmetric behaviour of the temperature is observed while the lid-walls move in the opposite (outward) direction. In case of an inward direction of walls the temperature decreases on the left wall and increases on the right half wall as shown in Fig. 8.7(b). Observing the concentration profile in Fig. 8.7(c) for various direction of lid-walls, the behaviour of concentration is similar to the behaviour of temperature profile. Fig. 8.7(d) depicts the behaviour of heat rate flow of the temperature in local Nusselt number against the directions of lid-walls. The same direction of lid-walls affects the heat transform to be increasing when the walls move to the right and decreasing when the wall moves to the left. In Fig. 8.7(d), the opposite (inward) direction of lid-walls results in the maximum heat transfer at the middle of the cavity. On the contrary, the minimum heat transfer is seen at the middle of the cavity while

moving the lid-walls in opposite (outward) direction.

Effects of Lewis number:

The Lewis number is a ratio of a fluid's thermal diffusivity to its mass diffusivity. As a result, a high Lewis number indicates a low mass diffusivity value. In the ongoing inquiry, the Lewis number was varied between 0.1 and 10. Fig. 8.8 illustrates the effects of Lewis number on streamline, isotherms and iso-concentration for fixed Ri. The mass diffusion rate tends to be stratified in the vertical direction at $Le = 0.1$, with the exception of the top right corner, where the moving lid causes flow circulation. In this case, forced convection is dominated due to partial lid walls. A large bolus is developed near the lid-walls. Circular clockwise and counter clockwise rotation formed due to the opposite direction of partial lid-walls. The temperature in isotherms has no significant effects on Lewis numbers. It can be observed clearly that the wavy isotherms are formed at the top of the cavity and heat converges around the cold elliptic obstacle at the centre. In other words, as the value of Le rises, the strength of the simple mass flow patterns decreases. Furthermore, the findings show that Le appears to have a major impact on the isotherms, as shown in Fig. 8.8(e-h). Fig. 8.8(i-l) depicts the iso-concentration at different values of Le for fixed $Ri = 0.01$. For $Le = 0.1$, the iso-concentration becomes smaller wavy at the top of cavity and with the gradual increase in Lewis number, the fluid becomes thicker in the middle and higher mass transfer is observed for the maximum value of $Le = 10$ which occurs due to the higher mass diffusivity. Thinner solutal boundary layers cluster underneath the hot lid and above the cold floor, indicating a significant increase in mass transfer rate. This is further shown by the fact that Le has been raised to a value of 10 (dominant mass transfer regime).

Fig. 8.9(a-d) represent the effects of Lewis number on horizontal velocity, temperature, concentration and Nusselt number. Horizontal velocity decreases in the region (0.15–0.3) and suddenly increases to zero at the centre

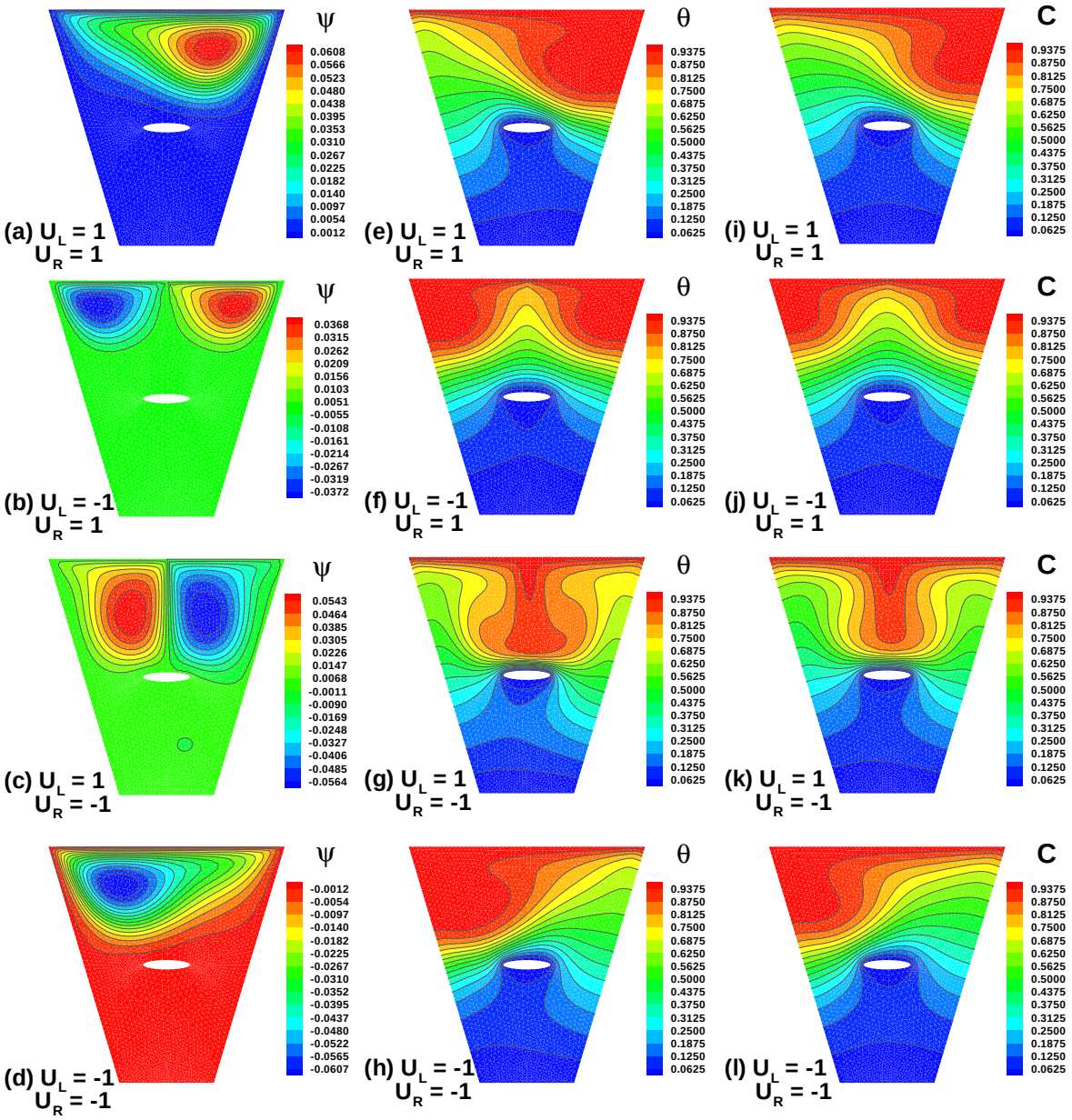

Figure 8.6: Variation of (a-d) streamlines, (e-h) isotherms and (i-l) concentration with respect to various directional velocity of lid-walls when $Ri = 0.1$, $Re = 300$, $Le = 0.5$, $Br = 4$ for cold elliptic obstacle

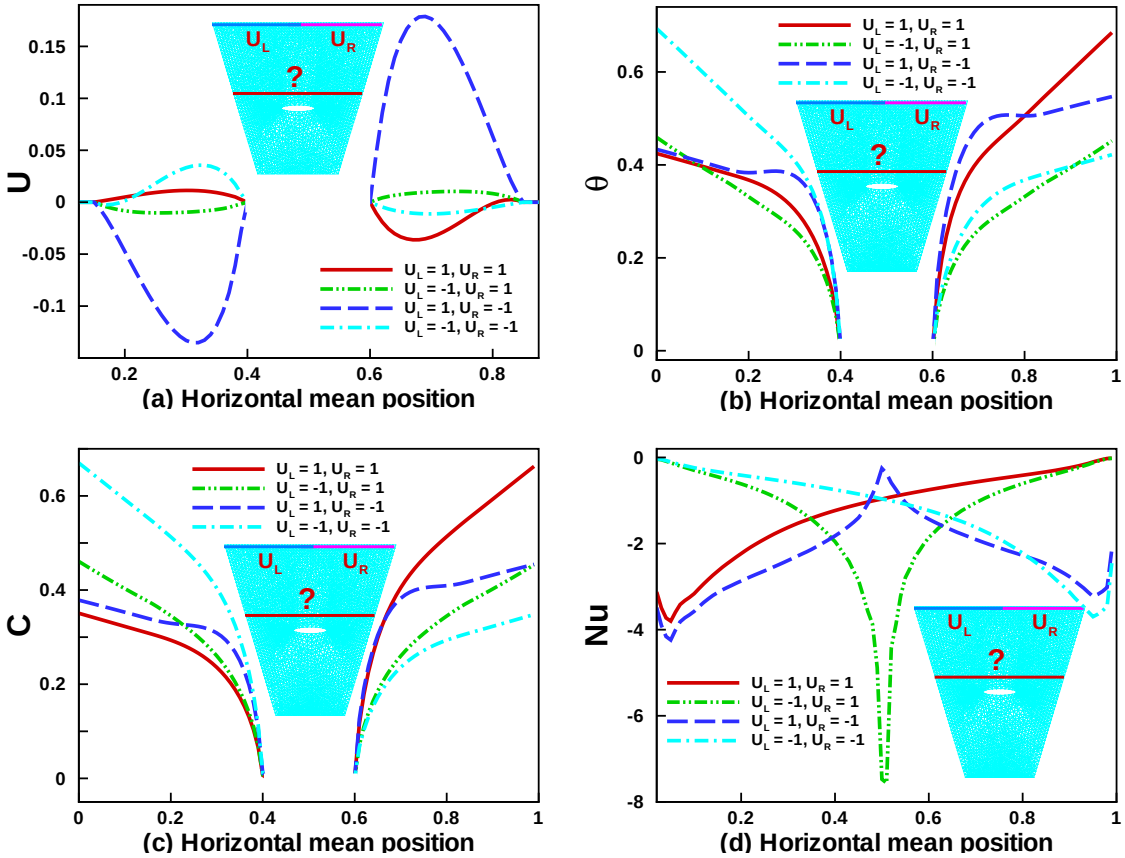

Figure 8.7: Variation of (a) horizontal velocity, (b) temperature, (c) concentration and (d) local Nusselt number with respect to various directional velocity of lid-walls for cold elliptic obstacle

due to clockwise rotation of the left partial lid-wall for increasing Le. On the same Lewis number to the horizontal velocity, the converse behaviour is seen in the region (0.6–0.85) because of the counter-clock rotation of right lid wall. In Fig. 8.9(b), the increasing behaviour of temperature on top left side of the cavity has been demonstrated with the increase in Le and inverse behaviour is observed on the top right side of the cavity for the same values of Lewis number. In Fig. 8.9(c), the effects of Lewis number on iso-concentration profile its horizontal mean position is illustrated that the concentration increases at the mean position with the increase in Le due to thermal diffusivity and this behaviour is observed on both the moving partial lid-walls. In Fig. 8.9(d), the heat transfer is slightly increasing with the increase in Lewis number while moving the left partial lid wall towards right. On the moving of the right partial lid wall towards left, the obvious decrease in the heat transfer has been observed with the same values of Le.

Effects of Reynolds Number:

Fig. 8.10(a-c) depict the effects of Reynolds number on streamlines. For $Re = 300$, small circular vortex rotation is created near the lid-wall. With increase in Re, vortex rotation size increases and is quite stable and symmetric for higher values of Reynolds number. Temperature in the form of isotherms is observed in cavity with the increase in Re. For various values of Reynolds number, the left partial wall moves to the right and right partial wall moves to the left. In other words, direction of lid walls is opposite inward. Due to inward direction of lid-walls, maximum heat is recorded at the centre of cavity and decreases at the end of walls as shown in Fig. 8.10(d-f). The streamline patterns depict a primary clockwise recirculating cell that is mostly caused by the moving lid and takes up the majority of the cavity volume. The flow characteristics are caused by the mechanical or shear effect of the moving top lid at the wall, which overcomes the buoyancy force. Fig. 8.10(g-i) represents the iso-concentration profile with variations of Re in cavity, smaller lines are

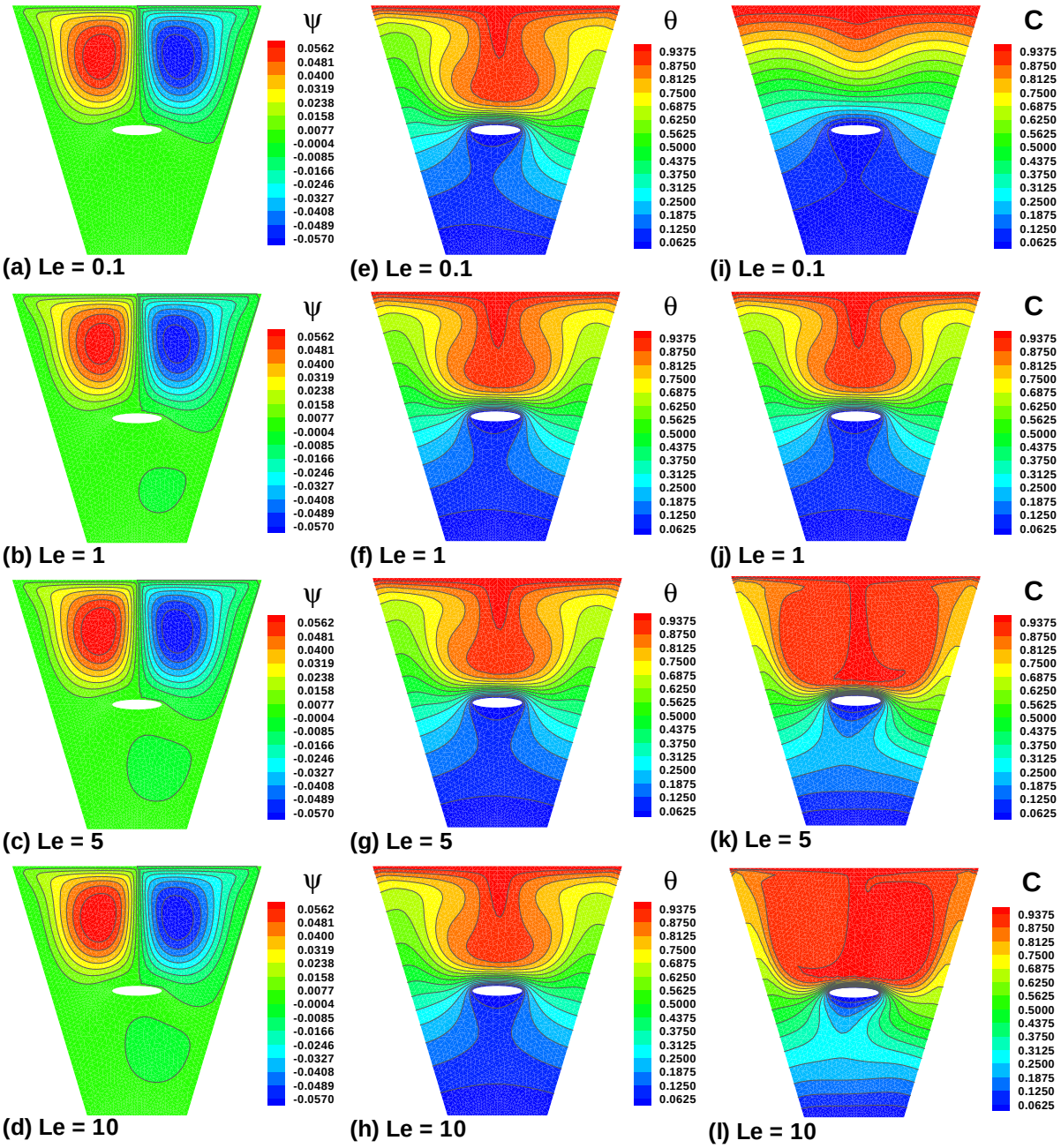

Figure 8.8: Variation of (a-d) streamline, (e-h) isotherms and (i-l) concentration with respect to Le when $Re = 200$, $Ri = 0.1$, $Br = 4$ for cold elliptic obstacle

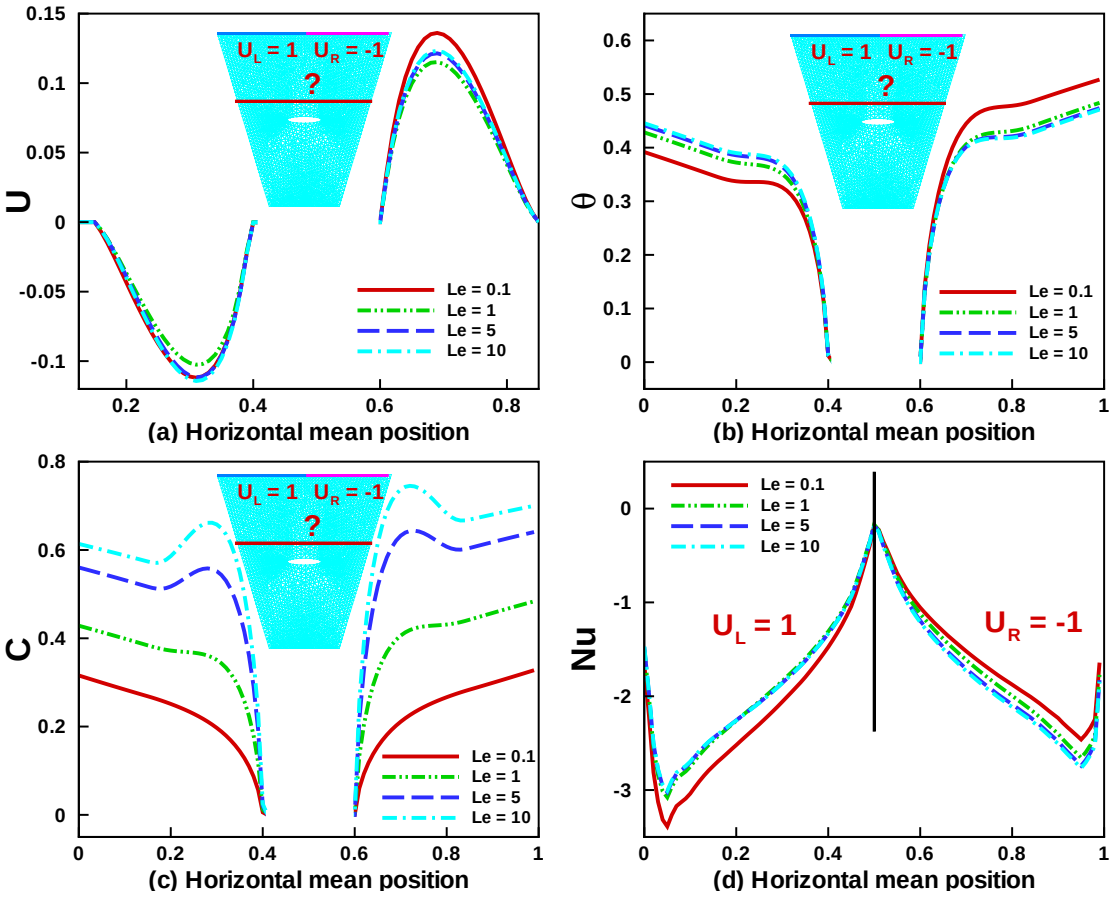

Figure 8.9: Variation of (a) horizontal velocity, (b) vertical velocity, (c) temperature and (d) local Nusselt number with respect to ϕ for cold cylindrical obstacle

observed. The wavy heated lines increase with increase in Reynolds number.

Fig. 8.11(a-d) shows the effect of Re on horizontal velocity, temperature and concentration profile and local Nusselt number at the mean position. Horizontal velocity increases on the left side of the cavity due to maximum heat flow with increase in Re, and decreases at right face of cavity with increasing of Reynolds number. Temperature profile for different values of Reynolds number illustrates that heat production at left side is minimum and increases on right side due to opposite inward direction of partial lid walls. Forced convection is dominated near the left lid-wall so maximum heat is developed near the walls but conversely near the right phase of lid. Similar effect is observed in Fig. 8.11(c) for concentration profile. Fig. 8.11(d) represents the heat transfer rate for different Re. Phase of heat transfer in cavity is not symmetric due to opposite directional velocity of top walls. Maximum heat transfer is depicted in middle of cavity for small values of Reynolds number due to inward direction of lid walls.

Effects of Buoyancy ratio:

Fig. 8.12(a-d) demonstrate the effects of Br on the streamlines in which the boundary layer thickness decreases with the increase in Buoyancy ratio and circular vortex of the streamline decreases on the both of the partial partial lid-walls. The strength of flow circulation is observed to increase as the buoyancy ratio increases. Fig. 8.12 depicts the influence of the buoyancy ratio on the isotherms (e-h). The isotherm values increase marginally as the buoyancy ratio increases. Fig. 8.12 demonstrates the iso-concentration contours for various Br values (i-l). The concentration lines are horizontal at the top surfaces of the cavity and vertical in the region. The concentration boundary layers at the right and left parts of the split walls are deformed as the Br value is increased. A concentration vortex appeared near the centre of the top surface as Br increased. It has also been discovered that increasing the buoyancy ratio contributes to higher concentration contour values. The

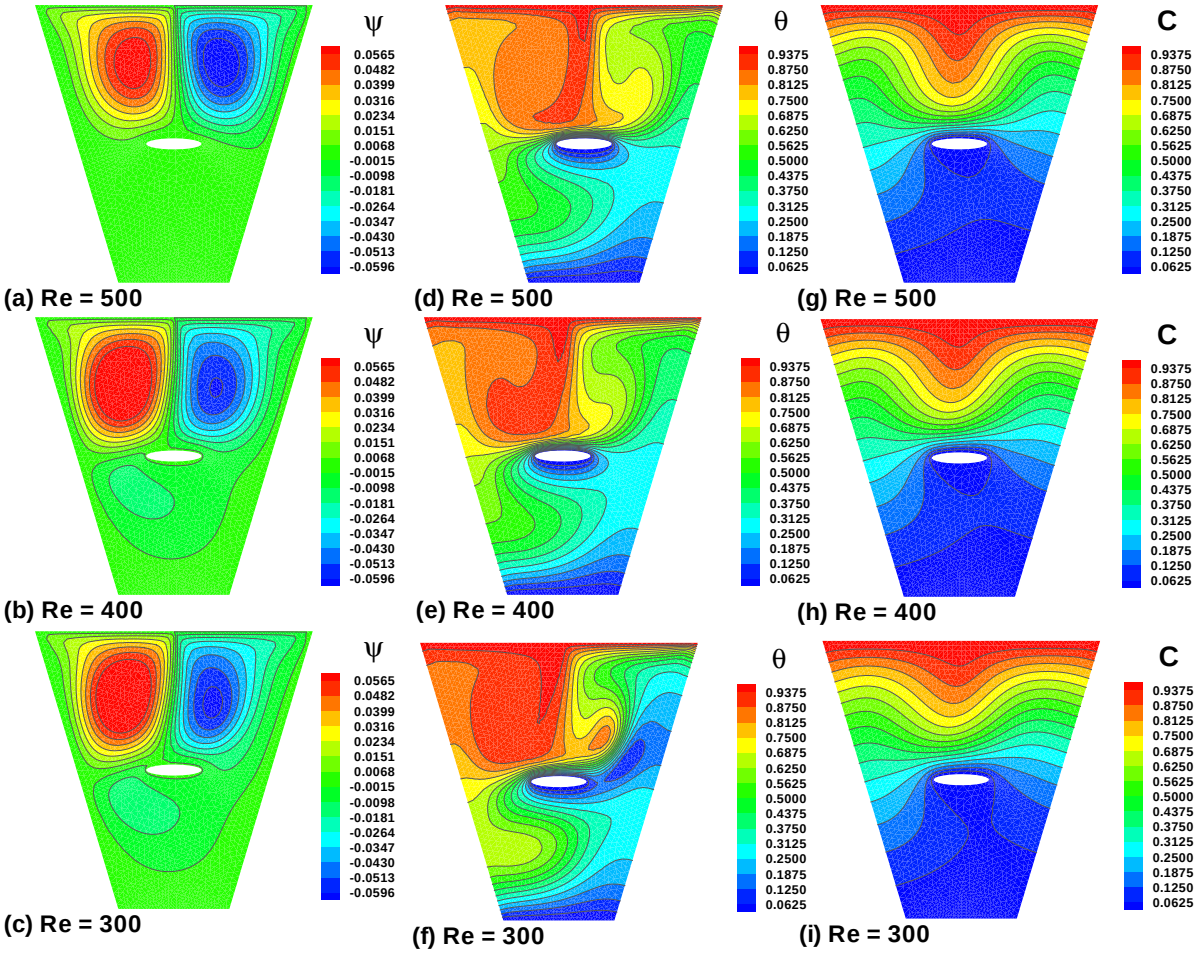

Figure 8.10: Variation of (a-c) streamline, (d-f) isotherms and (g-i) concentration with respect to Re when $Ri = 0.01$, $Le = 0.1$, $Br = 5$ for cold elliptic obstacle

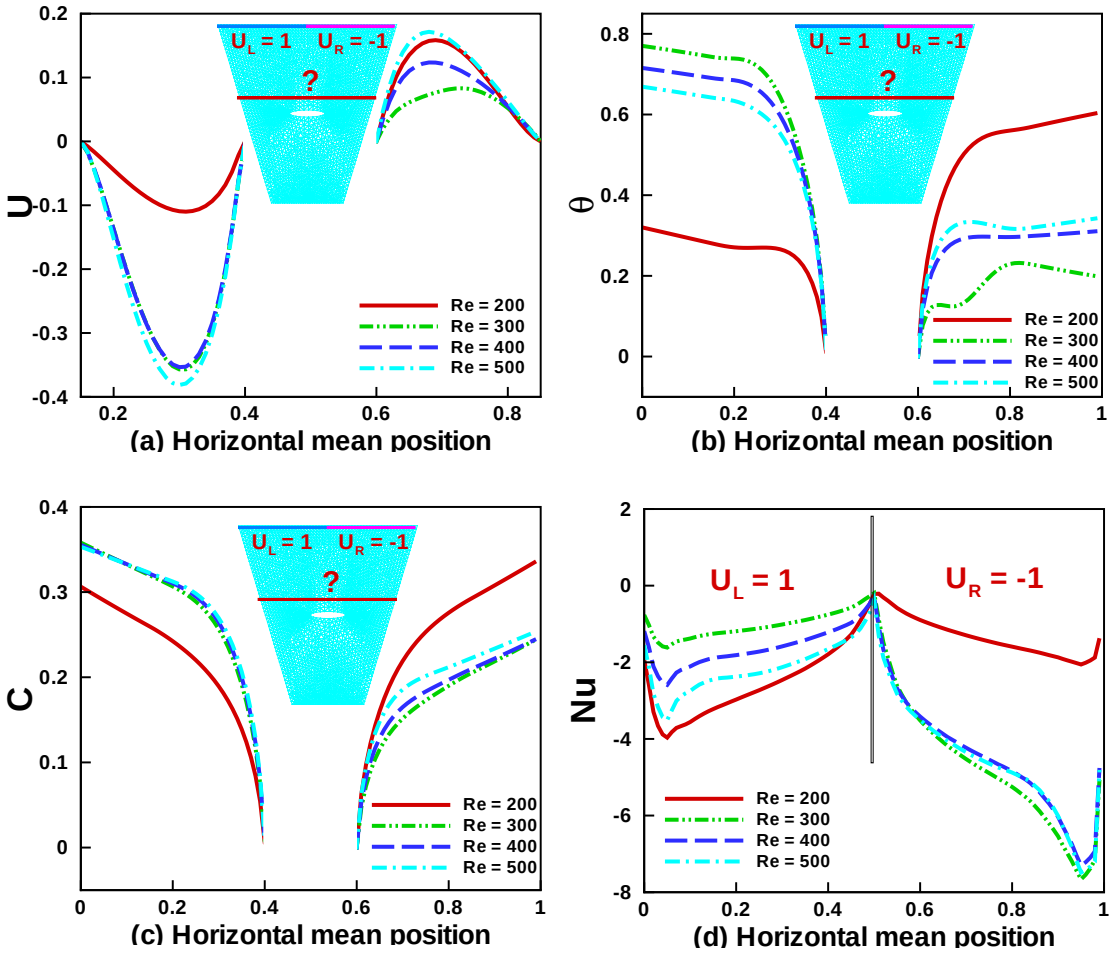

Figure 8.11: Variation of (a) horizontal velocity, (b) temperature, (c) concentration and (d) local Nusselt number with respect to *Re* for cold elliptic obstacle

iso-concentration profile shows that high mass transfer in the form of molecular movement has been recognized for $Br = 10$. Cavity near the lid walls is gradually filled due to high mixture of species particle for maximum buoyancy ratio.

In Fig. 8.13(a), the effects of Br on horizontal velocity at the mean position demonstrate the opposite behaviour of the velocity on both the partial lid-walls that is velocity increases on the left and decreases on the right partial lid wall. Conversely, the heat and mass transfer imply the behaviour of temperature and concentration as seen in Fig. 8.13(a). Fig. 8.13(d) shows the behaviour of Br on Nusselt number that increasing the Br decreases heat transfer on the left partial lid-wall and increases on the right partial lid-wall. The effect of Richardson number with variance of Reynolds number is represented in Fig. 8.14(a) on the average Nusselt number. Heat transfer increases steadily for smaller Re heat transfer and unexpectedly increases heat transfer for greater value of $Re = 300$ at smaller value of Ri while in the middle, less heat transfer is acquired. The end decreases for the highest value of the Ri Nusselt number. While the Lewis number increases, concentration and temperature increases, so heat transfer with the consequence of greater Richardson number against greater Lewis number also increases, as depicted in Fig. 8.14(b). Fig. 8.14(c) indicates that the rate of heat transfer improves with the increase in the buoyancy ratio as well as the increase in Ri. For greater value of Br, further heat transferred into cavity. Fig. 8.15 illustrates variation of the average Sherwood number with variation of Richardson number for $Pr = 0.71$ and various values of Re, Le, Br and different directional split lid movement. In Fig. 8.15(a) Sh_{avg} decreases with increasing of Re and Ri. For Re = 300, average Sherwood number increases with increase in Ri which happens due to less mass transfer with increasing of Re. The rate of mass transfer are stable for various value of Le and it slightly decreases with increase in Ri as shown in Fig. 8.15(b).

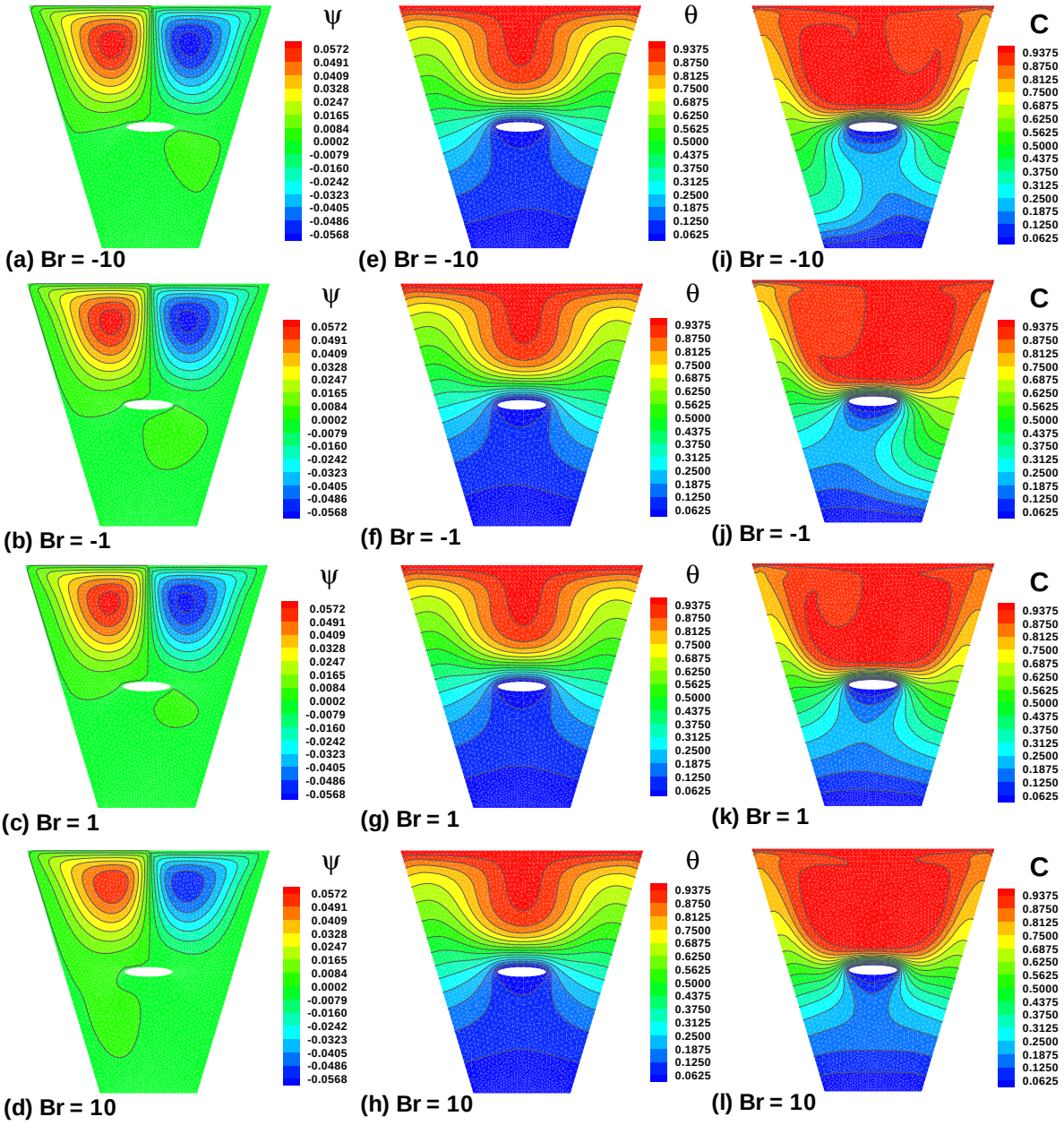

Figure 8.12: Variation of (a-c) streamline, (d-f) isotherms and (g-i) concentration with respect to Br when $Ri = 0.1$, $Re = 100$, $Le = 10$ for cold elliptic obstacle

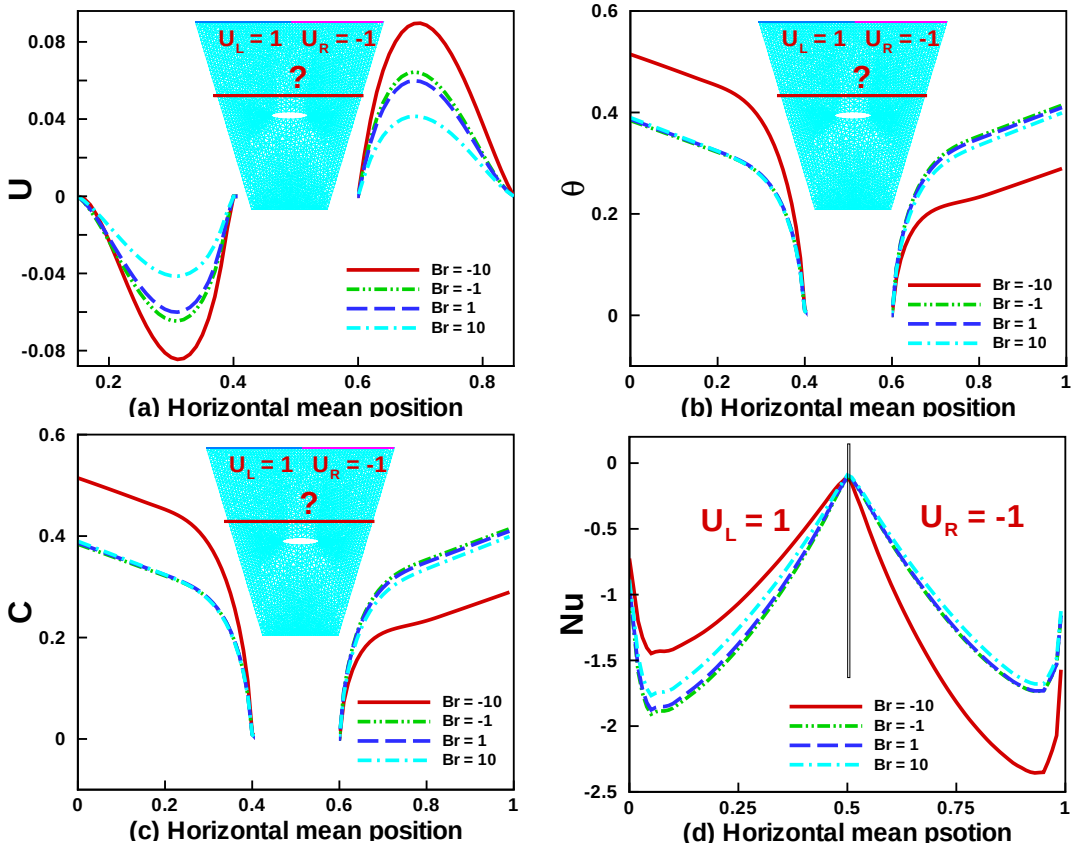

Figure 8.13: Variation of (a) horizontal velocity, (b) temperature, (c) concentration and (d) local Nusselt number with respect to Br for cold elliptic obstacle

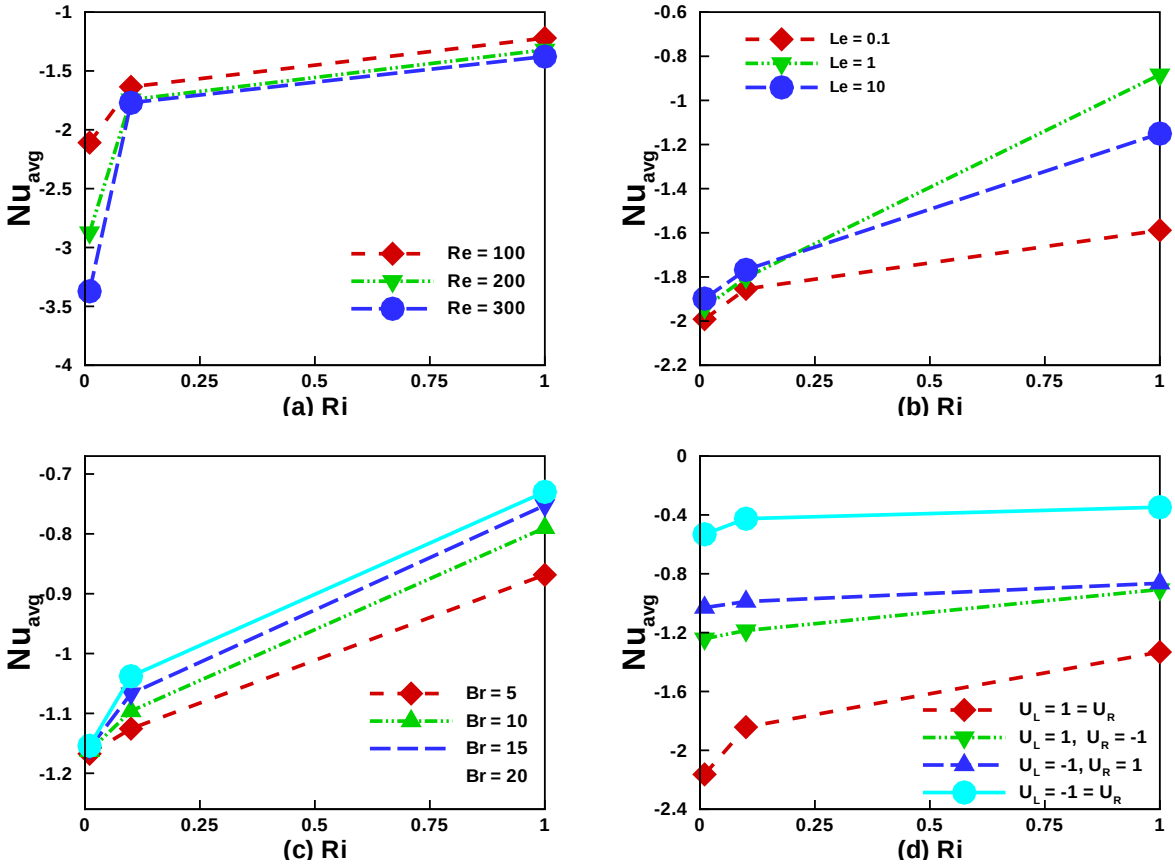

Figure 8.14: Variation of average Nusselt number with respect to the Richardson number at the different values of (a) Reynolds number (b) Lewis number (c) Buoyancy ratio (d) velocity direction

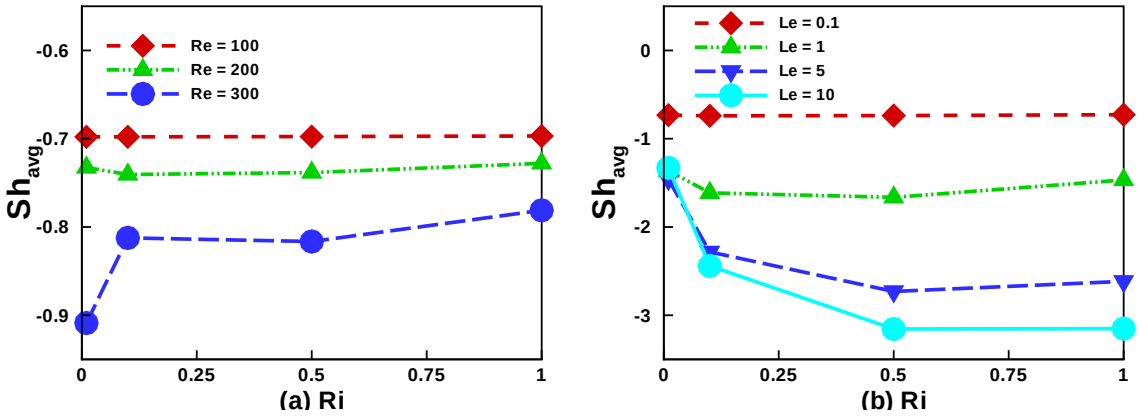

Figure 8.15: Variation of average Sherwood number with respect to the Richardson number at the different values of (a) Reynolds number (b) Lewis number

8.5 Conclusion

Forced convective heat transfer is implemented in a two-dimensional, partially lid-driven trapezoidal cavity with elliptic cold obstacle concentration. The effect on streamlines, isotherms and iso-concentration activity is taken into account by the different directional velocity of the partial lid wall. Lewis, Reynolds, Richardson numbers, and buoyancy ratio roles are shown.

- Moving partial lid walls have a larger impact on isotherms. The core of the cavity tends to have optimum streamlines in the case of opposite inner path of the lid walls.
- With velocity direction of partially lid walls, the heat and mass transfer rate has been greatly attained.
- Converse variation of Ri is observed on the horizontal velocity, temperature, concentration and local Nusselt number because of the opposite direction of the velocity on partial lid-walls.
- Mass transfer in the cavity is significantly increased with the increase

in Lewis number whereas heat transfer rate has a contrary impact of increasing and decreasing on different lid walls with the variation of Le.

- The impact of the streamlines and the isotherms has been addressed with their increasing nature. However, transfer rate of the heat in the cavity has partially been increased when the Reynolds number has increased and vice versa.

- The effect of buoyancy ratio parameter on local Nusselt number is seen that the smaller value of Br affects the increase in mass transfer in the cavity.

CHAPTER 9

THERMAL DRIFT AND FORCED CONVECTION ANALYSIS OF NANOFLUID DUE TO PARTIALLY HEATED TRIANGULAR FINS IN A POROUS CIRCULAR ENCLOSURE

9.1 Introduction

In the presence of Magnetohydrodynamics (MHD), partially lid triangular walls in circular ducts can be used to improve heat transfer. In several physical applications, such as nuclear engineering, plasma physics, and geophysics, the presence of a magnetic field is capable of altering the characteristics of fluid flow and heat transfer. The main emphasis of this model simulation is to analyze the simultaneous effects of thermal drift and forced convection on water based single wall carbon nanotubes (SWCNTs) in a porous circular duct. Equilateral triangular fins which are enclosed in a circular cavity having vertical and horizontal side of triangular fins are moving. Internal heat generation/absorption is considered to determine the thermal drift. Impact of inclined Magnetohydrodynamics (MHD) has been introduced. The governed equations are solved through weighted residue method of FEM. Effects of various parameters, they are Reynolds number, nanoparticles, porous medium and absorption/generation on flow patterns and heat transfer were worked out. The heat transfer rate at different heated fins has been investi-

gated for various parameters. This study carries out significant impact of Q on temperature profile and local Nusselt. Local Nusselt number against heated walls decreases with increase in porosity parameter and also increases in case of heat generation. Streamlines decrease with increase of quantity in solid volume fraction in enclosure. Significant effect of Re is observed in transformation of heat in circular duct. Numerous physical applications of this flow configuration exist, such as the cooling of high-temperature electronics, thermal control of nuclear reactors, and improved heat transfer in geothermal energy systems. The efficiency and efficacy of these systems can be greatly enhanced by using partially lid triangular walls in circular ducts to increase exchange of heat in the presence of MHD. Fluid mixing may also be accomplished by partially moving the triangle walls of a circular duct. It is possible to improve the mixing of various fluids, which is advantageous for applications including chemical reactions, emulsion formation, and particle suspension.

Table 9.1: A table demonstrating the contrasts between the approaches being offered

Authors	Enclosure	Obstacle	MHD	Heat generation
Sheikholeslami *et al.* [19]	Elliptic	Rectangular	Inclined	No
Sheikholeslami *et al.* [21]	Curved	No	Inclined	No
Chamkha [39]	Square	No	Normal	Yes
Saha *et al.* [79]	Square	No	Normal	Yes
Present	Circular	Triangular	Inclined	Yes

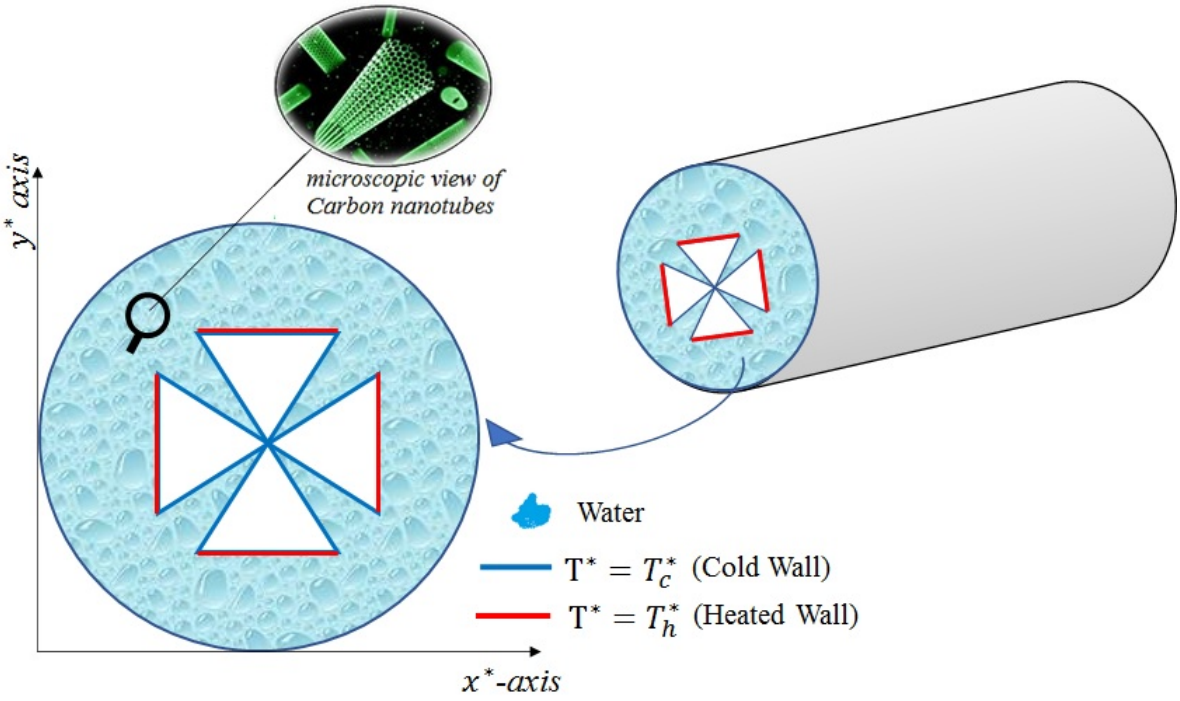

Figure 9.1: Physical domain of circular duct with partially heated fins

9.2 Problem Formulation

The necessary assumptions were added in this section which are applied on momentum and energy equations. The constructed equations are based upon two-dimensional flow enclosed in a circular duct that contain partially heated triangular fins. Vertical and horizontal sides of triangular fins are moving with constant velocity that provide the anti-clockwise source of heat transfer and fluid motion. Water-based SWCNTs are analyzed for current model. In order to manage the heat transfer output inside the closed cavity, different restrictions were modified on the fins. Fig. 9.1 defines the geometry of the model.

9.2.1 Mathematical Model

A mathematical model that emerges with nanofluid expression in the form of continuity, momentum and energy is constructed based on the constraints described in the problem description [98].

$$\nabla \cdot \mathbf{V}^* = 0, \tag{9.1}$$

$$\begin{aligned} \mathbf{V}^* \cdot \nabla u^* = -\frac{1}{\rho_{nf}} \frac{\partial p^*}{\partial x^*} + \ \nu_{nf} \nabla^2 u^* - \frac{\nu_{nf}}{k} u^* \\ + \frac{\sigma_{nf} B_0^2}{\rho_{nf}} \left(v^* sin\Phi cos\Phi - u^* sin^2\Phi \right), \end{aligned} \tag{9.2}$$

$$\begin{aligned} \mathbf{V}^* \cdot \nabla v^* = -\frac{1}{\rho_{nf}} \frac{\partial p^*}{\partial y^*} + \nu_{nf} \nabla^2 v^* - \frac{\nu_{nf}}{k} v^* + \frac{(\rho\beta)_{nf}}{\rho_{nf}} g(T^* - T_c^*) \\ + \frac{\sigma_{nf} B_0^2}{\rho_{nf}} \left(u^* sin\Phi cos\Phi - v^* cos^2\Phi \right), \end{aligned} \tag{9.3}$$

$$\mathbf{V}^* \cdot \nabla T^* = \alpha_{nf} \nabla^2 T^* + \frac{Q_0}{(\rho C_p)_{nf}} (T^* - T_c^*), \tag{9.4}$$

Thermal diffusivity of the nanofluid is defined by [99] as Eq. (2.8) and electrical conductivity mentioned in Eq. (2.7) introduced by [83–85]. k_{nf} considering the nanoparticle shape's impact are defined as:

$$\frac{k_{nf}}{k_f} = 1 + \frac{k_{CNT} \phi r_l}{3k_l(1-\phi) r_{CNT}}, \tag{9.5}$$

Introducing the following dimensionless set;

$$\begin{aligned} X = \frac{x^*}{H},\ Y = \frac{y^*}{H},\ U = \frac{uH}{\alpha_f},\ V = \frac{vH}{\alpha_f},\ \theta = \frac{T^* - T_c^*}{T_h^* - T_c^*}, \\ P = \frac{p^* H^2}{\rho_f \alpha_f^2},\ \nu_f = \frac{\mu_f}{\rho_f},\ Ra = \frac{g\beta_f (T_h^* - T_o^*) H^3}{\mu \alpha_f}, \\ Ha = B_o H^2 \sqrt{\frac{\sigma_f}{\rho_f \nu_f}},\ Pr = \frac{\nu_f}{\alpha_f},\ \alpha_{nf} = \frac{k_{nf}}{(\rho C)_{nf}}. \end{aligned} \tag{9.6}$$

Where, the characteristic length is H, kinematic viscosity ν, Reynold number Re, and Prandtl number Pr. By invoking the defined variable the non-dimensional form of equations (9.1)–(9.4) are

$$\frac{\partial U}{\partial X}+\frac{\partial V}{\partial Y}=0, \tag{9.7}$$

$$\begin{aligned} U\frac{\partial U}{\partial X}+V\frac{\partial U}{\partial Y}=&-\frac{\rho_f}{\rho_{nf}}\frac{\partial P}{\partial X}+Pr\frac{\nu_{nf}}{\nu_f}\left(\frac{\partial^2 U}{\partial X^2}+\frac{\partial^2 U}{\partial Y^2}-\frac{U}{Da}\right)\\ &+\frac{\frac{\sigma_{nf}}{\sigma_f}}{\frac{\rho_{nf}}{\rho_f}}Ha^2Pr(Vsin\Phi cos\Phi-Usin^2\Phi), \end{aligned} \tag{9.8}$$

$$\begin{aligned} U\frac{\partial V}{\partial X}+V\frac{\partial V}{\partial Y}=&-\frac{\rho_f}{\rho_{nf}}\frac{\partial P}{\partial Y}+Pr\frac{\nu_{nf}}{\nu_f}\left(\frac{\partial^2 V}{\partial X^2}+\frac{\partial^2 V}{\partial Y^2}-\frac{V}{Da}\right)\\ &+\frac{(1-\phi)\rho_f\beta_f+\phi\rho_p\beta_p}{\rho_f\beta_f}RaPr\theta+\frac{\frac{\sigma_{nf}}{\sigma_f}}{\frac{\rho_f}{\rho_f}}Ha^2Pr(Usin\Phi cos\Phi-Vcos^2\Phi), \end{aligned} \tag{9.9}$$

$$U\frac{\partial \theta}{\partial X}+V\frac{\partial \theta}{\partial Y}=\frac{\alpha_{nf}}{\alpha_f}\left(\frac{\partial^2 \theta}{\partial X^2}+\frac{\partial^2 \theta}{\partial Y^2}\right)+Q\frac{(\rho C_p)_f}{(\rho C_p)_{nf}}\theta. \tag{9.10}$$

9.2.2 Dimensionless boundary conditions:

At the outer circular surface (Ω_1)***:***

$$\begin{aligned} U=0,\ \ V=0 \text{ and } \theta=0,\\ \Omega_1=\left\{(X-h)^2+(Y-k)^2=r^2/\text{ radius}=0.5 \text{ and center } h=k=0.5\right\}. \end{aligned} \tag{9.11}$$

At horizontals fins of upper (Ω_9) ***and lower*** (Ω_2) ***triangular fin:***

$$\begin{aligned} U=-1,\ \ V=0\ \text{ and }\ \theta=1,\\ \text{when } \Omega_2=\ L_H=\ \{(X,Y)\ \in\mathcal{R}/0.35\le X<0.65 \text{ and } Y=0.25\},\\ U=1,\ \ V=0\ \text{ and }\ (\theta=1),\\ \text{when } \Omega_9=\ L_H=\ \{(X,Y)\ \in\mathcal{R}/0.35\le X<0.65 \text{ and } Y=0.75\}. \end{aligned} \tag{9.12}$$

At vertical fins of right (Ω_5) ***and left*** (Ω_{13}) ***sides of triangular fin:***

$$\begin{aligned} U=0,\ \ V=-1 \text{ and }\ (\theta=1),\\ \text{when } \Omega_5=\ L_H=\ \{(X,Y)\ \in\mathcal{R}/0.35\le Y<0.65 \text{ and } X=0.25\},\\ U=0,\ \ V=1 \text{ and }\ (\theta=1),\\ \text{when } \Omega_{13}=\ L_H=\ \{(X,Y)\in\mathcal{R}/0.35\le Y<0.65 \text{ and } X=0.25\}. \end{aligned} \tag{9.13}$$

At inclined sides of triangular fin:

$$
\begin{aligned}
U = \ V = 0 = \theta, \\
\text{when} \ \ \Omega_3 = \left\{(X,Y) \ \in \mathcal{R}/0.5 < X \leq 0.65 \text{ and } Y = -\frac{5}{3}X + \frac{1}{3}\right\}, \\
U = \ V = 0 = \theta = 0, \\
\text{when} \ \ \Omega_4 = \left\{(X,Y) \ \in \mathcal{R}/0.5 < X \leq 0.65 \text{ and } Y = \frac{5}{3}X - \frac{1}{3}\right\}, \\
U = \ V = 0 = \theta, \\
\text{when} \ \ \Omega_6 = \left\{(X,Y) \ \in \mathcal{R}/0.5 < X \leq 0.75 \text{ and } Y = -\frac{3}{5}X + \frac{1}{5}\right\}, \\
U = \ V = 0 = \theta, \\
\text{when} \ \ \Omega_7 = \left\{(X,Y) \ \in \mathcal{R}/0.5 < X \leq 0.75 \text{ and } Y = -\frac{3}{5}X + \frac{4}{5}\right\}, \\
U = \ V = 0 = \theta, \\
\text{when} \ \ \Omega_8 = \left\{(X,Y) \ \in \mathcal{R}/0.5 < X \leq 0.65 \text{ and } Y = \frac{5}{3}X - \frac{1}{3}\right\}, \\
U = \ V = 0 = \theta, \\
\text{when} \ \ \Omega_{10} = \left\{(X,Y) \ \in \mathcal{R}/0.35 < X \leq 0.5 \text{ and } Y = -\frac{5}{3}X + \frac{4}{3}\right\}, \\
U = \ V = 0 = \theta, \\
\text{when} \ \ \Omega_{11} = \left\{(X,Y) \ \in \mathcal{R}/0.25 < X \leq 0.5 \text{ and } Y = \frac{3}{5}X + \frac{1}{5}\right\}, \\
U = \ V = 0 = \theta, \\
\text{when} \ \ \Omega_{12} = \left\{(X,Y) \ \in \mathcal{R}/0.25 < X \leq 0.5 \text{ and } Y = -\frac{3}{5}X + \frac{4}{5}\right\}.
\end{aligned}
\tag{9.14}
$$

The average Nusselt number

$$Nu = \int_0^1 Nu_X dX$$

and Nusselt number along the heated fins are written as;

At lower (Ω_2) triangular heated fin:

$$Nu_X = -\frac{k_{nf}}{k_f}\left(\frac{\partial \theta}{\partial Y}\right)_{Y=0.25}, \tag{9.15}$$

At right (Ω_5) triangular heated fin:

$$Nu_Y = -\frac{k_{nf}}{k_f}\left(\frac{\partial\theta}{\partial X}\right)_{X=0.75}, \tag{9.16}$$

At upper (Ω_9) triangular heated fin:

$$Nu_X = -\frac{k_{nf}}{k_f}\left(\frac{\partial\theta}{\partial Y}\right)_{Y=0.75}, \tag{9.17}$$

At upper (Ω_{13}) triangular heated fin:

$$Nu_Y = -\frac{k_{nf}}{k_f}\left(\frac{\partial\theta}{\partial X}\right)_{X=0.25}. \tag{9.18}$$

9.3 Results and Discussion

In this chapter, a numerical study is performed to investigate the influence of the inclined magnetic field by heating the horizontal and vertical sides of the triangular fins etched in the circular cavity. The study is performed for Reynolds number ($300 \leq Re \leq 1000$) where Richardson number is fixed as 0.05, nanoparticles of volume fraction ($0 \leq \phi \leq 0.2$), Darcy number ($10^5 \leq Da \leq 10$) and heat absorption/generation parameter ($-100 \leq Q \leq 50$). These effects are obtained for the fixed parameter $Pr = 6.2$, $\Phi = 45$ and the diameter of circular cavity is 1.

Effects of Reynolds number:

The impact of Reynolds number on the isotherms and streamlines is illustrated in Fig. 9.2(a)–(h). For increasing Re, heat transfer in cavity also increases and distributes into the whole cavity. With this effect the wall of circular cavity becomes fully heated. Fig. 9.2(e)–(h) represents the streamlines effect with variation of Re, streamlines are symmetrically stable near the heated fins,for the fixed value of Ri. It means that the velocity of the whole duct is modified with the equal proportions to the velocity of the heated connectives and this is because of the internal heat generation. Fig. 9.3(a)–(b) represents the temperature profile with variation of Re. The heated vertical

and horizontal fins, which are the sides of triangular shape, are inscribed in circular cavity. However, the temperature profile increases with the enhancement of Reynolds number. At the mediate section of the duct, maximum height is obtained. For the horizontal and vertical cases, the same transfer of heat is developed in cavity. The Nusselt number for various heated fins due to the variation of Re is represented in Fig. 9.3(c)–(f). Due to the lid walls, by increasing the Reynolds number isotherm lines increases near the circular wall of cavity, that's why maximum amount of local Nusselt can be observed. Conversely, at the opposite side of the heated fin, there is a decrease in local Nusselt number. In all such cases, every heated fin reduces the transfer of heat at lower side and increases towards the heated fins.

Effects of nanoparticles:

The streamlines and temperature field inside the circular cavity with horizontal and vertical heat source for different nanoparticles are represented in Fig. 9.4(a)–(h). Reynolds number, Darcy number and heat absorption/generation are fixed. For increasing volume fraction of nanoparticles, the intensity of the central cells decrease. Heated lines gradually decreases with increasing quantity of volume fraction of nanoparticles. Fig. 9.4(c)–(d) clearly identifies that streamlines are restricted near the heated lid fins. For maximum quantity of nanofluid, heated lines are quite stable and confined near the fins. The temperature field at the end is fixed on the heated walls. Fig. 9.4(e)–(h) shows the streamlines, which is quite stable with increasing the nanoparticles. In circular duct, the effect of nanoparticles plays a significant role with the existence of heat generation/absorption parameter. Fig. 9.5(a)–(f) illustrates the heat transfer variations as volume fraction varies. In enclosure, heat transfer increases with the enhancement of nanoparticle for vertical and horizontal implementation of heated fins. With increasing the solid concentration the heat transfer increases near the wall. With increasing the concentration of nanofluid the flow rate increases at the middle of cavity. At the middle local

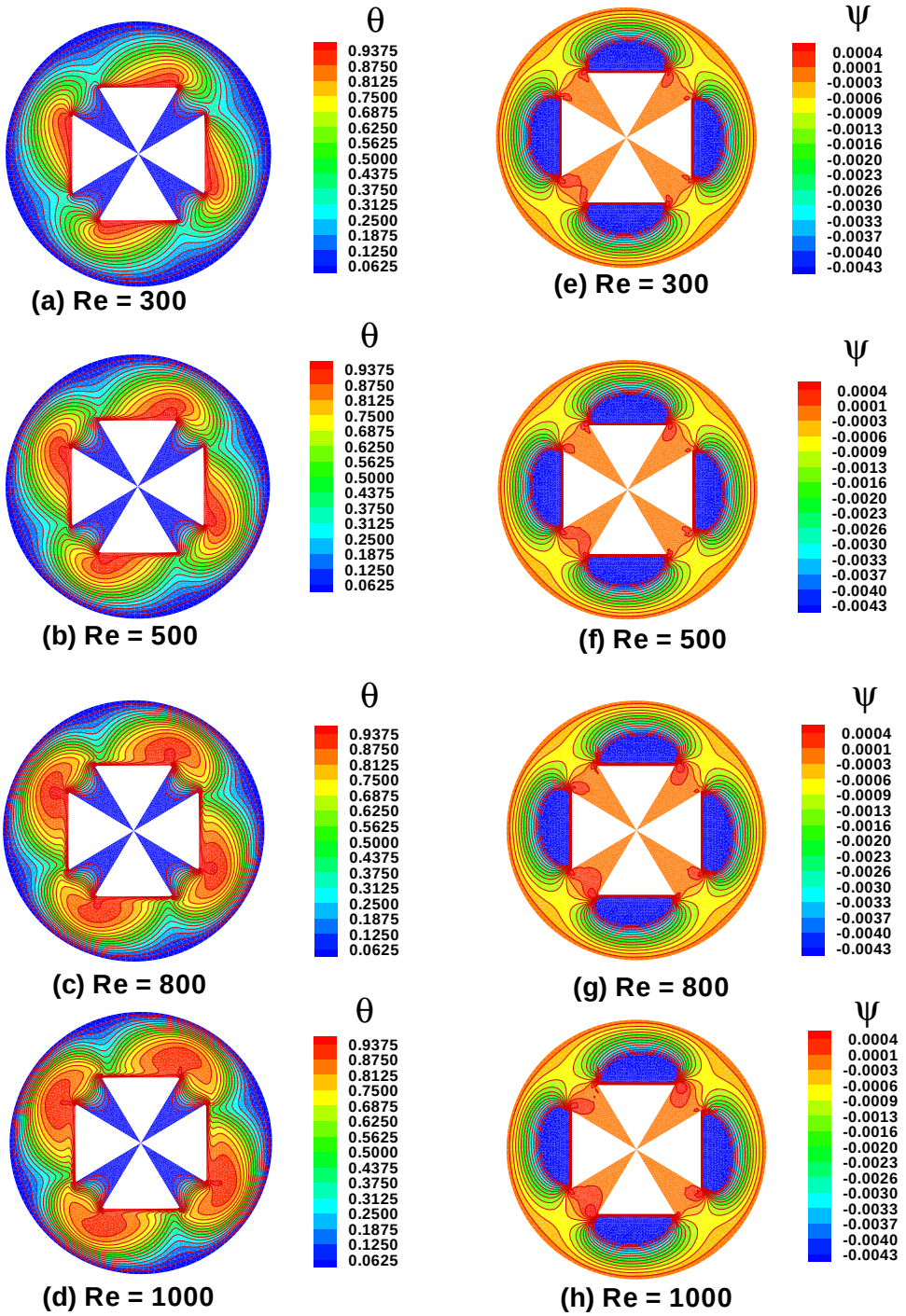

Figure 9.2: Steady state isotherms and flow pattern due to the variation of Reynolds number

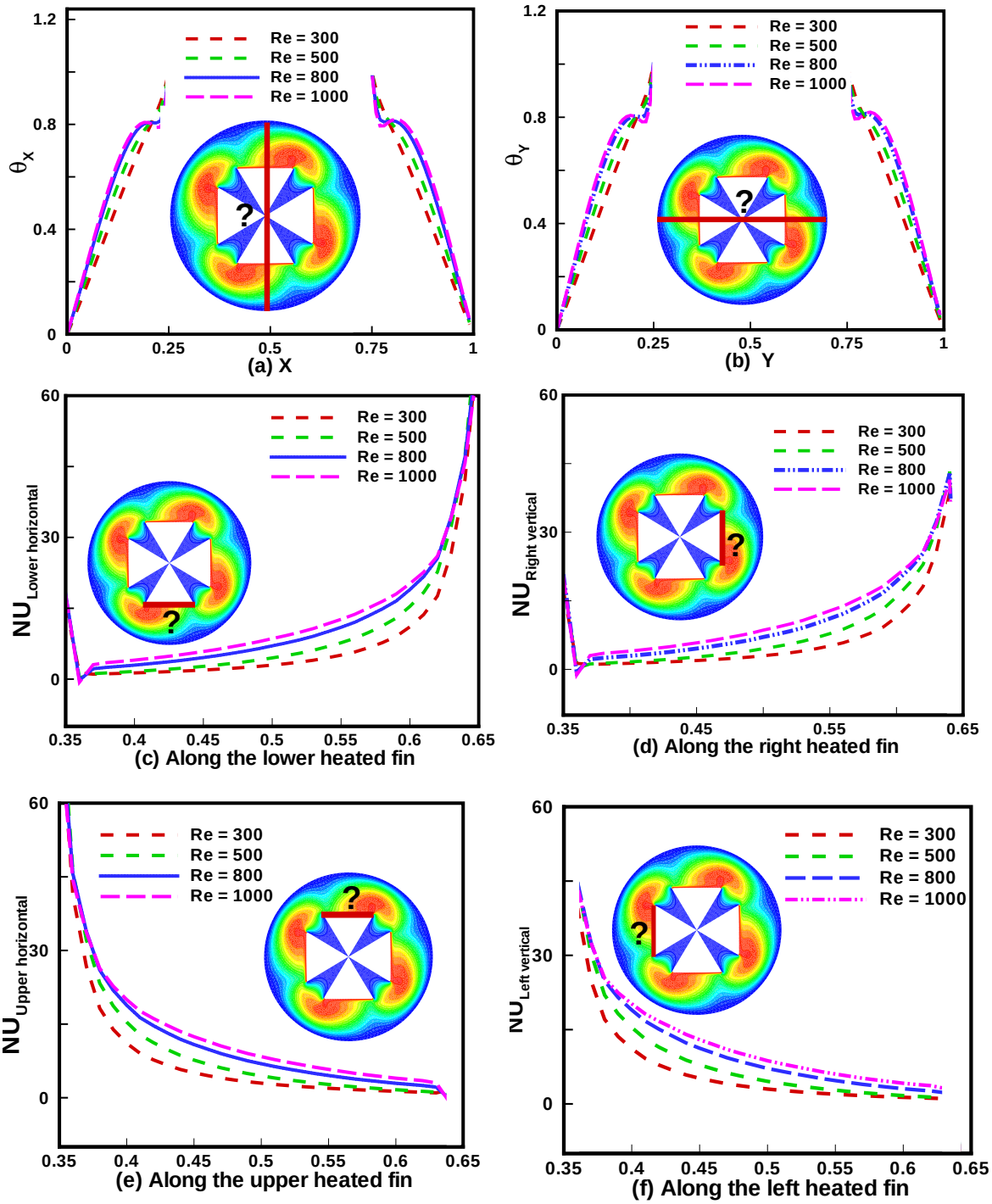

Figure 9.3: Influence of Re on temperature distribution and Nu

Nusselt number sufficiently increases due to less resistance in heat flow. Impact of volume fraction on flow rate against different heated lengths are similarly repeated on left and right side of figure. Fig. 9.5(c)–(f) shows the Nusselt number at heated fins for different nanoparticles. As thermal conductivity increases, nanoparticle also increases near the heated fins and it increases from left to right as examined in Fig. 9.5(c)–(d) but is converse in the case when heated fins are at left position.

Effects of Porous medium:

As an inexpensive and promising way of improving the energy efficiency of houses, numerous researchers have explored porous materials. In addition, some of the physical media that are used in the development of energy technologies are porous. Darcy number (Da) is the permeability measurement in porous cavity or medium. Fig. 9.6(a)–(h) illustrates the streamlines and isotherms as Darcy number varies. Due to the high resistance, the flow of heat is minimum in cavity for low Darcy number. The Darcy number effect illustrates the impact of changing permeability of the porous medium on the thermal field. However, by increasing the Darcy number resistance decreases and heat moves outside the porous medium and circulates circular wall. Fig. 9.6(e)–(h) represents the streamlines effect, which clearly shows that the flow penetrates deeper into the cavity with increasing of Da. In the present problem, four various horizontal and vertical heated fins are investigated. Heated fins are inscribed in circular cavity in the form of the sides of triangles. Fig. 9.7(a)–(b) conforms that with an increase the Darcy number the temperature linearly increases or decreases where the permeability of medium increases. It means that the flow resistance decreases and hence there is an increase in the porosity of heat transfer in cavity. The impact of Darcy number on Nusselt number at heated fins (horizontal and vertical) is represented in Fig. 9.7(c)–(f). It can be seen that at the boundary, heat transfer increases with an increase in Da. But it decreases near the cold inclined fins. Nusselt number rises as the

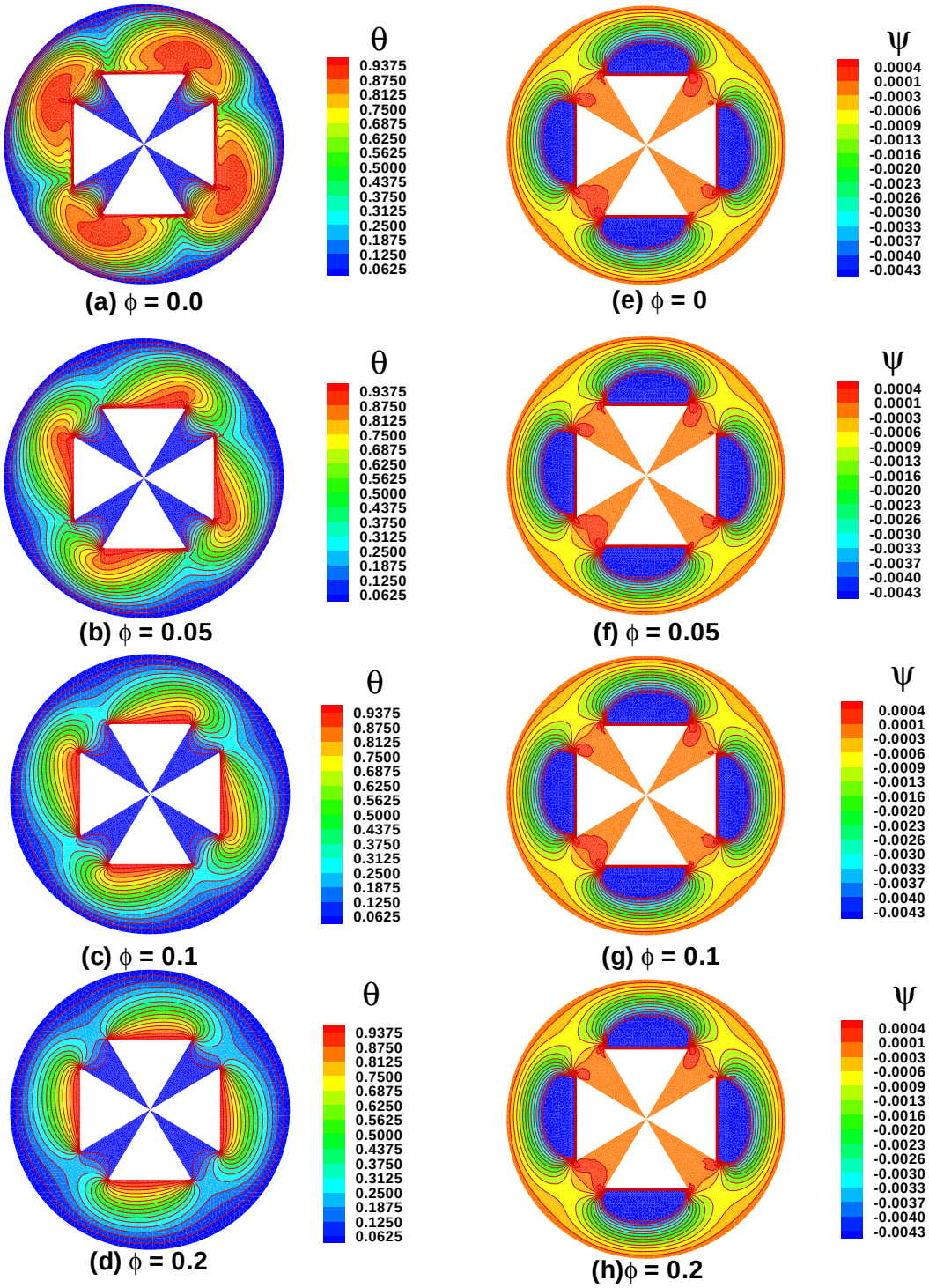

Figure 9.4: Steady state isotherms and flow pattern due to the variation of solid volume fraction

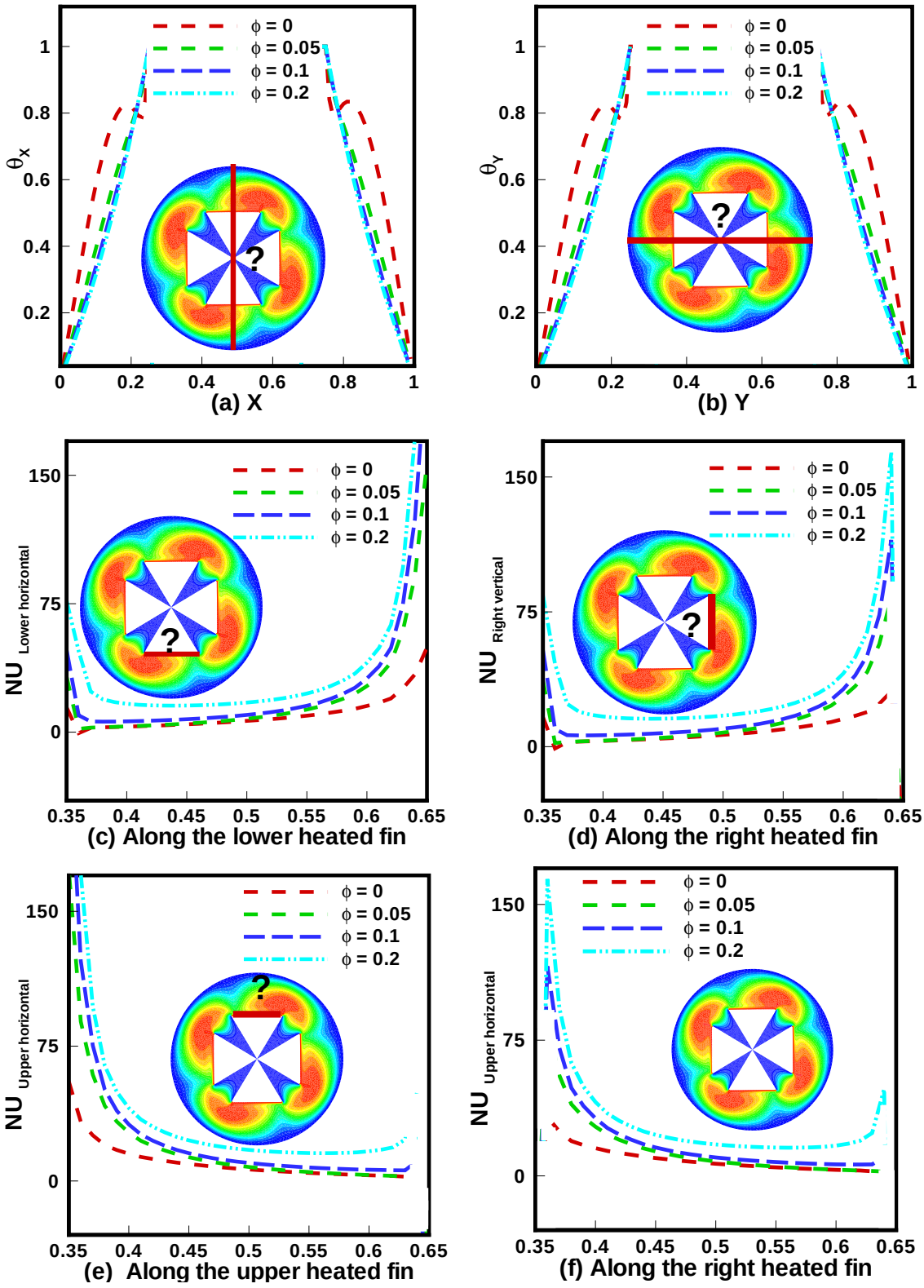

Figure 9.5: Influence of solid volume fraction on temperature profile and Nu

porosity increases. Further, heat transfer also increases as Da increases. At the lower heated fin, there is a significance of buoyancy effect and heat transfer increases with increasing the Da. Similarly, left and right sided vertical fins also transfer heat with increasing the permeability region.

Effects of heat generation/absorption:

Thermal effect in circular cavity through fins has significant role in industrial field. Heat development in circular duct through fins and external source has significant impact in industrial field. The impact of absorption/generation is illustrated on the temperature profile (against horizontal and vertical mean position), Nusselt number (Nu) on the surface of heated fins in Fig. 9.8(a)–(f). Heat increases due to convection near the heat fins in generation case and decreases in case of absorption. In both horizontal and vertical temperature profiles behave same with the variation of Q. The impact of Q on Nusselt number at lower and right triangular fins is examined in Fig. 9.8(c)–(d). It can be observed that as Q increases, there is a decrease in Nusselt number. Due to the lid walls of triangular fins, it is predicted that heat absorption increases the Nusselt number, on the contrary, the heat generation coefficient increases as the Nusselt number decreases.

9.4 Conclusion

The mixed convection of transfer of heat in circular duct with partially lid-driven fins in triangular form is numerically investigated. The cavity is filled with copper nanoparticles, $Pr = 6.2$, $Ri = 0.05$, $Ha = 10$ and $\Phi = 45$ are fixed. The effects of Reynolds number ($300 \leq Re \leq 1000$), where Richardson number is fixed as 0.05, nanoparticle volume fraction ($0 \leq \phi \leq 0.2$); Darcy number ($10^{-5} \leq Da \leq 10$) and heat absorption/generation parameter ($-100 \leq Q \leq 50$) on isotherm, streamlines, temperature profile and local Nusselt number were investigated. After the simulation, the outcomes are as follows:

- With increasing the Reynolds number (Re), there is also an increase in

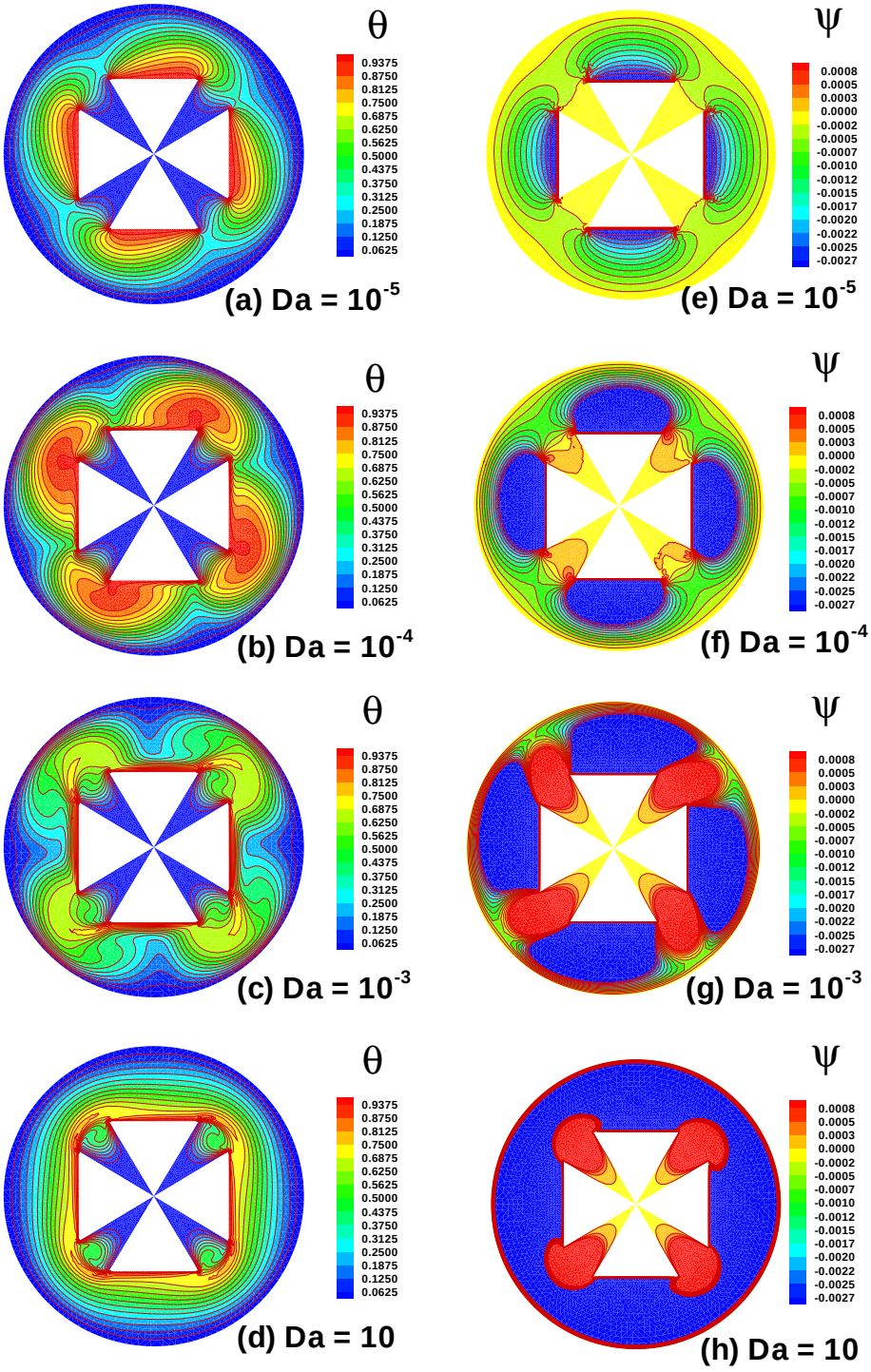

Figure 9.6: Steady state isotherms and flow pattern due to the variation of Darcy number

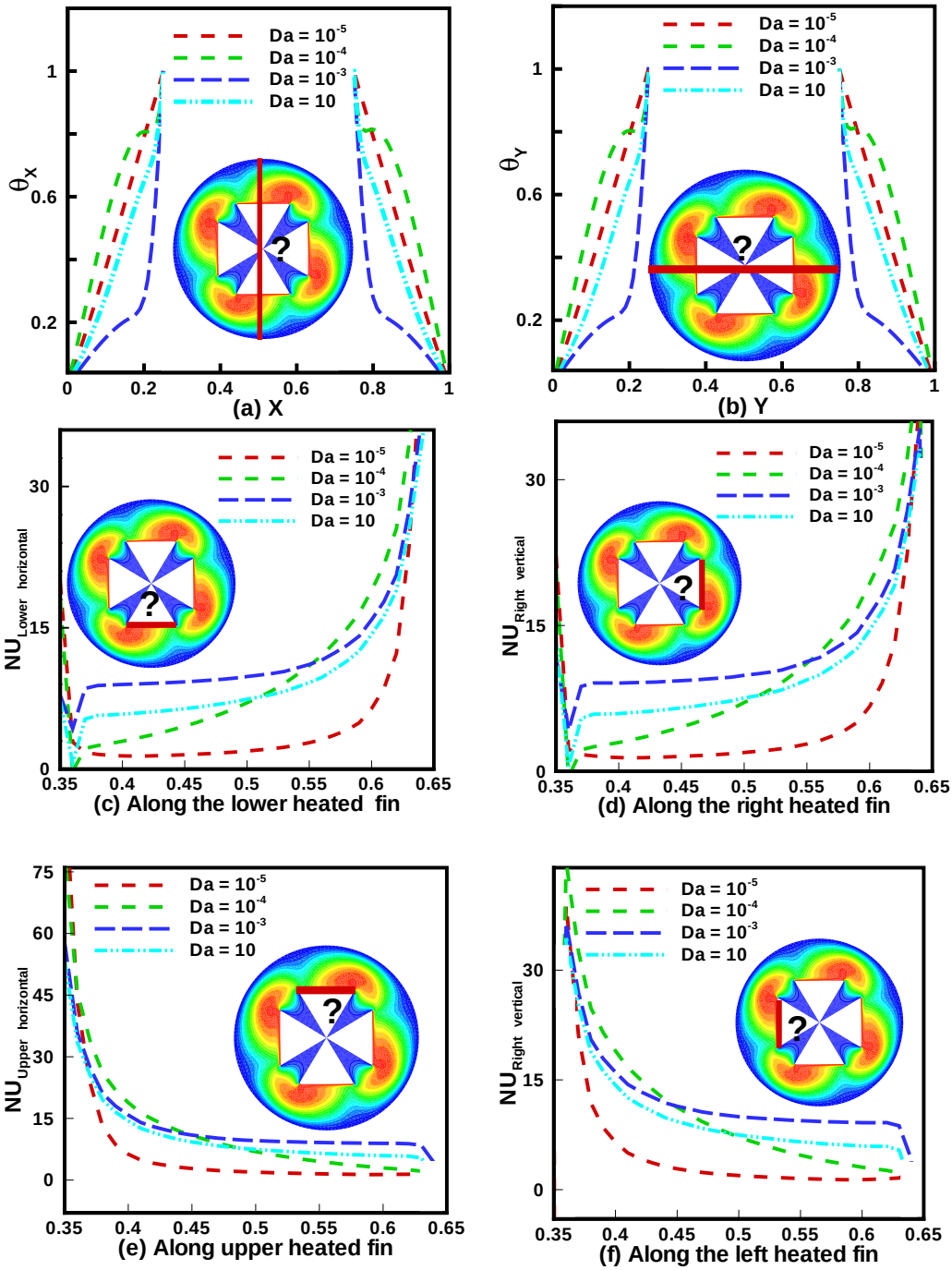

Figure 9.7: Influence of Darcy number on temperature profile and Nu

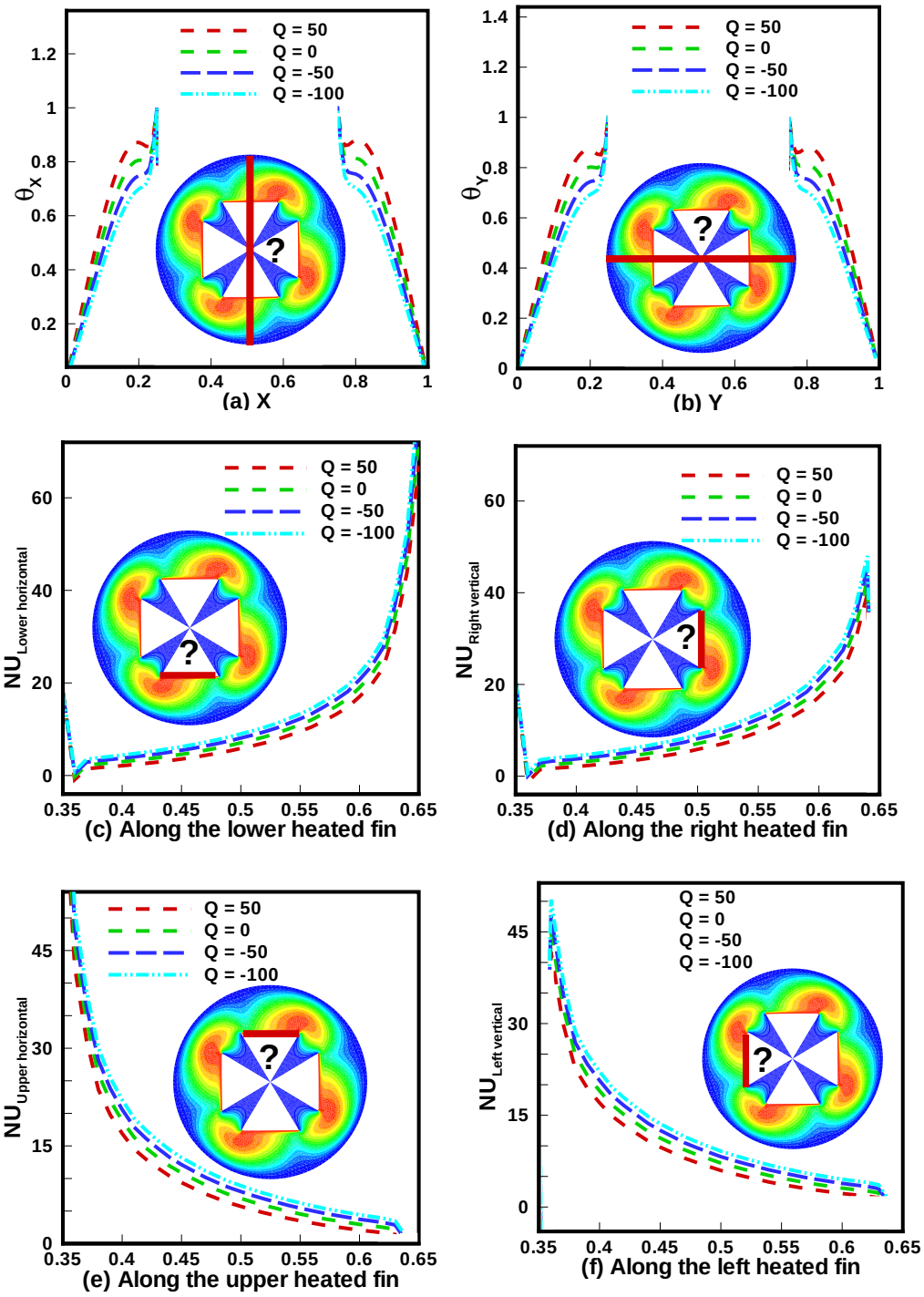

Figure 9.8: Influence of internal heat generation/absorption on temperature profile and Nu

the local Nusselt number. The stream function values increases due to the convective heat transfer at higher Re.

- Significant effect on temperature distribution evaluated in duct with increase in Reynolds number. In case of forced convection the temperature in cavity exceeds with increasing Re.

- The result of isotherms and streamlines were analysed against the different nano-particles. The study concludes that isotherms decrease with increasing nanoparticles. The lines gradually emerging to the heated surface of fins.

- As temperature and Nusselt number increase volume fraction of nanoparticles also increases. Further, in case of nanoparticles, the heat transfer is surplus as compared to base fluid (water).

- The effect of Da can be seen when the flow patterns are highly affected by permeability within the duct. Heat transfer in cavity augments as Darcy number increases. For increasing Q, the internal heat transfer also increases. Temperature profile is enhanced in cavity in case of $Q > 0$.

CHAPTER 10

CONCLUSION AND FUTURE WORK

10.1 Conclusion

We investigated heat and mass transport processes in a variety of cavity models using nanoparticles in this dissertation. The role of nanoparticles in natural and forced convection in regular and irregular enclosures is investigated from a physical standpoint. In the literature, there exists a variety of nonlinear partial differential equations of nanofluid models. The models provided by Buongiorno, Tiwari and Das are the most popular among them. The Buongiorno nanofluid model adds a transport equation for nanoparticle concentration to the fundamental transport equations for fluid flow and heat transfer. The Brownian diffusion (deterministic motion of nanoparticles), thermophoresis (particle diffusion owing to temperature gradient), and Brownian motion are differentiated by Buongiorno, whereas the Tiwari and Das model focus on the various thermophysical characteristics of the nanofluid. Fine grid meshing is utilized for a 2-D steady flow to maintain the flow as laminar in closed geometry. In this case, the obtained numerical solution remains stable across the cavity.

10.1.1 *Comprehensive finding of entire thesis:*

Natural convection (Chapters 4 and 5) and forced convection (Chapters 6, 7 and 9) are the two primary forms of flows, studied in this research.

FEM is being used to systematically assess steady laminar incompressible two-dimensional nanofluid flows in complex geometries. In case of square cavity fins play a vital role for heat generation and transfer. Heated length of fins directly influence the transfer rate of heat. In natural convection local Nusselt number increases with increase in heated length. Chapter 5 includes curved cavity and partially heated curve is allocated for heat flow inside cavity. For this, we use extended equation with the addition of porous medium for simulation and an energy equation with heat generation/absorption term for heat creation and elimination. In such situation, porosity plays significant role to maintain heat in cavity. In curved cavity, transfer rate of heat increases with increasing porosity of the medium. In square cavity, heat is developed through horizontal fin whereas, split curved plays a vital role for heat generation and transfer in cavity. One factor Q, which is used for heat generation plays important role to develop heat inside the porous cavity. For maintenance of heat this parameter is also used as absorption. In this presence of Q, heat flow faster with the help of porosity in this situation. In both problems free convection is adopted, that is generated with the help of fin and curved heated wall. Deformation of the lower heated curved wall also works for more heat generation and in square enclosure the same work is done due to the length of fin. Similar impact of the fin and heated curved wall are also developed on velocity, temperature and local Nusselt number on square and curved cavity. In both cavities, FEM is applied for numerical solution of heat transfer.

Unlike the previous two chapters, chapters (6,7 and 9) represented to forced convection analysis on different cavities (irregular and corrugated heated walls). In chapter 6, the cavity is taken as corrugated which has one side moving lid wall with the uniform velocity. A circular obstacle is also placed inside the cavity which is helpful in heat transfer. The medium of corrugated enclosure is kept porous. Heat generation and absorption are applied to maintain the heat transfer in the cavity. In addition to 6, chapter 7 is taken

with the double sided lid driven on the corrugated duct. Same parameters for heat flow are utilized to check and measure the effects of heat in the cavity without circular obstacle whereas various directional velocity of lid walls on streamlines, isotherms, velocity, temperature, and Nusselt number has been observed. It is evident to see the effects of heat transfer with the movement of lid walls. Moving the lid walls inside produces heat inside the cavity while the movement of lid walls outside produces heat away from the corrugated wall. In connection to the previous chapter, chapter 8 discuss as the third type of convection that is the mixed convection. This convection is taken in the trapezoidal cavity with the split lid driven on the top wall moving in various direction that affects the heat mass transfer in enclosure. The effects of buoyancy ratio parameter and lewis number are observed in the enclosure with the impact of upper wall (lid driven). Chapter 9 deals with partially heated triangular fins and lid driven in the fins. Heat is generated in the cavity in the presence of inclined MHD and porosity. Heated lines or flow of heat decreases with increasing ϕ in all cases of geometry. Darcy number or resistance effect on isotherm clearly shows that with increasing of porosity parameter isotherm decreases. Heat generation coefficient creates heat inside cavity, so rate of heat transfer decreases in all problems.

10.1.2 *Parametric based finding for flow and heat transfer:*

When the Rayleigh number is raised in natural convection, the streamlines near the lower heated fin or wall become very strong. When the buoyancy driven is at its maximum, the streamline moves closer to the heated area, progressively heating the entire cavity. As Ra increases, there is more free convection on the free flow of the isotherm. When Rayleigh number is rising in the left and right regions of vertical fins, vertical velocity against heated lower fins increases in cavity. It is also realized that its velocity is zero as it approaches the solid fins' end point. When Ra is raised, the location of the

bottom face lower heated fin drops. The heat transfer from the bottom heated fin's lower face may be seen distinctly. This shows when the Rayleigh number rises, the thermal flow drops.

This research work focuses on convection through lid walls in several complex geometries. For low Richardson numbers, isotherms are confined near the lid wall. Shear forces dominate in the cavity at $Ri = 0.01$, and streamlines are primarily limited to the area near the moving wall. When Ri is increased to 1, both shear and buoyancy forces contribute equally, resulting in more streamlines near the wall. Due to free convection, fluid flow has been detected throughout the cavity around the centre impediment as Ri increases from 1 to 10. With an increase in Ri, the velocity at the vertical and horizontal mean position decreases. In this instance, the temperature gradient is the most vital role. The rate of heat transfer decreases as the Richardson number increases due to the dominance of heat in cavity.

The influence of Reynolds number on isotherms and streamlines demonstrates that symmetrical undistorted isotherms cover the most of the cavity, while the isotherms endorse some sort of distortion towards the top moving lid. The isotherm is dispersed throughout the enclosure at low Reynolds number and gradually decreases as Re increases. The heat effect around the moving heated vertical wall should be maximised for maximum Re. It is obvious, when the Reynolds number rises, the velocity at centre rises with it. The centre of vortices layer is obviously smaller than towards the cavity's corner. Furthermore, as Re increases, the layers form at the solid wall's boundary, and heat is emitted with a uniform vorticity from the solid boundary. The effect of Reynolds number on nanofluid particle streamlines and isotherms in a corrugated enclosure, in case of a double lid is observed. At low Re, the contour is uniformly distributed, with temperature on both sides of the lid walls. Isotherm lines form a circular rotation, and when Re rises, the isotherm lines become stronger. For lower values of Re, the effect of forced convection

is smaller, and the number of heated lines is reduced. The heat flux rises as Re increases, making forced convection the dominant mode of transport. This suggests that forced convection is the primary mode of heat transfer in the cavity.

For base fluid, the flow structure of molecular movement near the heated wall is quite laminar and congested. The strength of heated lines in isotherms increases as the concentration of nanofluid in the base fluid increases. When 5% mixture is added to the fluid in a natural convection instance, the velocity at mean position increases as well. However, due to the highest rate of heat transfer, the temperature in cavity declines at that instant. The transfer of heat is increased in the case of forced convection because the vertical lid wall moves with a specific velocity. In this case, the role of free convection is limited, and the isotherm profile shows a clockwise circular flow of the fluid. With an increase in nanoparticle concentration in the cavity, the circular rotation near the obstacle increases. Due to the movement of the lid wall, eddy develops around it in streamlines.

In the case of natural convection, the effect of a heated fin on heat transport in the cavity is significant. The maximum length of a fin has a greater impact on the isotherm, but the flow structure in the form of streamlines near the fins decreases. Heated lines vary in structure and cluster around the other cold fins in the case of adiabatic fins. However, heat is confined around the top and lower fins in the case of cold fins. For a cool middle fin case, the horizontal and vertical velocity are relatively low. The rate of heat transfer at the upper and lower faces of the heated fin is inversely proportional to the length of the heated fin. Heat rises inside the circular duct when the lid is driven with a specific velocity.

Heat transfer increases as the heat generation coefficient is reduced, and temperature distribution lines or heat transfer is restricted near the heated wall. Inside the cavity, when $Q = 0$, stable symmetric heat transport is ob-

served. Heat infection is transmitted in various cavity models as a result of natural and lid wall action. As the internal generation increases, more heat is generated along the heated walls, which then spreads throughout the cavity. As shown in cavities, vertical velocity rises when the heat generation coefficient is high and falls when the heat generation coefficient is low. For larger values of Q, the temperature profile shows that more heat is produced. Heat transportation increases as the heat generation coefficient is reduced, and temperature distribution lines or heat transfer is restricted near the heated wall.

For natural convection, Darcy number has significant influence on the heat transfer rate. For maximum porosity, more heat generated in the cavity. As a result of its high rate of heat transfer, velocity decreases at the mean location. Heated lines in forced convection emphasize that permeability is restricted at the lid walls for minimum permeability. For maximum porosity, a parabolic bolus of velocity is found. The Darcy effect which is caused by the double lid driven walls, has an effect on the isotherms and streamlines. Eddies are more stable and bigger when the material is less porous. Due to the high velocity on the lid walls, velocity also decreases for $Da = 10$, but heat transfer rate increases. The generation of heat by moving fins in a circular cavity has developed as the cavity has become larger, as has the transfer rate in the case of maximal porosity. The effect of the Darcy parameter on the circular duct's vital element in the isotherm profile in the current steady state. The average Nusselt number rises as the porosity of the medium rises.

Due to the dominance of lid velocity, the role of Lewis number on streamlines vortex is constructed for all Le with equal flow strength filling essentially the whole enclosure. At $Ri = 0.1$, forced convection domination occurs, and the flow pattern is nearly same for all Le, with the vortex rotating clockwise to generate eddies. There is also a stagnated zone in the enclosure's upper mid wall. Overall, this indicates that at $Ri = 0.1$, the Le has no influence on the streamlines. The iso-concentrations near the top of the cavity get wavy

as Le approaches 1. For $Le = 5$, the iso-concentrations begin to collect around the cavity's top wall and finally thicken for $Le = 10$, indicating increased mass transport due to mass diffusivity depreciation. Due to the asymmetrical movement of the lid walls, Le has the opposite effect on velocity, temperature, Nusselt, and concentration profile on both split lid walls. The mass diffusivity has a considerable influence on the concentration profile for high Le.

The effects of buoyancy ratio on streamlines, where the boundary layer thickness reduces as the buoyancy ratio increases, and the circular vortex of the streamline decreases on both partial lid-walls. As the buoyancy ratio increases, the strength of the flow circulation is found to increase. As the buoyancy ratio rises, the isotherm values rise to some extent. At the cavity's upper surfaces, the concentration lines are horizontal, while in the area, they are vertical. As the buoyancy ratio value rises, the concentration boundary layers at the right and left sections of the split walls distort. As Br grew, a concentration vortex emerged at the top surface's centre. Significant effect of buoyancy ratio on velocity profile it develops parabolic bolus, which decreases on left phase of the cavity and increases on the right section of the cavity with variation of buoyancy ratio parameter.

10.2 Future Work

So far, this dissertation has dealt with several regular or irregular geometries of convection problems for the steady case, but future work will be focused on physical difficulties such as phase change material, solidification, and melting. In such instances, several unsteady flow challenges for both free and forced convection models are also taken into account.

REFERENCES

[1] R. U. Haq, F. A. Soomro, H. F. Öztop, T. Mekkaoui, Thermal management of water-based carbon nanotubes enclosed in a partially heated triangular cavity with heated cylindrical obstacle, International Journal of Heat and Mass Transfer 131 (2019) 724–736.

[2] N. A. Bakar, R. Roslan, Mixed convection in a lid-driven horizontal cavity in the presence of internal heat generation or absorption, Journal of Advanced Research in Numerical Heat Transfer 3 (1) (2020) 1–11.

[3] A. Ababaei, M. Abbaszadeh, A. Arefmanesh, A. J. Chamkha, Numerical simulation of double-diffusive mixed convection and entropy generation in a lid-driven trapezoidal enclosure with a heat source, Numerical Heat Transfer, Part A: Applications 73 (10) (2018) 702–720.

[4] N. Bakar, R. Roslan, A. Karimipour, I. Hashim, Mixed convection in lid-driven cavity with inclined magnetic field, Sains Malaysiana 48 (2) (2019) 451–471.

[5] F. Garoosi, G. Bagheri, F. Talebi, Numerical simulation of natural convection of nanofluids in a square cavity with several pairs of heaters and coolers (hacs) inside, International Journal of Heat and Mass Transfer 67 (2013) 362–376.

[6] C.-J. Ho, M. Chen, Z. Li, Numerical simulation of natural convection of nanofluid in a square enclosure: effects due to uncertainties of viscosity

and thermal conductivity, International Journal of Heat and Mass Transfer 51 (17-18) (2008) 4506–4516.

[7] K. Khanafer, K. Vafai, M. Lightstone, Buoyancy-driven heat transfer enhancement in a two-dimensional enclosure utilizing nanofluids, International Journal of Heat and Mass Transfer 46 (19) (2003) 3639–3653.

[8] R.-Y. Jou, S.-C. Tzeng, Numerical research of nature convective heat transfer enhancement filled with nanofluids in rectangular enclosures, International Communications in Heat and Mass Transfer 33 (6) (2006) 727–736.

[9] E. Abu-Nada, H. F. Oztop, Effects of inclination angle on natural convection in enclosures filled with Cu–water nanofluid, International Journal of Heat and Fluid Flow 30 (4) (2009) 669–678.

[10] M. A. Sheremet, T. Groşan, I. Pop, Steady-state free convection in right-angle porous trapezoidal cavity filled by a nanofluid: Buongiorno's mathematical model, European Journal of Mechanics-B/Fluids 53 (2015) 241–250.

[11] A. S. Dogonchi, A. J. Chamkha, S. M. Seyyedi, M. Hashemi-Tilehnoee, D. D. Ganji, Viscous dissipation impact on free convection flow of Cu-water nanofluid in a circular enclosure with porosity considering internal heat source, Journal of Applied and Computational Mechanics 5 (4) (2019) 717–726.

[12] M. Sheikholeslami, M. Gorji-Bandpy, D. Ganji, S. Soleimani, Effect of a magnetic field on natural convection in an inclined half-annulus enclosure filled with Cu–water nanofluid using cvfem, Advanced Powder Technology 24 (6) (2013) 980–991.

[13] S. Soleimani, M. Sheikholeslami, D. Ganji, M. Gorji-Bandpay, Natural convection heat transfer in a nanofluid filled semi-annulus enclosure, International Communications in Heat and Mass Transfer 39 (4) (2012) 565–574.

[14] E. Abu-Nada, A. J. Chamkha, Effect of nanofluid variable properties on natural convection in enclosures filled with a CuO–EG–water nanofluid, International Journal of Thermal Sciences 49 (12) (2010) 2339–2352.

[15] K. Beukema, S. Bruin, J. Schenk, Three-dimensional natural convection in a confined porous medium with internal heat generation, International Journal of Heat and Mass Transfer 26 (3) (1983) 451–458.

[16] K. M. Khanafer, A. J. Chamkha, Hydromagnetic natural convection from an inclined porous square enclosure with heat generation, Numerical Heat Transfer, Part A Applications 33 (8) (1998) 891–910.

[17] A. J. Chamkha, M. Mansour, S. E. Ahmed, Double-diffusive natural convection in inclined finned triangular porous enclosures in the presence of heat generation/absorption effects, International Journal of Heat and Mass Transfer 46 (7) (2010) 757–768.

[18] M. Sheikholeslami, M. M. Rashidi, Effect of space dependent magnetic field on free convection of Fe_3O_4–water nanofluid, Journal of the Taiwan Institute of Chemical Engineers 56 (2015) 6–15.

[19] M. Sheikholeslami, A. Zeeshan, Analysis of flow and heat transfer in water based nanofluid due to magnetic field in a porous enclosure with constant heat flux using cvfem, Computer Methods in Applied Mechanics and Engineering 320 (2017) 68–81.

[20] S. Hussain, H. F. Öztop, K. Mehmood, N. Abu-Hamdeh, Effects of inclined magnetic field on mixed convection in a nanofluid filled double lid-

driven cavity with volumetric heat generation or absorption using finite element method, Chinese Journal of Physics 56 (2) (2018) 484–501.

[21] M. Sheikholeslami, M. Bhatti, Forced convection of nanofluid in presence of constant magnetic field considering shape effects of nanoparticles, International Journal of Heat and Mass Transfer 111 (2017) 1039–1049.

[22] M. Sheikholeslami, S. Shehzad, Simulation of water based nanofluid convective flow inside a porous enclosure via non-equilibrium model, International Journal of Heat and Mass Transfer 120 (2018) 1200–1212.

[23] N. Rudraiah, R. Barron, M. Venkatachalappa, C. Subbaraya, Effect of a magnetic field on free convection in a rectangular enclosure, International Journal of Engineering Science 33 (8) (1995) 1075–1084.

[24] M. Y. Ha, J. G. Kim, Numerical simulation of natural convection in annuli with internal fins, KSME International Journal 18 (4) (2004) 718–730.

[25] K. Venkatadri, S. A. Gaffar, V. R. Prasad, B. M. H. Khan, O. A. Beg, et al., Simulation of natural convection heat transfer in a 2-d trapezoidal enclosure, International Journal of Automotive and Mechanical Engineering 16 (4) (2019) 7375–7390.

[26] F. M. Abir, S. Barua, S. Barua, S. Saha, Numerical analysis of marangoni effect on natural convection in two-layer fluid structure inside a two-dimensional rectangular cavity, in: AIP Conference Proceedings, Vol. 2121, AIP Publishing LLC, 2019, p. 030025.

[27] D. Poulikakos, A. Bejan, Natural convection experiments in a triangular enclosure (1983).

[28] X. Xu, Z. Yu, Y. Hu, L. Fan, K. Cen, A numerical study of laminar natural convective heat transfer around a horizontal cylinder inside a concentric

air-filled triangular enclosure, International Journal of Heat and Mass Transfer 53 (1-3) (2010) 345–355.

[29] H. F. Oztop, E. Abu-Nada, Numerical study of natural convection in partially heated rectangular enclosures filled with nanofluids, International Journal of Heat and Fluid flow 29 (5) (2008) 1326–1336.

[30] M. Sheikholeslami, M. Gorji-Bandpy, S. Soleimani, Two phase simulation of nanofluid flow and heat transfer using heatline analysis, International Communications in Heat and Mass Transfer 47 (2013) 73–81.

[31] M. Sheikholeslami, M. Gorji-Bandpy, I. Pop, S. Soleimani, Numerical study of natural convection between a circular enclosure and a sinusoidal cylinder using control volume based finite element method, International Journal of Thermal Sciences 72 (2013) 147–158.

[32] M. Billah, M. Rahman, U. M. Sharif, M. Islam, Numerical simulation on buoyancy-driven heat transfer enhancement of nanofluids in an inclined triangular enclosure, Procedia Engineering 90 (2014) 517–523.

[33] R. Iwatsu, J. M. Hyun, K. Kuwahara, Mixed convection in a driven cavity with a stable vertical temperature gradient, International Journal of Heat and Mass Transfer 36 (6) (1993) 1601–1608.

[34] K. M. Khanafer, A. J. Chamkha, Mixed convection flow in a lid-driven enclosure filled with a fluid-saturated porous medium, International Journal of Heat and Mass Transfer 42 (13) (1999) 2465–2481.

[35] N. Alleborn, H. Raszillier, F. Durst, Lid-driven cavity with heat and mass transport, International Journal of Heat and Mass Transfer 42 (5) (1999) 833–853.

[36] K. Khanafer, K. Vafai, Double-diffusive mixed convection in a lid-driven enclosure filled with a fluid-saturated porous medium, Numerical Heat Transfer: Part A: Applications 42 (5) (2002) 465–486.

[37] A. Al-Amiri, K. Khanafer, J. Bull, I. Pop, Effect of sinusoidal wavy bottom surface on mixed convection heat transfer in a lid-driven cavity, International Journal of Heat and Mass Transfer 50 (9-10) (2007) 1771–1780.

[38] M. Moallemi, K. Jang, Prandtl number effects on laminar mixed convection heat transfer in a lid-driven cavity, International Journal of Heat and Mass Transfer 35 (8) (1992) 1881–1892.

[39] A. J. Chamkha, Hydromagnetic combined convection flow in a vertical lid-driven cavity with internal heat generation or absorption, Numerical Heat Transfer: Part A: Applications 41 (5) (2002) 529–546.

[40] V. Sivakumar, S. Sivasankaran, P. Prakash, J. Lee, Effect of heating location and size on mixed convection in lid-driven cavities, Computers & Mathematics with Applications 59 (9) (2010) 3053–3065.

[41] N. Ouertatani, N. B. Cheikh, B. B. Beya, T. Lili, A. Campo, Mixed convection in a double lid-driven cubic cavity, International Journal of Thermal Sciences 48 (7) (2009) 1265–1272.

[42] A. S. Dogonchi, M. Sadeghi, M. Ghodrat, A. J. Chamkha, Y. Elmasry, R. Alsulami, Natural convection and entropy generation of a nanoliquid in a crown wavy cavity: effect of thermo-physical parameters and cavity shape, Case Studies in Thermal Engineering 27 (2021) 101208.

[43] F. Selimefendigil, H. F. Öztop, Magnetohydrodynamics forced convection of nanofluid in multi-layered u-shaped vented cavity with a porous region considering wall corrugation effects, International Communications in Heat and Mass Transfer 113 (2020) 104551.

[44] A. Shafee, T. Muhammad, R. Alsakran, I. Tlili, H. Babazadeh, U. Khan, Numerical examination for nanomaterial forced convection within a permeable cavity involving magnetic forces, Physica A: Statistical Mechanics and its Applications 550 (2020) 123962.

[45] D. Ebrahimi, S. Yousefzadeh, O. A. Akbari, F. Montazerifar, S. A. Rozati, S. Nakhjavani, M. R. Safaei, Mixed convection heat transfer of a nanofluid in a closed elbow-shaped cavity (cesc), Journal of Thermal Analysis and Calorimetry 144 (6) (2021) 2295–2316.

[46] M. Fayz-Al-Asad, M. Yavuz, M. N. Alam, M. M. A. Sarker, O. Bazighifan, Influence of fin length on magneto-combined convection heat transfer performance in a lid-driven wavy cavity, Fractal and Fractional 5 (3) (2021) 107.

[47] R. Zhang, S. Aghakhani, A. H. Pordanjani, S. M. Vahedi, A. Shahsavar, M. Afrand, Investigation of the entropy generation during natural convection of newtonian and non-newtonian fluids inside the l-shaped cavity subjected to magnetic field: application of lattice boltzmann method, The European Physical Journal Plus 135 (2) (2020) 184.

[48] J. Zheng, L. Zhang, H. Yu, Y. Wang, T. Zhao, Study on natural convection heat transfer in a closed cavity with hot and cold tubes, Science Progress 104 (2) (2021) 00368504211020965.

[49] H. S. Majdi, A. M. Abed, L. J. Habeeb, Mixed convection heat transfer of cuo-h2o nanofluid in a triangular lid-driven cavity with circular inner body, J. Mech. Eng. Res. Dev 44 (2021) 164–175.

[50] M. Hamid, M. Usman, Z. Khan, R. Haq, W. Wang, Heat transfer and flow analysis of casson fluid enclosed in a partially heated trapezoidal cavity, International Communications in Heat and Mass Transfer 108 (2019) 104284.

[51] Z. Khan, W. Khan, M. Hamid, H. Liu, Finite element analysis of hybrid nanofluid flow and heat transfer in a split lid-driven square cavity with y-shaped obstacle, Physics of Fluids 32 (9) (2020) 093609.

[52] H. Sajjadi, A. A. Delouei, M. Atashafrooz, M. Sheikholeslami, Double mrt lattice boltzmann simulation of 3-d mhd natural convection in a cubic cavity with sinusoidal temperature distribution utilizing nanofluid, International Journal of Heat and Mass Transfer 126 (2018) 489–503.

[53] N. Ali, M. Nazeer, T. Javed, F. Abbas, A numerical study of micropolar flow inside a lid-driven triangular enclosure, Meccanica 53 (13) (2018) 3279–3299.

[54] K. M. Gangawane, H. F. Oztop, M. E. Ali, Mixed convection in a lid-driven cavity containing triangular block with constant heat flux: Effect of location of block, International Journal of Mechanical Sciences 152 (2019) 492–511.

[55] F. Selimefendigil, H. F. Öztop, Mixed convection in a partially heated triangular cavity filled with nanofluid having a partially flexible wall and internal heat generation, Journal of the Taiwan Institute of Chemical Engineers 70 (2017) 168–178.

[56] M. Muthtamilselvan, D. H. Doh, Mixed convection of heat generating nanofluid in a lid-driven cavity with uniform and non-uniform heating of bottom wall, Applied Mathematical Modelling 38 (13) (2014) 3164–3174.

[57] K. Vafai, M. Sozen, Analysis of energy and momentum transport for fluid flow through a porous bed (1990).

[58] A. Amiri, K. Vafai, Analysis of dispersion effects and non-thermal equilibrium, non-darcian, variable porosity incompressible flow through porous

media, International Journal of Heat and Mass Transfer 37 (6) (1994) 939–954.

[59] P.-X. Jiang, Z.-P. Ren, Numerical investigation of forced convection heat transfer in porous media using a thermal non-equilibrium model, International Journal of Heat and Fluid Flow 22 (1) (2001) 102–110.

[60] M. Izadi, A. Behzadmehr, D. Jalali-Vahida, Numerical study of developing laminar forced convection of a nanofluid in an annulus, International Journal of Thermal Sciences 48 (11) (2009) 2119–2129.

[61] D. A. Nield, A. Bejan, et al., Convection in porous media, Vol. 3, Springer, 2006.

[62] K. Vafai, Handbook of porous media, Crc Press, 2015.

[63] I. A. Badruddin, A. A. Al-Rashed, N. S. Ahmed, S. Kamangar, K. Jeevan, Natural convection in a square porous annulus, International Journal of Heat and Mass Transfer 55 (23-24) (2012) 7175–7187.

[64] I. A. Badruddin, Z. Zainal, Natural convection through an annular vertical cylindrical porous medium, International Journal of Heat Exchangers 7 (2) (2006) 251–262.

[65] I. A. Badruddin, Z. Zainal, Z. A. Khan, Z. Mallick, Effect of viscous dissipation and radiation on natural convection in a porous medium embedded within vertical annulus, International Journal of Thermal Sciences 46 (3) (2007) 221–227.

[66] I. A. Badruddin, Z. Zainal, P. A. Narayana, K. Seetharamu, Heat transfer by radiation and natural convection through a vertical annulus embedded in porous medium, International Communications in Heat and Mass Transfer 33 (4) (2006) 500–507.

[67] I. A. Badruddin, Z. Zainal, P. A. Narayana, K. Seetharamu, Numerical analysis of convection conduction and radiation using a non-equilibrium model in a square porous cavity, International Journal of Thermal Sciences 46 (1) (2007) 20–29.

[68] I. A. Badruddin, Z. Zainal, P. A. Narayana, K. Seetharamu, Thermal non-equilibrium modeling of heat transfer through vertical annulus embedded with porous medium, International Journal of Heat and Mass transfer 49 (25-26) (2006) 4955–4965.

[69] I. A. Badruddin, N. S. Ahmed, A. A. Al-Rashed, J. Kanesan, S. Kamangar, H. Khaleed, Analysis of heat and mass transfer in a vertical annular porous cylinder using fem, Transport in Porous Media 91 (2) (2012) 697–715.

[70] N. A. Ahamad, M. E. M. Soudagar, I. A. Badruddin, Double diffusion in arbitrary porous cavity: Part i, in: AIP Conference Proceedings, Vol. 1859, AIP Publishing LLC, 2017, p. 020050.

[71] A. A. Nandalur, S. Kamangar, I. A. Badruddin, Heat transfer in a porous cavity in presence of square solid block, International Journal of Numerical Methods for Heat & Fluid Flow (2019).

[72] A. Mahmoudi, I. Mejri, M. A. Abbassi, A. Omri, Lattice boltzmann simulation of mhd natural convection in a nanofluid-filled cavity with linear temperature distribution, Powder Technology 256 (2014) 257–271.

[73] I. V. Miroshnichenko, M. A. Sheremet, H. F. Oztop, K. Al-Salem, Mhd natural convection in a partially open trapezoidal cavity filled with a nanofluid, International Journal of Mechanical Sciences 119 (2016) 294–302.

[74] M. A. Sheremet, H. Oztop, I. Pop, Mhd natural convection in an inclined wavy cavity with corner heater filled with a nanofluid, Journal of Magnetism and Magnetic Materials 416 (2016) 37–47.

[75] S. Parvin, A. Akter, Effect of magnetic field on natural convection flow in a prism shaped cavity filled with nanofluid, Procedia engineering 194 (2017) 421–427.

[76] A. Sahi, D. Sadaoui, N. Sadoun, A. Djerrada, Effects of magnetic field on natural convection heat transfer in a t-shaped cavity, Mechanics & Industry 18 (4) (2017) 407.

[77] R. U. Haq, F. A. Soomro, T. Mekkaoui, Q. M. Al-Mdallal, Mhd natural convection flow enclosure in a corrugated cavity filled with a porous medium, International Journal of Heat and Mass Transfer 121 (2018) 1168–1178.

[78] A. Chamkha, A. Rashad, M. Mansour, T. Armaghani, M. Ghalambaz, Effects of heat sink and source and entropy generation on mhd mixed convection of a *cu*-water nanofluid in a lid-driven square porous enclosure with partial slip, Physics of Fluids 29 (5) (2017) 052001.

[79] L. K. Saha, K. S. Uddin, M. Taher, Effect of internal heat generation or absorption on mhd mixed convection flow in a lid driven cavity, American Journal of Applied Mathematics 3 (1-1) (2015) 20–29.

[80] J. C. Maxwell, A Treatise on Electricity and Magnetism: pt. III. Magnetism. pt. IV. Electromagnetism, Vol. 2, Clarendon press, 1881.

[81] H. Masuda, A. Ebata, K. Teramae, Alteration of thermal conductivity and viscosity of liquid by dispersing ultra-fine particles. dispersion of Al_2O_3, SiO_2 and TiO_2 ultra-fine particles (1993).

[82] S. U. Choi, J. A. Eastman, Enhancing thermal conductivity of fluids with nanoparticles, Tech. rep., Argonne National Lab., IL (United States) (1995).

[83] B. C. Pak, Y. I. Cho, Hydrodynamic and heat transfer study of dispersed fluids with submicron metallic oxide particles, Experimental Heat Transfer an International Journal 11 (2) (1998) 151–170.

[84] S. P. Jang, S. U. Choi, Role of brownian motion in the enhanced thermal conductivity of nanofluids, Applied Physics Letters 84 (21) (2004) 4316–4318.

[85] K. S. Hwang, S. P. Jang, S. U. Choi, Flow and convective heat transfer characteristics of water-based Al_2O_3 nanofluids in fully developed laminar flow regime, International Journal of Heat and Mass Transfer 52 (1-2) (2009) 193–199.

[86] J. Maxwell, Electricity and magnetism, part ii, 3rd edn, clarendon (1904).

[87] R. L. Hamilton, O. Crosser, Thermal conductivity of heterogeneous two-component systems, Industrial & Engineering Chemistry Fundamentals 1 (3) (1962) 187–191.

[88] Q. Xue, Model for thermal conductivity of carbon nanotube-based composites, Physica B: Condensed Matter 368 (1-4) (2005) 302–307.

[89] A. Einstein, A new determination of molecular dimensions, Ann. Phys. 19 (1906) 289–306.

[90] A. Einstein, On the theory of the brownian movement, Ann. Phys 19 (4) (1906) 371–381.

[91] A. Einstein, Berichtigung zu meiner arbeit: Eine neue bestimmung der moleküldimensionen, Annalen Der Physic 339 (3) (1911) 591–592.

[92] H. C. Brinkman, The viscosity of concentrated suspensions and solutions, The Journal of Chemical Physics 20 (4) (1952) 571–571.

[93] R. K. Tiwari, M. K. Das, Heat transfer augmentation in a two-sided lid-driven differentially heated square cavity utilizing nanofluids, International Journal of Heat and Mass Transfer 50 (9-10) (2007) 2002–2018.

[94] R. U. Haq, S. N. Kazmi, T. Mekkaoui, Thermal management of water based swcnts enclosed in a partially heated trapezoidal cavity via fem, International Journal of Heat and Mass Transfer 112 (2017) 972–982.

[95] M. Paroncini, F. Corvaro, Natural convection in a square enclosure with a hot source, International Journal of Thermal Sciences 48 (9) (2009) 1683–1695.

[96] S. Sivasankaran, A. Malleswaran, J. Lee, P. Sundar, Hydro-magnetic combined convection in a lid-driven cavity with sinusoidal boundary conditions on both sidewalls, International Journal of Heat and Mass Transfer 54 (1-3) (2011) 512–525.

[97] M. Levin, M. Miller, Maxwell a treatise on electricity and magnetism, Uspekhi Fizicheskikh Nauk 135 (3) (1981) 425–440.

[98] F. Selimefendigil, H. F. Öztop, A. J. Chamkha, Mhd mixed convection and entropy generation of nanofluid filled lid driven cavity under the influence of inclined magnetic fields imposed to its upper and lower diagonal triangular domains, Journal of Magnetism and Magnetic Materials 406 (2016) 266–281.

[99] B. Ghasemi, S. Aminossadati, Mixed convection in a lid-driven triangular enclosure filled with nanofluids, International Communications in Heat and Mass Transfer 37 (8) (2010) 1142–1148.